Electron Wave Packet Dynamics on the Attosecond Time Scale

Klünder, Kathrin

2012

Electron Wave Packet Dynamics on the Attosecond Time Scale

Kathrin Klünder

Doctoral Thesis
2012

Lund University

Electron Wave Packet Dynamics on the Attosecond Time Scale

Printed in Sweden by Media-Tryck, Lund, 2012

Division of Atomic Physics
Department of Physics
Faculty of Engineering, LTH
Lund University
P.O. Box 118
SE–221 00 Lund
Sweden

http://www.atomic.physics.lu.se

ISSN: 0281-2762
Lund Reports on Atomic Physics, LRAP-457

ISBN: 978-91-7473-334-1

“Daß ich erkenne, was die Welt
Im Innersten zusammenhält.”

Goethes “Faust. Der Tragödie erster Teil”

Abstract

One objective of attosecond science is to study electron dynamics in atoms and molecular systems on their natural time scale. This can be done using attosecond light pulses. Attosecond pulses are produced in a process called high-order harmonic generation, in which a short, intense laser pulse interacts with atoms or molecules in a highly nonlinear process, leading to the generation of high-order frequencies of the fundamental laser with a large spectral bandwidth, supporting pulses with attosecond duration. In some condition the harmonics are locked in phase leading to a train of attosecond pulses or, in some cases, to a single attosecond pulse. This thesis presents experiments based on interferometry to study electron dynamics using attosecond pulses.

The first part describes a series of experiments, in which the dynamics of electrons was studied after photoionization with an attosecond pulse train. The time resolution in these experiments was achieved by measuring the accumulated phase of the free electron wave packet after photoemission using an interferometric technique. The phase carries temporal information about the ionization process, from which the delay in photoemission can be determined with a much better time resolution than that given by the temporal structure of the pulse train. The same technique was applied to investigate the phase behavior of resonant two-photon ionization in helium atoms.

The second part describes the application of an interferometric pump-probe technique to characterize bound electron wave packets. Single attosecond pulses are used to excite a broad electron wave packet containing bound and continuum states. The bound part of the wave packet is further ionized by an infrared laser with a variable delay. Analysis of the resulting interferogram allows for full reconstruction of the bound wave packet, since both the amplitude and the phase of all ingoing states in the wave packet are encoded in the interference pattern.

Populärvetenskaplig sammanfattning

Har en galopperande häst vid något tillfälle alla hovarna i luften samtidigt? Den här till synes enkla frågan är inte helt enkel att svara på eftersom det inte går att avgöra med blotta ögat om så är fallet. För att avgöra om hovarna verkligen är i luften på samma gång behöver vi andra redskap med bättre tidsupplösning än våra ögon. Första gången någon lyckades göra en sådan mätning var 1878 då Eadweard Muybridge med hjälp av en nyutvecklad kamera kunde ta en serie bilder av en galopperande häst. Den bildsekvensen visade med all tydlighet att alla hovarna vid vissa tillfällen verkligen är i luften samtidigt. Att experimentet lyckades berodde framförallt på den förbättrade bildkvaliten som Muybridge lyckades uppnå. Om man vill ta skarpa bilder av ett föremål i rörelse måste kamerans slutartid vara tillräckligt kort och Muybridge kamera hade en slutartid på 1 ms (1 ms = 10^{-3} s) vilket i slutet av 1800-talet betraktades som ultrasnabbt. För att avbilda ännu snabbare förlopp behövs ännu kortare slutartider, men tillslut begränsas slutartiden av vad som är mekaniskt möjligt att åstadkomma. En alternativ metod är att låta slutaren vara öppen hela tiden och istället belysa föremålet som ska avbildas med en kort ljusblixt.

En galopperande häst rör sig väldigt långsamt jämfört med mikroskopiska objekt och att avbilda föremål i mikrokosmos är därför ännu mer utmanande. Vattenmolekyler rör sig till exempel genom en lösning på en pikosekundstidsskala (1 ps = 10^{-12} s) medan atomer rör sig ännu fortare och måste avbildas på en femtosekundstidsskala (1 fs = 10^{-15} s). I allmänhet rör sig föremål fortare ju lättare de är. En elektron som är 2000 gånger lättare än den lättaste atomen rör sig därför mycket fortare. För en elektron i en väteatom tar det till exempel bara 150 as (1 as = 10^{-18} s) att ta sig ett varv runt kärnan.

2001 lyckades två oberoende grupper för första gången att skapa och mäta attosekundspulser. Det öppnade helt nya möjligheter att studera elektronrörelser i realtid och ett nytt

forskningsområde som kallas attofysik såg dagens ljus. Teknikerna som används påminner i mycket om Muybridges ursprungliga experiment, men inte med mekaniska slutare. Elektroner studeras med något som kallas pump-prob teknik där elektronrörelsen startas av pumpen, en kort attosekundspuls, och senare fångas av en andra ljuspuls (proben). Tiden mellan de tvåpulserna måste kontrolleras och varieras med extremt hög noggrannhet. Att ta en serie bilder för olika tidsintervaller mellan de tvåljuspulserna gör det möjligt att följa elektronernas rörelser på ungefär samma sätt som Muybridge studerade hästen.

I den här avhandlingen presenteras flera olika studier av elektrondynamik. Antingen förblir elektronen bunden i atomen efter att den har växelverkat med pumppulsen, eller så tvingas den lämna atomen via fotojonisation. Den fotoelektriska effekten som fram tills nyligen antogs ske momentant tar faktiskt en liten stund. Efter det att ljuspulsen träffar atomen, tills det att elektronen lossnar hinner en kort tid passera, det är en kort tid, men den är inte försumbar.

List of Publications

This thesis is based on the following papers, which will be referred to in the text by their roman numerals.

I **Atomic and Macroscopic Measurements of Attosecond Pulse Trains**
J. M. Dahlström, T. Fordell, E. Mansten, T. Ruchon, M. Swoboda, K. Klünder, M. Gisselbrecht, A. L'Huillier and J. Mauritsson.
Phys. Rev. A **80**, 033836 (2009).

II **Probing Single-Photon Ionization on the Attosecond Time Scale**
K. Klünder, J. M. Dahlström, M. Gisselbrecht, T. Fordell, M. Swoboda, D. Guénot, P. Johnsson, J. Caillat, J. Mauritsson, A. Maquet, R. Taïeb and A. L'Huillier.
Phys. Rev. Lett. **106**, 143002 (2011).

III **Photoemission Time-Delay Measurements and Calculations close to the 3s Ionization Minimum in Argon**
D. Guénot, K. Klünder, C. L. Arnold, D. Kroon, J. M. Dahlström, M. Miranda, T. Fordell, M. Gisselbrecht, P. Johnsson, J. Mauritsson, E. Lindroth, A. Maquet, R. Taïeb, A. L'Huillier and A.S. Kheifets.
(2012) *Accepted for publication in Phys. Rev. A* .

IV **Theory of Attosecond Delays in Laser-Assisted Photoionization**
J. M. Dahlström, D. Guénot, K. Klünder, M. Gisselbrecht, J. Mauritsson, A. L'Huillier, A. Maquet and R. Taïeb.
(2012) *Accepted for publication in Chem. Phys.*.

V **Phase Measurement of Resonant Two-Photon Ionization in Helium**
M. Swoboda, T. Fordell, K. Klünder, J. M. Dahlström, M. Miranda, C. Buth, K. J. Schafer, J. Mauritsson, A. L'Huillier and M. Gisselbrecht.
Phys. Rev. Lett. **104**, 103003 (2010).

VI **Attosecond Pump-Probe Electron Interferometry**
J. Mauritsson, T. Remetter, M. Swoboda, K. Klünder, A. L'Huillier, K. J. Schafer, O. Ghafur, F. Kelkensberg, W. Siu, P. Johnsson, M. J. J. Vrakking, I. Znakovskaya, T. Uphues, S. Zherebtsov, M. F. Kling, F. Lépine, E. Benedetti, F. Ferrari, G. Sansone and M. Nisoli.
Phys. Rev. Lett. **105**, 053001(2010).

VII **Reconstruction of Attosecond Electron Wave Packets with Quantum State Holography**
K. Klünder, P. Johnsson, M. Swoboda, A. L'Huillier, M. J. J. Vrakking, K. J. Schafer and J. Mauritsson.
(2012) *Manuscript in preparation.*

VIII **Attosecond Stark Effect in Molecules**
Ch. Neidel, J. Klei, C. Yang, A. Rouzée, M. J. J. Vrakking; K. Klünder, M. Miranda, C. Arnold, T. Fordell, A. L'Huillier, M. Gisselbrecht, P. Johnsson and F. Lépine.
(2012) *Manuscript in preparation.*

Abbreviations

APT	Attosecond Pulse Train
AOPDF	Acousto Optic Programmable Dispersive Filter
CEO	Carrier Envelope Offset
CI	Configuration Interaction
CPA	Chirped Pulse Amplification
EWP	Electron Wave Packet
FSCI	Final State Configuration Interaction
FROG	Frequency-Resolved Optical Gating
FROG-CRAB	FROG for Complete Reconstruction of Attosecond Bursts
FWHM	Full Width at Half Maximum
GD	Group Delay
GDD	Group Delay Dispersion
HF	Hartree-Fock
HHG	High-Order Harmonic Generation
IR	Infra Red
ISCI	Initial State Configuration Interaction
MBES	Magnetic Bottle Electron Spectrometer
R2PI	Resonant 2-Photon Ionization
RABITT	Reconstruction of Attosecond Beating by Interference of Two-photon Transitions
RPAE	Random-Phase-Approximation with Exchange
SAP	Single Attosecond Pulse
TOF	Time Of Flight
VMIS	Velocity Map Imaging Spectrometer
XUV	eXtreme Ultraviolet

Contents

Papers

Chapter 1

Introduction

"Does a horse take all four hooves off the ground while galloping?" This seemingly simple question was not easy to answer. The human visual system is not capable of resolving the motion of the horse's hooves when it is galloping. To understand the course of movements in the horse's stride we have to apply suitable tools. In 1878 the photographer Eadweard Muybridge used animated photography to capture the motion of a galloping horse in a series of pictures, such as shown in Figure 1.1, and could prove in this way that there is indeed an instance in time when all four of the horse's hooves are in the air. Two things were essential to resolve the horse's stride. Firstly, the series of photographs had to be taken sufficiently rapidly to capture the complete course of movements. In this case a photograph was taken every millisecond ($1\ \text{ms} = 10^{-3}\ \text{s}$). Additionally, to get a sharp image, the shutter speed of the camera had to be faster than the speed of the moving object, so Muybridge also needed a shutter time of about 1 ms. At the end of the 19th century 1 ms was considered to be ultrafast, and in a way, Muybridge's study of the galloping horse can be regarded as the first ultrafast experiment.

"How long does it take an electron to escape from an atom?" A racing horse is very slow compared to events on the atomic scale, and studying motion in the quantum world is far more challenging. Water molecules move through a solution on the picosecond time scale ($1\ \text{ps} = 10^{-12}\ \text{s}$), while atoms move and form bonds to become molecules within femtoseconds ($1\ \text{fs} = 10^{-15}\ \text{s}$) [2]. In general, the lighter a particle the faster it will travel. An electron is almost 2000 times lighter than the lightest nucleus, and the electrons that orbit a nucleus thus move much faster than the nucleus itself. In the lightest atom, hydrogen, it takes the single electron only 150 attoseconds ($1\ \text{as} = 10^{-18}\ \text{s}$) to complete one orbit.

To capture such rapid events, extremely short shutter times

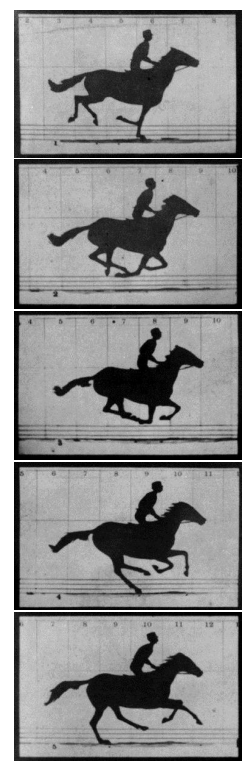

Figure 1.1. *A series of photographs reveal the horse's course of movements [1].*

are needed, but the shutter speed is ultimately limited by the underlying mechanics of the camera. An alternative approach is to use a slow shutter together with very short flashes of light (also called light pulses) to illuminate the object. Light pulses with a duration of attoseconds are needed to resolve the motion of electron.

A fundamental relation states that the product of the duration and the bandwidth[1] of a light pulse is equal to, or greater than, a constant of the order of one, i.e., $\Delta\tau\Delta\nu \geq 1$. This implies, that if we want to generate short pulses we have to include more light frequencies. But even if we would include the complete visible spectrum, from red up to violet, this would only allow pulse durations on the order of 1 fs, which is not short enough to resolve the motion of electrons. A much larger bandwidth is needed, and the main challenge was and still is to generate such a large bandwidth. Shortly after the discovery of a process called high-order harmonic generation (HHG) in 1987 [3, 4] possibilities were explored to use the process for the generation of attosecond pulses [5–8]. In HHG, a short laser pulse, nowadays usually femtoseconds long, interacts with atoms or molecules in a highly nonlinear process, leading to the generation of new frequencies that are multiples of the laser frequency, resulting in a large bandwidth that supports attosecond pulse durations. The first attosecond light pulses were measured by two independent research groups in 2001, first as a train of attosecond pulses by Paul *et al.* [9] and shortly after as single attosecond pulses by Hentschel *et al.* [10]. This provided the opportunity to study electron motion in real time and led to the new field of research called attosecond physics.
The techniques used to study electrons are similar to Muybridge's original idea, but due to the short time scale it is difficult to know when to make the exposure and also how to take a sufficient number of photographs within these short time periods. Electron motion is therefore studied with a technique called the *pump-probe* method. First, the electron dynamics is initiated by a light pulse (the pump pulse), then the motion is captured using a second pulse (the probe pulse), where the timing between the two pulses can be set with very high accuracy. Repeated pumping and probing at different time intervals provides a series of images from which the electron motion can be followed, similar to Muybridge's photographs of the galloping horse. The pump-probe technique was used by Ahmed H. Zewail to resolve chemical reactions on the femtosecond time scale, and in 1999 he was awarded with the Nobel Prize in Chemistry for his work [11].
The first attosecond pump-probe experiment using single attosec-

[1] The bandwidth is a measure for the range of frequencies ν that together form a light pulse.

ond pulses was reported in 2002 by Drescher *et al.* [12]. For the first time, the emission of an Auger electron resulting from ionization of an atom could be followed in real time. Using similar techniques, attosecond pulses have been used to study other processes such as atomic photoexcitation [13] and ionization [14, 15], as well as electron dynamics in solids [16] and molecules [17].

1.1 Aim and Outline of this Thesis

Attosecond pulses were measured for the first time in Lund in 2003 [18], and reliable techniques for the generation [19–22] and characterization [18, 23, 24] of attosecond pulses were established soon thereafter. Effective post-generation pulse compression was demonstrated leading to attosecond pulse durations of 130 as, the shortest pulses generated at that time [25]. When I started my PhD studies at the end of 2007 the main focus of attosecond research in Lund was shifting towards the application of attosecond pulse trains [26–29], and the content of this thesis reflects this transition. Paper **I** describes in detail a proposed method for the characterization of attosecond pulses [30], while all the other papers included in this thesis present applications of attosecond pulses to atomic and molecular physics.

The main measurement technique applied in the work presented here is interferometry. Interferometry is a measurement technique in which coherent waves are superimposed to determine their phase difference by measuring intensity modulations. It is a very powerful tool since small changes in phase, and also wavelength lead to considerable changes in the intensity of the signal. Trains of attosecond pulses have relatively good spectral resolution, but are, at first sight, not directly applicable in pump-probe experiments due to the ambiguity of the excitation event. In the series of experiments described in Papers **II**, **III** and **IV** this limitation was circumvented by measuring the phase of an electron wave packet after ionization with an attosecond pulse train using an interferometric technique. The phase carries temporal information, and it was thus possible to study time delays in photoionization with a much better time resolution than given by the temporal structure of the pulse train. The same technique was applied to investigate the phase behavior of resonant two-photon ionization of helium atoms (Paper **V**). Papers **VI** and **VII** present a pump-probe technique using single attosecond pulses. By using a delayed probe pulse combined with an interferometric technique a better spectral resolution was achieved than that given by the broad spectral bandwidth of the single attosecond pulse. Since the phase information is also preserved, a full reconstruction of arbitrary excited bound-electron wave packets was possible.

Paper **VIII** describes how the time-dependent polarization of a

neutral molecule under the influence of an IR laser field was studied by measuring the changes in the ionization yield using attosecond pulse trains.
The structure of this thesis is as follows. This introduction concludes with the connection between the electron wave packets considered in this work and the attosecond pulses used to create them. Chapter 2 introduces the underlying physics of attosecond pulse generation and describes the experimental realization together with the essential characterization methods. Chapter 3 concentrates on the theoretical framework needed to describe the formation of the electron wave packets by means of the excitation and ionization of atoms with attosecond pulses. This chapter extends from well established descriptions of light-matter interactions to the novel theoretical results obtained in connection with the interpretation of experimental results present in this work. Chapter 4 summarizes the results given in the previous chapters and presents examples of interferometric measurement techniques to study electron dynamics using attosecond pulses. The concluding chapter, Chapter 5, gives a summary and outlook.

1.2 From Optical Wave Packets to Electron Wave Packets

The electron wave packets (EWPs) studied are the result of the interaction of atoms with attosecond pulses, which are described in terms of optical wave packets. These optical wave packets will partially imprint their properties on the EWPs through the interaction with the atom, so it is worth looking at their properties.
Optical wave packets can be described as the sum of monochromatic waves that obey the electromagnetic wave equation. The resulting electric field is given by:[2]

$$E(\mathbf{r},t) = \int d\Omega\ \tilde{E}(\Omega)\, e^{i(\mathbf{k}(\Omega)\mathbf{r}-\Omega t)}, \tag{1.1}$$

where $\Omega = 2\pi\nu$ is the angular frequency and $\mathbf{k}$ the wave vector. $\tilde{E}(\Omega)$ is the spectral amplitude that defines the spectral content of the optical wave packet. In general, $\tilde{E}(\Omega)$ is complex, so $\tilde{E}(\Omega) = |\tilde{E}(\Omega)|\exp[i\phi_i(\Omega)]$, where $\phi_i(\Omega)$ is the intrinsic phase of each spectral component. Using the dispersion relation $k(\Omega) = \Omega n(\Omega)/c$, where $n(\Omega)$ is the refractive index, Equation (1.1) can be rewritten for a fixed position in space as:

$$E(t) = \int d\Omega\ \tilde{E}(\Omega)\, e^{-i\Omega t + i\phi_p(\Omega)}, \tag{1.2}$$

where $\phi_p(\Omega)$ is the phase accumulated during propagation. The resulting spectral phase $\phi(\Omega)$ is then given by $\phi(\Omega) = \phi_i(\Omega) +$

[2] The magnetic component will be neglected in the following.

$\phi_p(\Omega)$. The group delay (GD), which is a measure of the relative delay of different spectral components, can be defined as:

$$\mathrm{GD} = \frac{d\phi(\Omega)}{d\Omega}. \tag{1.3}$$

The variation in GD is called the group delay dispersion (GDD) and can be expressed as:

$$\mathrm{GDD} = \frac{d^2\phi(\Omega)}{d\Omega^2}. \tag{1.4}$$

GD and GDD are commonly used to describe optical wave packets such as attosecond pulses.
Alternatively, the phase properties of an optical wave packet can be described in the time domain by the temporal phase $\phi(t)$, which is defined the complex phase of $E(t)$, and from this the instantaneous frequency of a pulse can be defined as:

$$\frac{d\phi(t)}{dt} = \Omega(t)\,. \tag{1.5}$$

If $\Omega(t)$ varies in time, the pulse is said to be chirped with a chirp rate given by $d^2\phi(t)/dt^2 = a(t)$. A constant chirp rate, a, corresponds to a linear change in $\Omega(t)$ with time. A chirp is equivalent to a GDD $\neq 0$.
The pulse duration, Δt, is usually given as the Full Width at Half Maximum (FWHM) of the intensity $I(t) = |E(t)|^2$. Similarly, the spectral bandwidth, $\Delta\Omega$, is defined as the FWHM of the spectral intensity, $S(\Omega) = |\tilde{E}(\Omega)|^2$. Together they form the time-bandwidth product, which sets the lower limit on the pulse duration for a given bandwidth. For a Gaussian pulse, the time-bandwidth product is given by $\Delta t\Delta\Omega = 4\ln 2\sqrt{1+a^2}$. When the chirp rate is equal to zero the pulse is said to be transform limited, which means that the pulse duration is as short as the bandwidth allows, while a chirped pulse exhibits a longer duration.

In the same manner, a free-EWP can be defined as the coherent sum of plane waves that satisfies the free Schrödinger equation for a free particle:

$$\Psi(\mathbf{r},t) = \int d\mathbf{k}\; g(\mathbf{k})\, e^{i(\mathbf{k}(\omega)\mathbf{r}-\omega t)}. \tag{1.6}$$

$\mathbf{k}$ is the wave vector which is related to the electron momentum $\mathbf{p}$ via the de Broglie relation $\mathbf{p} = \hbar\mathbf{k}$, where $|\mathbf{k}| = 2\pi/\lambda_{deB}$. The interesting quantity is the complex momentum envelope $g(\mathbf{k})$. The interaction between an attosecond pulse and an atom or molecule that leads to the formation of an EWP is usually described by perturbation theory. In this case, $g(\mathbf{k})$ can be written as:

$$g(\mathbf{k}) \approx \tilde{E}(\Omega)\cdot\mu_{\mathbf{k}i}, \tag{1.7}$$

where $\mu_{\mathbf{k}i}$ gives the atomic details of the interaction for an electron initially in state i. The complex envelope depends directly on $\tilde{E}(\Omega)$ and the momentum components $\mathbf{k}$ are given by energy conservation: $E = \hbar k^2/2m = \hbar\Omega - I_p$, where I_p is the ionization potential. The intrinsic phase of the attosecond pulses will be transferred to the EWP. However, the EWP is far more than just an electronic replica of the ionizing pulse. The atom or molecule from which the EWP originates will imprint its unique signature on the amplitude and phase of $g(\mathbf{k})$ and influence the dynamics of the EWP in the form of $\mu_{\mathbf{k}i}$. The first generation of attosecond experiments used the EWP to study and characterize the attosecond pulses by concentrating on $\tilde{E}(\Omega)$. The well characterized attosecond pulses available today allow attosecond physicists to turn their attention more and more to the atomic signature on the EWP to study its creation and the connected electron dynamics.

Chapter 2

Attosecond Pulse Generation

Attosecond pulses are the tool used for the study of electron dynamics presented in this thesis. This chapter provides an introduction to the theory and the experimental realization of these pulses. First, the underlying process of high-order harmonic generation is reviewed using classical arguments. The second part of this chapter provides a detailed introduction to the generation and metrology of attosecond pulse trains, while the last section gives an overview of single attosecond pulse generation and characterization.

2.1 High-order Harmonic Generation

Attosecond pulses are generated when intense laser pulses are focused into a diffuse ensemble of atoms.[1] The basic aspects are illustrated in Figure 2.1. Each atom will respond to the laser field by the emission of high-order harmonics of the fundamental laser frequency ω. The details of this microscopic response will be covered in Section 2.1.1. Apart from the single-atom response, the effects of collective emission must be taken into account, and this will be discussed in Section 2.1.2. Post-generation pulse shaping in frequency and time can then be applied. Examples are given Section 2.2.1.

2.1.1 Microscopic Physics

An intuitive understanding of the interaction between atoms and strong laser fields is given by a semi-classical three-step model [31, 32]. For laser pulses with intensities exceeding $10^{13}\,\mathrm{W/cm^2}$ the electric field of the laser pulse becomes comparable to the strength of the binding Coulomb potential. Under these conditions, the

[1] Alternative generation media such as molecules or solid surfaces will not be considered in this thesis.

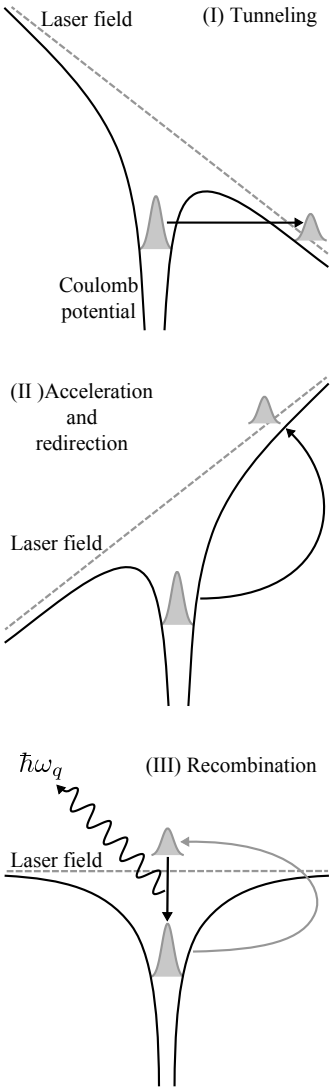

Figure 2.2. *The three-step model for high-harmonic generation.*

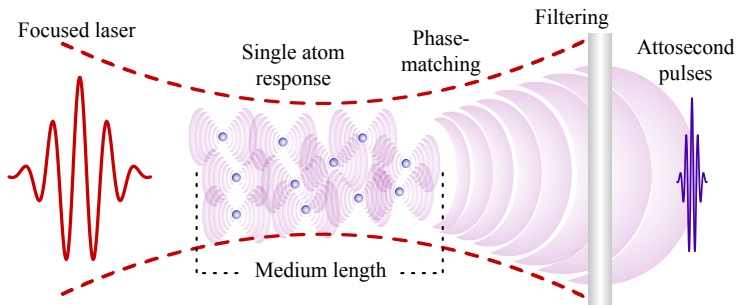

Figure 2.1. *Schematic overview of attosecond pulse generation.*

electron may tunnel through the Coulomb barrier modified by the presence of the assumed, slowly varying, linearly polarized electric field, as depicted in Figure 2.2. After tunnel ionization, which is considered as step (I), the electron is treated as a classical particle. In the following step (II) the electron is accelerated by the oscillating laser field and gains kinetic energy, E_{kin}. During the motion of the electron in the continuum, the Coulomb potential of the remaining nucleus is assumed to be small. Depending on the phase of the electric field at the time of ionization, t_i, the electron can be redirected and driven back to the vicinity of the nucleus at a return time t_r. It may then recombine to the ground state emitting a photon with an energy that is given by the ionization potential of the atom, I_p, plus E_{kin}. The recombination and subsequent emission of radiation is considered to be step (III).
Useful information about the harmonic radiation can be gained by solving Newton's equation of motion of the unbound electron during the excursion. Figure 2.3 shows the trajectories for the charged particle in the laser field, simply described as $E = E_0 \sin \omega t$. Within the first half of the optical cycle, T, only electrons tunneling between $T/4$ and $T/2$ will contribute to the generation of harmonics, as shown by the black curves in Figure 2.3. The process will then repeat itself every half-cycle. Figure 2.4 illustrates the relationship between t_r and E_{kin} for the recombining electrons. The maximum energy is equal to 3.17 U_p, where U_p is the ponderomotive energy defined as the quiver motion of the electron in the oscillating laser field averaged over one period:

$$U_p = \frac{e^2}{2m_e\omega^2} \cdot \frac{I}{\epsilon_0 c}, \tag{2.1}$$

where I is the laser intensity. The maximum photon energy at the so-called cutoff is thus given by:

$$\hbar\omega_c = I_p + 3.17U_p. \tag{2.2}$$

It is apparent from Figure 2.4 that, apart from the cutoff region, there are always two trajectories leading to the same kinetic energy. They differ in the excursion time, t_{exc}, of the electron in the continuum, which is also depicted in Figure 2.4. Two kinds of trajectories are then defined depending on whether they are longer or shorter than the cutoff trajectory.

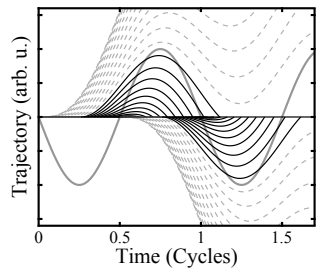

Figure 2.3. *Classical electron trajectories for different ionization times t_i. Trajectories in black are redirected to the parent ion. Also shown is the electric field of the laser (*solid gray line*).*

Time and Frequency Picture

In a more complete description, the three-step process will repeat itself every half-cycle as long as the intensity during the pulse duration is sufficient for tunnel ionization, and the gas is not completely ionized. During every half-cycle, a short burst of light with a duration shorter than one 1 fs will be emitted.[2] For multi-cycle pulses this leads to an attosecond pulse train (APT) with a spacing of $T/2$ in time. Interference will occur between the multiple emission events. In the frequency domain this will give rise to a frequency comb with a spacing of 2ω, which is the inverse of $T/2$. Consider the resulting electric field of one harmonic frequency, $\Omega = q\omega$, for two consecutive emission events, as shown in Figure 2.5:

$$E(t) = \hat{E}(t)\, e^{-i\Omega t} + \hat{E}(t + T/2)\, e^{-(i\Omega t + i\Omega T/2)}, \qquad (2.3)$$

where $\hat{E}(t + T/2) = -\hat{E}(t)$ due to the symmetry of the process. The expression for $E(t)$ depends on the phase difference, $\Omega T/2 = q\pi$, and vanishes if q is even, so that only odd harmonic orders will be observed.

One way to break the symmetry and produce even harmonics is to apply an asymmetric field to the atom. This can be done by introducing a small fraction of the second harmonic of the fundamental field into the generation process. The generation of even harmonics can be optimized by varying the ratio of the amplitudes and the phase between the two fields. This so-called two-color generation is described in Paper **I**.

For very short, few-cycle laser pulses the intensity required for HHG may only occur during one half-cycle, leading to the emission of only one isolated pulse with a broad continuous frequency spectrum. This calls for a controlled carrier envelope phase (CEP) of the driving field.

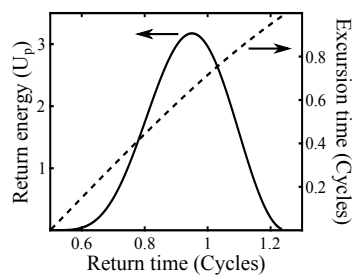

Figure 2.4. *Kinetic energy as a function of return times t_r (*solid line*) and corresponding time spent in the continuum (*dashed line*).*

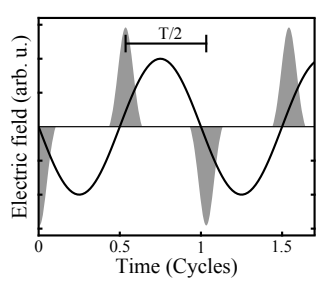

Figure 2.5. *Illustration of the symmetry in HHG.*

Phase Properties

In the classical picture, each harmonic order arises from a different electron trajectory with a different return time t_r. The temporal distribution of kinetic energies is transferred to the emitted light

[2] Assuming a fundamental wavelength of 800 nm, corresponding to $T = 2.67$ fs.

burst, causing a variation in the spectral phase of the attosecond pulse. The group delay of an attosecond pulse is then given by:

$$t_r = \mathrm{GD} = \frac{\partial \phi}{\partial \omega}, \tag{2.4}$$

where $\omega = (E_{kin} + I_p)/\hbar$. The short trajectories are positively chirped (compare Figure 2.4):

$$\partial t_r / \partial \omega = \partial^2 \phi / \partial \omega^2 > 0 \tag{2.5}$$

The chirp can be approximated as being linear over a large range of energies, leading to a constant group delay dispersion [24]. The long trajectories show the opposite behavior. Since, in principle, all trajectories contribute to harmonic emission, this would lead to a distorted temporal profile [7]. In attosecond experiments usually only the short trajectories are selected by choosing the correct phase matching conditions and a hard aperture in the beam, as explained below.

2.1.2 Macroscopic Effects

Besides the single-atom response, collective effects must to be considered to account for all the properties of the harmonic signal, especially the intensity. Different macroscopic effects, such as reabsorption of the generated harmonics and propagation of the fields in the generating media, come into play [33].
The most important factor for efficient energy transfer between the driving laser field and the harmonic fields is phase matching, which is achieved if each individual atom emits in phase with the rest of the ensemble. The generalized phase matching condition in the strong-field regime is given by [34]:

$$\mathbf{k}_q = q\mathbf{k} + \nabla \Phi_q, \tag{2.6}$$

where $\mathbf{k}$ is the wave vector of the fundamental and $\mathbf{k}_q$ is the wave vector of the q$^{\mathrm{th}}$ harmonic. Φ_q denotes the phase of the component oscillating at $q\omega$ of the laser induced atomic dipole moment and is governed by the accumulated phase of the electron wave packet along the trajectories leading to the emission of harmonic q. It can be approximated by $\Phi_q \simeq U_p t_{exc} \simeq -\alpha I$, where the coefficient α depends on the harmonic order and on the excursion time, t_{exc}, spent in the continuum [24]. It is interesting that α depends on t_{exc} because it implies that the phase matching conditions will be different for the long and short trajectories.
Different effects may lead to a wave vector mismatch, $\Delta\mathbf{k} \neq 0$, between $\mathbf{k}$ and $\mathbf{k}_q$. One such effect is the dispersion of the fundamental field. Although the gas densities are very small, dispersion arises from the neutral atoms, leading to $\Delta\mathbf{k}_{atom}$. Another contribution, $\Delta\mathbf{k}_e$, originates from the free electron

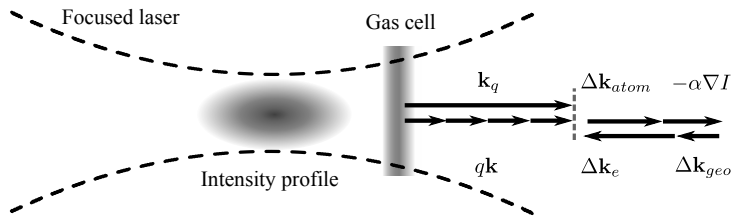

Figure 2.6. *Optimized on-axis phase matching condition [35].*

density inherent to the generation process. The dispersion caused by the neutral atoms is of the opposite sign to the free-electron dispersion. Another possible source of phase mismatch, $\Delta\mathbf{k}_{geo}$, is of geometrical origin. Focusing a Gaussian beam will lead to an additional phase variation, the Gouy phase shift, across the focus. This mainly affects the fundamental field.

The sign and magnitude of the dipole phase factor, $-\alpha\nabla I$, depends on the position both along and perpendicular to the beam direction in the focal volume. The main challenge in the laboratory is to find experimental conditions where all these contributions cancel each other out. Different parameters are available to experimentalists, e.g., gas pressure and medium length, laser intensity, focusing parameters (for example, focal length or guided focusing) and the relative position of the focus and generating medium. Figure 2.6 presents an example of optimized on-axis phase matching for HHG in a gas cell [35]. Here, the medium is located behind the focus, which minimizes the geometrical contribution. In addition, the intensity gradient is negative and thus the contribution of the dipole phase is positive, and compensates for the geometric and electronic dispersion. Normally, in this configuration, only a small contribution of the dipole phase is needed to achieve phase-matching, thus favoring on-axis phase matching for short trajectories. Phase matching for the harmonic radiation originating from the long trajectories will be realized off-axis, leading to a greater divergence. It can therefore be easily blocked using a hard aperture in the beam, providing a cleaner time structure of the attosecond pulses [24]. At optimized generation conditions, an energy conversion efficiency of 10^{-6} to 10^{-4} into one harmonic peak can be achieved, depending on the generating gas [33, 36, 37].

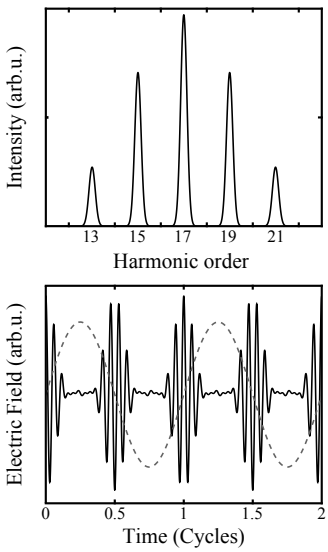

Figure 2.7. *An APT in the frequency and time domain. (top) A harmonic spectrum. (bottom) Harmonics 13 to 21 add up constructively.*

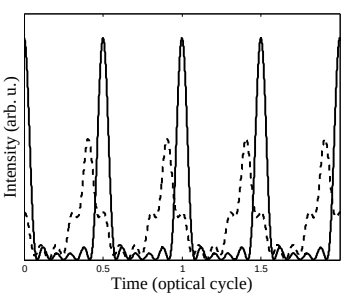

Figure 2.8. *Resulting intensity profile in time for an APT with a flat phase relationship (solid curves) and with a linear chirp (dashed curves).*

2.2 Attosecond Pulse Trains

An APT is generated by the process of HHG, when a short, intense laser pulse is focused into an ensemble of atoms, as described in the previous section. The laser pulses generated in the attosecond laboratory at Lund University in this work have a pulse duration of about 35 fs at a central wavelength of 800 nm, and a standard pulse energy of 3 mJ per pulse. For a wavelength of 800 nm, which is equal to a period of $T = 2.67$ fs, this corresponds to approximately 10 cycles with sufficient intensity for HHG, assuming a Gaussian intensity profile in time. The resulting 20 emission events have a duration of less than 1 fs, and form a train of attosecond pulses. Due to the repetition of the process the frequency spectrum of the APT will exhibit a frequency comb of odd harmonics of the driving laser field. The spectral width of each harmonic peak is inverse proportionally to the number of events, N. A single emission corresponds to a broad structure-less continuum. With increasing N the harmonic peaks become sharper (analogous to the increasing *finesse* of a Fabry-Pérot etalon). This leads to a good spectral resolution combined with attosecond time resolution, which was used in Papers **II**, **III** and **V**.

Although the origin of attosecond pulses can be understood in the time domain, it is convenient to describe the pulse properties in the frequency domain, in analogy with conventional optics. The process of HHG produces a comb of high-order harmonics with photon energies ranging from a couple of eV up to the ultraviolet or the soft x-ray regime [38–40]. The bandwidth of the harmonic comb, $\Delta\Omega$, is large enough to support pulse durations in the attosecond regime. Consider a comb of monochromatic harmonics: the resulting electric field will be given by:

$$E(t) = \sum_{q\ odd} \hat{E}_q e^{-i(\omega_q t + \phi_q)}. \tag{2.7}$$

If the individual fields are synchronized, meaning that they have a fixed phase relationship, they may add constructively, and the resulting amplitude $E(t)$ will then vary much faster than T/2 of the driving laser field, as depicted in Figure 2.7.

However, as discussed in Section 2.1.1, the attosecond emission exhibits an inherent chirp, which is approximately linear over a large range of energies. The influence of the chirp is illustrated in Figure 2.8, which shows the intensity profile $I = |E(t)|^2$ of an APT including harmonics 13 to 21. The solid line illustrates the Fourier-limited pulse duration according to the bandwidth, while the dashed line corresponds to an APT with the same bandwidth, but quadratic phase behavior, i.e., a linear chirp.

To achieve the shortest possible pulses it is therefore important to be able to control the phase properties. This can be done by

optimizing the generation process [41] and by post-generation pulse shaping [19, 25]. Additionally, long trajectories, which exhibit the opposite phase behavior, must to be suppressed in order to obtain a clean time structure.

2.2.1 Pulse Shaping

To achieve short attosecond pulses post-generation pulse shaping is necessary. The short trajectories used for attosecond pulse generation cause a positively chirped emission, i.e., GDD $= \partial^2\phi\backslash\partial\omega^2$, which is positive over the harmonic spectrum. Thin metallic foils can be used to compensate the positive atto-chirp. These foils cause a negative GDD on the low-energy side of their transmission window, so that when the light passes through the medium, low-frequency components travel slower than the higher frequency ones, leading to the desired synchronization.
The choice of material depends on the photon energy range [19, 25]. A standard combination of generating medium and metallic filter used throughout the work described in this thesis was argon gas together with a thin aluminum foil. Figure 2.9 shows the transmittance and group delay for a 200 nm thick aluminum foil. The transmission onset of aluminum at low frequencies together with the cutoff on the high-energy side acts as a bandpass filter. Over the spectral range between 25 and 45 eV (corresponding to harmonics 17 to 29) aluminum exhibits an almost constant negative group delay. Pulse compression can be achieved by choosing the appropriate filter thickness. Below the 17th harmonic the group delay varies rapidly and aluminum is not suitable for synchronization. In this region the transmittance of aluminum is so low so that the lower orders are sufficiently absorbed. An additional advantage of metallic filters is that they effectively filter out the fundamental laser pulse.

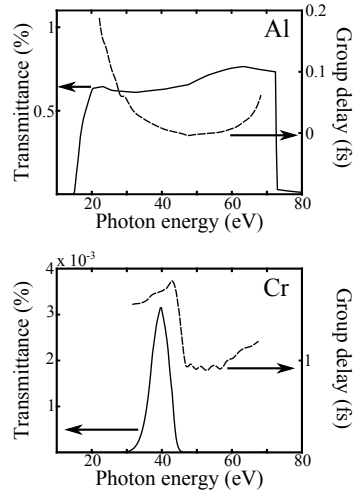

Figure 2.9. *Transmittance and group delay for aluminum and chromium.*

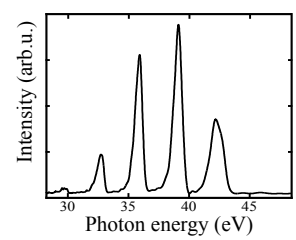

Figure 2.10. *Harmonic spectrum through a 200 nm thick chromium filter.*

In some applications, the shortest pulse duration may not be the decisive factor. In the experiments presented in Papers **II** and **III** a chromium filter was used to tailor the bandwidth of the harmonic spectrum. Figure 2.9 presents the optical properties of chromium. A small transmission window between 30 and 45 eV allows for the selection of harmonics 21 to 29. Figure 2.10 shows the resulting harmonic spectrum generated in argon. The spectrum is confined by the transmittance on the low-energy side and by the cutoff at high energies. The GDD in this energy region is positive, indicating that chromium is not suitable for pulse compression, on the contrary, attosecond pulses passing through a chromium filter will gain additional chirp. However, in the experiments described in Papers **II** and **III** the actual pulse length was only of secondary interest. The temporal resolution in these experiments is the result of an interferometric measurement technique.

2.2.2 Characterization of Attosecond Pulse Trains

The main characterization method used in this work was RABITT (Reconstruction of Attosecond Beating by Interference of Two-photon Transitions). RABITT measures the pulses 'on target' including propagation effects and filtering. Another method of probing the attosecond pulses when they are generated, proposed by Dudovich *et al.* [30], namely the *in situ* method, has also been investigated.

RABITT

RABITT is a widely used method for the characterization of attosecond pulses in a train [9, 19, 20, 41, 42]. RABITT is a cross-correlation method in which the XUV pulses are probed with a small fraction of the fundamental IR pulse used for generation. The method relies on the fact that the two fields, XUV and IR, are locked in phase. In a RABITT measurement, both the spectral phase and the amplitudes are measured for all frequency components, thus full reconstruction of the pulses is possible.
The basic idea of a RABITT measurement is depicted in Figure 2.11. An attosecond pulse train ionizes an atom leading to a photoelectron spectrum with equally spaced peaks at energies of $\hbar\omega_q - I_p$, where q is the harmonic order. The presence of a small fraction of the fundamental laser pulse with the energy $\hbar\omega$ will introduce two-photon transitions, where the electron either absorbs or emits an additional IR photon.[3] Additional photoelectron peaks, denoted sidebands S, will appear corresponding to even harmonic orders. The two possible quantum paths to the same sideband will lead to interference, and the sideband intensity S will be sensitive to the phase between the two fields [43]. Since both intensities, XUV and IR, are small, it is possible to use second-order perturbation theory. Assuming equal amplitudes for the two pathways, the sideband signal will oscillate as a function of phase, i.e., the delay τ, between the XUV and IR pulses [9]:

$$S_q(\tau) \propto 1 + \cos\left(2\omega\tau - \Delta\phi_q - \Delta\phi_q^{at}\right), \tag{2.8}$$

where $\Delta\phi_q = \phi_{q+1} - \phi_{q-1}$ is the difference in spectral phase between two consecutive harmonics. The phase term $\Delta\phi_q^{at}$ is called the atomic phase and denotes an additional phase factor that arises from to the two-photon ionization process itself. The atomic phase is usually small compared to $\Delta\phi_q$ and can be neglected or calculated [9, 44]. However, since $\Delta\phi_q^{at}$ contains valuable information about the dynamics of the ionization process, an extended version of the RABITT method was used in this work to determine $\Delta\phi_q^{at}$.

[3] The case where the electron first absorbs an IR photon and then an XUV photon will be neglected since the probability for this transition is small.

Under some circumstances the contribution of $\Delta\phi_q^{at}$ may be considerable, for example, in the case of a resonant two-photon transition. In the studies presented in Paper **V** the RABITT method was used to study the resonant behavior of two-photon ionization of helium. A similar approach was used by Haessler *et al.* [45] and Caillat *et al.* [46] to investigate 'complex resonances' of nitrogen molecules. A more detailed derivation of the RABITT Equation 2.8 is given in Section 4.1.1.

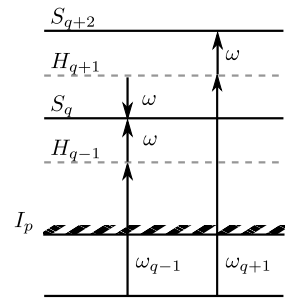

Figure 2.11. *Principle of the RABITT technique. Ionization with an APT in the presence of a fraction of the fundamental will lead to sideband peaks. The interference signal from the two pathways contains information on the chirp of the XUV pulses.*

Figure 2.12 gives an example of a complete RABITT scan, showing photoelectron spectra as a function of the delay between the APT and the IR pulse. The oscillating sideband signal for even harmonic orders is clearly visible. The sidebands are modulated at a frequency of 2ω and have a characteristic phase offset. A Fourier transformation of the sideband signal along the delay axis, τ, will give a frequency contribution at 2ω with a phase given exactly by $\Delta\phi_q + \Delta\phi_q^{at}$. Neglecting $\Delta\phi_q^{at}$ for now, the measured phases provide insight into the synchronization between consecutive harmonics, i.e., the GD of the attosecond pulse:

$$\mathrm{GD} = \frac{\Delta\phi_q}{2\omega}. \tag{2.9}$$

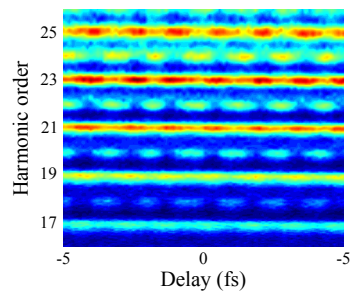

Figure 2.12. *A complete RABITT scan when using argon as generation and detection gas. The sideband modulations are clearly visible at even harmonics.*

By setting the phase of the lowest measured harmonic, q_i, to zero, the phase of the following harmonics can be obtained from a recursive relationship:

$$\phi_{q>q_i} = \sum_{n=q_i+1}^{q} \Delta\phi_n. \tag{2.10}$$

The pulses are then reconstructed as:

$$I(t) = \left| \sum_{q=q_i,odd}^{q_f} \hat{E}_q e^{-i(\omega_q t+\phi_q)} \right|^2. \tag{2.11}$$

For a complete reconstruction not only the phases but also the amplitudes of each harmonic must be known. These can either be measured using an XUV spectrometer, or derived directly from the photoelectron spectra. In the latter case the harmonic amplitudes result from the ionization cross-section-corrected intensities $\hat{E}_q = \sqrt{I_q/\sigma_q}$.
There are several limitations to the RABITT method. One lies in the fact that Equation 2.11 assumes monochromatic harmonics, in other words, harmonics that are infinitely long in time. In reality, the harmonic emission is limited to less than the duration of the driving pulse. Moreover, since the cutoff energy varies as a function of intensity, the lower orders will be produced over a longer time, while the generation of higher orders is limited to the center

of the intensity envelope of the generating laser pulse. This results in a variation in the pulse duration along the train, as well as a non-uniform spacing of the pulses in the train [23, 24, 47]. RABITT consequently measures only the average pulse in the train. In addition, the derivation of Equation 2.8 is based on a perturbative treatment which assumes low IR intensities. For higher intensities, higher multi-photon transitions have to be included, which compromises the phase determined at 2ω. Swoboda *et al.* [48] showed how the RABITT method could be generalized for high probe intensities by including higher-order transitions.

In Situ Method

In contrast to RABITT the *in situ* method provides characterization of attosecond pulses when they are 'born' [30]. This is done by introducing a small perturbation in the generation process. In an *in situ* measurement a small fraction of the second harmonic of the fundamental is included in the generation (less than $< 10^{-3}$). Due to the symmetry breaking of the driving field experienced by the atom, even harmonics will be generated. When changing the relative phase between the two generation fields the signal of the even harmonics will be modulated. The phase of the oscillation maxima $\Delta\phi_{max}(\omega_q)$ for the even harmonics in the plateau region can be related to the return time of the electron trajectory, t_r, and therefore to the GD [49]:

$$\mathrm{GD} = t_r(\omega_q) \propto \frac{\Delta\phi_{max}(\omega_q)}{\omega}, \tag{2.12}$$

which allows for a reconstruction of the attosecond pulses. The validity of the *in situ* method was investigated in terms of generation pressure and IR intensity by comparison with the corresponding RABITT measurements (Paper **I**). A recent, more thorough theoretical investigation, however, revealed that the *in situ* method must be improved to account correctly for the intensity and the wavelength of the fundamental, as well as for the ionization potential, in order for it to be applicable in quantitative studies [50].

2.2.3 The Experimental Setup in Lund

The experimental setup used for the experiments described in Papers **I**, **II**, **III**, **V** and **VIII** is located in the attosecond laboratory of the Lund High Power Laser Facility. It can be divided into three parts: (i) the laser system, (ii) the optical setup including the HHG chamber and a Mach-Zehnder interferometer for time-resolved pump-probe experiments, and (iii) the detection part including different types of electron spectrometers.

The Laser System

Figure 2.13 gives a schematic overview of the laser system. It is based on the chirped-pulse amplification (CPA) technique and delivers pulses in the IR region, centered at 800 nm, with a bandwidth of approximately 30 nm, corresponding to a pulse duration of 35 fs. Standard pulse energies are about 3 mJ. CEP-controlled operation with pulse energies up to 6 mJ was demonstrated in 2009 [51]. However, this feature was not used in the current work.

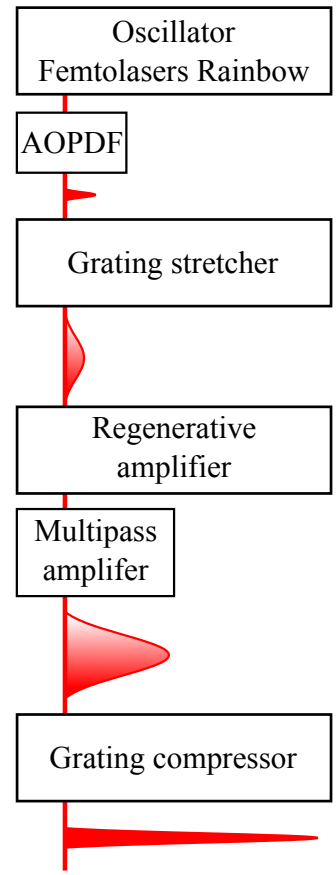

Figure 2.13. *Overview of the laser system in the attosecond laboratory.*

The CPA chain is seeded by a Femtolasers *Rainbow* oscillator, using a chirped mirror configuration for intracavity dispersion management [52]. The *Rainbow* oscillator delivers pulses with a duration of 7 fs and a bandwidth of 300 nm at a central wavelength of 800 nm. The pulse energy is about 2.5 nJ. The CEP can be controlled by a feedback loop, utilizing a monolithic, collinear geometry [53, 54]. The oscillator is followed by a *Fastlite* Dazzler. This is an acousto optic programmable dispersive filter (AOPDF) to fine control dispersion and to shape the spectrum for optimal gain. The AOPDF reduces the oscillator bandwidth to 80-100 nm. The pulses are then stretched in an Öffner type of grating stretcher to a pulse duration of 200 ps, before entering the regenerative amplifier. Here the repetition rate is reduced from 78 kHz to 1 kHz by a pulse picker. In the regenerative amplifier the pulse energy saturates at 0.5 mJ after about 12 round trips. The second amplification stage employs a five-pass bow-tie amplifier using a cryogenically cooled Ti:Sapphire crystal. The amplifier is designed for an output of 10 mJ. Both amplifiers are pumped with a 30 W diode-pumped, frequency-doubled Nd:YLF laser from *Photonics Industries*. For pulse energies above 5 mJ the multipass amplifier can be pumped by a second pump laser (YLF 20W, *B.M. Industries*). Most experiments presented here were performed without the additional pump laser, resulting in pulses with a usable energy of about 3 mJ after compression. After amplification the beam diameter is expanded to about 1.6 cm with a telescope to avoid damage to the following optics, especially to the gratings of the compressor. The final stage is a standard double-pass grating compressor, optimized at 800 nm. Frequency-Resolved Optical Gating (FROG) measurements indicate a minimum pulse length of about 35 fs FWHM after compression.

As mentioned above, the AOPDF can be used to shape the spectrum. This feature was explored to change the carrier frequency of the IR pulses and therefore the photon energy of the generated harmonics (Paper **V**). Tuning was achieved by changing the position of the selected 80 nm bandwidth from the oscillator output, or by introducing a dip or hole at a given wavelength to shift the relative contribution from different wavelengths and thus changing the 'center of mass' of the pulse (see Figure 2.14. However, the ability

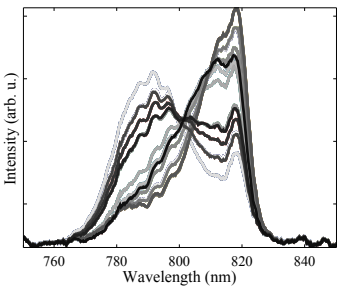

Figure 2.14. *Spectra for the laser tuning used in Paper* ***V****.*

to alter the central wavelength is limited by the bandwidth of the dielectric optical elements following the AOPDF (about 40 nm centered at 800 nm), thus limiting the possible tunability. Another limiting factor is gain narrowing during amplification. This will act as an additional bandpass filter and manifest itself mainly as a red shift during amplification. The limitations on the tuning are clearly visible in Figure 2.14.

The Mach-Zehnder Interferometer

The most important part of the experimental pump-probe setup used in this work is the Mach-Zehnder interferometer, shown in Figure 2.15. After the pulses leave the compressor a small fraction of the beam is split off by a beam splitter to serve later as a probe pulse. The main fraction of the beam is focused into a gas cell for HHG, situated in a separate part of a vacuum chamber. The gas cell is pulsed and synchronized to the repetition rate of the laser. Pulsed operation keeps the background pressure at a minimum to reduce propagation effects of the XUV radiation. The generation cell is motorized for signal optimization (see Section 2.1.2). Different cell lengths are available, but a length of 6 mm was most commonly used. A hard aperture can be placed in front of the vacuum chamber to reduce the generation intensity if necessary, and serves as an additional means of achieving good phase matching conditions. The standard focal length is 50 cm, but focal lengths between 30 and 75 cm were also used. After generation, the IR pump beam is blocked by a thin metallic foil, which is also used to spectrally alter and temporally compress the XUV pulses, as described in Section 2.2.1.

Two different delay stages are implemented in the probe arm: one for the coarse delay with a range of about 600 ps, and a small piezo-driven translation stage with a range of about 150 fs for high-resolution scans. Recently, a system was implemented that actively stabilizes the length of the probe arm with respect to the pump arm. The probe intensity can be varied by a combination of a $\lambda/2$ plate and a thin polarizer at the Brewster angle. The probe beam is recombined with the XUV beam using a holey mirror which simultaneously serves as a hard aperture to spatially filter out the long trajectories. The recombination mirror is convex so that the probe beam wave fronts match the wave front of the XUV for HHG with a focal length of 50 cm. After recombination the two collinear beams are focused into the sensitive region of an electron spectrometer using a toroidal mirror.

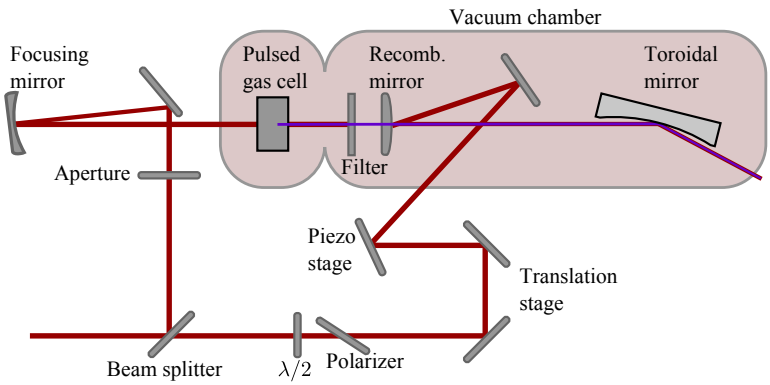

Figure 2.15. *The Mach-Zehnder interferometer. While the main fraction of the pulse is used for HHG, the smaller part serves as a probe pulse with variable delay. After recombination both beams are focused with a toroidal mirror into an electron spectrometer.*

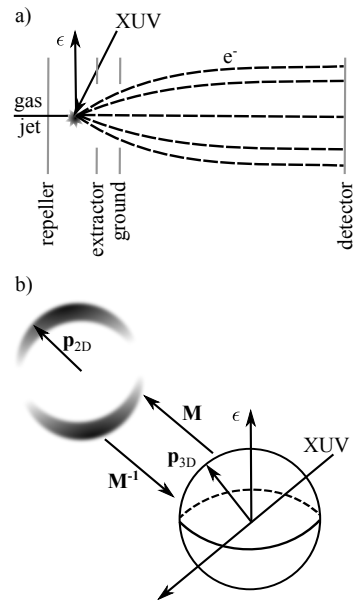

Figure 2.16. *Principle of the VMIS. a) Schematic of the electrode arrangement. b) Projection of a mono-energetic momentum distribution. In both figures ϵ denotes the direction of the polarization of the XUV and IR fields.*

Electron Detection

Two different types of electron spectrometer are available in the attosecond laboratory. In the experiments described in Papers **I**, **II**, **III** and **V** the photoelectron spectra were collected using a magnetic bottle electron spectrometer (MBES). The MBES records the number of electrons as a function of the time of flight (TOF) in a drift tube [55]. The XUV and IR pulses are focused into the interaction region containing a diffuse gas target. A relatively strong magnetic field ($\approx$1 T) is present and forces the photoelectrons to spiral around the magnetic field lines, which are parallel to the spectrometer axis. The magnetic field strength decreases adiabatically towards the flight tube where it is kept constant ($\approx$1 mT). The gradient of the magnetic field lines resembles a bottle neck, hence the name. The adiabatic change in magnetic field strength causes an increase in the parallel velocity component, while the total velocity is conserved. This leads to parallelization of the electron trajectories so that the TOF depends only on the initial velocity, not on the direction. All electrons that have an initial velocity component towards the detector can be detected in this way, resulting in an acceptance angle of 2π sr with a high energy resolution. The high collection efficiency is beneficial in experiments with a small signal strength as the case in multi-photon ionization. The collection efficiency for electrons below 1 eV kinetic energy can be further enhanced if a small acceleration potential is applied in the interaction region. This was used in Paper **II**, **III** and **V**.

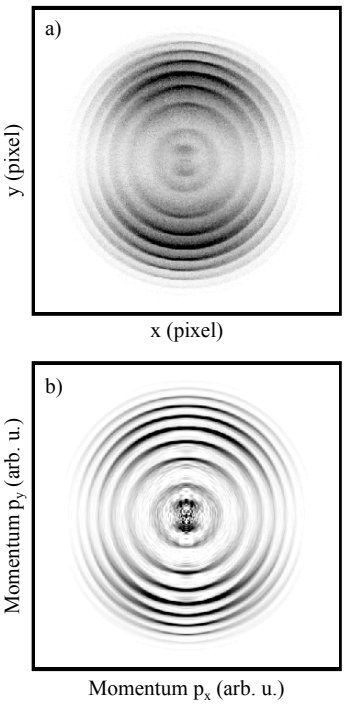

Figure 2.17. *Velocity map image of electrons from argon ionized with an APT generated in argon. a) Raw image. b) Momentum distribution after inversion using the Legendre polynomial expansion.*

The other electron spectrometer used in this work was a velocity map imaging spectrometer (VMIS). It is an angularly resolved technique, which not only detects the kinetic energy, as the MBES does, but also the direction of the photoelectrons. Figure 2.16 a) illustrates the principle of the VMIS. The focused beams are crossed with a diffuse gas jet and the following ionization of the target gas results in a 3D distribution of outgoing photoelectrons. The interaction takes place in an electrostatic potential applied between the repeller and extractor electrodes, with $V_{rep} < V_{ext} < 0$. The potential is usually on the order of several keV so that the electrons are strongly accelerated towards a position-sensitive detector consisting of a stack of multi-channel plates, a phosphor screen and a charge-coupled device camera. The position, where the electron hits the detector, is directly related to its initial momentum and origin in the source volume. Velocity focusing can be achieved by choosing the ratio between the repeller and extractor voltage, V_{rep}/V_{exc}, such that all electrons with the same initial momentum are focused onto the same position on the detector. The result is a 2D projection of the initially 3D momentum distribution.
Figure 2.17 a) presents an example of the projection at the detector. If the original 3D momentum distribution contains a symmetry axis in the detector plane, it can be reconstructed from the 2D projection by means of the inverse Abel transform [56]. All ionization experiments included in this thesis fulfill this criterion, since the radiation electric fields is chosen to be linearly polarized perpendicular to the detector axis, as depicted in Figure 2.16 a). Various numerical implementations of the Abel inversion exist [56–58]. The inversion method used in connection with Paper **VI** is based on a Legendre polynomial expansion [59] and briefly described below.
The angular distribution in photoionization can be expressed in terms of Legendre polynomials: $P_{3D} = \sum_\ell a_{\mathbf{p}3D} P_\ell(\cos\theta_{3D})$, where the maximum ℓ is determined by the order of the ionization process. Similarly, the 2D projection can be expressed using a Legendre expansion, i.e.: $P_{2D} = \sum_\ell b_{\mathbf{p}2D} P_\ell(\cos\theta_{2D})$. The Abel projection states the 2D image is fully characterized by the 3D data set. Organizing the elements $a_{\mathbf{p}3D}$ and $b_{\mathbf{p}2D}$ in vector form $\mathbf{a}$ and $\mathbf{b}$ gives the projection simply by a matrix multiplication $\mathbf{b} = M\mathbf{a}$. The matrix M can be constructed from projections of single monoenergetic momentum distributions with angular distributions described by a single Legendre polynomial, $P_\ell(\cos\theta)$, shown in Figure 2.16 b). The initial 3D angular distribution can then be reconstructed by the inverse Abel transform: $\mathbf{a} = M^{-1}\mathbf{b}$. Figure 2.17 b) shows a cut through the 3D momentum distribution reconstructed from Figure 2.17 a). The Legendre based inversion has the advantage that the necessary inversion of the raw data already yields the physical meaningful asymmetry parameters describing the differential cross-sections.

A VMIS was used in the experiments described in Papers **VI** and **VIII**. In the latter, the repeller and extractor voltages were chosen for momentum imaging of positively charged ions, e.g., $V_{rep} > V_{ext} > 0$.

2.3 Single Attosecond Pulses

For few-cycle laser pulses with pulse durations as short as 5 fs the electric field varies significantly from one half-cycle to another. Since the cutoff energy in HHG scales with the field strength, the highest photon energies can only be generated during one half-cycle, leading to a continuous spectrum for the highest energies. Lower photon energies, on the other hand, are more likely to be generated during more than one cycle, leading to a harmonic spectrum. In consequence, a short APT is generated, from which a single attosecond pulse (SAP) can be isolated using a bandpass filter, as illustrated in Figure 2.18. This technique was used to demonstrate the first single attosecond pulses [10]. With pulse duration as short as a few optical cycles it is crucial to control the CEP, since the maximum field strength is strongly dependent on the CEP. In the illustration shown in Figure 2.18, a cosine pulse for generation (CEP = 0) was assumed. Under the same conditions a sine pulse would result in two equally strong emission maxima and hence two pulses after filtering [60].

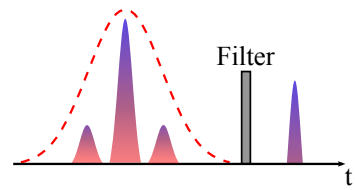

Figure 2.18. *Principle of SAP generation, in which only the continuum part in the cutoff region is used.*

An alternative approach for the generation of SAPs is to use a polarization gating [61, 62]. Within the three-step model it is clear that the generation efficiency is drastically decreased for polarization states other than linear polarization, since the returning electron is likely to miss the parent ion. An ellipticity as small as $\xi = 0.2$ will reduce the generation efficiency by an order of magnitude. The polarization gate is realized with a driving field that has a time dependent ellipticity. These kinds of pulses can be constructed by a left circularly polarized pulse followed by a delayed right circularly polarized pulse, as depicted in Figure 2.19. For a short duration, where the wings overlap, a window, or gate, of linear polarization is introduced and effective HHG is possible. This technique was used in the experiment presented in Paper **VI**.

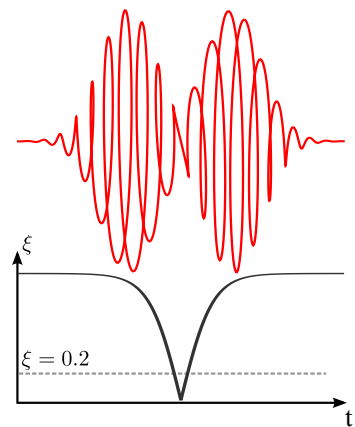

Figure 2.19. *Principle of the polarization gate, showing the ellipticity as function of time for the resulting electric field (red).*

The polarization gating technique is less demanding on the duration of the IR pulses. It has been demonstrated that SAPs can be generated using pulse durations of up to 28 fs with the slightly modified method of double optical gating, combining polarization gating and two color generation [63–65]. Another advantage is the lower photon energies. Since the usable spectrum is not limited to the cutoff region it was possible to choose the energy region around the ionization threshold of helium at 24.6 eV (see Paper **VI**).

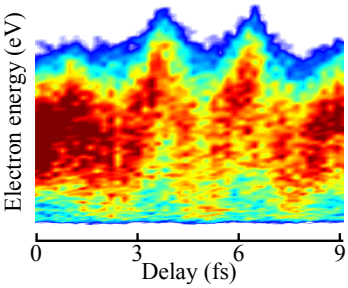

Figure 2.20. *Experimental spectrogram recorded for Paper **VI**.*

2.3.1 Characterization of Single Attosecond Pulses

As for RABITT, the characterization of an SAP relies on a cross-correlation where an atom is ionized by the XUV pulse in the presence of a probing IR field. In contrast to RABITT, rather high IR intensities are used and, in general, a perturbative treatment is not valid.
The principle of the measurement can be understood in terms of classical mechanics [66]. When an atom is ionized by an XUV field, the photoelectron energy will depend on the ionization time, t, as:

$$E_{kin}(t) = \frac{1}{2}m\mathbf{v}^2(t) = \hbar\Omega(t) - I_p, \tag{2.13}$$

where $\Omega(t) = \partial\phi(t)/\partial t$ is the instantaneous frequency of the SAP. Due to the presence of the IR field the electrons are further accelerated, and the final energy, after the IR pulse has passed, is given by:

$$E_{kin}(t \to \infty) = \frac{[m\mathbf{v}(t) + e\mathbf{A}(t-\tau)]^2}{2m}, \tag{2.14}$$

where $\mathbf{A}(t-\tau)$ is the vector potential of the IR field. The additional momentum picked up by the electron depends the delay, τ, between the XUV and IR pulses. For a transform-limited, very short SAP, $\mathbf{A}(t-\tau)$ can be assumed to be quasi-static for the duration of the XUV pulse. Collecting photoelectron spectra as a function of τ will provide an image of the vector potential of the IR pulse, since all possible kinetic energies are emitted at the same time, t. In general, for ionization with a chirped XUV pulse, electrons leaving the atom with $E_{kin}(t)$ will experience a different value of $\mathbf{A}(t-\tau)$, which will affect the width and the peak value in the photoelectron spectra. This is the principle of the attosecond streak camera [67, 68].

A streaking trace obtained during the experimental work described in Paper **VI** is shown in Figure 2.20. It can be interpreted as a FROG spectrogram [69], and its extension to the attosecond regime is dubbed FROG-CRAB (FROG for Complete Reconstruction of Attosecond Bursts) [70, 71]. The reconstructed pulses from the spectrogram shown in Figure 2.20 had a duration of 350±20 as. The bandwidth would support a duration of 180 as, indicating a chirp on the XUV emission, which is visible in the trace as an asymmetric electron distribution.
Using FROG-CRAB pulse characterization is, in principle, possible for both IR and XUV fields simultaneously. In addition, arbitrary pulse shapes including APTs can be reconstructed [70, 72].

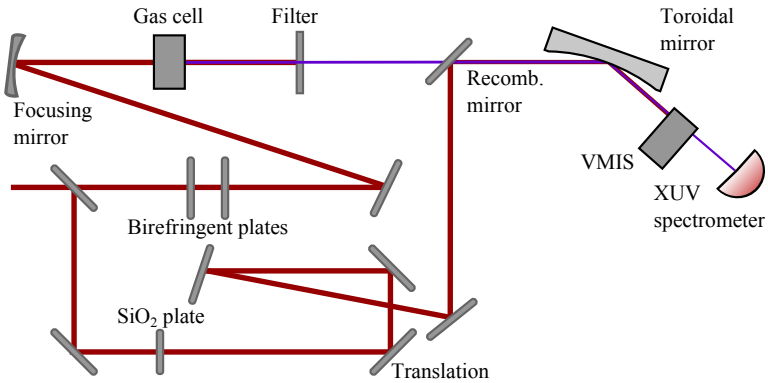

Figure 2.21. *Experimental setup in Milan. The pulses are split using a holey mirror. SAP are generated by polarization gating and afterwards are overlapped with a few-cycle IR pulse with a variable delay. Both beams are focused into the sensitive region of a VMIS. Also attached to the beamline is XUV spectrometer to monitor the SAP.*

2.3.2 Experimental Setup in Milan

Isolated attosecond pulses were used in the experiment described in Paper **VI**. The experiment was carried out in collaboration with a group led by Professor Mauro Nisoli at the Politecnico di Milano and was the first attosecond experiment I took part in.

As in Lund, the IR pulses are generated by a Ti:Sapphire-based CPA system with a pulse duration after compression of 25 fs at a central wavelength of 750 as, but with a lower pulse energy of 0.7 mJ. Few-cycle pulses are then generated by a combination of an argon-filled hollow-core fiber and a set of ultrabroadband chirped mirrors. When the laser output is coupled to the fiber, self-phase modulation will substantially broaden the spectrum, while recompression by the chirped mirrors result in ultra-short pulses with a pulse duration down to 5 fs [62]. The CEP is stabilized and can be controlled, which, together with the short pulse duration, is a key factor in SAP generation.

The compressed pulses are split using a mirror with a hole at the center. Due to the radial intensity distribution in the hollow-core fiber the output is broadest on-axis, leading to a pulse duration with a radial distribution. When the inner and outer parts of the beam are separated by the holey mirror the outer part will have a slightly longer pulse duration of 7 fs. The experimental setup used in Milan is shown in Figure 2.21. The pump pulse passes through a pair of birefringent plates to achieve the desired time-dependent ellipticity for the polarization gating. The first plate splits the linearly polarized beam into two orthogonally polarized pulses with

a delay of 5.8 fs. The second plate converts the two pulses into circularly polarized pulses with opposite helicity [62]. The width of the linearly polarized window can be fine tuned by changing the relative orientation of the plate. The altered IR pulses are then focused into a gas cell containing xenon at a static pressure for HHG. After generation the fundamental is filtered out by an aluminum filter, which also compresses the SAP in time, as described in Section 2.2.1.
The IR probe pulse is recombined with the XUV pulse after a variable delay. A silica plate is inserted into the probe arm to balance the dispersion in the two interferometer arms. Both beams are focused into a gas jet in a VMIS. Additionally, the XUV can be monitored using an XUV spectrometer.

Chapter 3

Interaction of Atoms with Light

While the previous chapter covered the generation of attosecond pulses as a result of exposing atoms to strong fields, this chapter will concentrate on the interaction of atoms with electromagnetic radiation at low and moderate field intensities. Two-photon ionization is central to the studies of electron dynamics presented in this thesis. The interpretation of some of the experimental results led to theoretical progress in the description of above-threshold two-photon ionization. For a better understanding of this theoretical work, basic concepts, which can be found in many textbooks, will also be reviewed.
The chapter is organized as follows. Starting with a short introduction of the theoretical framework, the first section reviews one-photon excitation processes. This is followed by the description of two-photon ionization in Section 3.2. The influence of electron correlation is briefly discussed in Section 3.3.

Two main approximations are used to describe the process of photoexcitation and photoionization. First, the interaction between the atom and electromagnetic radiation is described using time-dependent perturbation theory [73, 74], and second, the reduction of the complex atomic system with N interacting electrons to one active electron only.

Time-Dependent Perturbation Theory

At low intensities the electromagnetic field can be treated as a small perturbation, and the atomic processes are usually described using the field-free atomic states. Under this small perturbation only a small fraction of the initial state is transferred into higher lying excited or continuum states.
For times $t < t_0$ the atom is in a field-free initial state i satisfying

the stationary Schrödinger equation:

$$H_0|\varphi_k\rangle = E_k|\varphi_k\rangle, \tag{3.1}$$

where $|\varphi_k\rangle$ forms a complete set of basis functions including bound and unbound continuum states. At $t = t_0$ a perturbation $H_{int}(t)$ starts to act so that the Hamiltonian becomes time-dependent, $H_0 \rightarrow H(t) = H_0 + H_{int}(t)$. Between t_0 and t the evolution of the system is given by the time-dependent Schrödinger equation:

$$i\hbar\frac{d}{dt}|\Psi(t)\rangle = \left[H_0 + H_{int}(t)\right]|\Psi(t)\rangle. \tag{3.2}$$

The solution of this first-order differential equation with the initial condition $|\Psi(t_0)\rangle = |\varphi_i\rangle$ can be approximated by expanding $|\Psi(t)\rangle$ onto field-free states:

$$\begin{aligned} |\Psi(t)\rangle &\approx |\Psi^{(0)}(t)\rangle + |\Psi^{(1)}(t)\rangle + |\Psi^{(2)}(t)\rangle + \ldots \\ &= |\varphi_i\rangle e^{-iE_it/\hbar} + \sum_k c_k^{(1)}(t)\,|\varphi_k\rangle e^{-iE_kt/\hbar} \\ &\quad + \sum_k c_k^{(2)}(t)\,|\varphi_k\rangle e^{-iE_kt/\hbar} + \ldots \end{aligned} \tag{3.3}$$

The coefficients of $|\varphi_k\rangle$ corresponding to the first-order perturbation are given by:

$$c_k^{(1)}(t) = \frac{1}{i\hbar}\int_{t_0}^{t} dt'\ \langle\varphi_k|H_{int}(t')\,|\varphi_i\rangle\ e^{i\omega_{ki}t'}, \tag{3.4}$$

where $\omega_{ki} = (E_k - E_i)/\hbar$ is the Bohr frequency. The second-order coefficients are:

$$\begin{aligned} c_k^{(2)}(t) &= -\frac{1}{\hbar^2}\sum_s \int_{t_0}^{t} dt'\ \langle\varphi_k|H_{int}(t')\,|\varphi_s\rangle e^{i\omega_{ks}t'} \times \\ &\quad \int_{t_0}^{t'} dt''\ \langle\varphi_s|H_{int}(t'')\,|\varphi_i\rangle\ e^{i\omega_{si}t''}. \end{aligned} \tag{3.5}$$

The expression for $c_k^{(2)}(t)$ depends recursively on the first-order solution. It can be viewed as a sequential process where the first-order final state serves as an initial state for the second excitation.

A special case is a harmonic perturbation in the form of $H_{int}(t) = H_\Omega e^{-i\Omega t}e^{\varepsilon t} + \text{cc}$, where Ω is the frequency of the perturbation. The expression for $H_{int}(t)$ carries an exponential 'turn-on' in the form of $e^{\varepsilon t}$, where ε is an infinitesimal quantity such that $H_{int}(t_0 \rightarrow -\infty) \approx 0$. The integrals in Equations (3.4) and (3.5) can then be extended to $-\infty$. At the end of the calculation the limit $\varepsilon \rightarrow 0^+$ is adopted.

For a harmonic perturbation, the first-order amplitudes $c_k^{(1)}(t)$ become:

$$c_k^{(1)}(t) = \underbrace{\frac{1}{i\hbar}\langle\varphi_k|H_\Omega|\varphi_i\rangle}_{M_{ki}^{(1)}}\left[\frac{e^{i(\omega_{ki}-\Omega-i\varepsilon)t}}{i\,(\omega_{ki}-\Omega-i\varepsilon)} + \frac{e^{i(\omega_{ki}+\Omega-i\varepsilon)t}}{i\,(\omega_{ki}+\Omega-i\varepsilon)}\right]. \tag{3.6}$$

The first term has a resonant character for $\Omega \approx \omega_{ki}$, which corresponds to the situation of photoabsorption [73]. In this case, the second term is small and will be neglected in the following. The matrix element $M_{ki}^{(1)}$, defined in Equation (3.6), is a measure of the coupling between the states i and k by the perturbation. The probability of finding the system in a final state f at time t is given by $\mathcal{P}_{fi}(t) = |c_f^{(1)}(t)\,|^2$, and the time-independent transition rate W_{fi} is defined as:

$$W_{fi}^{(1)} = \lim_{\varepsilon\to 0^+}\frac{d}{dt}|c_f^{(1)}(t)\,|^2 = \frac{2\pi}{\hbar^2}|\langle\varphi_f|H_\Omega|\varphi_i\rangle|^2\delta(\omega_{fi}-\Omega)\,, \tag{3.7}$$

where the identity $\lim_{\varepsilon\to 0^+}\frac{2\varepsilon}{(\omega_{fi}-\Omega)^2+\varepsilon^2} \to 2\pi\delta(\omega_{fi}-\Omega)$ was used. Equation (3.7) has a strong resonance character expressed by the δ-function and is known as Fermi's rule. It can easily be generalized for a continuum of final states [73].
When the first-order correction vanishes, or if the atom interacts with two photons, second-order perturbation theory may be used. In the case of laser-assisted photoionization discussed in Section 3.2 the photons have different energies, and a second perturbation of the form of $H_\omega e^{-i\omega t}e^{\varepsilon t}$+cc is added. Including only the absorption term as before, the coefficients $c_k^{(2)}(t)$ from Equation (3.5) become:

$$c_k^{(2)}(t) = \underbrace{\frac{1}{i\hbar^2}\sum_s \frac{\langle\varphi_k|H_\omega|\varphi_s\rangle\langle\varphi_s|H_\Omega|\varphi_i\rangle}{\omega_i+\Omega-\omega_s+i\varepsilon}}_{M_{ki}^{(2)}}\left[\frac{e^{i(\omega_{ki}-\Omega-\omega-i2\varepsilon)t}}{i\,(\omega_{ki}-\Omega-\omega-i2\varepsilon)}\right]. \tag{3.8}$$

The sum is performed over all possible intermediate states, s. The matrix element for the two-photon transition $M_{ki}^{(2)}$ can be defined in a similar manner as for the first-order amplitudes. Accordingly, Fermi's rule for the two-photon transition is given by:

$$W_{fi}^{(2)} = \frac{2\pi}{\hbar^4}\left|\sum_s \frac{\langle\varphi_f|H_\omega|\varphi_s\rangle\langle\varphi_s|H_\Omega|\varphi_i\rangle}{\omega_i+\Omega-\omega_s+i\varepsilon}\right|^2\delta(\omega_{fi}-\Omega-\omega)\,. \tag{3.9}$$

The energy conservation expressed by the δ-function is only required between the initial and final states. The intermediate state s has a short lifetime and is therefore not very well defined in energy, so no energy conservation is required for the transition to the intermediate state.

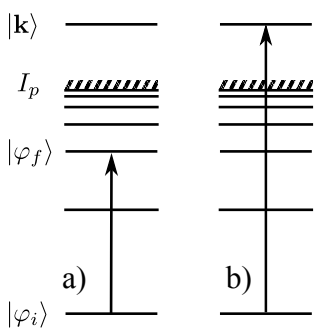

Figure 3.1. *One-photon absorption. (a) The electron is excited into a higher-lying state. (b) For a photon energy $\hbar\Omega > I_p$ the electron is released into the continuum.*

Electrons in a Central Field

The perturbative treatment described above was expressed in rather general terms. For atoms, the eigenfunctions $|\varphi_k\rangle$ are known exactly only for hydrogenic systems. However, N-electron atoms can be conveniently described using the central-field approximation.
Considering only the electrostatic interaction, the Hamiltonian of an N-electron atom with a nuclear charge of Z is given by:

$$H_0 = \sum_{i=1}^{N} \left(\frac{\mathbf{p}_i^2}{2m} - \frac{Ze^2}{r_i} \right) + \sum_{i>j=1}^{N} \frac{e^2}{|\mathbf{r}_i - \mathbf{r}_j|}. \tag{3.10}$$

The first sum describes the kinetic and potential energy of each individual electron in the Coulomb field of the nucleus, while the second sum includes the repulsive electrostatic potential between the electron pairs [75]. In the central-field model this exact Hamiltonian is approximated by a sum of single-electron terms that describes the independent motion of N electrons in a central potential $V(r)$:

$$H_{\mathrm{CF}} = \sum_{i=1}^{N} \left(\frac{\mathbf{p}_i^2}{2m} + V(r_i) \right), \tag{3.11}$$

where $V(r)$ includes the Coulomb potential of the nucleus as well as the electron-electron repulsion. The motion of each electron is now decoupled from the remaining (N-1) electrons. Without loss of generality, it is sufficient to consider only one active electron of these independent electrons:

$$H_0 \to H_i = \frac{\mathbf{p}_i^2}{2m} + V(r_i)\,. \tag{3.12}$$

In the central-field approximation several processes that stem from a direct electron-electron interaction are neglected. Some examples of these interactions will be discussed in Section 3.3.

3.1 Interaction with One Photon

The interaction of atoms with electromagnetic radiation at low intensities is usually described by the dipole approximation [73, 74]. Figure 3.1 shows the transitions considered in this work, where the electron is either excited into a higher excited state or where the photon energy is sufficient for ionization.

3.1.1 Dipole Transitions

Using the Coulomb gauge, the electric field that interacts with the electron is given by:

$$\mathbf{E}(\mathbf{r}, t) = E_\Omega \hat{\epsilon} e^{i(\mathbf{k}\cdot\mathbf{r} - \Omega t)}, \tag{3.13}$$

where $\mathbf{k}$ is the wave vector, Ω the frequency and $E_\Omega = |E_\Omega| \exp[i\phi_\Omega]$ is the complex amplitude with the intrinsic phase ϕ_Ω. The polarization $\hat{\epsilon}$ is assumed to be linear along the $\hat{z}$-direction. Within the dipole approximation the corresponding interaction Hamiltonian becomes:

$$H_{int}(t) = i\frac{eE_\Omega}{m\Omega}\hat{\epsilon}\cdot\mathbf{p}e^{-i\Omega t}e^{\varepsilon t}. \tag{3.14}$$

Again an exponential turn-on was added. $\mathbf{p}$ is the electron momentum for the field-free case. Equation (3.14) takes the form of a harmonically time-dependent perturbation as assumed for Equation (3.6). Accordingly, the matrix element for the transition amplitude to a final state, f, becomes:

$$M_{fi}^{(1)} = \frac{i}{\hbar}\frac{\omega_{fi}}{\Omega}E_\Omega e\langle\varphi_f|z|\varphi_i\rangle, \tag{3.15}$$

where z was chosen as the quantization axis. Additionally, the identity $[z, H_0] = \frac{i\hbar}{m}p_z$ was used.

The matrix element $M_{fi}^{(1)}$ defined in Equation (3.15) is proportional to $e\langle\varphi_f|z|\varphi_i\rangle$, which represents the component of a dipole moment in the $\hat{z}$-direction between the initial and the final states. It is that dipole moment the electric field couples to. Whether a dipole transition is said to be forbidden or allowed depends on the matrix element $M_{fi}^{(1)}$. If it is non-vanishing the transition is allowed. Since the electron moves in a spherical potential $V(r)$, $|\varphi_k\rangle$ can be written as a product of a radial part $R(r)$ and an angular part $Y(\hat{r})$:

$$\varphi_{n_k\ell_k m_k}(\mathbf{r}) = R_{n_k\ell_k}(r)\,Y_{l_k m_k}(\hat{r})\,, \tag{3.16}$$

where n is the principal quantum number, and ℓ and m are the angular and magnetic quantum numbers, respectively. $Y_{lm}(\hat{r})$ are spherical harmonics, while $\hat{r}$ denotes a unit vector in the direction of $\mathbf{r}$. By rewriting z in spherical coordinates as $z = r\cos(\theta) = (4\pi/3)^{1/2}\ rY_{10}(\hat{r})$, the dipole matrix element $M_{fi}^{(1)}$ can be separated into an angular and a radial part:

$$M_{fi}^{(1)} \propto \langle\varphi_f|z|\varphi_i\rangle = (4\pi/3)^{1/2}\langle Y_{l_f m_f}|Y_{10}|Y_{l_i m_i}\rangle\langle R_{n_f l_f}|r|R_{n_i l_i}\rangle. \tag{3.17}$$

The integral product of three spherical harmonics can be evaluated using $3j$ symbols [76]:

$$\begin{aligned}\langle Y_{l_f m_f}|Y_{10}|Y_{l_i m_i}\rangle \;&=\; \sqrt{\frac{3}{4\pi}}\hat{\ell}_i\hat{\ell}_f \\ &\times \begin{pmatrix} \ell_f & 1 & \ell_i \\ 0 & 0 & 0 \end{pmatrix}\begin{pmatrix} \ell_f & 1 & \ell_i \\ -m_f & 0 & m_i \end{pmatrix},\end{aligned} \tag{3.18}$$

where $\hat{\ell} = \sqrt{2\ell+1}$. The $3j$ symbols are non-vanishing for $\ell_f = \ell_i \pm 1$ and $m_f = m_i$, which are the dipole selection rules for linear polarization. As a rule of thumb the transition $\ell \to \ell+1$ is usually favored according to Fano's propensity rule [77].

3.1.2 Photoionization

In scenario b) of Figure 3.1 the photon energy is $\hbar\Omega > I_p$ (or more generally $\hbar\Omega + E_i > 0$). The atom will be ionized and the final state of the electron is a continuum state. The wavefunction of this photoelectron $|\mathbf{k}\rangle$ is the result of an electron scattering from the atomic potential and can, in principle, be expressed as a superposition of spherical harmonic functions [78]:

$$\langle \mathbf{k}|\mathbf{r}\rangle = \sum_{LM} c_{L,M} e^{i\eta_L(k)} Y_{LM}(\hat{k}), \tag{3.19}$$

where $\hat{k}$ is the unit vector in the direction of $\mathbf{k}$, and $k = |\mathbf{k}|$ is restricted by energy conservation, $E_k = \hbar^2 k^2/2m = \hbar\Omega + E_i$. The coefficients c_{LM} contain angular and radial information about the state from which the scattering occurred, and $\eta_L(k)$ are the scattering-induced phase shifts. A more complete analysis shows that the final state wave function takes the form of [79]:

$$\langle \mathbf{k}|\mathbf{r}\rangle = (8\pi)^{3/2} \sum_{L,M} i^L e^{-i\eta_L(k)} Y^*_{LM}(\hat{k}) Y_{LM}(\hat{r})\, R_{k,L}(r)\,, \tag{3.20}$$

where the radial part $R_{kL}(r)$ shows asymptotic behavor [80, 81]:

$$\lim_{r\to\infty} R_{kL}(r) \propto \sin\left[kr - L\pi/2 + \ln(2kr)/k + \eta_L(k)\right]. \tag{3.21}$$

Equations (3.20) and (3.21) can be understood in the following way. After the ionization far away from the ion when the electron is detected, it should behave as a plane wave in the $\hat{k}$-direction. Since the electron wave packet is formed in the vicinity of the atomic potential the influence of the potential manifests itself as a phase shift, $e^{-i\eta_L(k)}$, for each partial wave in the expansion.
Using Equation (3.20), the dipole matrix element from Equation (3.15) in the case of ionization is given by:

$$\begin{aligned} M^{(1)}_{ki} &= i\frac{e}{\hbar}\frac{\omega_{ki}}{\Omega}(8\pi)^{3/2} E_\Omega \sum_{\substack{L=\ell_i\pm1\\ M=m_i}} i^{-L} e^{i\eta_L(k)} Y_{LM}(\hat{k}) \hat{L}\hat{\ell}_i \\ &\quad \times \begin{pmatrix} L & 1 & \ell_i \\ 0 & 0 & 0 \end{pmatrix} \begin{pmatrix} L & 1 & \ell_i \\ -M & 0 & m_i \end{pmatrix} \langle R_{kL}|r|R_{n_i l_i}\rangle, \end{aligned} \tag{3.22}$$

where the angular part was evaluated according to Equation (3.18). The radial part $M^{(1)}_{ki}$ is real valued, so the phase of the transition matrix element for one-photon ionization becomes:

$$\arg\left[M^{(1)}_{ki}\right] \approx \phi_\Omega + \eta_L(k) + \arg\left[Y_{LM}(\hat{k})\right] - L\frac{\pi}{2}, \tag{3.23}$$

for $L = \ell_i \pm 1$ and $M = m_i$. This includes the phase of the ionizing field and the scattering phase shift.

Phase Shifts

The phase shifts of the photoelectron wave function in Equations (3.20) and (3.21) are a result of the atomic potential. They are phase shifts compared to a free electron wave function with no potential present. As illustrated in Figure 3.2, the total accumulated phase has different origins: the factor $-L\pi/2$ arises due to the centrifugal potential barrier. The phase shifts $\eta_L(k)$ are the scattering phases, and are given as $\eta_L(k) = \sigma_L(k) + \delta_L(k)$, where $\sigma_L(k)$ are the Coulomb phases due to the Coulomb potential. These phases can be expressed analytically with the aid of the complex gamma function. The asymptotic phase shifts, $\delta_L(k)$, depend on the deviation of the short-range potential from the pure Coulombic case [80]. In the central-field model this deviation is due to the (N-1) electrons that modify the potential seen by the electron. $\delta_L(k)$ are a very important quantity, since they carry information about the physical effect of the inner potential into the outer asymptotic region [80], and thus give direct insight into the atom.

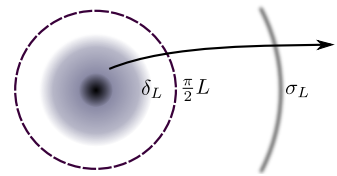

Figure 3.2. *Different phase shifts accumulated by the photoelectron.*

Time Delay in Photoemission

In the context of scattering problems, Eugene Wigner introduced the concept of time delay [82, 83]. This is defined as the extra time the scattered particle spends in the scattering region, i.e., the potential, compared to a free particle subject to the same conditions [84]. The physical meaning of the time delay can be understood in an intuitive way: a positive time indicates a delay while a negative time difference can be seen as a acceleration. The Wigner time delay is defined as $\tau_{\mathrm{W}} = 2\hbar\, d\eta_L/dE$, where η_L is exactly the scattering phase of the L-partial wave introduced above. As photoionization can be seen as half a scattering problem (the electron leaves the potential but it does not enter it), a corresponding time delay for photoemission can be defined as half the Wigner time delay:

$$\tau = \hbar \frac{d\eta_L}{dE}. \tag{3.24}$$

The potential introduces dispersion into the motion of the electron, which speeds up or slows down compared to the motion if it were in a field-free region. The derivative of the scattering phase, $d\eta_L/dE$, is a measure of this dispersion. Electrons ionized from different shells of an atom 'see' a different potential and the time delays are expected to be different for photoionization of different shells [85].

In photoionization the scattering phases appear as the phase of the dipole matrix element $M_{ki}^{(1)}$. However, in conventional photoelectron spectroscopy the possibility of accessing the phase, and therefore the timing of an photoelectron wave packet, is limited.

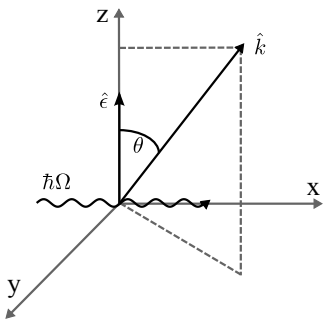

Figure 3.3. *Photoionization coordinate system used for linear polarized light.*

One option is to use angularly resolved measurements (see below), but they only provide a measure of the phase difference between partial waves in the outgoing wave packet. Papers **II**, **III** and **IV** describe how the phase properties of a photoelectron can be obtained using an extension of the RABITT method to measure the difference in delay between electrons ionized from the $3s$ and $3p$ subshells in argon.
Note that the photoemission time delay is given as $\tau = d\eta_L/dE$ only for one dominant ionization channel into an L-like final state. For more than one ionization channel with comparable amplitudes, the resulting time delay is given by a mixture of the different η_L weighted by the cross-section.

3.1.3 Total and Partial Cross-Sections

The absorption cross-section σ_{fi} for process a) in Figure 3.1 is defined as the rate of absorption of energy from a radiation field divided by its intensity, $I(\omega_{fi})$ [74]:

$$\sigma_{fi} = \frac{\hbar\omega_{fi} W_{fi}^{(1)}}{I(\omega_{fi})}, \tag{3.25}$$

where $W_{fi}^{(1)}$ is the time-independent transition rate for absorption introduced in Equation (3.7). Taking the expression for the transition amplitude derived in Equation (3.15), the absorption cross-section can be rewritten as:

$$\sigma_{fi} = 4\pi^2 \alpha \omega_{fi} |\langle \varphi_f | z | \varphi_i \rangle|^2 \delta(\omega_{fi} - \Omega)\,, \tag{3.26}$$

where several constants are merged into the fine-structure constant $\alpha = e^2/4\pi\epsilon_0\hbar c$.
From Equation (3.26) it is easy to define the total cross-section for photoionization by integrating over all final states, $\mathbf{k}$, of the ejected electron:

$$\sigma_{tot} = \int d\mathbf{k}\ \sigma_{\mathbf{k}i}. \tag{3.27}$$

The integration element $d\mathbf{k}$ can be written $d\mathbf{k} = k^2 dk d\Theta$, where $d\Theta$ is the differential solid angle in the direction of $\hat{k}$. The assumed geometry is shown in Figure 3.3. Using energy conservation, the final energy of the photoelectron is given by $E_k = \hbar^2 k^2/2m$, and the total ionization cross-section becomes:

$$\sigma_{tot} = \int d\Theta \int dE_k\ \frac{mk}{\hbar^2}\sigma_{\mathbf{k}i} = \frac{4\pi^2 \alpha m k \Omega}{\hbar} \int d\Theta\ |\langle \mathbf{k} | z | \varphi_i \rangle|^2, \tag{3.28}$$

where the integration over E_k was performed with the help of the δ-function. For angularly resolved measurements it is convenient

to define the differential cross-section for electron ejection within the solid angle $d\Theta$:

$$\frac{d\sigma}{d\Theta} = \frac{4\pi^2 \alpha m k \Omega}{\hbar} |\langle \mathbf{k}|z|\varphi_i\rangle|^2. \tag{3.29}$$

The evaluation of $|\langle \mathbf{k}|z|\varphi_i\rangle|^2$ yields the general expression for the angular distribution of photoelectrons:

$$\frac{d\sigma}{d\Theta} = \frac{\sigma_{tot}}{4\pi} \left(1 + \beta P_2(\cos\theta)\right), \tag{3.30}$$

where $P_2(\cos\theta)$ is the second-order Legendre polynomial, and β is the asymmetry parameter. The angle θ is measured with respect to the quantization axis, as indicated in Figure 3.3. For multi-photon ionization higher-order Legendre polynomials must be included, where the highest order is connected to the order of the multi-photon process [59]. The angular distribution in photoionization will further discussed for some selected examples in section 4.2.

The asymmetry parameter depends on the angular momentum of the initial and final states as well as on the radial part of $\langle \mathbf{k}|z|\varphi_i\rangle$. In general, the angular distribution includes an interference pattern between partial waves with different angular momenta, intensities and phase shifts. This leads to constructive lobes or destructive nodes in the angular distribution, with positions that are very sensitive to the relative phase $(\eta_{\ell_i+1} - \eta_{\ell_i-1})$ between the interfering partial waves [78]. In Papers **VI** and **VII** the angular distribution was used to distinguish between different pathways into the continuum.

The ultimate goal of photoionization studies is to perform a 'complete experiment' enabling the whole photoionization dynamics to be captured [78]. Complete experiments require the determination of the magnitudes of the radial dipole matrix element for the partial wave of each contributing photoelectron and the phase differences between them. Angular-resolved measurements are essential for complete experiments since the measured β-parameter depends strongly on the amplitudes and their scattering phases. However, only the difference between partial waves in the outgoing wave packet are available in conventional angular-resolved measurement (see, for example Reference [86]). The interferometric pump-probe experiment presented in Papers **VI** and **VII** provide additional information for the characterization of the photoionization processes.

3.2 Interaction with Two Photons

All experiments presented in this thesis rely on two-color two-photon ionization, where one color is XUV and the other one is IR.

Figure 3.4 displays the most interesting ionization pathways. First, the electron absorbs an XUV photon with the energy $E = \hbar\Omega$ and then in the second step the electron interacts with an additional IR photon $E = \hbar\omega$. The intermediate state can either be below a) or already above the ionization threshold b).
The dipole matrix element for two-photon ionization can be calculated in a similar manner as for one photon. Using second-order perturbation theory the two-photon ionization dipole matrix element can be expressed as:

$$M_{ki}^{(2)} = \frac{-i}{\hbar^2}\frac{E_\omega}{\omega}\frac{E_\Omega}{\Omega}e^2 \lim_{\varepsilon\to 0^+} \sum\!\!\!\!\!\!\int_s \omega_{ks}\omega_{si}\frac{\langle \mathbf{k}|z|\varphi_s\rangle\langle\varphi_s|z|\varphi_i\rangle}{\omega_i + \Omega - \omega_s + i\varepsilon}. \quad (3.31)$$

As before, the incident light is linearly polarized in the $\hat{z}$-direction, which is also chosen as the quantization axis. The initial state is denoted φ_i with the energy E_i and the final continuum state has the asymptotic momentum $\mathbf{k}$. The sum runs over all possible intermediate states, s, which can either be discrete bound states or in the continuum. The complex amplitudes of the laser and the XUV fields are denoted E_ω and E_Ω, respectively.
As for one-photon ionization, the initial, intermediate and final states can be factorized into a radial and an angular part. Using again a partial wave expansion for the continuum state, the transition matrix element takes the form:

$$\begin{aligned} M_{ki}^{(2)} &= \frac{-i}{\hbar^2}\frac{E_\omega}{\omega}\frac{E_\Omega}{\Omega}e^2(8\pi)^{3/2} \\ &\quad\times \sum_{\substack{L=\lambda\pm1,\lambda=l_i\pm1\\ M=\mu=m_i}} \omega_{ks}\omega_{si} i^{-L} e^{i\eta_L(k)} Y_{LM}(\hat{k})\ \hat{L}\hat{\lambda}^2\hat{\ell}_i \\ &\quad\times \begin{pmatrix} L & 1 & \lambda \\ 0 & 0 & 0 \end{pmatrix}\begin{pmatrix} L & 1 & \lambda \\ -M & 0 & \mu \end{pmatrix} \\ &\quad\times \begin{pmatrix} \lambda & 1 & l_i \\ 0 & 0 & 0 \end{pmatrix}\begin{pmatrix} \lambda & 1 & l_i \\ -\mu & 0 & m_i \end{pmatrix} T_{L\lambda}^{(2)}(k)\,. \end{aligned} \quad (3.32)$$

The sum was reduced by taking the dipole selection rules into account: $L = \lambda \pm 1$, $\lambda = \ell_i \pm 1$ and $M = \mu = m_i$ where $\{\lambda, \mu\}$ are the orbital and the magnetic quantum numbers of the intermediate state. The radial part is given by:

$$\begin{aligned} T_{L\lambda}^{(2)} &= \sum_{s, E_s<0} \frac{\langle R_{kL}|r|R_{\lambda\mu}\rangle\langle R_{\lambda\mu}|r|R_{n_i\ell_i}\rangle}{\omega_i + \Omega - \omega_s} \\ &\quad + \lim_{\varepsilon\to 0^+}\int_0^{+\infty} dE_\kappa \frac{\langle R_{kL}|r|R_{\kappa\lambda}\rangle\langle R_{\kappa\lambda}|r|R_{n_i\ell_i}\rangle}{\omega_i + \Omega - \omega_\kappa + i\varepsilon}. \end{aligned} \quad (3.33)$$

The discrete and the continuous parts are now separated. For the situation illustrated in Figure 3.4 a) the intermediate state is below the ionization threshold. In the presence of a resonance

state $|\varphi_r\rangle$ where $\Omega \approx \omega_{ri}$ the denominator for the term $s = r$ in the first sum becomes so small so that the expression for $T^{(2)}_{L\lambda}$ can be approximated by the dominant term. When the photon energy is scanned across such a resonance it will cause a sign change of $T^{(2)}_{L\lambda}$, i.e., a π phase jump of the complex amplitude.[1] The phase behavior was studied as a function of detuning $\delta = (\Omega - \omega_{ri})$ from the $1s3p\ ^1\mathrm{P}_1$ state in helium, and is described in Paper **V**. The measurement method is presented in Section 4.1.

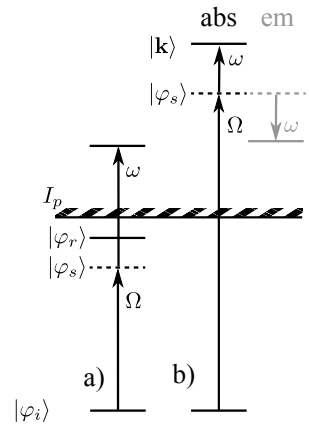

Figure 3.4. *Two-photon ionization. a) The intermediate state is still a bound state. b) The XUV photon energy is already sufficient to ionize so that the intermediate state is in the continuum. Two possible continuum-continuum transitions are shown: absorption and emission of one IR photon.*

Asymptotic Approximation

For $\hbar\Omega > I_p$ the intermediate state will be a continuum state. The momentum κ in Equation (3.33), which corresponds to the absorption of an XUV photon, is $\hbar^2\kappa^2/2m = E_i + \hbar\Omega$. As a consequence, the denominator in the second line in Equation (3.33) approaches zero, and the radial part becomes a complex quantity. This is in contrast to one-photon ionization, where the radial part is real. To obtain an estimate of the phase of the radial part of above-threshold two-photon ionization an asymptotic approximation was developed (Paper **II**), the main steps of which will be described below. A more detailed and improved derivation can be found in Paper **IV**.
The radial part can be rewritten as:

$$T^{(2)}_{L\lambda} = \langle R_{kL}|r|\rho_{\kappa\lambda}\rangle, \tag{3.34}$$

introducing the perturbed wavefunction,

$$|\rho_{\kappa\lambda}\rangle = \lim_{\varepsilon\to 0^+} \sum\!\!\!\!\!\!\int_s \frac{|R_{\kappa\lambda}\rangle\langle R_{\kappa\lambda}|r|R_{n_i\ell_i}\rangle}{\omega_i + \Omega - \omega_s + i\varepsilon}. \tag{3.35}$$

This perturbed wave function is in its nature an outgoing wave and represents the electron wave packet after the first ionization step. It can be shown that in the asymptotic limit as $r \to \infty$ it takes the form [87, 88]:

$$\rho_{\kappa\lambda}(r) \approx -\frac{\pi N_\kappa}{r} \exp(i[\kappa r + \frac{\ln(2\kappa r)}{\kappa} + \eta_\lambda(\kappa) - \lambda\frac{\pi}{2}])\langle R_{\kappa\lambda}|r|R_{n_i\ell_i}\rangle, \tag{3.36}$$

where N_κ is a normalization constant. The integral in Equation (3.34) can then be solved using the asymptotic form of $\rho_{\kappa\lambda}(r)$ and the asymptotic form of the final state introduced in Equation (3.21). The phase of the complex quantity $T^{(2)}_{L\lambda}$ is then given by:

$$\arg\left[T^{(2)}_{L\lambda}\right] \approx \frac{\pi}{2}(L - \lambda - 1) + \eta_\lambda(\kappa) - \eta_L(k) + \phi_{cc}(k,\kappa)\,. \tag{3.37}$$

[1] At resonance, i.e., when $\Omega = \omega_{ri}$, the first term in Equation (3.33) goes to infinity. To properly describe such a situation the XUV bandwidth must be included.

The radial part contains the difference between the scattering phases of the two continuum states involved plus an additional phase factor $\phi_{cc}(k,\kappa)$. This phase is associated with the continuum-continuum radiative transition resulting from the additional absorption of the IR photon in the presence of the Coulomb potential. The continuum-continuum phase $\phi_{cc}(k,\kappa)$ does not depend on the details of the atomic potential, only on the momenta $\{k,\kappa\}$ of the continuum states. In its simplest form it is given by [88]:

$$\phi_{cc}(k,\kappa) = \arg\left[\frac{(2\kappa)^{i/\kappa}}{(2k)^{i/k}}\,\frac{\Gamma\left[2+i(1/\kappa-1/k)\right]}{(\kappa-k)^{i(1/\kappa-1/k)}}\right]. \tag{3.38}$$

The expression for $\phi_{cc}(k,\kappa)$ is analytical and can be calculated. Since it does not depend on the atomic potential it is universal and can be applied, in principle, to arbitrary systems.
Within the asymptotic approximation the phase of the complete matrix element from Equation (3.32) becomes:

$$\arg\left[M_{ki}^{(2)}\right] \approx \phi_\Omega + \phi_\omega + \eta_\lambda(\kappa) + \arg\left[Y_{LM}(\hat{k})\right] - \lambda\frac{\pi}{2} + \phi_{cc}(k,\kappa)\,. \tag{3.39}$$

The main outcome of the asymptotic treatment is that the scattering phase of the final state cancels out, and except for the additional continuum-continuum phase the expression recovers the phase of one-photon ionization in Equation (3.23).
The derivation for the emission of an IR photon instead of absorption (see Figure 3.4) is similar, but ω is replaced by $-\omega$. In Papers **II** and **III** the asymptotic approximation was used to extract the one-photon ionization phase from the measured two-photon phase in order to determine the time delay of photoelectrons in photoemission (see Section 4.1).

3.3 Electron Correlations

The physics of photoionization presented so far utilizes the central-field approximation, which leads to a description of N independent electrons. In some cases, the collective response of the electrons must be considered, for example, to explain processes such as one-photon double ionization, shake-up processes, Auger decay or post-collision interactions, where the electrons may directly interact with each other.
A good starting point to include electron-electron interactions is the Hartee-Fock (HF) method, where the effective potential and the electronic eigenstates can be calculated with good accuracy [89]. In the HF method the electron-electron Coulomb interaction is incorporated into a mean-field, while taking into account the anti-symmetry of the electronic wave function. This leads to a correlation of the electron position for electrons having

parallel spin since they cannot have the same position (Pauli principle). The HF method already accounts for this part of the electron-electron interaction while still being an independent particle model [90]. All interactions beyond HF are usually referred to as electron correlations.
The interesting quantity in photoionization is the matrix element M_{fi}. Electron correlations can either be included directly in the initial and final wave functions or indirectly as an additional field in the operator z. Within the framework of configuration interaction (CI) the real N-electron wavefunctions Ψ, which include electron correlation, are expanded in terms of a complete set of uncorrelated basis functions, $\Psi^{(0)}$, where the basis functions differ in the occupation of their orbitals, and hence in their electron configuration [74]. It is possible to distinguish between initial state configuration interaction (ISCI) and final state configuration interaction (FSCI) [89].
Instead of incorporating electron correlations into the wave functions, one can describe the influence of electron correlations as an induced field which adds to the external field during photoionization, so that $z \rightarrow Z$. This approach is the basis for the random-phase approximation with exchange (RPAE) method, which was used in Paper **III**. The basic idea of RPAE is that the amplitude of the photoionization process can be expressed as the sum of two terms: one that describes the direct photoionization and one that describes the ejection of an electron as a consequence of the change in the N-electron field due to the external perturbation. Physically, one can imagine that the electron cloud is deformed and polarized by the external field, so that the actual field seen by the ionized electron differs from the pure external field [91]. The application of RPAE to photoionization shows very good agreement for cross-sections of outer-shell ionization in rare-gas atoms [89]. A detailed list of theoretical methods including correlation effects is given, for example, in References [89, 92].

Figure 3.5 shows diagrams[2] of important electron-electron interactions in photoionization as included in RPAE. Single-particle photoionization ($n \rightarrow k$) is shown in a). The symbols n and k characterize the active electron. The wavy line represents the dipole photon interaction, and the dashed lines b) and c) denote the Coulomb interaction. The index s denotes all possible discrete and continuous orbitals. The diagrams are read from the bottom to the top with respect to the time axis t. In b) the atom in the ground state has two virtually excited electrons from the n shell. Upon absorbing a photon, one of the electrons is de-excited into

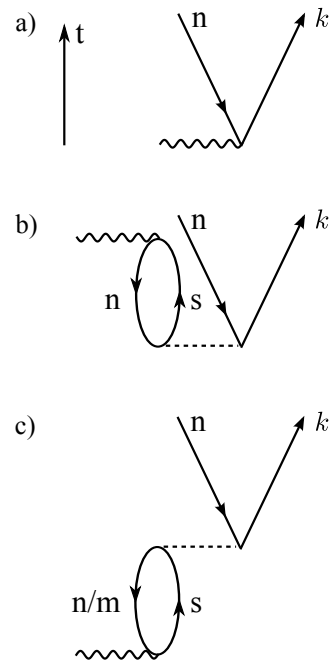

Figure 3.5. *Single photoionization. a) Single-particle ionization. b) Photoabsorption by a virtually doubly-excited state. c) Intra-/Interchannel coupling following photoabsorption. From [75].*

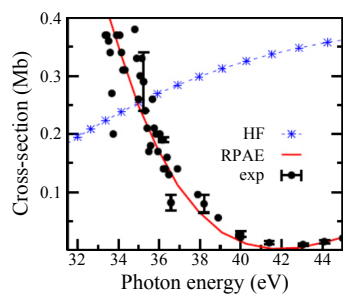

Figure 3.6. *Partial cross-section for the argon $3s \rightarrow \epsilon p$ transition. Experimental data from [93].*

[2] A detailed description of Feynman diagrams for photoionization can be found, for example, in Reference [91].

its original state while the other is ionized [75]. In the CI picture this corresponds to ISCI. In diagram c) an electron is excited, but during its escape it interacts with another electron so that the second electron is ionized and the original electron is de-excited into its ground state. This process can be classified as FSCI, since the interaction takes place after photoabsorption. When the electron is from the same subshell, n, this is called intrachannel coupling, and if the electron is from a different subshell, m, it is called interchannel coupling. While intrachannel coupling is included in the HF model, interchannel coupling is treated as a correlation.

Interchannel coupling is of particular importance for s subshell ionization [75]. Figure 3.6 compares experimental data and theoretical calculations of the partial cross-section for the $3s \rightarrow \epsilon p$ transition in argon. The experimental data show a distinct minimum between 40 and 45 eV. The results of HF calculations do not reproduce this minimum, while RPAE, which includes interchannel coupling, reproduces the strong destructive interference between pathways a) and c) in Figure 3.6 [75]. The phase variation close to the cross-section minimum was investigated in Paper **III**.

Further electron correlations beyond RPAE include relaxation processes, i.e., FSCI in the CI picture, as shake-up or shake-off processes or Auger decay. The independent particle approximation implies that the orbitals of the passive electrons do not change under photoionization; this is the so-called frozen core approximation. However, the ejection of one electron through photoionization will alter the Coulomb field seen by the remaining electrons. In the shake-up model this unrelaxed wavefunction is projected onto the relaxed ionic states with the result that one of the remaining electrons may be shaken into a higher unoccupied orbital. These states can either be bound (shake-up) or free (shake-off), and the latter will lead to double ionization.[3] Shake-up transitions are governed by monopole selection rules $\Delta\ell = \Delta m = 0$. It should be noted that the shake-up model explains the existence of shake-up processes in helium qualitatively but not quantitatively. Other correlations in the form of CI have to be taken into account to fully describe shake-up in helium [89].

The theoretical studies presented in Paper **VII** on shake-up processes in helium do not reflect this complexity. However, this does not compromise the study presented in Paper **VII**, as discussed in Section 4.2.

[3] Shake-up excitation can also lead to double ionization if the final state is an autoionizing state.

Chapter 4

Attosecond Interferometry

When an attosecond pulse interacts with an atom or molecule it excites a broad electronic wave packet. This wave packet can either be bound, free or a mixture of both. Characterization of the EWP and following its evolution give valuable insight into the dynamics of the excitation process, as well as information on the system it originated from. The phase is of particular interest, not only because it is necessary for complete reconstruction of the EWP, but because it carries information about the timing of the excitation process, as introduced in Chapter 3. Interferometry is a very powerful tool since small changes in the phase or the wavelength can be detected. This allows for the determination of phase differences of EWPs that correspond to delays on the order of ~ 100 *as. By including phase-sensitive techniques in classical time-resolved pump-probe arrangements, not only the temporal resolution, which is no longer given by the pulse duration,* τ*, but also the spectral resolution (usually given by the Fourier limit* $\propto 1/\tau$*) can be improved significantly.*
This chapter is organized as follows. In the first section some examples of interferometry using attosecond pulse trains are presented, followed by the description of an interferometric pump-probe method using single attosecond pulses in the Section 4.2. In Section 4.3 the concept of attosecond stark spectroscopy is introduced and the first experimental results are presented.

4.1 Interferometry Using Attosecond Pulse Trains

This section gives examples of interferometric measurements using the phase-locked harmonic radiation from attosecond pulse trains in combination with the fundamental laser field.

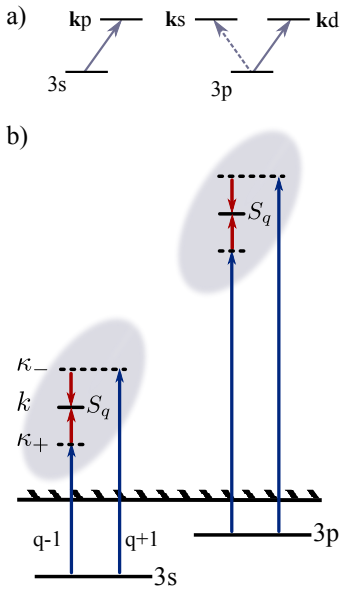

Figure 4.1. *Photoionization of the valence shell in argon. a) Possible ℓ-channels. b) Principle of the measurement.*

4.1.1 Time Delay Measurements

When an atom interacts with an attosecond pulse whose energy is higher than the ionization potential of the atom a coherent free EWP is created. When the photoelectron leaves the atom its phase will depend on the atomic potential it has to overcome and the kinetic energy of the final state.

The general concept of group delay of a wave packet in a dispersive medium can be applied to the outgoing EWP in the atomic potential, and a group delay can be defined as the energy derivative of the phase of the complex matrix element for the bound-free transition. The group delay of the photoelectron then provides a measure of the relative timing of the spectral components in the photoemission process.

Papers **II** and **III** describe measurements of the time delay of photoemission of electrons from the valence shell in argon using an interferometric method to access the phase difference between spectral components of the EWP. It is similar to the technique used to determine the spectral phase of the attosecond pulses (see Section 2.2.2), but the emphasis is on the atomic contribution to the measured phases.

Whether or not the group delay in photoemission can be reduced to the Wigner time delay introduced in Section 3.1.2 depends on the number of ionization channels open for a given transition and on the strength of possible electron correlations. For the sake of simplicity only non-interacting electrons are considered here. The validity of this assumption will be discussed at the end of this section. Figure 4.1 a) shows the ionization channels for the $3s^2$ and $3p^6$ shells in argon given by the dipole selection rules. There is only one open channel for s shell ionization but in principle two different final states for the photoionization from the p shell. The transition $\ell \rightarrow \ell + 1$ is usually favored, but under some conditions the probability of this transition can be greatly reduced, for example, due to a Cooper minimum. This is the case for argon at a photon energy of about 48 eV, so that the relative strength of the $\ell \rightarrow \ell - 1$ transition increases. For photon energies below 48 eV, which were used in these experiments, photoionization from the p shell in argon was approximated by the $3p \rightarrow \mathbf{k}d$ channel.

The basic idea behind the delay measurements is shown in Figure 4.1 b). The argon atoms are ionized using the phase-locked high-order harmonics from a train of attosecond pulses. The central frequency of the harmonic comb is well above the $3s$ ionization threshold, so two independent EWPs are created simultaneously. The EWPs are then probed with a small fraction of the fundamental laser field with a frequency ω. Due to the presence of the IR field, two-photon transitions are introduced where the electron either picks up or emits an additional photon, which leads to the formation of sideband peaks, S_q. The two different quantum paths

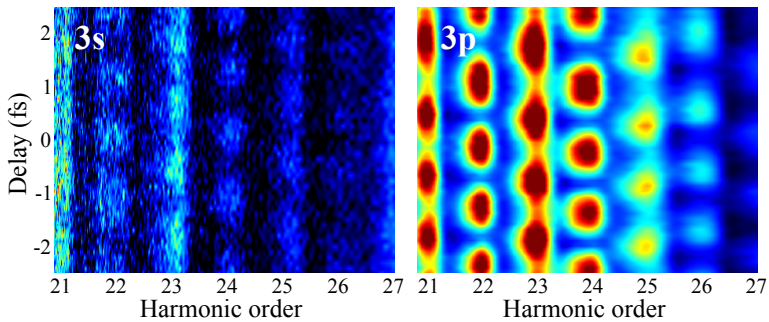

Figure 4.2. *Interferometric measurement of EWPs liberated from the 3s- and 3p-shell in argon. The interference signal at even harmonic orders oscillates as a function of XUV-IR delay.*

to the same final state will interfere, and changing the delay between the attosecond pulse train and the probe field will cause modulation of the sideband signal.
Figure 4.2 presents the interferometric measurements for the $3s$ and $3p$ photoelectrons. A 0.2 μm thin chromium filter was used to select a 10 eV-broad spectral window corresponding to harmonics 21 to 27 at a central energy of 37 eV. The filter was necessary to separate the two EWPs in energy.

The RABITT Equation (2.8) describing the sideband oscillations can be derived using the asymptotic approximation for two-photon ionization from Section 3.2, within which the phase of the complex matrix elements $M_{\pm}^{(2)}(k)$, where the electron picks up (+) or emits (−) an additional photon (see Figure 4.1 b)) is given by:

$$\arg\left[M_{\pm}^{(2)}(k)\right] \approx \phi_{q\mp1} \mp \phi_{\omega} + \eta_{\lambda}(\kappa_{\pm}) + \arg\left[Y_{LM}(\hat{k})\right] + \phi_{cc}(k,\kappa_{\pm})\,. \tag{4.1}$$

Here, $\phi_{q\mp1}$ is the spectral phase of the harmonic $q \mp 1$ and ϕ_{ω} is the relative phase of the IR field with respect to the attosecond pulse train. The phase shifts $\eta_{\lambda}(\kappa_{\pm})$ are the one-photon scattering phases of the intermediate states, $\kappa_{\pm}$, with the angular momentum λ and $\phi_{cc}(k,\kappa_{\pm})$ are the continuum-continuum phases due to the second transition from the intermediate states to the final state, k. The interference between the two pathways will be governed by the phase difference between them:

$$\begin{aligned} S_q(\tau) \quad &\propto \quad |M_{+}^{(2)} + M_{-}^{(2)}|^2 = |M_{+}^{(2)}|^2 + |M_{-}^{(2)}|^2 \\ &\quad +2|M_{+}^{(2)}||M_{-}^{(2)}|\cos(2\omega\,(\tau - \tau_{\mathrm{A}} - \tau_{\mathrm{I}}))\,, \end{aligned} \tag{4.2}$$

where

$$\tau_{\mathrm{A}} = \frac{\phi_{q+1} - \phi_{q-1}}{2\omega} \tag{4.3}$$

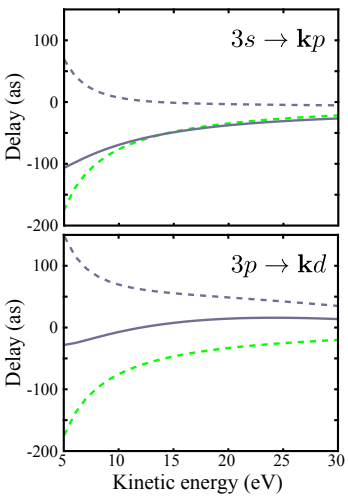

Figure 4.3. *Computed delays associated with the two dominant ionization channels. The blue dashed lines are the single-photon Wigner time delays. The green lines represent the estimated measurement delay τ_{cc}. The ionization delay τ_{I} is the sum of both and plotted as solid lines.*

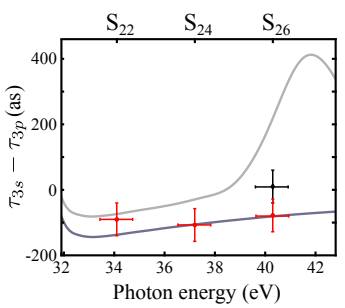

Figure 4.4. *Comparison between experimental results (red 2009, black 2011) and theoretical calculations (blue HF, gray RPAE).*

is the group delay of the attosecond pulse. The ionization delay, τ_{I}, caused by the two-photon transition contains two terms:

$$\tau_{\mathrm{I}} = \underbrace{\frac{\eta_\lambda(\kappa_-) - \eta_\lambda(\kappa_+)}{2\omega}}_{\tau_{\mathrm{W}}} + \underbrace{\frac{\phi_{cc}(k,\kappa_-) - \phi_{cc}(k,\kappa_+)}{2\omega}}_{\tau_{cc}}. \tag{4.4}$$

The first term, denoted τ_{W}, is a finite difference approximation of the Wigner time delay, and reflects the properties of the EWP from single-photon ionization into the angular momentum channel λ. The second contribution, τ_{cc}, stems from the continuum-continuum transition due to the IR field. In this process, the IR field acts as a probe for single-photon ionization, changing the final state energy, causing the two paths to interfere. The delay, τ_{cc}, can then be interpreted as a measurement-induced delay, which is independent of the characteristics of the initial atomic state.

Figure 4.3 presents the delays of the two dominant ionization channels in argon as a function of kinetic energy. The Wigner time delay was assumed to be the derivative of the scattering phase in an independent-electron model [81]. The measurement delay τ_{cc} was calculated with a photon energy of $\hbar\omega = 1.55$ eV, and is the same for the two channels. The Wigner time delay has an intuitive interpretation: i.e., low-kinetic-energy electrons take longer to escape the potential for a given shell. Also, ionizing electrons into a channel with a higher angular momentum λ takes a longer time because of the centrifugal potential. The measurement delay shows the opposite behavior, leading to an apparently faster escape of the electron compared to field-free emission.

The delay encoded in the sidebands is the sum of τ_{A} and τ_{I}. These two contributions are difficult to separate. However, the simultaneous measurements of the two EWPs can be used to cancel the influence of the attosecond group delay, τ_{A}, and to determine $\tau_{\mathrm{I}}(3s) - \tau_{\mathrm{I}}(3p)$ at the same photon energy. The results of the difference measurement are plotted in Figure 4.4. The red circles indicate the results from a first series of measurements carried out in 2009. They agree well with the computed difference in delay within the independent particle approximation. A second series of measurements performed in 2011 with an improved experimental setup reproduced the lower energy data points, but show a different behavior for the sideband S_{26} (shown in black in Figure 4.4). At about the same time, the theoretical model was also improved. In cooperation with Anatoli Kheifets, the Wigner time delay was replaced by a more general time delay including electron correlations (see Section 3.3). The corresponding RPAE calculations show a rapid change in the delay in the energy region 40-45 eV. This is

due to a phase variation of the matrix element for the $3s$ ionization close to a Cooper-like minimum in the partial cross-section due to interchannel coupling. The discrepancy in the experimental results for S_{26} could be caused by this large variation in time delay and the uncertainty of the energy calibration which is self-referencing. Even a small change in the harmonic photon energy due to a shift of the fundamental spectrum together with different generation conditions would lead to a considerable change in the measured delay. This is shown by the error bars in photon energy. Further details concerning the RPAE calculations can be found in Paper **III**.

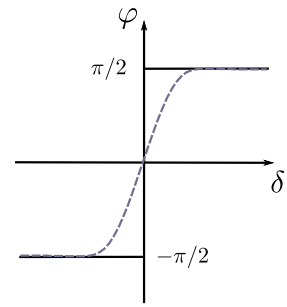

Figure 4.5. *Illustration of the phase behavior within perturbation theory for a R2PI as function of detuning from the resonance δ. The dashed line represents the expected variation including the XUV bandwidth.*

4.1.2 Resonant Two-Photon Ionization

If an electron is excited by two photons with a combined photon energy that is sufficient for ionization, this is referred to as two-photon ionization, as discussed in Section 3.2. In more general terms, this is often expressed as two-color two-photon ionization if the two photons have different energies.

The probability of a two-photon transition is strongly enhanced if the energy of one photon is close to an intermediate state, r. The transition amplitude is then governed by the resonant term and the matrix element from Equation (3.31), and can be approximated by:

$$M_{\mathbf{k}i}^{(2)} \propto E_\omega E_\Omega \frac{\langle \mathbf{k}|z|\varphi_r\rangle\langle\varphi_r|z|\varphi_i\rangle}{E_i - E_r + \hbar\Omega}, \tag{4.5}$$

where E_r is the energy of the resonant state and $\hbar\Omega$ the photon energy. When the photon energy is scanned across the resonance, $M_{\mathbf{k}i}^{(2)}$ changes sign, which manifests itself as a π phase jump of the matrix element. The phase behavior as a function of detuning from the resonance δ is shown in Figure 4.5. The phase of $M_{\mathbf{k}i}^{(2)}$ is therefore very sensitive to the photon energy if it is close to a resonant transition. In the presence of a resonant state, this two-photon ionization is usually referred to as resonant two-photon ionization (R2PI).

Paper **V** describes a study of the resonant phase behavior of the R2PI of helium via the 1s3p $^1P_1$ state. The basic principle is illustrated in Figure 4.6. The 15th harmonic (H_{15}), with a photon energy of 23.25 eV generated from a fundamental IR field with a wavelength of 800 nm (corresponding to $\hbar\omega = 1.55$ eV photon energy), was chosen as the first color. The energy of H_{15} is close to that of resonant transition $1s^2 \rightarrow 1s3p$ at 23.087 eV. With an ionization potential of 24.59 eV the 3p state can be ionized with a single IR photon, which was chosen as the second color.

Changing the fundamental wavelength using the Dazzler (see Section 2.2.3), and therefore the photon energy of H_{15}, allows the detuning between the photon energy and the resonant transition

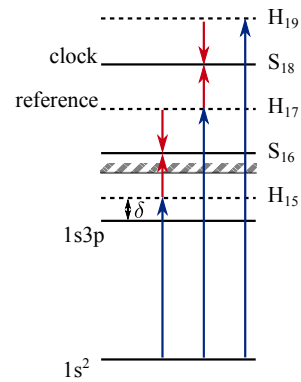

Figure 4.6. *Principle of the phase measurement in a R2PI.*

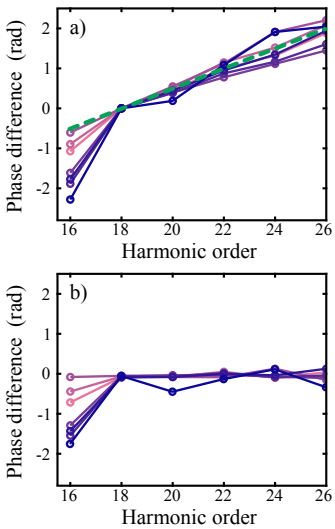

Figure 4.7. *Harmonic phase difference for different detunings. a) While S_{16} varies with δ are the higher-order sidebands unaffected and only exhibit a linear chirp indicated with the green line. b) The same measurements corrected for a linear chirp fit.*

δ to be scanned. The change in phase is measured as a function of δ by interference with a second pathway to the same final state, which is unaffected by the detuning. Figure 4.6 shows that the direct ionization with H_{17} together with the stimulated emission of one IR photon serves as such a reference. When the fundamental wavelength is changed, all the photon energies will change, and thus the interference signal is independent of the fundamental wavelength. The final state can be identified as sideband S_{16} in a conventional RABITT measurement, where the intensity of the sideband signal will be modulated as function of the delay τ between the harmonic fields and the IR field:

$$S_{16}(\tau) \propto 1 + \cos\big(2\omega\tau - \Delta\phi_{16} - (\phi_e^{at} - \phi_a^{at})\big)\,. \tag{4.6}$$

The interesting term in the equation above is the atomic phase term, ϕ_a^{at}, which contains the contribution from the resonant transition (a indicates the pathway involving the absorption of one IR photon). The atomic phase contribution from the second pathway, ϕ_e^{at}, can be identified from Equation (3.39), but only causes a small constant phase offset compared to the phase variation due to the presence of the resonance. The phase $\Delta\phi_{16} = \phi_{17} - \phi_{15}$ gives the group delay of the attosecond pulses, which must to be determined independently in order to extract ϕ_a^{at}. As discussed in Section 2.1.1, the variation in the spectral phase of an attosecond pulse can assumed to be linear, and can therefore be measured using higher-order sidebands excluding S_{16}. Figure 4.7 shows the phases extracted from RABITT measurements for different degrees of detuning and the way in which the phase of S_{16} is corrected for the attosecond group delay.

To compare the measurements made with different amounts of detuning, δ, the absolute delay between the XUV and the IR pulses must be known. The phase of S_{16} was therefore referenced to the respective phase of S_{18}, which was unaffected by the detuning and could be used as an absolute clock.

Measurements were performed, in which δ was either changed by tuning the fundamental wavelength, or by tuning the position of the 1s3p state using the intensity-dependent AC-Stark effect. Combining the two measurements allowed the intensity dependence of the $1s^2 \rightarrow 1s3p$ transition energy to be determined. Further details can be found in Paper **V**.

4.2 Interferometry using Single Attosecond Pulses

When an atom interacts with an attosecond pulse whose photon energy is not sufficient for ionization it may create a broad bound EWP instead. This EWP can be studied after further ionization

using interferometry, as introduced in Paper **VI** and further explored in Paper **VII**.
The basic idea of the measurements is shown in Figure 4.8 a). Helium atoms are excited using a broadband SAP with a photon energy centered around the ionization threshold at 24.6 eV. A broad EWP is created that includes several bound states as well as continuum states. After initial excitation the EWP evolves freely in time. The excited helium atoms are further ionized, at a variable delay, with an IR pulse locked in phase to the SAP, and the resulting electron momentum distribution is recorded using a VMIS. For long delays, when the XUV and the IR pulses are clearly separated in time, the momentum distribution exhibits interference due to the two distinct ionization pathways. One of the pathways stems from ionization with the SAP (the *direct* pathway), while the other is the result of delayed ionization with the IR pulse (the *indirect* pathway). Figure 4.9 presents a momentum distribution obtained during the experimental work presented in Paper **VI**.

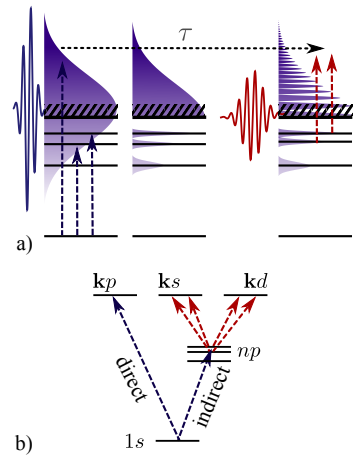

Figure 4.8. *a) Principle of the pump-probe interferometer. b) Possible ionization channels in the interferometer.*

In contrast to Papers **VI** and **VII**, where traditionally notation in quantum beat spectroscopy was used, the following analysis of the interferences will carried out within the framework introduced in Chapter 3. Figure 4.8 b) depicts the ionization channels in the interferometer leading to a final state with energy $E = \hbar^2 k^2/2m$. For the direct pathway the only possible ionization channel is the $1s \rightarrow \mathbf{k}p$ channel, and the corresponding dipole matrix element is:

$$M_{dir}(\mathbf{k}) \propto E_\Omega \, e^{i\eta_1(k)} T^{(1)}(k)\, Y_{10}(\theta,\varphi) = a_1(k)\, Y_{10}(\theta,\varphi)\,, \quad (4.7)$$

where $T^{(1)}(k) = \langle R_{kp}|r|R_{1s}\rangle$ is the radial part of the dipole matrix element. E_Ω is the complex amplitude of the XUV pulse corresponding to a photon energy $\hbar\Omega + E_{1s} = E$ and $\eta_1(k)$ is the scattering phase for $\ell = 1$. In contrast to the previous section, the angular dependence now is explicitly singled out. The coefficient $a_1(k)$ is complex with a phase given by $\arg[a_1(k)] = \phi_\Omega + \eta_1(k)$. (It is assumed throughout that $m = 0$.) The indirect pathway consists of two ionization channels $1s \rightarrow np \rightarrow \mathbf{k}\{sd\}$, where n is the principal quantum number for the intermediate state with the binding energy E_n. The dipole matrix element in this case is given by:

$$\begin{aligned} M_{ind}(\mathbf{k}) &\propto E_{\Omega'} E_\omega \sum_{\ell=0,2} e^{i\eta_\ell(k)} T^{(2)}(k)\, Y_{\ell 0}(\theta,\varphi) \\ &= \sum_{\ell=0,2} a_\ell(k)\, Y_{\ell 0}(\theta,\varphi)\,, \end{aligned} \quad (4.8)$$

where $T^{(2)}(k)$ is the corresponding radial part. The XUV photon energy is given by $\hbar\Omega' + E_{1s} = E_n$. The complex amplitude, E_ω, of the IR field corresponds to a photon energy of $\hbar\omega + E_n = E$.

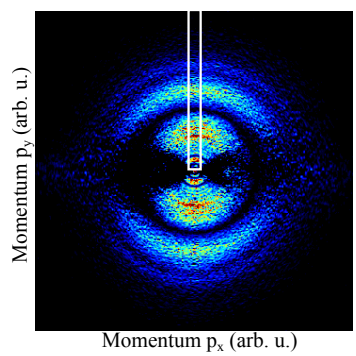

Figure 4.9. *Inverted VMIS image taken during the experimental work for Paper* **VI**. *Interferences are visible due to the two pathways. Also indicated is the cutout taken for the interferogram.*

The phase of E_ω is given by the relative phase of the IR pulse with respect to the SAP. The phase of the complex coefficients $a_\ell(k)$ is $\arg[a_\ell(k)] = \phi_{\Omega'} + \phi_\omega + \eta_\ell(k)$.
The resulting angle-dependent intensity for a given energy becomes:

$$\begin{aligned} I \;\propto\; & |M_{dir} + M_{ind}|^2 = |\sum_{\ell=0}^{2} a_\ell(k) \cdot Y_{\ell 0}(\theta,\varphi)\,|^2 \\ =\; & |a_1|^2|Y_{10}(\theta,\varphi)\,|^2 + |a_0|^2|Y_{00}(\theta,\varphi)\,|^2 + |a_2|^2|Y_{20}(\theta,\varphi)\,|^2 \\ & +2|a_1||a_0|\cos(\arg[a_1 a_0^*])\, Y_{10}(\theta,\varphi)\, Y_{00}^*(\theta,\varphi) \\ & +2|a_1||a_2|\cos(\arg[a_1 a_2^*])\, Y_{10}(\theta,\varphi)\, Y_{20}^*(\theta,\varphi) \\ & +2|a_0||a_2|\cos(\arg[a_0 a_2^*])\, Y_{00}(\theta,\varphi)\, Y_{20}^*(\theta,\varphi)\,. \end{aligned} \tag{4.9}$$

The intensity distribution depends on three different interference terms. The first two terms are the result of the interference between the direct and the indirect pathways. They vary as a function of E and the delay τ:

$$\cos\big(\arg[a_1 a_{0,2}^*]\big) = \cos((E - E_n)\tau/\hbar + (\eta_1(k) - \eta_{0,2}(k))). \tag{4.10}$$

The XUV pulse was assumed to be transform limited, so that $\phi_\Omega = \phi_{\Omega'}$, and ϕ_ω was rewritten as $\phi_\omega = \omega\tau = (E - E_n)\tau/\hbar$. The third interference term in Equation (4.9) is independent of τ and describes the interference between the partial waves s and d, as expected from conventional angular-resolved studies.
Figure 4.10 a) presents a calculated interferogram considering only the $2p$ state, and shows the photoelectron spectra along the common polarization axis of the ionizing fields as a function of delay. The cutout from the momentum distribution is indicated in Figure 4.9. Since the direct-indirect interference depends on both the observation energy and the delay, this gives rise to a hyperbolic fringe pattern in the interferogram. Figure 4.10 c) presents the same type of interferogram, but including two states, the $2p$ and $3p$ states. Besides the hyperbolic fringes, an overall intensity modulation is visible. This is due to quantum beating between the two states.
The composition of EWP can be extracted from the interferogram by performing a Fourier transform along the delay axis for all final energies. The result is a 2D function of E and the conjugate variable of τ from the Fourier transform, E'. The results of Fourier analysis of the two interferograms are shown in Figure 4.10 b) and d). The interference between the direct and the indirect pathways is seen as lines tilted at an angle of 45° because the oscillations in the fringe pattern are directly proportional to E. The different EWP components can be identified from the Fourier analysis by their binding energies, E_n, which are given by the intersection of the tilted lines with the horizontal line for $E = 0$, i.e., at threshold.

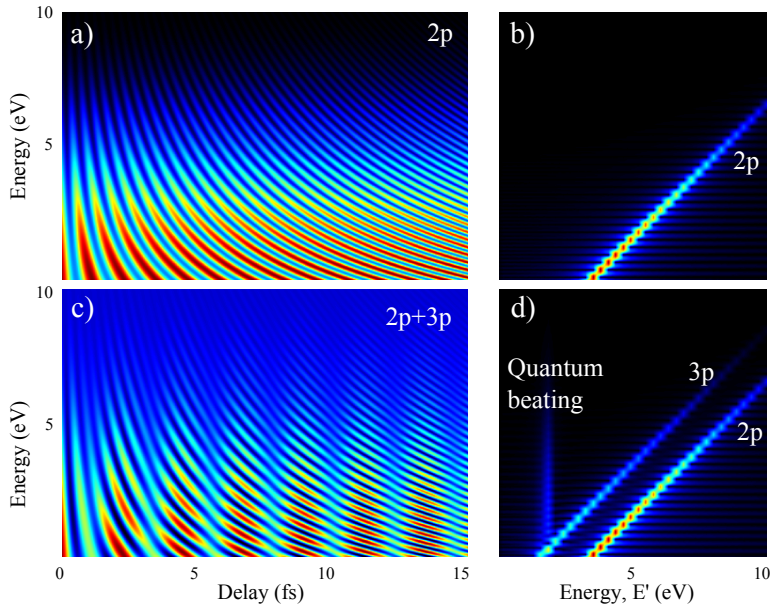

Figure 4.10. *a) Calculated interferogram for the 2p state. b) Fourier analysis showing the 2p component. c) Calculated interferogram including the 2p and 3p state in the wave packet. d) Fourier analysis showing the different components plus the quantum beating.*

The relative strength of each Fourier component is directly related to its relative contribution to the EWP. No real information is obtained about the continuum part of the EWP, and it can simply be seen as a reference to determine the composition of the bound part. Using this interferometric approach the energy resolution is no longer limited by the bandwidth of the XUV and IR pulse, but by the maximum delay τ used in the experiments.
In principle the energy dependent phase offset in Equation (4.10), $\eta_1(k) - \eta_{0,2}(k)$, can be read out from the Fourier analysis as the phase of each frequency component that gives rise to the tilted lines. However, one should keep in mind that, for more than one dominant ionization channel, it will be a mixture of scattering phases $\eta_\ell(k)$.

The interference between the direct and the indirect pathway is only detected because the measurement is angularly resolved. In the angle-integrated signal the interferences would vanish since the spherical harmonics $Y_{\ell m}(\theta, \varphi)$ are orthogonal. More information can be extracted from the complete 3D momentum distribution. The momentum distribution can be expressed as an expansion of

Legendre polynomials, $P_J(\cos\theta)$:

$$\begin{aligned} I(E,\theta) &= \int_0^{2\pi} d\varphi \, |\sum_{\ell=0}^{2} a_\ell(E)\, Y_{\ell 0}(\theta,\varphi)\,|^2 \\ &= \sum_{J=0}^{4} \beta_J(E)\, P_J(\cos\theta)\,, \end{aligned} \tag{4.11}$$

where the expansion coefficients β_J can be calculated using the algebraic properties of the spherical harmonics [76]:

$$\beta_J = \frac{2J+1}{2} \sum_{\ell,\ell'} a_\ell(E)\, a^*_{\ell'}(E)\, V(\ell,\ell',J)\,, \tag{4.12}$$

where

$$V(\ell,\ell',J) = \hat{\ell}\hat{\ell}' \begin{pmatrix} \ell & \ell' & J \\ 0 & 0 & 0 \end{pmatrix}^2 . \tag{4.13}$$

The $3j$ symbols in Equation (4.13) are non-vanishing for even β_J coefficients, if ℓ and ℓ' have the same parity. If ℓ and ℓ' have opposite parities the expansion will also contain odd coefficients. Therefore, the interference described in Equations (4.9) and (4.10) can be separated by the Legendre expansion:

$$\begin{aligned} \beta_0 &= \frac{1}{2}(|a_0|^2 + |a_1|^2 + |a_2|^2) \\ \beta_1 &= \sqrt{3}\ |a_0||a_1|\cos(\arg[a_1 a_0^*]) \\ &\quad +\sqrt{15}\ \frac{6}{5}\ |a_2||a_1|\cos(\arg[a_1 a_2^*]) \\ \beta_2 &= |a_1|^2 + \frac{10}{7}|a_2|^2 + \sqrt{5}\ |a_0||a_2|\cos(\arg[a_0 a_2^*]) \\ \beta_3 &= \sqrt{15}\ \frac{3}{5}\ |a_1||a_2|\cos(\arg[a_1 a_2^*]) \\ \beta_4 &= \frac{9}{7}\ |a_2|^2. \end{aligned} \tag{4.14}$$

The direct and indirect pathways have opposite parity, since they pick up a different number of photons, and thus the direct-indirect interference appears in β_1 and β_3. The partial wave interference in the indirect pathway have the same parity and appear in β_2. The parity-dependent form of the Legendre coefficients is general and can be used to differentiate different processes that lead to the same final energy. The quantum beating, which is not included in Equation (4.14), appears in the even β_J coefficients since the two pathways via different bound states also have the same parity. Other pathways can also be identified in this way, for example, ionization with two IR photons. Consider the case where two-photon transition can lead to the same final state as single-photon ionization, due to the broad bandwidth of the probe pulse. The

period of the oscillation is the same, since it depends only on the difference between the binding energy, E_n, and the observation energy. The two processes can, however, be studied separately using the Legendre analysis.

The possibility of full reconstruction of an arbitrary excited EWP, using the interferometric pump-probe technique introduced above, was explored in Paper **VII**. A simplified 'toy model' was developed to show how the phase of each component could be retrieved, and thus achieve complete characterization of the EWP. In this model, an EWP is created in helium via a shake-up excitation. The shake-up is strictly treated within the sudden approximation, so that the EWP consists of a coherent superposition of ns-states and s-like continuum states, as shown in Figure 4.11. The use of shake-up excitations reduces the number of ionization channels and simplifies the analysis.
To characterize the EWP, the relative phase of each component must be measured. To separate the interference pattern for each component filter functions were applied in the Fourier analysis, and then an inverse Fourier transform was performed back to the time domain, as shown for the 3s state in Figure 4.12 a). The accumulated phase difference that leads to the interference pattern (see Equation (4.10)) can be rewritten in more general terms as:

$$\Delta\Phi(E,t) = \varphi_n + (E - E_n)(t - t_0)/\hbar + \Delta\phi^{ion}(E)\,. \qquad (4.15)$$

Here, φ_n denotes the initial phase of the component n and $\Delta\phi^{ion}(E)$ is the phase difference between the two pathways due to the excitation. The delay τ is now written in absolute values $t - t_0$. An illustration of the phase evolution is shown in Figure 4.12 b). The measured phase $\Delta\Phi(t)$ is plotted for two states, i and j, and three different final energies. For a given energy the phase evolution is linear and can be traced back to the origin, which is defined as the time at which all lines intersect, and is the time when the EWP was created, t_0. The phase offset at t_0 is the initial phase. The slope of each line is given by the difference between E and E_i or E_j. In principle, $\Delta\phi^{ion}(E)$ must also be included, however, only knowledge of the relative phases is required for a full reconstruction. In a first approximation, the offset $\Delta\phi^{ion}(E)$ is considered to be equal for all components, so it can be neglected in the following.
To correctly retrieve the phase, φ_n, it is necessary to know the exact energy, E_n, and the exact timing at which the reference was created, t_0. The E_n can be extracted from the Fourier analysis, as described above. The time t_0 is obtained by differentiating $\Delta\Phi(E,t)$ with respect to E:

$$\hbar\Delta\Phi' = t - t_0. \qquad (4.16)$$

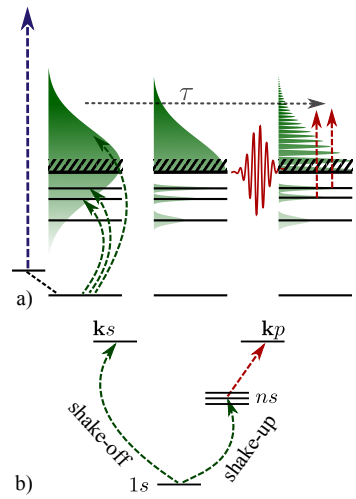

Figure 4.11. *a) Interferometric measurement of an EWP created via a shake-up excitation. b) Possible ionization channel in the interferometer.*

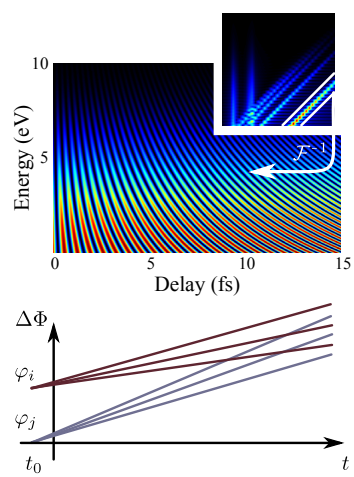

Figure 4.12. *The interference signal of one state can be separated using a window function in the Fourier analysis.*

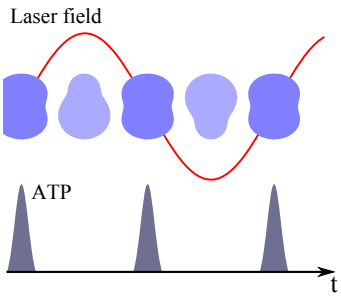

Figure 4.13. *Principle of the attosecond stark spectroscopy. The electron cloud of the molecule is deformed by the electric field of the laser. Depending on the IR-XUV delay the APT ionizes the molecule with a different degree of polarization.*

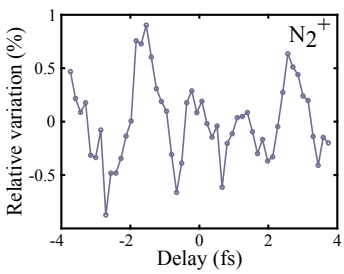

Figure 4.14. *Total yield of N_2^+ as a function IR-XUV delay.*

Complete characterization of the EWP is now possible. Further details on the phase retrieval and the numerical calculation for shake-up can be found in Paper **VII**.

4.3 Attosecond Stark Spectroscopy

Apart from using attosecond pulses to initiate electron dynamics and IR radiation to probe it, as described in the previous sections, they can also be used to probe the dynamics induced by IR excitation. Paper **VIII** presents a study on the instantaneous polarization of molecules induced by the electric field of an IR laser pulse and probed using trains of attosecond pulses.

Figure 4.13 illustrates the idea of the measurement. The electric field of an IR laser pulse induces time-dependent polarization in a molecule, where the displacement of the electron cloud follows the instantaneous field strength adiabatically. This is due to the laser frequency being non-resonant, and the laser intensity being lower than what is necessary for significant multi-photon ionization or dissociation. Classically, this time-dependent dipole oscillation corresponds to the motion of the electrons along the molecular axis. This motion can be probed through ionization with an ATP at variable delays within a laser cycle.

Experiments were carried out for a series of small and medium-sized molecules (N_2, O_2, CH_2 and C_2H_4) in a collaboration with Franck Lépine from Université Lyon and the group of Marc Vrakking at the MBI in Berlin and at the AMOLF in Amsterdam. The measurements in N_2 and O_2 were performed in Lund, where the parent ion yields N_2^+ and O_2^+ were measured as a function of the delay between the XUV and the IR pulse using a VMIS. The result for $N_2{}^+$ is shown Figure 4.14. The signal is modulated with twice the laser frequency, which is expected, since the molecules were not aligned. The modulation depth is equal to 0.5 %, which is relatively small. The modulation depth for O_2 is also 0.5 %. Measurements at MBI on CH_2 and C_2H_4 showed relative variations of 1.0 % and 1.5 %, respectively. This coincides with the evolution of the total polarizability α in this series of molecules, which increases with increasing molecule size and is smallest for N_2 and O_2.

The variation in the ionization yield can be interpreted in terms of the Stark effect. Since the expected Stark shifts of the electronic states are proportional to the polarizability of the molecule in an external field, a greater change in the ionization yield is expected with an increase in polarizability. Further details including supporting time-dependent density functional theory calculations can be found in Paper **VIII**.

Chapter 5

Summary and Outlook

This thesis describes studies on different types of electron wave packets created by absorption of attosecond pulses, both in the form of attosecond pulse trains and as isolated pulses. The key technique applied in almost all experiments was interferometry, which allows very small changes in the phase and energy content of the electron wave packet to be detected. Both features, the phase and the frequency sensitivity, were used in new applications of attosecond pulses, which go beyond the boundaries set by the Fourier-limit for both attosecond pulse trains and single attosecond pulses.

Attosecond pulse trains allow to achieve high spectral resolution due to their harmonic comb structure. Combining excitation of an electron wave packet using attosecond pulse trains and an interferometric measurement technique to determine the phase evolution of this electron wave packet allows to achieve both high spectral and temporal resolution at the same time.
In the first part of this work, the phase properties of free electron wave packets were studied using the phase-locked harmonic comb structure of an attosecond pulse train in combination with the fundamental laser. The ionization of atoms with an attosecond pulse train in the presence of the IR field led to two-photon transitions whose interference provided information on the phase variation between the spectral components of the electron wave packet. The technique was used to investigate the phase behavior of resonant two-photon ionization in helium (Paper **V**), allowing the response of an excited state in an external electric field to be studied.
The same interferometric technique was applied to measure the relative phase variation of electron wave packets originating from different subshells in the valence shell of argon (Papers **II** and **III**). Using an asymptotic approximation, the phase of the one-photon

ionization could be extracted from the two-photon transition, allowing the phase measurements to be interpreted in terms of time delays in photoionization. A photon-energy-dependent delay was measured between electrons emitted from the $3s$ shell and electrons photoionized from the $3p$ shell.
The first study of photoemission time delays was presented by Schultze *et al.* in 2010 [15]. They used the streaking technique to study photoemission from the valence shell in neon, and found a delay between the emission of $2s$ electrons and electrons from the $2p$ shell of 21 as, causing a lively theoretical discussion [94–98]. The question that was raised was the extent to which the influence of the probing IR field should to be included to account for the measured delay. Papers **II** and **IV** answered this question. The measured delay must be adequately corrected for the influence of the additional interaction with the IR photon in order to obtain the time delay in single-photon ionization. In a sense, this is another example of a well known problem in physics, i.e., the observer effect.
Attosecond pulse trains are also most suitable to study sub-cycle dynamics, due to the fixed phase relationship between the pulses. This was in Paper **VIII**, where the time-dependent polarization of neutral molecules under the influence of an IR laser field was studied. In this case, electron motion was resolved by measuring the changes in the ionization yield using attosecond pulse trains.

The use of single attosecond pulses allows directly for a good temporal resolution but to the expense of poor spectral resolution. However, the spectral resolution can be improved by using a coherent double excitation separated in time, analog to Ramsey spectroscopy.
In the second part of this work, such an interferometric pump-probe technique was developed to characterize bound electron wave packets. This technique makes use of the broad bandwidth of single attosecond pulses to create a reference wave simultaneously with the bound wave packet. When the electron wave packet is probed by further ionization after a variable delay it will interfere with the reference wave. Analysis of the resulting interference pattern allows spectral resolution of all ingoing states, together with their relative strength, as reported in Paper **VI**. Since the phase information is also preserved in the interference pattern, this allows for full characterization of the wave packet. Paper **VII** describes how to completely reconstruct an arbitrarily excited electron wave packet.

Each improvement of light sources brought a large impetus to science [89]. The Lund High Power Laser Facility underwent major changes during the fall and winter 2011, when the laboratory was extended. The time of this forced shutdown of all experimental ac-

tivities was used to incorporate an upgrade of the laser system in the attosecond laboratory. The improved laser will deliver pulses with durations of 20 fs, and one goal will be to generate single attosecond pulses using the polarization gating technique. This will allow for further investigations of the experimental feasibility of the interferometric pump-probe technique (Papers **VI** and **VII**), with the ultimate goat to apply this technique to characterize electron wave packets and the processes that led to their formation in complex systems.

Additionally, the wavelength of the new laser will be tunable over a few tens of nm (80 nm is promised by the manufacture). This feature is highly desirable to study phase behavior in resonant excitation processes as described in Paper **V**, and can be applied to more complex problems, see for example Haessler *et al.* [45] and Caillat *et al.* [46].

The most exciting prospect of this large tunability range is the possibility to access time delays in photoemission over a broad and almost continuous spectral region using attosecond pulse trains with tunable harmonic frequencies, e.g., close to the $3s$ ionization minimum in argon as discussed in Paper **III**. Another aim is to combine the tunability with higher photon energies. Gustafsson *et al.* [25] have shown the possibility to obtain attosecond pulse trains with a central energy at 80 eV using high-order harmonic generation in a neon gas target. To develop a reliable attosecond pulse source using neon is a difficult task due to the low conversion efficiency for neon and the difficulty to remove the IR radiation for these XUV photon energies. This will be tackled in a near future. It should allow the access to the dynamics of inner shells in rare gases and other systems where one would expect electron correlations to have a huge impact on delay measurements.

In the course of improvements in the attosecond laboratory the Mach-Zehnder interferometer will be rebuilt, whose design I took part in. The new design will be more compact to improve the total stability. It will also include an active stabilization and a measure of the absolute arm lengths in the interferometer to be able to directly compare consecutive acquired data.

In cooperation with the Division of Synchrotron Radiation Research at Lund University a new 3D-spectrometer is tested, which allows 3D momentum detection of particles in coincidence, and first time delay measurements on sequential and non-sequential (direct and indirect) double ionization of xenon have been performed.

Comments on the Papers

I **Atomic and Macroscopic Measurements of Attosecond Pulse Trains**
In this paper we characterize attosecond pulse trains by means of two different methods, one being the well established RABITT method, the other the recently proposed *in situ* method. By comparison of the two methods it was possible to extract the single-atom response in HHG. I contributed to the experimental work.

II **Probing Single-Photon Ionization on the Attosecond Time Scale**
In this paper we study single-photon ionization of the valence shell in argon. We measure a difference in photoemission delay between electrons liberated from the $3s$ and the $3p$ shell. The measured delay can be interpreted as a sum of two contributions: the Wigner time delay and an additional contribution due to the measurement process. To account for the latter we develop an asymptotic approximation for the laser-assisted photoionization. I was responsible for the preparation and execution of the experiment. I analyzed the experimental data and wrote the main parts of the manuscript.

III **Photoemission Time-Delay Measurements and Calculations close to the 3s Ionization Minimum in Argon**

In this paper we study the photoionization time delay of the $3s$ and $3p$ shells in argon with special emphasis on the region where strong interchannel coupling led to a Cooper-like minimum in the $3s$ ionization cross-section. We include the electron correlations between the two shells within the framework of RPAE in the theoretical calculations. I was involved in the preparation of the experiment, I analyzed the experimental data and contributed to writing the manuscript.

IV **Theory of Attosecond Delays in Laser-Assisted Photoionization**

In this paper we derive an asymptotic expression for the phase of laser-assisted photoionization and establish a connection to different types of time-delay measurements, namely techniques using attosecond pulse trains and others based on single attosecond pulses. The measured time delays can be interpreted as the sum of two contributions: the one-photon Wigner time delay and an additional delay introduced by probing the photoelectron wave packet with an IR laser pulse. I was involved in the early work that led the formulation of the asymptotic approximation.

V **Phase Measurement of Resonant Two-Photon Ionization in Helium**

In this paper we study the phase behavior of resonant two-photon ionization in helium as a function of detuning from the resonant $1s3p\ ^1\mathrm{P}_1$ transition. From that we can determine the intensity dependence of the transition energy. I participated in the experiments and helped with the preparation of the manuscript.

VI **Attosecond Pump-Probe Electron Interferometry**

In this paper we present an interferometric pump-probe technique for the characterization of bound electron wave packets using single attosecond pulses. Analysis of the resulting interferogram yielded the spectral composition of wave packets with a resolution no longer limited by the spectral bandwidth of the attosecond pulses. I took part in the experiments in Milan, analyzed the experimental data and help with the preparation of the manuscript.

VII **Reconstruction of Attosecond Electron Wave Packets with Quantum State Holography**

In this paper we present a feasibility study for the full reconstruction of bound electron wave packets using single attosecond pulses. We show that it is possible to fully characterize an unknown electron wave packet in amplitude and phase by interferometric measurements. I performed the data analysis, derived the analytical expressions and wrote the manuscript.

VIII **Attosecond Stark Effect in Molecules**

In this paper we present a two-color attosecond pump-probe experiments, where the time-dependent polarization of a neutral molecule under the influence laser field is monitored. A series of small to medium-size molecules are exposed to a femtosecond IR laser pulse and a co-propagating attosecond pulse train, and oscillations are observed in the parent molecular ion yield as a function of the pump-probe delay. I participated in the experiments performed in Lund and did parts of the data analysis.

Acknowledgments

The completion of this work would not have been possible without the support and hard work of the many people involved in the different projects.
First and foremost I owe my gratitude to my supervisor Anne L'Huillier for her enthusiasm and encouragement, her scientific intuition and her great sense of humor. I am also very grateful to my co-supervisor Johan Mauritsson for his support, his visionary words and his good taste in small-sized clothing. A special thanks to Mathieu 'Sonntag' Gisselbrecht, who has been an exceptional source of knowledge.
To shed light on new physics it requires to have the right light sources. I am grateful to Anders Persson for his laser expertise, as well as to the whole team of Dispersion Management and Plumbing AB for its continuous effort.

Many of the experiments have been carried out in international collaborations. Those whom I would like to thank especially are Marc Vrakking for his deep knowledge of inversions, Mauro Nisoli and Giuseppe Sansone for their hospitality during the experimental work in Milan and Franck Lépine, who provides excellent beamtime dinners. I am also most grateful to Ken Schafer, Alfred Maquet, Richard Taïeb and Anatoli Kheifets for providing a lot of the theory behind this work.

It has been a privilege and a great pleasure to be part of the attosecond physics group for the past years. The spirit in the group it truly outstanding and I would like to thank all current and former members: Cord Arnold, Diego Guénot, Esben Witting Larsen, Per Johnsson, Aaron von Conta, Eric Månsson, Jörg Schwenke, Christoph Heyl, Piotr Rudawski, Fernando Brizuela, Thomas Remetter, David Kroon, Linnea Rading, Stefanos Carlstöm, Filippo Campi, Xinkui He, Christian Erny, Eric Mansten and Rafal Rakowski. Especially I would like to thank Marcus Dahlström for the instructive discussions and being a perfect 'work spouse', my office mates Thomas Fordell and Marko Swoboda (**** *** guys, in the most sincere way),

Eleonora Lorek for being always on the same page, and Miguel Miranda, o meu melhor amigo do mundo, por ser a minha luz na escuridão Sueca.

I enjoyed the friendly and inspiring atmosphere at the Division of Atomic Physics at Lund University very much and I would like to thank all members for making it a place worth working at. In particular: Sune Svanberg and Claes-Göran Wahlström, the former and present head of the division, and Camilla Nilsson, Harriett Lindahl, Minna Ramkull and Bertil Hermansson for taking care of administrative and technical things and for always speaking Swedish to me.

I am very glad to have found good friends in Lund Guillaume Genoud and Satu Tanskanen, Agnieszka Nowacka e ao meu querido amigo Tiago Ferreira, que me ensinou tudo o que há para saber sobre a profunda e rica alma Portuguesa.
Außerdem möchte ich mich bei meiner Familie für die bedingungslose Unterstützung, besonders während der letzten Phase dieser Arbeit, von ganzem Herzen danken.

Och ett speciellt tack till mitt Spädbarno.

References

1. Eadweard Muybridge. The Horse in Motion (1878). URL `http://www.loc.gov/pictures/resource/cph.3a45870/`. [online, accessed 22 Apr 2012].
2. L. F. DiMauro. *Attophysics: Atomic photography.* Nature **419**, 789–790 (2002).
3. A. McPherson, G. Gibson, H. Jara, U. Johann, T. S. Luk, I. A. McIntyre, K. Boyer and C. K. Rhodes. *Studies of multiphoton production of vacuum-ultraviolet radiation in the rare gases.* J. Opt. Soc. Am. B **4**, 595 (1987).
4. M. Ferray, A. L'Huillier, X. F. Li, G. Mainfray and C. Manus. *Multiple-harmonic conversion of 1064 nm radiation in rare gases.* J. Phys. B **21**, L31 (1988).
5. G. Farkas and C. Tóth. *Proposal for attosecond light pulse generation using laser induced multiple-harmonic conversion processes in rare gases.* Phys. Lett. A **168**, 447 (1992).
6. P. B. Corkum, N. H. Burnett and M. Y. Ivanov. *Subfemtosecond pulses.* Opt. Lett. **19**, 1870 (1994).
7. Ph. Antoine, A. L'Huillier and M. Lewenstein. *Attosecond Pulse Trains Using High-Order Harmonics.* Phys. Rev. Lett. **77**, 1234 (1996).
8. Ph. Antoine, D. B. Milosevic, A. L'Huillier, M. B. Gaarde, P. Salières and M. Lewenstein. *Generation of attosecond pulses in macroscopic media.* Phys. Rev. A **56**, 4960 (1997).
9. P. M. Paul, E. S. Toma, P. Breger, G. Mullot, F. Augé, Ph. Balcou, H. G. Muller and P. Agostini. *Observation of a train of attosecond pulses from high harmonic generation.* Science **292**, 1689 (2001).
10. M. Hentschel, R. Kienberger, Ch. Spielmann, G. A. Reider, N. Milosevic, T. Brabec, P. Corkum, U. Heinzmannß, M. Drescher and F. Krausz. *Attosecond metrology.* Nature **414**, 509 (2001).

11. Press Release: The 1999 Nobel Prize in Chemistry (1999). URL `http://www.nobelprize.org/nobel_prizes/chemistry/laureates/1999/press.html`. [online, accessed 21 Apr 2012].

12. M. Drescher, M. Hentschel, R. Kienberger, M. Uiberacker, V. Yakovlev, A. Scrinzi, Th. Westerwalbesloh, U. Kleineberg, U. Heinzmann and F. Krausz. *Time-resolved atomic inner-shell spectroscopy.* Nature **419**, 803 (2002).

13. E. Goulielmakis, Z. Loh, A. Wirth, R. Santra, N. Rohringer, V. S Yakovlev, S. Zherebtsov, T. Pfeifer, A. M. Azzeer, M. F. Kling, S. R. Leone and F. Krausz. *Real-time observation of valence electron motion.* Nature **466**, 739–743 (2010).

14. M. Uiberacker, Th. Uphues, M. Schultze, A. J. Verhoef, V. Yakovlev, M. F. Kling, Rauschenberger, N. M. Kabachnik, H. Schröder, M. Lezius, K. L. Kompa, H.-G. Muller, M. J. J. Vrakking, S. Hendel, U. Kleineberg, U. Heinzmann, M. Drescher and F. Krausz. *Attosecond real-time observation of electron tunnelling in atoms.* Nature **446**, 627 (2007).

15. M. Schultze, M. Fie, N. Karpowicz, J. Gagnon, M. Korbman, M. Hofstetter, S. Neppl, A. L. Cavalieri, Y. Komninos, Th. Mercouris, C. A. Nicolaides, R. Pazourek, S. Nagele, J. Feist, J. Burgdrfer, A. M. Azzeer, R. Ernstorfer, R. Kienberger, U. Kleineberg, E. Goulielmakis, F. Krausz and V. S. Yakovlev. *Delay in Photoemission.* Science **328**, 1658–1662 (2010).

16. A. L. Cavalieri, N. Müller, Th. Uphues, V. S. Yakovlev, A. Baltuška, B. Horvath, B. Schmidt, L. Blümel, R. Holzwarth, S. Hendel, M. Drescher, U. Kleineberg, P. M. Echenique, R. Kienberger, F. Krausz and U. Heinzmann. *Attosecond spectroscopy in condensed matter.* Nature **449**, 1029 (2007).

17. G. Sansone, F. Kelkensberg, J. F. Pérez-Torres, F. Morales, M. F. Kling, W. Siu, O. Ghafur, P. Johnsson, M. Swoboda, E. Benedetti, F. Ferrari, F. Lépine, J. L. Sanz-Vicario, S. Zherebtsov, I. Znakovskaya, A. LHuillier, M. Yu. Ivanov, M. Nisoli, F. Martìn and M. J. J. Vrakking. *Electron localization following attosecond molecular photoionization.* Nature **465**, 763766 (2010).

18. R. López-Martens, J. Mauritsson, P. Johnsson, K. Varju, A. L'Huillier, W. Kornelis, J. Biegert, U. Keller, M. Gaarde and K. Schafer. *Characterization of high-order harmonic radiation on femtosecond and attosecond time scales.* Appl. Phys. B **78**, 835–840 (2004).

19. R. López-Martens, K. Varjú, P. Johnsson, J. Mauritsson, Y. Mairesse, P. Salières, M. B. Gaarde, K. J. Schafer, A. Pers-

son, S. Svanberg, C.-G. Wahlström and A. L'Huillier. *Amplitude and phase control of attosecond light pulses.* Phys. Rev. Lett. **94**, 033001 (2005).

20. K. Varjú, P. Johnsson, R. López-Martens, T. Remetter, E. Gustafsson, J. Mauritsson, M. B. Gaarde, K. J. Schafer, Ch. Erny, I. Sola, A. Zaïr, E. Constant, E. Cormier, E. Mével and A. L'Huillier. *Experimental Studies of Attosecond Pulse Trains.* Laser Physics **15**, 888–898 (2005).

21. J. Mauritsson, P. Johnsson, E. Gustafsson, A. L'Huillier, K. J. Schafer and M. B. Gaarde. *Attosecond Pulse Trains Generated Using Two Color Laser Fields.* Phys. Rev. Lett. **97**, 013001 (2006).

22. T. Ruchon, C. P. Hauri, K. Varjú, E. Mansten, M. Swoboda, R. López-Martens and A. L'Huillier. *Macroscopic effects in attosecond pulse generation.* New. J. Phys. **10 No. 2**, 025027 (2008).

23. K. Varjú, Y. Mairesse, P. Agostini, P. Breger, B. Carré, L. J. Frasinski, E. Gustafsson, P. Johnsson, J. Mauritsson, H. Merdji, P. Monchicourt, A. L'Huillier and P. Salières. *Reconstruction of Attosecond Pulse Trains Using an Adiabatic Phase Expansion.* Phys. Rev. Lett. **95**, 243901 (2005).

24. K. Varjú, Y. Mairesse, B. Carre, M. B. Gaarde, P. Johnsson, S. Kazamias, R. Lopez-Martens, J. Mauritsson, K. J. Schafer, Ph. Balcou, A. L'Huillier and P. Salières. *Frequency chirp of harmonic and attosecond pulses.* J. Mod. Opt. **52**, 379 (2005).

25. E. Gustafsson, T. Ruchon, M. Swoboda, R. López-Martens, Ph. Balcou and A. L'Huillier. *Broadband attosecond pulse shaping.* Optics Letters **32**, 1353–1355 (2007).

26. P. Johnsson, R. López-Martens, S. Kazamias, J. Mauritsson, C. Valentin, T. Remetter, K. Varjú, M. B. Gaarde, Y. Mairesse, H. Wabnitz, P. Salières, Ph. Balcou, K. J. Schafer and A. L'Huillier. *Attosecond Electron Wave Packet Dynamics in Strong Laser Fields.* Phys. Rev. Lett. **95**, 013001 (2005).

27. T. Remetter, P. Johnsson, J. Mauritsson, K. Varjú, Y. Ni, F. Lépine, E. Gustafsson, M. Kling, J. Khan, R. López-Martens, K. J. Schafer, M. J. J. Vrakking and A. L'Huillier. *Attosecond Electron Wave Packet Interferometry.* Nature Phys. **2**, 323 (2006).

28. P. Johnsson, J. Mauritsson, T. Remetter, A. L'Huillier and K. J. Schafer. *Attosecond Control of Ionization by Wave-Packet Interference.* Phys. Rev. Lett. **99**, 233001 (2007).

29. J. Mauritsson, P. Johnsson, E. Mansten, M. Swoboda, T. Ruchon, A. L'Huillier and K. J. Schafer. *Coherent Electron Scat-*

tering Captured by an Attosecond Quantum Stroboscope. Phys. Rev. Lett. **100**, 073003 (2008).

30. N. Dudovich, O. Smirnova, J. Levesque, Y. Mairesse, M. Yu. Ivanov, D. M. Villeneuve and P. B. Corkum. *Measuring and controlling the birth of attosecond XUV pulses*. Nature Phys. **2**, 781 (2006).

31. K. J. Schafer, B. Yang, L. F. DiMauro and K. C. Kulander. *Above threshold ionization beyond the high harmonic cutoff*. Phys. Rev. Lett. **70**, 1599 (1993).

32. P. B. Corkum. *Plasma perspective on strong-field multiphoton ionization*. Phys. Rev. Lett. **71**, 1994 (1993).

33. E. Constant, D. Garzella, P. Breger, E. Mével, Ch. Dorrer, C. Le Blanc, F. Salin and P. Agostini. *Optimizing High Harmonic Generation in Absorbing Gases: Model and Experiment*. Phys. Rev. Lett. **82**, 1668 (1999).

34. P. Balcou, P. Salières, A. L'Huillier and M. Lewenstein. *Generalized phase-matching conditions for high harmonics: The role of field-gradient forces*. Phys. Rev. A **55**, 3204–3210 (1997).

35. Thomas Brabec, editor. *Strong Field Laser Physics* volume 134 of *Springer Series in Optical Science*. Springer (2009).

36. A. Rundquist, C. Durfee III, Z. Chang, C. Herne, S. Backus, M. Murnane and H. C. Kapteyn. *Phase matched generation of coherent soft X-rays*. Science **280**, 1412 (1998).

37. M. Schnürer, Z. Cheng, M. Hentschel, F.Krausz, T.Wilhein, D.Hambach, G. Schmahl, M. Drescher, Y. Lim and U. Heinzmann. *Few-cycle-driven XUV laser harmonics: generation and focusing*. Appl. Phys. B **70**, S227 (2000).

38. Z. Chang, A. Rundquist, H. Wang, M. M. Murnane and H. C. Kapteyn. *Generation of Coherent Soft X Rays at 2.7 nm Using High Harmonics*. Phys. Rev. Lett. **79**, 2967 (1997).

39. M. Schnürer, Ch. Spielmann, P. Wobrauschek, C. Streli, N. H. Burnett, C. Kan, K. Ferencz, R. Koppitsch, Z. Cheng, T. Brabec and F. Krausz. *Coherent 0.5-keV X-Ray Emission from Helium Driven by a Sub-10-fs Laser*. Phys. Rev. Lett. **80**, 3236–3239 (1998).

40. M.-C. Chen, P. Arpin, T. Popmintchev, M. Gerrity, B. Zhang, M. Seaberg, D. Popmintchev, M. M. Murnane and H. C. Kapteyn. *Bright, Coherent, Ultrafast Soft X-Ray Harmonics Spanning the Water Window from a Tabletop Light Source*. Phys. Rev. Lett. **105**, 173901 (2010).

41. Y. Mairesse, A. de Bohan, L. J. Frasinski, H. Merdji, L. C. Dinu, P. Monchicourt, P. Breger, M. Kovačev, R. Taïeb, B. Carré, H. G. Muller, P. Agostini and P. Salières. *Attosecond*

synchronization of high-harmonic soft X-rays. Science **302**, 1540 (2003).

42. H. G. Muller. *Reconstruction of attosecond harmonic beating by interference of two-photon transitions.* Appl. Phys. B **74**, 17 (2002).

43. V. Véniard, R. Taïeb and A. Maquet. *Phase dependence of (N+1) - color (N>1) ir-uv photoionization of atoms with higher harmonics.* Phys. Rev. A **54**, 721 (1996).

44. J. Mauritsson, M. B. Gaarde and K. J. Schafer. *Accessing properties of electron wave packets generated by attosecond pulse trains through time-dependent calculations.* Phys. Rev. A **72**, 013401 (2005).

45. S. Haessler, B. Fabre, J. Higuet, J. Caillat, T. Ruchon, P. Breger, B. Carré, E. Constant, A. Maquet, E. Mével, P. Salières, R. Taïeb and Y. Mairesse. *Phase-resolved attosecond near-threshold photoionization of molecular nitrogen.* Phys. Rev. A **80**, 011404 (2009).

46. Jérémie Caillat, Alfred Maquet, Stefan Haessler, Baptiste Fabre, Thierry Ruchon, Pascal Salières, Yann Mairesse and Richard Taïeb. *Attosecond Resolved Electron Release in Two-Color Near-Threshold Photoionization of* N_2. Phys. Rev. Lett. **106**, 093002 (2011).

47. J. Mauritsson, P. Johnsson, R. López-Martens, K. Varjú, W. Kornelis, J. Biegert, U. Keller, M. B. Gaarde, K. J. Schafer and A. L'Huillier. *Measurement and control of the frequency chirp rate of high-order harmonic pulses.* Phys. Rev. A **70**, R021801 (2004).

48. M. Swoboda, J. M. Dahlström, T. Ruchon, P. Johnsson, J. Mauritsson, A. LHuillier and K. J. Schafer. *Intensity Dependence of Laser-Assisted Attosecond Photoionization Spectra.* Las. Phys. **19**, 1591–1599 (2009).

49. J. M. Dahlström, T. Fordell, E. Mansten, T. Ruchon, M. Gisselbrecht, K. Klünder, M. Swoboda, A. L'Huillier and J. Mauritsson. *Atomic- and macroscopic measurements of attosecond pulse trains.* Phys. Rev. A **80**, 033836 (2009).

50. J. M. Dahlström, A. L'Huillier and J. Mauritsson. *Quantum mechanical approach to probing the birth of attosecond pulses using a two-colour field.* Journal of Physics B: Atomic, Molecular and Optical Physics **44**, 095602 (2011).

51. T. Fordell, M. Miranda, A. Persson and A. L'Huillier. *Carrier-envelope phase stabilization of a multi-millijoule, regenerative-amplifier-based chirped-pulse amplifier system.* Opt. Express **17**, 21091–21097 (2009). URL `http://www.opticsinfobase.`

org/oe/abstract.cfm?uri=oe-17-23-21091.

52. R. Szipöcs and A. Köházi-Kis. *Theory and design of chirped dielectric laser mirrors.* Appl. Phys. B **65**, 115 (1997).

53. Takao Fuji, Jens Rauschenberger, Alexander Apolonski, Vladislav S. Yakovlev, Gabriel Tempea, Thomas Udem, Christoph Gohle, Theodor W. Hänsch, Walter Lehnert, Michael Scherer and Ferenc Krausz. *Monolithic carrier-envelope phase-stabilization scheme.* Opt. Lett. **30**, 332–334 (2005). URL http://www.opticsinfobase.org/ol/abstract.cfm?id=82497.

54. J. Rauschenberger, T. Fuji, M. Hentschel, A. J. Verhoef, T. Udem, C. Gohle, T. W. Hansch and F. Krausz. *Carrier-envelope phase-stabilized amplifier system.* Laser Physics Letters **3**, 37–42 (2006).

55. P. Kruit and F. H. Read. *Magnetic field paralleliser for 2π electron-spectrometer and electron-image magnifier.* J. Phys. E **16**, 313 (1983).

56. M. J. J. Vrakking. *An iterative procedure for the inversion of two-dimensional ion/photoelectron imaging experiments.* Rev. Sci. Instr. **72**, 4084 (2001).

57. Vladimir Dribinski, Alexei Ossadtchi, Vladimir A. Mandelshtam and Hanna Reisler. *Reconstruction of Abel-transformable images: The Gaussian basis-set expansion Abel transform method.* Review of Scientific Instruments **73**, 2634–2642 (2002).

58. Gustavo A. Garcia, Laurent Nahon and Ivan Powis. *Two-dimensional charged particle image inversion using a polar basis function expansion.* Review of Scientific Instruments **75**, 4989–4996 (2004).

59. M. J. J. Vrakking. *Abel inversion of 2D velocity map images using a Legendre polynomial expansion.* Not published (2008).

60. A. Baltuška, Th. Udem, M. Uiberacker, M. Hentschel, E. Goulielmakis, Ch. Gohle, R. Holzwarth, V. S. Yakovlev, A. Scrinzi, T. W. Hänsch and F. Krausz. *Attosecond control of electronic processes by intense light fields.* Nature **421**, 611 (2003).

61. Bing Shan, Shambhu Ghimire and Zenghu Chang. *Generation of the attosecond extreme ultraviolet supercontinuum by a polarization gating.* Journal of Modern Optics **52**, 277–283 (2005).

62. G. Sansone, E. Benedetti, F. Calegari, C. Vozzi, L. Avaldi, R. Flammini, L. Poletto, P. Villoresi, C. Altucci, R. Velotta, S. Stagira, S. De Silvestri and M. Nisoli. *Isolated single-cycle*

attosecond pulses. Science **314**, 443 (2006).

63. P. Tzallas, E. Skantzakis, C. Kalpouzos, E. P. Benis, G. D. Tsakiris and D. Charalambidis. *Generation of intense continuum extreme-ultraviolet radiation by many-cycle laser fields*. Nature Phys. **3**, 846 (2007).

64. H. Mashiko, S. Gilbertson, C. Li, S. D. Khan, M. M. Shakya, E. Moon and Z. Chang. *Double optical gating of high-order harmonic generation with carrier-envelope phase stabilized lasers*. Phys. Rev. Lett. **100**, 103906 (2008).

65. Ximao Feng, Steve Gilbertson, Hiroki Mashiko, He Wang, Sabih D. Khan, Michael Chini, Yi Wu, Kun Zhao and Zenghu Chang. *Generation of Isolated Attosecond Pulses with 20 to 28 Femtosecond Lasers*. Physical Review Letters **103**, 183901 (2009).

66. G. Sansone, F. Calegari and M. Nisoli. *Attosecond Technology and Science*. Selected Topics in Quantum Electronics, IEEE Journal of **18**, 507 –519 (2012).

67. M. Kitzler, N. Milosevic, A. Scrinci and T. Brabec. *Quantum Theory of Attosecond XUV Pulse Measurement by Laser Dressed Photoionization*. Phys. Rev. Lett. **88**, 173904 (2002).

68. J. Itatani, F. Quéré, G. L. Yudin, M. Yu. Ivanov, F. Krausz and P. B. Corkum. *Attosecond Streak Camera*. Phys. Rev. Lett. **88**, 173903 (2002).

69. Rick Trebino. *Frequency-resolved optical gating: the measurement of ultrashort laser pulses*. Kluwer Academic Publishers (2000).

70. Y. Mairesse and F. Quéré. *Frequency-resolved optical gating for complete reconstruction of attosecond bursts*. Phys. Rev. A **71**, 011401(R) (2005).

71. F. Quéré, Y. Mairesse and J. Itatani. *Temporal characterization of attosecond XUV fields*. J. Mod. Opt. **52**, 339 (2005).

72. Kyung Taec Kim, Dong Hyuk Ko, Juyun Park, Valer Tosa and Chang Hee Nam. *Complete temporal reconstruction of attosecond high-harmonic pulse trains*. New Journal of Physics **12**, 083019 (2010).

73. C. Cohen-Tannoudji, B. Diu and F. Laloë. *Quantum Mechanics* volume 2. Wiley-Interscience (1977).

74. B. H. Bransden and C. J. Joachain. *Physics of Atoms and Molecules*. Prentice Hall (2003).

75. A.F. Starace. *Atomic Photoionization*. FUNDAMENTAL PROCESSES IN ENERGETIC ATOMIC COLLISIONS. Plenum Press, in cooperation NATO Scientific Affairs Division

(1983).

76. R.D. Cowan. *The Theory of Atomic Structure and Spectra*. University of California Press, Berkeley (1981).

77. U. Fano. *Propensity rules: An analytical approach*. Phys. Rev. A **32**, 617–618 (1985).

78. Katharine L. Reid. *PHOTOELECTRON ANGULAR DISTRIBUTIONS*. Annu. Rev. Phys. Chem **54**, 397–424 (2003).

79. E. Arnous, S. Klarsfeld and S. Wane. *Angular Distribution in the Two-Quantum Atomic Photoeffect*. Phys. Rev. A **7**, 1559–1568 (1973).

80. H. Friedrich. *Theoretical atomic physics*. Springer Verlag (1994).

81. D. J. Kennedy and S. T. Manson. *Photoionization of the Noble Gases: Cross Sections and Angular Distributions*. Phys. Rev. A **5**, 227 (1972).

82. Eugene P. Wigner. *Lower Limit for the Energy Derivative of the Scattering Phase Shift*. Phys. Rev. **98**, 145–147 (1955).

83. C.A.A. de Carvalho and H.M. Nussenzveig. *Time delay*. Physics Reports **364**, 83 – 174 (2002).

84. W. O. Amrein and Ph. Jacquet. *Time delay for one-dimensional quantum systems with steplike potentials*. Phys. Rev. A **75**, 022106 (2007).

85. S. T. Manson. Private communiation (2012).

86. Louis H. Haber, Benjamin Doughty and Stephen R. Leone. *Continuum phase shifts and partial cross sections for photoionization from excited states of atomic helium measured by high-order harmonic optical pump-probe velocity map imaging*. Phys. Rev. A **79**, 031401 (2009).

87. M. Aymar and M. Crane. *Two-photon ionisation of atomic hydrogen in the presence of one-photon ionisation*. J. Phys. B **13**, L287 (1980).

88. J.M. Dahlström, D. Guénot, K. Klünder, M. Gisselbrecht, J. Mauritsson, A. LHuillier, A. Maquet and R. Taïeb. *Theory of attosecond delays in laser-assisted photoionization*. Chemical Physics page in press (2012).

89. Volker Schmidt. *Photoionization of atoms using synchrotron radiation*. Rep. Prog. Phys. **55**, 1483–1659 (1992).

90. A. Groß. *Theoretical Surface Science*. Springer Verlag (2009).

91. M. Ya. Amusia. *Atomic Photoeffect*. Plenum Press, New York (1990).

92. C. D. Lin, editor. *Review of Fundamental Processes and Applications of Atoms and Ions*. World Press (1993).

93. B. Möbus, B. Magel, K.-H. Schartner, B. Langer, U. Becker, M. Wildberger and H. Schmoranzer. *Measurements of absolute Ar 3s photoionization cross sections*. Phys. Rev. A **47**, 3888–3893 (1993).

94. V. S. Yakovlev, J. Gagnon, N. Karpowicz and F. Krausz. *Attosecond Streaking Enables the Measurement of Quantum Phase*. Phys. Rev. Lett. **105**, 073001 (2010).

95. Jan Conrad Baggesen and Lars Bojer Madsen. *Polarization Effects in Attosecond Photoelectron Spectroscopy*. Phys. Rev. Lett. **104**, 043602 (2010).

96. C.-H. Zhang and U. Thumm. *Electron-ion interaction effects in attosecond time-resolved photoelectron spectra*. Phys. Rev. A **82**, 043405 (2010).

97. A. S. Kheifets and I. A. Ivanov. *Delay in Atomic Photoionization*. Phys. Rev. Lett. **105**, 233002 (2010).

98. M. Ivanov and O. Smirnova. *How Accurate Is the Attosecond Streak Camera?* Phys. Rev. Lett. **107**, 213605 (2011).

Papers

Paper I

Atomic and Macroscopic Measurements of Attosecond Pulse Trains

J. M. Dahlström, T. Fordell, E. Mansten, T. Ruchon, M. Swoboda, K. Klünder, M. Gisselbrecht, A. L'Huillier and J. Mauritsson.

Phys. Rev. A **80**, 033836 (2009).

PHYSICAL REVIEW A **80**, 033836 (2009)

Atomic and macroscopic measurements of attosecond pulse trains

J. M. Dahlström,[1] T. Fordell,[1] E. Mansten,[1] T. Ruchon,[2] M. Swoboda,[1] K. Klünder,[1] M. Gisselbrecht,[1,3] A. L'Huillier,[1] and J. Mauritsson[1]

[1]*Department of Physics, Lund University, P.O. Box 118, SE-221 00 Lund, Sweden*

[2]*DSM, Service des Photons, Atomes et Molcules, CEA-Saclay, 91191 Gif sur Yvette, France*

[3]*UMR8624, LIXAM, CNRS–Université Paris Sud, Bat. 350, 91405 Orsay, France*

(Received 12 May 2009; published 25 September 2009)

We characterize attosecond pulses in a train using both the well established "reconstruction of attosecond beating by interference of two-photon transitions" (RABITT) technique and the recently demonstrated *in situ* method, which is based on a weak perturbation of the harmonic generation process by the second harmonic of the laser field. The latter technique determines the characteristics of the single atom emission, while RABITT allows one to measure attosecond pulses "on target." By comparing the results of the two methods, the influence of propagation and filtering on the attosecond pulses can be extracted.

DOI: 10.1103/PhysRevA.80.033836 PACS number(s): 42.65.Ky, 32.80.Qk, 32.80.Rm

I. INTRODUCTION

Attosecond pulse trains (APTs) are created when intense infrared (ir) laser pulses interact with a gas of atoms or molecules [1]. The characteristics of the attosecond pulses depend both on the quantum-mechanical single atom dynamics as well as on macroscopic effects due to propagation in the nonlinear medium [2]. Under normal experimental conditions, the pulse train contains two pulses per cycle of the laser field [3–5]. The properties of these pulses can be modified by transmission through filters [6] or reflection by gratings and/or multilayer mirrors [7]. Several techniques to characterize attosecond pulse trains have been proposed, each with specific advantages and limitations. In this paper we concentrate on analyzing and comparing two of these techniques: the reconstruction of attosecond beating by interference of two-photon transitions (RABITT) [1] and a two-color *in situ* method [8], which uses a weak perturbation of the high-order harmonic generation (HHG) by the second harmonic of the fundamental laser field. Both techniques aim to characterize the average attosecond pulse structure in an APT.

Figure 1 illustrates schematically the difference between these two techniques. RABITT allows us to determine the *final* structure of the attosecond pulses after propagation in the gas cell and filtering. The attosecond pulses are characterized "on target," i.e., in the chamber where they can be used for applications. The RABITT scheme is implemented by ionizing an atomic gas with the APT in presence of a synchronized weak ir field. The perturbation due to the ir field results in sidebands in the photoelectron spectra as shown in Fig. 2(a). Information about the structure of the attosecond pulses can then be obtained by studying the intensity oscillations of these sidebands with respect to the subcycle delay between the probe field and the APT.

The *in situ* method measures the single atom emission from the individual atoms. In contrast to RABITT, the *initial* shape of the attosecond pulses, before propagation and filtering, is now measured [Fig. 1]. This is important for applications that are conducted in the generation process itself, e.g., the tomography of electronic orbitals [9]. The presence of a weak second harmonic (blue) field in the generation chamber leads to the generation of even harmonics as shown in Fig. 2(b) [10]. The harmonic generation process is nonlinear beyond the perturbative regime, which results in comparable probabilities for the processes shown in Fig. 2(b) even though the number of ir photons absorbed differs by 4. Information about the initial properties of the attosecond pulse is obtained by studying the intensity oscillations of the even harmonics with respect to the phase between the ir and the blue field.

In this paper we present a detailed theoretical and experimental comparison between the two characterization methods. Implementing both schemes allows us to measure both the initial and final shapes of the attosecond pulses. From these measurements the influence of propagation as well as

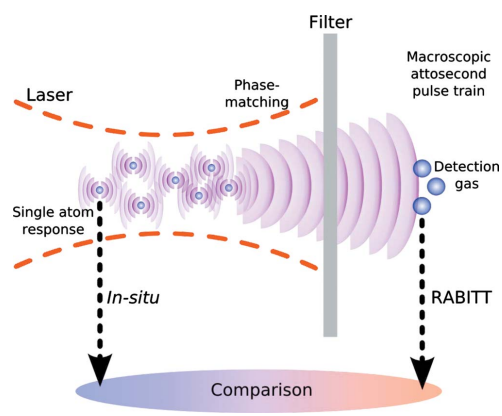

FIG. 1. (Color online) Cartoon illustrating the differences between the two characterization methods. The *in situ* method measures the single atom emission, while the RABITT scheme determines the corresponding attosecond pulses "on target." The influence of phase matching and filtering on the attosecond pulses can be deduced through the implementation of both methods on the same HHG setup.

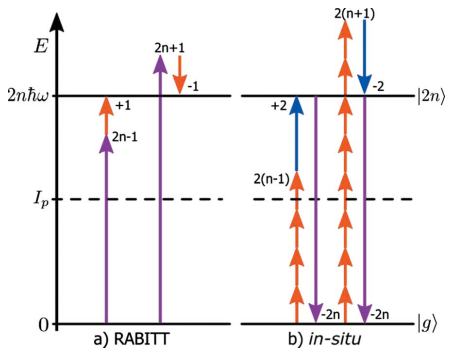

FIG. 2. (Color online) Energy diagrams associated with the two characterization methods. (a) Sidebands are created through the absorption and emission of an ir photon (ω_R) in the RABITT method. (b) Even harmonics are produced in the *in situ* method due to the presence of a weak blue field ($2\omega_R$). Attosecond pulses are characterized by studying the interferences arising from the degenerate ways of reaching the sidebands or even harmonics.

filtering can be determined. The paper is composed as follows: Sec. II reviews the theory of the two characterization methods, Sec. III gives an overview of the experimental setup, Sec. IV presents results from both methods at low gas generation pressure, Sec. V discusses the reasons for the difference observed at higher gas pressures, and Sec. VI summarizes the paper with an outlook.

II. THEORY

The electric field of an attosecond pulse can be written as $\tilde{E}(t)=\tilde{\Lambda}(t)\exp[i\tilde{\phi}(t)]$, where $\tilde{\Lambda}(t)$ and $\tilde{\phi}(t)$ represent the temporal envelope and phase, respectively. It can also be described through its Fourier transform

$$E(\omega)=\Lambda(\omega)\exp[i\phi(\omega)] \tag{1}$$

$$=\int dt\tilde{\Lambda}(t)\exp[i\tilde{\phi}(t)-i\omega t], \tag{2}$$

where $\Lambda(\omega)$ and $\phi(\omega)$ are the spectral envelope and phase. The Fourier integral in Eq. (2) can be approximated using the saddle point method when the linear part in the temporal phase cancels the Fourier component,

$$\left.\frac{d\tilde{\phi}}{dt}\right|_{t=t'(\omega)}-\omega=0, \tag{3}$$

and the quadratic part of the temporal phase is large,

$$\left.\left|\frac{d^2\tilde{\phi}}{dt^2}\right|\right|_{t=t'(\omega)}\gg 0. \tag{4}$$

Note that the temporal phase must be expanded at different times for different Fourier components, i.e., the saddle point time is a function of frequency, $t'(\omega)$. The saddle point approximation yields

$$E(\omega)\approx\left.\sqrt{\frac{2\pi}{\left|\frac{d^2\tilde{\phi}}{dt^2}\right|}}\tilde{\Lambda}(t)\exp\left[i\tilde{\phi}(t)-i\omega t\pm\frac{i\pi}{4}\right]\right|_{t=t'(\omega)}, \tag{5}$$

where the positive (negative) phase factor corresponds to a positive (negative) chirp which is the case for attosecond pulses from the short (long) branch. The spectral phase is approximately equal to

$$\phi(\omega)=\tilde{\phi}(t'(\omega))-\omega t'(\omega)\pm\frac{\pi}{4} \tag{6}$$

and its first derivative is

$$\frac{d\phi}{d\omega}=-t'(\omega), \tag{7}$$

which is obtained using the chain rule and Eq. (3). We can, therefore, interpret the group delay (GD$=-d\phi/d\omega$) as the time when the temporal phase oscillates as ω. A deeper analysis is needed if Eqs. (3) and (4) are not satisfied, which is the case of frequencies above the harmonic cutoff.

We define the relative timing of spectral components (or relative group delay) as

$$t^{(rel)}(\omega,\omega_0)=t'(\omega)-t'(\omega_0)=-\frac{d\phi}{d\omega}+\left.\frac{d\phi}{d\omega}\right|_{\omega_0}, \tag{8}$$

where $t^{(rel)}(\omega,\omega_0)$ is the time it takes for the attosecond pulse to go from oscillating at ω_0 to oscillating at ω. The reference frequency, ω_0, is arbitrarily chosen to be the lowest frequency of the pulse.

In the present work performed with relatively long (multicycle) driving pulses, the emission spectrum contains peaks at harmonic frequencies. In what follows, we use the following notation for the spectral phase $\Phi_n=\phi(n\omega_R)$, where n is the harmonic number and ω_R is the angular frequency of the ir laser field.

A. RABITT

The sidebands that appear in the RABITT method can be understood through the use of second-order perturbation theory [1]: absorption of a high-order harmonic photon followed by absorption or emission of an ir photon. Interferences occur between the different quantum paths that lead to the same sideband [Fig. 2(a)]. If we assume that the competing quantum paths have the same amplitude, then the intensity of the sideband varies as

$$I_{2n}(\varphi)\propto 1+\cos[2\varphi-\Delta\Phi_{2n}-\Delta\Phi_{2n}^{at}], \tag{9}$$

where φ is the phase of the probe field oscillations relative to the attosecond pulses, $\Delta\Phi_{2n}=\Phi_{2n+1}-\Phi_{2n-1}$ is the difference between the phases of the corresponding harmonics, and $\Delta\Phi_{2n}^{at}$ is the difference in atomic phase for the corresponding energies [11]. The atomic phase is neglected in the following because it only has a small effect on the final result in the spectral region that we consider. The first derivative of the

spectral phase can then be determined using the approximate relation

$$\left.\frac{d\phi}{d\omega}\right|_{2n\omega_R} \approx \frac{\Delta\Phi_{2n}}{2\omega_R}. \tag{10}$$

The final shape of an average attosecond pulse in the APT can be reconstructed using Eq. (10) combined with a measurement of the spectrum [12]. The aim of this paper is, however, not to reconstruct attosecond pulses but rather to study how the corresponding relative timing is affected by macroscopic dispersion in the generation cell. Using Eqs. (8)–(10), the relative timing can be written as a function of experimental observables as

$$t_{final}^{(rel)}(\omega,\omega_0) \approx -\frac{1}{\omega_R}[\varphi_{min}(\omega) - \varphi_{min}(\omega_0)], \tag{11}$$

where $\varphi_{min}(\omega)$ is the relative phase between the probe and the APT that minimizes the sideband intensity, $I_{2n}[\varphi_{min}(\omega)]=0$, for $\omega=2n\omega_R$. The subscript final is used to indicate that this is the final state of the pulse as it is detected on target.

B. *In situ*

We will now derive an analog to Eq. (11) for the *in situ* method, where the relative timing of the initial attosecond pulses is determined from the oscillation of the induced even harmonics. Using the strong field approximation (SFA), the Fourier components of the HHG dipole can be approximated as [13]

$$\vec{x}_n \propto \int dt d\tau d^3\vec{p}\, \exp\left[\frac{iS(\vec{p},t,\tau)}{\hbar} - in\omega_R t\right], \tag{12}$$

where $\vec{p}$ is the canonical (drift) momentum, τ is the time between tunneling and recombination, S is the quasiclassical action, and n is the harmonic order. Finding the stationary points of the quasiclassical action and then applying the saddle point approximation five times reduce the integrals in Eq. (12) to a sum of discrete contributions, each corresponding to a quasiclassical trajectory [5,14]. In the limit of a vanishing ionization potential, the quasiclassical trajectories become classical and the quasiclassical action becomes the classical action,

$$S[x(t,t')] = \int_{t-\tau(t)}^{t} dt' \left\{\frac{mv(t,t')^2}{2} + qx(t,t')E(t')\right\}, \tag{13}$$

where x, v, m, and q are the position, velocity, mass, and charge of the electron, respectively. We label the electron trajectories as $x=x(t,t')$, where t is the return time and t' is the integration variable for the action. The electron is released from the atom at time $t-\tau$ and accelerated by the laser field, E, until it returns and recombines with the atom at time t. In the one-color HHG, where $E=E_R=E_{R0}\sin(\omega_R t)$, the process is repeated with an alternating sign every half period, $x_R(t,t')=-x_R(t+T_R/2,t'+T_R/2)$, since $E_R(t')=-E_R(t'+T_R/2)$. The action is, however, the same, $S_R(t)=S_R(t+T_R/2)$.

Adding a weak blue field, $E=E_R+E_B$, $E_B=E_{B0}\sin(2\omega_R t+\varphi)$, induces a small change in the trajectories and the accumulated action. We treat the blue field as a perturbation and expand the trajectory,

$$m\frac{d^2}{dt^2}\sum_{n=0}^{\infty}\lambda^n x^{(n)} = qE_R + \lambda qE_B, \tag{14}$$

where λ is the usual perturbation parameter. The zeroth-order solution is the same as in the one-color case, $x^{(0)}=x_R$, and the first-order solution is purely given by the blue field, $x^{(1)}=x_B$. Higher orders, $n>1$, are equal to zero. We expand the action as $S=S^{(0)}+\lambda S^{(1)}+\lambda^2 S^{(2)}$. The zeroth-order action is the same as in the one-color case, $S^{(0)}=S_R$. The first-order action, $S^{(1)}=\sigma$, is composed of three cross terms that can be rewritten using a few partial integrations,

$$\sigma = \int_{t-\tau}^{t} dt' \{mv_R v_B + qx_R E_B + qx_B E_R\} \tag{15}$$

$$= q\int_{t-\tau}^{t} dt' x_R E_B, \tag{16}$$

where the following boundary conditions are used: $x_R(t,t)=x_R(t,t-\tau)=v_R(t,t-\tau)=x_B(t,t)=0$. It is interesting to note that σ can be written as an integral over the unperturbed trajectory, x_R, and the blue field (or as an integral over the trajectory perturbation, x_B, and the red field). Unlike S_R, the first-order action changes sign between opposite half cycles of the ir field, $\sigma(t)=-\sigma(t+T_R/2)$, which reflects the fact that the electron is now moving differently in the two half cycles, $x(t,t')\neq -x(t+T_R/2,t'+T_R/2)$. The second order action is given purely by the blue field, $S^{(2)}=S_B$, and it has, therefore, the same sign in opposite half cycles of the ir. The sum of the contributions from the zeroth and the second order is labeled as $\Sigma=S^{(0)}+S^{(2)}$.

The integrals of Eq. (12) are evaluated for the two-color case using the saddle point solutions for the ir field only, i.e., we assume that σ and S_B are slowly varying compared to S_R. Only the two stationary points corresponding to the short branch of trajectories in two neighboring half cycles of the fundamental are used, in accordance with the experiment where the long branch has been removed using spatial filtering in a narrow aperture. The contributions from the first-order action can be combined using Euler's formula. The HHG dipole takes the following form for the odd harmonics:

$$\vec{x}_{n=2N+1} \propto \cos\left[\frac{\sigma_n}{\hbar}\right]\exp\left[\frac{i\Sigma_n}{\hbar} - in\omega_R t_n\right], \tag{17}$$

where the first-order change in action, σ_n, leads to a change in dipole amplitude. In the limit of a vanishing blue field, we recover the one-color case: $\cos(\sigma_n/\hbar)\to 1$ and $\Sigma_n\to S_{Rn}$. The HHG dipole for the even harmonics takes the following form:

$$\vec{x}_{n=2N} \propto \sin\left[\frac{\sigma_n}{\hbar}\right]\exp\left[\frac{i\Sigma_n}{\hbar} - in\omega_R t_n\right], \tag{18}$$

where the amplitude again is dependent on the change in action. The even harmonics vanish if there is no blue field since $\sin(\sigma_n/\hbar)\to 0$. The intensities of the odd and even har-

monics vary out of phase: the odd harmonics decrease when the even harmonics increase. A weak blue field implies that $\sin(\sigma_n/\hbar) \approx \sigma_n/\hbar$. In this regime the even harmonic amplitudes grow linearly with the applied blue field and oscillate with the relative phase, φ. It is in this regime that an *in situ* measurement can be carried out.

Using Eq. (16), we seek the relative phase, $\varphi_{min}(t)$, that induces no even harmonic amplitude,

$$\sigma(t, \varphi_{min}(t)) = q \int_{t-\tau(t)}^{t} dt' x_R(t,t') E_B(t', \varphi_{min}(t)) = 0, \tag{19}$$

where the return time, $t=t(\omega)$, is a saddle point solution to Eq. (12) and, therefore, a function of frequency [in close analogy with Eqs. (3) and (4)]. We find excellent agreement with the pioneering work of Dudovich *et al.* [8] using unperturbed classical trajectories in Eq. (19). The solution, $\varphi_{min}(t)$, is expanded to first order around the central return time, $t_c = 0.35T_R$,

$$\varphi_{min}(t) - \varphi_{min}(t_c) \approx -(1+\xi)\omega_R(t - t_c), \tag{20}$$

where $\xi \approx -0.06$ is the "systematic scaling difference" between φ_{min} and $\omega_R t$. Our numerical linearization of $\varphi_{min}(t)$ in Eq. (20) depends on the choice of t_c: ξ varies from 0.1 (in the shortest return) to 0 (in the cutoff regime). It is, however, the scaling around the central return time (central frequency) that is most appropriate for calculating the initial properties of the entire attosecond pulse. Using Eqs. (8) and (20), we find the following simple relation between the oscillations in the even harmonics and the relative emission time from the atom:

$$t_{initial}^{(rel)}(\omega, \omega_c) \approx -\frac{\gamma}{\omega_R}[\varphi_{min}(t(\omega)) - \varphi_{min}(t(\omega_c))], \tag{21}$$

where $\gamma = 1/(1+\xi) \approx 1.06$ is a correction factor. Equation (21) resembles Eq. (11) from the RABITT section in both form and interpretation. The even harmonic oscillations are mapping out the relative emission times from the atom much like the sidebands in a RABITT scan map out the relative arrival times on target. In contrast to RABITT, the *in situ* method needs a correction factor, γ, which is slightly larger than one for the short branch of trajectories. The validity of Eq. (21) is limited to the high-order harmonic plateau where the constant amplitude approximation [Eq. (12)] and the linearization of $\varphi_{min}(t)$ [Eq. (20)] are sound. The *in situ* method can also be applied to the second (long) branch of trajectories. The correction factor for the long branch is $\gamma \approx 0.88$ for $t_c = 0.55T_R$.

We want to stress that the *in situ* method is *not* a direct measure of the emission time (or the group delay) because $\varphi_{min}(t)$ is not related to the return time in a trivial way [Eq. (19)]. In fact, one could also interpret the *in situ* method as a measurement of the continuum time which is an equally good parameter of the process.

All technical details aside, we have found that the *in situ* method produces traces of oscillating even harmonics which, to reasonable agreement, can be treated as RABITT scans. In the following, we will present data which are uncorrected,

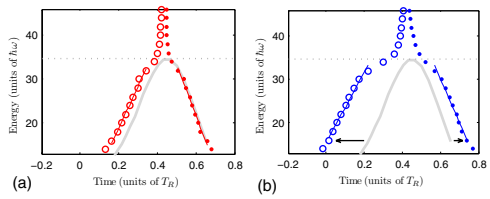

FIG. 3. (Color online) (a) The single atom response of the short (○) and the long (●) branches are calculated using SFA for a typical ir intensity, $I_R = 2 \times 10^{14}$ W/cm^2. The group delays, $-d\phi/d\omega$, of both branches are in good agreement with the simple classical model (gray line). The group delay branches merge beyond the cutoff (dotted line). (b) The numerical *in situ* scans generated using SFA with a weak blue field, $I_B/I_R = 0.1\%$, show qualitative agreement for both the short (○) and the long (●) branches with the simple classical model (gray line).

$\gamma = 1$, verifying numerically and experimentally the validity of $\gamma \approx 1$ for harmonics in the plateau. Unlike RABITT, the *in situ* method is not limited to sampling the relative timing at only even harmonic energies. The oscillations in the odd harmonic energies [Eq. (17)] can be treated in a similar way, thus doubling the number of sampling points for the relative timing compared to RABITT.

C. Numerical SFA calculation

We perform a numerical experiment using SFA to verify the analytical work presented in Sec. II B for an ir intensity of $I_R = 2 \times 10^{14}$ W/cm^2. Our numerical calculations are based on Eq. (13) in [5] where the saddle point approximation is done only over $\vec{p}$ space. The integration over continuum time, τ, and actual time, t, is done numerically. This allows us, in a simple way, to access either branch of trajectories by numerically restricting the integral over the continuum time, τ. We calculate the single atom response for the short branch of trajectories by restricting the continuum time integral to $0 < \tau < 0.65T_R$. Then we calculate the response from the long branch of trajectories by restricting the continuum time integral to $0.65T_R < \tau < T_R$. The corresponding group delays are calculated numerically from the first derivative of the spectral phase of the short branch dipole [Fig. 3(a), ○] and the long branch dipole [Fig. 3(a), ●]. The time-energy curves are compared to a simple classical model [Fig. 3(a), gray line], consisting in finding the classical kinetic return energy for a classical electron in a sinusoidal electric field, $E(t) = E_0 \sin \omega t$, which starts and returns to the origin, and then adding the ionization energy.

Next, we perform the numerical *in situ* measurement by calculating the single atom response from the same ir field plus a weak blue field with a relative intensity of $I_B/I_R = 0.1\%$. The phase of the blue field, φ, is then shifted relative to the ir and the atomic response is calculated again. As expected, we obtain weak oscillations in the even harmonics which vary with respect to φ. The relative phases, φ_{min}, that minimize the even harmonic signal are extracted from the short branch [Fig. 3(b), ○] and the long branch [Fig. 3(b),

●]. We find that the *in situ* method produces time-energy slopes [lines in Fig. 3(b)] that are in qualitative agreement with the simple classical model [Fig. 3(b), gray line] for harmonics below the cutoff [Fig. 3(b), dotted line]. There is, however, an absolute time difference between $-\varphi_{min}/\omega_R$, and the (unshifted) simple classical model [Fig. 3(b), gray line]. A careful study of the numerical experiment indicates that the *in situ* measurement suffers from a small systematic deviations from the group delay which can be attributed to the correction factor, γ. We stress that all data presented in Fig. 3(b) are uncorrected, i.e., $\gamma=1$.

A larger and possibly more interesting systematic deviation between the group delay and the *in situ* method arises for harmonics close to and beyond the cutoff [Figs. 3(a) and 3(b), dotted line]. This deviation occurs in a spectral region where Eqs. (3) and (4) are questionable and it is, therefore, more difficult to interpret the deviation. It is clear, however, that the *in situ* measurement is not a direct measurement of the group delay (or the relative timing) of the attosecond pulses and that a deeper analysis is needed for understanding the behavior beyond the cutoff.

The numerical experiment is repeated at progressively higher relative intensities to investigate the robustness of the *in situ* method. We observe the depletion of the odd harmonics, as expected from Eq. (17). The information retrieved from the even harmonics is intact as long as $I_B/I_R<1\%$ for $I_R=2\times10^{14}$ W/cm^2. Increasing the relative intensity further results in an invalid *in situ* measurement.

III. EXPERIMENTAL SETUP

The experimental work is carried out at the Lund Laser Center (LLC) using a kHz Ti-sapphire chirped pulse amplified laser operating at a wavelength of 800 nm (ir). The pulseenergy is 2 mJ and the pulse length is 35 fs. The APTs are generated by focusing the ir laser pulses into a synchronized pulsed argon gas cell [15]. Having a pulsed gas cell allows us to maintain a low average background pressure in the generation chamber while the effective gas pressure in the gas cell is high. We do not measure the instantaneous generation pressure in the gas cell but it is reasonable to assume that it scales with the average background pressure in the generation chamber.

We use aluminum filters after the HHG to

(i) remove the remaining ir and the low-order harmonics in the pump line and

(ii) compress the pulses in the APT.

Eliminating the intense ir beam after the generation cell is important since neither of the characterization schemes work if there is a strong ir field present in the detection process. The individual filters are 200 nm thick and the number of filters used can be changed using a motorized filter holder [6]. Being able to change the number of filters is important in order to access the effect of filters on the attosecond pulses [3]. The attosecond pulses are finally detected using a magnetic bottle electron spectrometer (MBES). The detection gas is argon which allows us to study the high-order harmonics from the plateau and cutoff regions.

In the RABITT method the ionization step in the MBES is perturbed by a synchronized weak ir probe field, which is coupled into the MBES using a Mach-Zehnder interferometer [Fig. 4(a)]. The relative phase, φ, between the APT and the ir is controlled using a piezoelectric translation stage in the interferometer. A typical RABITT scan is shown in Fig. 4(b).

In the *in situ* method the ir pulse is used to generate a second harmonic field (blue) with a 1.3-mm-thick potassium dideuterium phosphate (KDP) type-I crystal. The ir and the blue field are synchronized before the generation chamber using a three-dimensional dichroic interferometer [Fig. 4(c)]. A glass plate in the interferometer enables control of the relative phase, φ, between the ir and the blue fields. The interferometer is engineered so that the polarizations of the recombined red and blue fields are parallel [16]. A typical *in situ* scan is shown in Fig. 4(d). Using Eqs. (11) and (21), we know that the information about the attosecond pulses is derived in the same way from both methods, while the physical interpretation of the two measurements differs.

IV. PROOF OF PRINCIPLE FOR *IN SITU* MEASUREMENTS

In this section, we study the properties of an APT using both the RABITT and the *in situ* method. A direct comparison of the two measurements is not meaningful since attosecond pulses are probed at different times. Two main effects influence the properties of the attosecond pulses:

(i) dispersion from the Al filters;

(ii) phase matching in the generation cell.

To avoid effects due to phase matching as much as possible [2,17], we perform the measurement at the lowest possible pressure, corresponding to a background pressure of $P_G\approx1.5$ μbar. At this pressure, the high-order harmonic signal is weak but still stable enough for both characterization methods to work. The results from the RABITT method are shown in Fig. 5(a) and the results from the *in situ* method are shown in Fig. 5(b).

The change in relative timing induced to an attosecond pulse propagating through one aluminum filter, $\Delta t_{\mathrm{Al}}^{(rel)}(\omega,\omega_0)$, can be determined using two RABITT measurements,

$$\Delta t_{\mathrm{Al}}^{(rel)}(\omega)=t_{final_2}^{(rel)}(\omega)-t_{final_1}^{(rel)}(\omega), \tag{22}$$

where $t_{final_1}^{(rel)}$ is the relative timing of the attosecond pulse having passed one filter and $t_{final_2}^{(rel)}$ is the relative timing after passing two filters. Note that we now drop the notation for the reference frequency since it is $\omega_0=14\omega_R$ for all experimental data. We have verified that $\Delta t_{\mathrm{Al}}^{(rel)}(\omega)$ agrees with the GD deduced from the refractive index of aluminum [18]. Assuming that the two filters are identical we can calculate the relative timing of the attosecond pulse before passing the filter(s),

$$t_{final_0}^{(rel)}(\omega)=t_{final_1}^{(rel)}(\omega)-\Delta t_{\mathrm{Al}}^{(rel)}(\omega). \tag{23}$$

The "unfiltered" relative timing of attosecond pulses [Fig. 5(a), ○] is in good agreement with the simple classical model (gray line) for an effective intensity of $I_R\approx1$

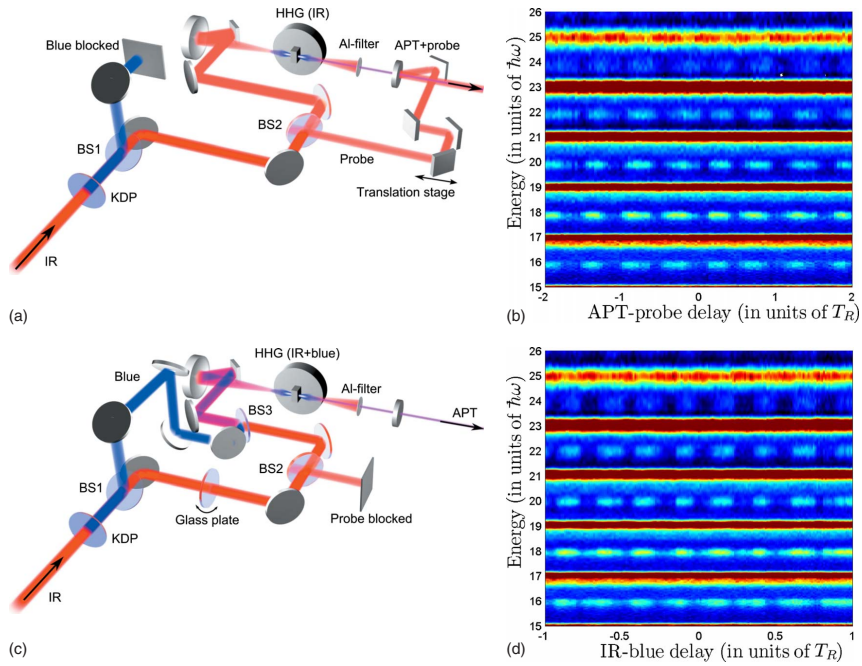

FIG. 4. (Color online) (a) In RABITT mode the blue field (from KPD) is split off (BS1) and blocked. A weak ir probe field is created (BS2) and delayed on the subcycle scale using a translation stage. The APT is generated from the intense ir pulses [HHG (ir)] in a synchronized pulsed gas cell. The intense ir field is eliminated using aluminum filter(s). The APT and the probe are recombined (APT +probe) using a mirror with a narrow aperture. The APT passes through the aperture while the probe is reflected on the mirror. The temporally overlapping APT and probe field are then focused using a toroidal mirror and detected using an electron spectrometer (not shown). (b) The RABITT scan is recorded using an electron spectrometer with subcycle synchronization of the APT and the probe in the detection chamber. (c) In *in situ* mode the ir and the blue field (from KDP) are separated (BS1) into a dichroic interferometer. The ir field is delayed on the subcycle scale using a glass plate (which can be tilted) before it is recombined with the blue field (BS3). The probe is blocked (after BS2). The APT is generated from intense ir pulses in the presence of a weak blue field [HHG (ir+blue)] in a synchronized pulsed gas cell. The ir and blue fields are eliminated using aluminum filter(s). The APT is detected using an electron spectrometer (not shown) after passing a narrow aperture. (d) The *in situ* scan is recorded using an electron spectrometer with subcycle synchronization of the ir and the blue fields in the generation cell [HHG (ir+blue)]. The color scale in (b) and (d) is saturated so that the interferometric beating is more clearly seen.

$\times 10^{14}$ W/cm^2. This intensity corresponds to a cutoff at harmonic (23), which agrees well with spectral measurements taken without the probe field present.

Having estimated the initial state of the attosecond pulses using the RABITT method, we now proceed with the *in situ* scheme. One important advantage of the *in situ* scheme is that all information is imprinted spectrally, which makes it possible to analyze attosecond processes with great accuracy using a photon spectrometer rather than an electron spectrometer. In this paper, however, we use the same MBES as for the RABITT so that a straightforward comparison of the two schemes is made.

The *in situ* measurements are taken immediately after their respective RABITT measurements for one and two aluminum filters [Fig. 5(b)]. The HHG conditions, therefore, have little time to evolve when changing schemes (a few seconds). The filters should not influence the *in situ* measurement because the information is imprinted spectrally already in the HHG process. Using the *in situ* scheme, we should ideally obtain identical information regardless of the number of filters. The measurements again nicely follow the classical model for $I=1\times10^{14}$ W/cm^2 (gray curve). We determine the initial relative timing, $t_{initial}^{(rel)}(\omega)$, and compare it to the relative timing obtained with the RABITT method, $t_{final_0}^{(rel)}(\omega)$, in Fig. 5(c). The corresponding group delay dispersion (GDD) is calculated by fitting a line to the relative timing using sidebands and even harmonics (14)–(22),

$$-\left.\frac{d^2\phi}{d\omega^2}\right|_{18\omega_R} \approx \begin{cases} 2.31\times10^4 \text{ as}^2/\text{rad} & \text{(RABITT)} \\ \gamma\times 2.24\times10^4 \text{ as}^2/\text{rad} & (\textit{in situ}), \end{cases} \tag{24}$$

with a root mean square deviation of approximately 23 as for

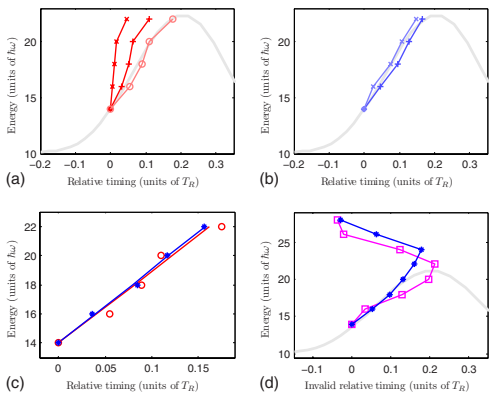

FIG. 5. (Color online) (a) RABITT measurements with one (+) and two (×) aluminum filters are used to determine the relative timing of the unfiltered attosecond pulses (○). All temporal measurements are presented as relative timings with reference to harmonic (14). (b) *In situ* measurements with one (+) and two (×) aluminum filters. The data are uncorrected, $\gamma=1$. The simple classical model ($I_R=1\times10^{14}$ W/cm^2) [(a) and (b) gray curve] is plotted for reference. (c) Unfiltered RABITT measurement (red, ○) compared to the average *in situ* measurement (blue, *). (d) A slight increase in the blue intensity (blue, *) has a small effect on the measurement in the harmonic plateau [harmonics (14)–(24). Increasing the blue intensity further (pink, □) results in an invalid measurement. The simple classical model ($I_R=0.9\times10^{14}$ W/cm^2) (gray line) is plotted for reference.

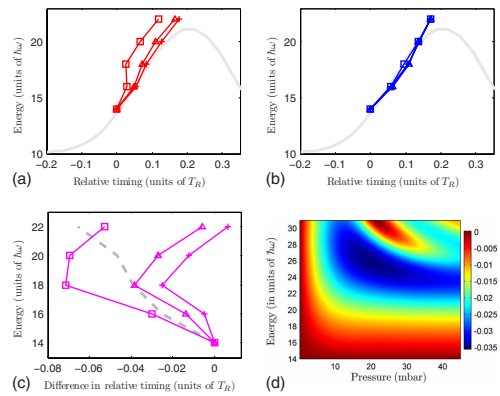

FIG. 6. (Color online) (a) Relative timing measurements from RABITT for a variety of high background pressures in the generation chamber: 5×10^{-3} (×), 6×10^{-3} (△), and 7×10^{-3} (□) mbar (the exact instantaneous pressure in the gas cell is unknown). The effect of the Al filter has been subtracted. At high pressures there is an increased deviation from the simple classical model ($I_R=0.9\times10^{14}$ W/cm^2) (gray curve). (b) The corresponding *in situ* measurements are mostly unaffected by the increased pressure. The data are not corrected, $\gamma=1$. (c) The difference in relative timing, $\Delta t^{(rel)}_{macro}(\omega,P_G)$ (pink ×, △, and □), is interpreted as the macroscopic delay due to phase matching in the gas cell. The symbols correspond to the same pressures as in the figures above. The delay from phase matching has approximately the same magnitude as an aluminum filter (gray dashed curve). (d) The relative timing due to phase matching (false color in units of T_R) is calculated using a one-dimensional model [17] for pressures ranging from 0 to 100 mbar. The intensity used in the model is 1.25×10^{14} W/cm^2 and the duration of the pulse is 35 fs. The length of the cell is modeled as 5 mm.

the corresponding difference in relative timing. We treat the *in situ* data as a RABITT scan, and the numerical value of the GDD must, therefore, be multiplied by the correction factor, γ. The experiment shows that the correction factor is close to unity for the short branch, as expected from the theory section. The good agreement between these measurements shows that either the RABITT or the *in situ* method can be used to characterize the APTs at low generation pressures for energies in the central and upper regions of the harmonic plateau.

It is tempting to increase the intensity of the blue field so that the even harmonics become stronger and more visible. We use an adjustable aperture in the blue arm of the three-dimensional dichroic interferometer so that the intensity of the blue field can be increased while all other experimental parameters are constant. It has been demonstrated that an increased blue intensity will alter the quasiclassical trajectories in the HHG process [19,20], but a systematic study of how the *in situ* method breaks down has not yet been reported. Even harmonic oscillations appear *beyond the cutoff* for a slight increase in the blue intensity. The information extracted from these oscillations show strong deviations with the expected group delays, while the information from the plateau region remains rather accurate [Fig. 5(d), *]. Even harmonic oscillation beyond the cutoff regime should, therefore, not be included in our simple interpretation [Eq. (21)] of the *in situ* method. The experimental results at high photon energy are in qualitative agreement with the numerical calculations of the long branch shown in Fig. 3(b) shifted by half their period. At moderately higher blue intensities we observe a shift of the modulations in the plateau [Fig. 5(d), □]. This shows that the *in situ* method now predicts the wrong relative timing for the initial attosecond pulses also in the plateau region and that the relative intensity must be reduced.

V. COMPARISON OF RABITT AND *IN SITU* MEASUREMENTS AT HIGHER PRESSURE

We now study how the phase of the attosecond pulses is modified due to a higher gas pressure in the generation chamber. It has recently been shown that in some conditions an increasing gas pressure can lead to a compression of the attosecond pulses [17]. The effect predicted theoretically was, however, small and difficult to demonstrate experimentally. Here, combined measurements using the RABITT and the *in situ* method allow us to unambiguously extract the contribution of phase matching to the temporal structure of attosecond pulses.

RABITT results obtained at different pressures are shown in Fig. 6(a). The data are collected with one aluminum filter,

but the effect of this filter is removed using Eq. (23). The corresponding *in situ* measurements are shown in Fig. 6(b). The *in situ* measurements are mostly insensitive to the increased gas pressure, while the RABITT measurements are deformed in a nontrivial way. Deviations in relative timing for attosecond pulses due to the macroscopic propagation through the gas cell can be extracted by subtracting the final and initial relative timings,

$$\Delta t^{(rel)}_{macro}(\omega, P_G) = t^{(rel)}_{final_0}(\omega, P_G) - t^{(rel)}_{initial}(\omega, P_G), \quad (25)$$

where we have explicitly written P_G to indicate that the macroscopic effects depend on the gas pressure. In $t^{(rel)}_{initial}(\omega, P_G)$, the P_G dependence refers to a possible change in the fundamental field in the nonlinear medium that could affect the single atom response. The results are shown in Fig. 6(c), together with the effect of a 200 nm Al filter (gray). Macroscopic effects introduce a (nontrivial) negative relative timing, first decreasing then increasing with frequency. The corresponding induced GDD might help to compensate for the single atom GDD for low orders, but for higher orders the GDD is increased. These results agree well with those presented in [17].

To understand the origin of the macroscopic group delay, we perform a simple model calculation [17,21]. We consider for simplicity a one-dimensional approximation along the propagation axis z, a homogeneous medium of length L, and a collimated geometry. In this simple case, the contribution of the single atom response and of propagation can be separated and the effect of propagation both on the phase (or more exactly phase variation) and amplitude of the nth harmonic can be described by

$$F_n = \frac{1 - \exp[(-i\Delta k_n - \kappa_n)L]}{i\Delta k_n + \kappa_n} = |F_n| \exp[i\phi_n^{mac}]. \quad (26)$$

The phase mismatch Δk_n is equal to $k_n - nk_1$, where k_n and k_1 denote the wave vector of harmonic n and the fundamental, respectively. Absorption at the nth harmonic frequency is described by κ_n. The macroscopic phase can be written as

$$\phi_n^{mac} = -\arctan\left[\frac{\sin[\Delta k_n L]}{\cos[\Delta k_n L] - \exp[\kappa_n L]}\right] - \arctan\left[\frac{\Delta k_n}{\kappa_n}\right]. \quad (27)$$

Figure 6(d) presents in color its derivative as a function of harmonic order and pressure. These results show a variation in the phase derivative that qualitatively agrees with the measured one. For a given pressure >20 mbar, the induced GD is negative, showing a decrease at low orders, a minimum around the 23rd harmonic, followed by an increase. We stress that this satisfactory agreement is obtained with a simple model, not including the geometric phase due to focusing or two-dimensional effects. Combined RABITT and *in situ* measurements provide a way to really unravel the effect of propagation in the generation of attosecond pulses.

VI. CONCLUSIONS

We have performed a proof of principle experiment for the *in situ* scheme by comparing it to the well established RABITT method. We have found excellent agreement between the methods at low generation gas pressures when the macroscopic phase matching plays a negligible role.

We have found that it is not possible to use the *in situ* scheme to predict the final relative timing of the average attosecond pulses if the generation pressure is high or if it passes through some unknown dispersive material. It is equally important to realize that accurate single atom measurements cannot be conducted at high generation gas pressures with the RABITT scheme. In a RABITT measurement there will always be a trade off between the number of harmonic photons generated and their phase perturbation from propagation through the generation cell.

The advantages and disadvantages of the two schemes become quite clear when the generation pressure is high and one could argue that *both* schemes are needed for a more complete understanding of the attosecond pulse production and propagation.

ACKNOWLEDGMENTS

We thank Lou DiMauro for valuable comments on this work. This research was supported by the Marie Curie programmes (MAXLAS, ATTOCO) of the European Union, the European and Swedish Reseach Councils and the Kunt and Alice Wallenberg Foundation.

[1] P. M. Paul *et al.*, Science **292**, 1689 (2001).
[2] M. B. Gaarde, J. L. Tate, and K. J. Schafer, J. Phys. B **41**, 132001 (2008).
[3] R. López-Martens *et al.*, Phys. Rev. Lett. **94**, 033001 (2005).
[4] Y. Mairesse *et al.*, Science **302**, 1540 (2003).
[5] M. Lewenstein, P. Balcou, M. Y. Ivanov, A. LHuillier, and P. B. Corkum, Phys. Rev. A **49**, 2117 (1994).
[6] E. Gustafsson *et al.*, Opt. Lett. **32**, 1353 (2007).
[7] A.-S. Morlens *et al.*, Opt. Lett. **31**, 1558 (2006).
[8] N. Dudovich *et al.*, Nat. Phys. **2**, 781 (2006).
[9] J. Itatani *et al.*, Nature (London) **432**, 867 (2004).
[10] Even harmonics are not generated if there is no blue field present due to parity conservation.
[11] J. Mauritsson, M. B. Gaarde, and K. J. Schafer, Phys. Rev. A **72**, 013401 (2005).
[12] Except for the carrier envelope phase of the attosecond pulse.
[13] M. Lewenstein, P. Salières, and A. L'Huillier, Phys. Rev. A **52**, 4747 (1995).
[14] P. Salières *et al.*, Science **292**, 902 (2001).
[15] D. Proch and T. Trickl, Rev. Sci. Instrum. **60**, 713 (1989).
[16] J. Mauritsson, J. M. Dahlström, and T. Fordell, J. Phys. B **42**, 134003 (2009).
[17] T. Ruchon *et al.*, New J. Phys. **10**, 025027 (2008).

[18] O. E. Martinez, J. P. Gordon, and R. L. Fork, J. Opt. Soc. Am. B **1**, 1003 (1984).
[19] J. Mauritsson, P. Johnsson, E. Gustafsson, A. LHuillier, K. J. Schafer, and M. B. Gaarde, Phys. Rev. Lett. **97**, 013001 (2006).
[20] E. Mansten *et al.*, New J. Phys. **10**, 083041 (2008).
[21] E. Constant, D. Garzella, P. Breger, E. Mevel, C. Dorrer, C. Le Blanc, F. Salin, and P. Agostini, Phys. Rev. Lett. **82**, 1668 (1999).

Paper II

Probing Single-Photon Ionization on the Attosecond Time Scale

K. Klünder, J. M. Dahlström, M. Gisselbrecht, T. Fordell, M. Swoboda, D. Guénot, P. Johnsson, J. Caillat, J. Mauritsson, A. Maquet, R. Taïeb and A. L'Huillier.

Phys. Rev. Lett. **106**, 143002 (2011).

PRL 106, 143002 (2011) PHYSICAL REVIEW LETTERS week ending 8 APRIL 2011

Probing Single-Photon Ionization on the Attosecond Time Scale

K. Klünder,[1] J. M. Dahlström,[1] M. Gisselbrecht,[1] T. Fordell,[1] M. Swoboda,[1] D. Guénot,[1] P. Johnsson,[1] J. Caillat,[2] J. Mauritsson,[1] A. Maquet,[2] R. Taïeb,[2] and A. L'Huillier[1,*]

[1]*Department of Physics, Lund University, P.O. Box 118, 22100 Lund, Sweden*

[2]*Laboratoire de Chimie Physique-Matière et Rayonnement, Université Pierre et Marie Curie, 11, Rue Pierre et Marie Curie, 75231 Paris Cedex, 05, France*

(Received 15 December 2010; published 5 April 2011; publisher error corrected 14 April 2011)

We study photoionization of argon atoms excited by attosecond pulses using an interferometric measurement technique. We measure the difference in time delays between electrons emitted from the $3s^2$ and from the $3p^6$ shell, at different excitation energies ranging from 32 to 42 eV. The determination of photoemission time delays requires taking into account the measurement process, involving the interaction with a probing infrared field. This contribution can be estimated using a universal formula and is found to account for a substantial fraction of the measured delay.

DOI: 10.1103/PhysRevLett.106.143002 PACS numbers: 32.80.Rm, 32.80.Qk, 42.65.Ky

The interaction of light with matter is an essential process in nature and, in particular, the photoelectric effect has been studied during decades using synchrotron radiation [1]. The development of ultrashort light pulses in the attosecond range allows scientists to tackle temporal aspects of electron transitions in atoms, molecules, and more complex systems. Cavalieri *et al.* [2] investigated photoemission from the valence and the conduction band in tungsten crystals using single attosecond pulses and an infrared (ir) probing field through the streaking technique [3]. Recently, Schultze *et al.* [4] implemented the same technique to study photoemission from the $2s^2$ and $2p^6$ shells in neon at a pulse energy of 100 eV. They measured a difference in photoemission time delays equal to 21 as, a value which is significantly larger than the expected theoretical value, as further discussed in a series of theoretical articles [5–8].

In this Letter, we examine photoemission of electrons from the $3s^2$ and $3p^6$ shells in argon. Our method uses a frequency comb of high-order harmonics with photon energies varying from 32 to 42 eV for the photoionization and a weak ir field for probing the outgoing electrons. It is based on interferometry and presents analogies with coherent control schemes used for phase measurements close to resonant states [9–11]. Here we explore single photoionization in the threshold region for the $3s^2$ shell, where one expects large variation in photoemission times. The measurement shows a delay between the ionization from the $3s^2$ and $3p^6$ shells which varies with photon energy. We investigate the influence of the interaction with the weak ir field, which is needed to do the interferometric measurement and get the temporal information. Probing the outgoing electron wave packet (EWP), even with a weak ir field, affects electron motion and therefore the measured delay. Fortunately, this effect can be analytically calculated and takes a universal form, that allows us to disentangle the different effects and gives us access to the single-photon ionization time, also called Wigner time [12,13].

The basic principle of our experiment is shown in Fig. 1. We ionize argon using a comb of high-order harmonics. With a central frequency of the harmonic comb above the binding energy of the $3s$ shell we simultaneously create two independent EWPs, one originating from the $3s^2$ and one from the $3p^6$ shell. The presence of a fraction of the fundamental laser field with frequency ω induces the formation of sideband peaks due to two-photon transitions including absorption or emission of an ir photon [14,15]. Two different and interfering quantum paths involving consecutive harmonics lead to the same sideband (see Fig. 1). When changing the delay τ between the harmonic comb and the laser field, the sideband signal from a given shell is modulated as [16]

$$S(\tau) = \alpha + \beta \cos[2\omega(\tau - \tau_A - \tau_I)], \quad (1)$$

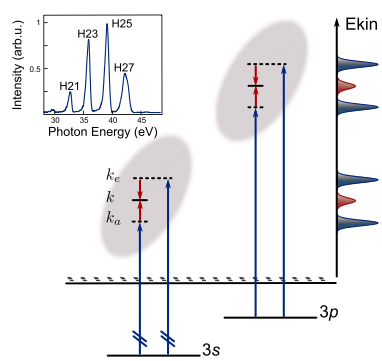

FIG. 1 (color online). Principle of the measurement. Two EWPs originating from different shells are simultaneously created using the same comb of high-order harmonics. The outgoing EWPs are further probed with a weak ir field. For simplicity only two harmonics are indicated. Also shown is the experimental harmonic spectrum used.

where α, β are two constants independent of τ. The term τ_A is proportional to the difference in phase between consecutive harmonics and describes the group delay of the attosecond pulses, while τ_I represents the atomic delay due to the two-photon ionization process [17]. As we will show below τ_I can be connected to the Wigner time delay τ_W for the single-photon ionization. The knowledge of τ_A as well as of the absolute value of the delay τ would enable us to determine τ_I directly. However, these variables are difficult to obtain separately. The simultaneous measurement of the two EWPs allows us to cancel the influence of the attosecond group delay τ_A and to determine $\tau_I(3s) - \tau_I(3p)$ at the same photon energy, i.e., at kinetic energies separated by the difference in binding energy between the two shells (13.5 eV).

Our experiments were performed with a 800 nm, 30 fs titanium-sapphire laser system [18]. High-order harmonics were generated in a pulsed Ar gas cell and spatially filtered using a small aperture [19]. We used a 0.2 μm thick chromium thin film to select a 10 eV-broad spectral window corresponding to harmonic 21 to 27 at 38 eV central energy (see Fig. 1). This filter was chosen to separate the wave packets emitted from the $3s$ and $3p$ shells in energy. The comb of four phase-locked harmonics, corresponding to a train of attosecond pulses with a 450 as duration, was focused by a toroidal mirror into the sensitive region of a magnetic bottle electron spectrometer containing a diffusive Ar gas jet. Part of the laser field was extracted prior to the high-order harmonic generation and recombined collinearly with the harmonics with a variable time delay τ. The precision of our measurement does not depend on the duration of the attosecond extreme-ultraviolet (xuv) pulses but on the interferometric stability of our experiment, estimated to be 50 as.

Figures 2(a) and 2(b) present electron spectra as a function of the delay τ between the xuv and the ir pulses. The low-energy spectrum in Fig. 2(a) shows electron peaks at energies corresponding to single-photon ionization from the $3s$ shell by the harmonics and additional sideband peaks due to two-photon transitions. The high-energy part of the spectrum shown in Fig. 2(b) presents the corresponding photoelectron spectra for $3p$ ionization. Although simultaneously recorded the results are presented separately due to the unequal signal strength caused by the difference in cross section and detector sensitivity (note the different color scales). For both channels the sideband signal oscillates, allowing us to extract the delay by Fourier transform along the time axis for a weak ir field [20]. The ir intensity was estimated to be well below 10^{12} W cm^{-2}. Figure 2(c) presents the delays obtained for the scan shown in (a) and (b), corrected for the influence of the Cr filter, which is positively dispersive in this region [21]. The variation in delay reflects mainly the positive chirp of the attosecond pulses. The main experimental result of the present work is the significant offset

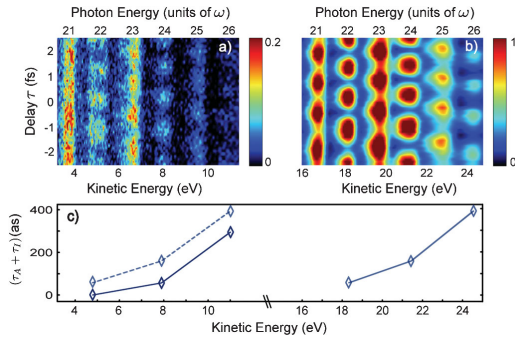

FIG. 2 (color). Energy spectra as a function of delay from electrons liberated from the $3s$ shell (a) and the $3p$ shell (b), respectively. (c) Retrieved delays corrected for the Cr group delay. Also shown are the $3p$ delays shifted down in energy for comparison with the $3s$ delays (dashed line).

between the delays measured for the two wave packets. To emphasize this result, we show as a dashed line the $3p$ delays shifted down in energy by 13.5 eV. Taking the difference between the measured delays at the same excitation energy allows us to eliminate the attosecond chirp and to reduce the effect of temporal drifts in the interferometer. Averaging over five independent measurements, we determine a difference in delays $\tau_I(3s) - \tau_I(3p)$ equal to -40 ± 10 as for sideband 22, -110 ± 10 as for sideband 24, and -80 ± 30 as for sideband 26.

To understand the meaning of these time delays, we need to establish the connection between single-photon ionization and the two-photon ionization process used in the measurement. The phase of the transition matrix element describing a single ionization process towards a final state with angular momentum ℓ is the scattering phase η_ℓ, i.e., the phase accumulated by the photoelectron when escaping from the atom. Its energy derivative $\tau_W = \hbar \partial \eta_\ell(\epsilon)/\partial \epsilon$ represents the "photoionization time delay" also called Wigner time delay [12,13]. Clearly, both η_ℓ and τ_W depend on the details of the atomic potential and their computation remains a challenge for theory. Using second-order perturbation theory, the transition matrix element for two-photon ionization involving absorption of a harmonic photon ω_H and an ir photon ω from an initial state φ_i to a continuum state $\varphi_{\vec{k}}$ with asymptotic momentum $\vec{k}$ can, using atomic units, be written as

$$M_a^{(2)}(\vec{k}) = -iE_L E_H \lim_{\varepsilon \to 0^+} \sum_n \frac{\langle \varphi_{\vec{k}} | \vec{\epsilon} \cdot \vec{r} | \varphi_n \rangle \langle \varphi_n | \vec{\epsilon} \cdot \vec{r} | \varphi_i \rangle}{\epsilon_i + \omega_H - \epsilon_n + i\varepsilon}. \quad (2)$$

The complex amplitudes of the laser and harmonic fields are denoted E_L and E_H and $\vec{\epsilon}$ is their common polarization vector. The energies of the initial and intermediate states are denoted ϵ_i and ϵ_n, respectively. The integral sum is performed over all possible intermediate states φ_n.

PRL 106, 143002 (2011) PHYSICAL REVIEW LETTERS week ending 8 APRIL 2011

The index a indicates that we first discuss a two-photon process with absorption of the ir photon.

We consider the channels $s \to p \to \ell$ with $\ell = s, d$. Using spherical coordinates, separating radial and angular parts, and expanding the final wave function into partial waves, the transition matrix element becomes

$$M_a^{(2)}(\vec{k}) = -iE_L E_H \sum_{\ell=0,2} C_{\ell 0} Y_{\ell 0}(\hat{k}) e^{i\eta_\ell(k)} T_a^{(2)}(k), \quad (3)$$

where $Y_{\ell 0}$ is a spherical harmonic, $C_{\ell 0}$ is the corresponding angular coefficient, and η_ℓ is the scattering phase of the final state. The radial two-photon transition matrix element $T_a^{(2)}(k)$ can be expressed as [15,17]

$$T_a^{(2)}(k) = \sum\!\!\!\!\!\!\int_n \frac{\langle R_{k\ell}|r|R_{n1}\rangle\langle R_{n1}|r|R_{i0}\rangle}{\epsilon_i + \omega_H - \epsilon_n + i\varepsilon} = \langle R_{k\ell}|r|\rho_{k_a 1}\rangle. \quad (4)$$

In the right part of Eq. (4) we introduce the perturbed wave function $\rho_{k_a 1}$ with the wave number k_a such that $k_a^2/2 = \epsilon_i + \omega_H = k^2/2 - \omega$ (see Fig. 1) [22]. To get an estimate of the phase of $T_a^{(2)}$, we consider the asymptotic behavior of the wave functions involved in Eq. (4). The perturbed wave function $\rho_{k_a 1}$ is an outgoing wave [23,24]

$$\lim_{r\to\infty} \rho_{k_a 1}(r) \propto e^{i[k_a r - 1/2\pi + 1/(k_a)\ln(2k_a r) + \eta_1(k_a)]}, \quad (5)$$

while $R_{k\ell}$ is real with an asymptotic behavior:

$$\lim_{r\to\infty} R_{k\ell}(r) \propto \sin\left[kr - \frac{\ell}{2}\pi + \frac{1}{k}\ln(2kr) + \eta_\ell(k)\right]. \quad (6)$$

The factor $\ell\pi/2$ arises from the centrifugal potential, while $\ln(2kr)/k$ is a correction due to the long-range Coulomb potential. Using Eqs. (3)–(6) we find an approximate expression for $M_a^{(2)}(k)$

$$M_a^{(2)}(k) \propto \underbrace{e^{i\eta_1(k_a)}}_{\text{(I)}} \times \underbrace{\left(\frac{i}{k_a - k}\right)^{iz} \frac{(2k)^{i/k}}{(2k_a)^{i/(k_a)}} \Gamma(2 + iz)}_{\text{(II)}}, \quad (7)$$

where $z = 1/k_a - 1/k$ and $\Gamma(z)$ is the complex gamma function. The first phase term (I) is the scattering phase of the intermediate state and identical to the phase of the corresponding one-photon ionization. The phase of term (II) can be assigned to the laser-driven transition connecting the two continuum states in the presence of the long-range Coulomb potential, φ_a^{cc}. It is independent of the short-range behavior of the atomic potential and therefore universal. Corrections to this approximation due to the core are expected to become important only at energies close to threshold.

The phase of the two-photon matrix element $M_e^{(2)}$ for the second pathway, i.e., absorption of an harmonic photon ω_H followed by emission of an ir photon ω via an intermediate state with wave number $k_e^2/2 = k^2/2 + \omega$ (see Fig. 1), can be derived in a similar manner. The total interference signal is obtained by angular integration of $|M_a^{(2)} + M_e^{(2)}|^2$. It can be written as Eq. (1), with

$$\tau_I = \underbrace{\frac{\eta_1(k_e) - \eta_1(k_a)}{2\omega}}_{\tau_W} + \underbrace{\frac{\varphi_e^{cc}(k) - \varphi_a^{cc}(k)}{2\omega}}_{\tau_{cc}}. \quad (8)$$

This result gives an intuitive understanding of the ionization time $\tau_I(3s)$. It can be expressed as the sum of the Wigner time delay τ_W for one-photon ionization $3s \to \epsilon p$ and an additional continuum-continuum delay τ_{cc} inherent to the measuring process. This analytical derivation can be easily generalized to other ionization channels.

Figure 3 shows the delays involved in the three ionization channels $3p \to \epsilon s$ (a), $3p \to \epsilon d$ (b), and $3s \to \epsilon p$ (c) in Ar as a function of kinetic energy. The Wigner time delay τ_W (dashed) is obtained by taking the derivative of the scattering phase (Coulomb phase plus phase shift taken from [25]). For comparison, we also show in (d) the delays for the pathway $1s \to \epsilon p$ in hydrogen in the same energy region, using the Coulomb phase. The continuum-continuum delay τ_{cc} (dash-dotted) is calculated for a 800 nm laser wavelength and identical for all the channels and atoms. The solid line indicates τ_I as the sum of the two contributions. The Wigner time delay variation can be nicely and intuitively interpreted. Low-energy electrons take a longer time to escape from a given shell than high-energy electrons. Furthermore, electrons escaping to a channel with higher angular momentum take a longer time than those escaping to a channel with low angular momentum because of the centrifugal barrier. The continuum-continuum delay has the opposite behavior

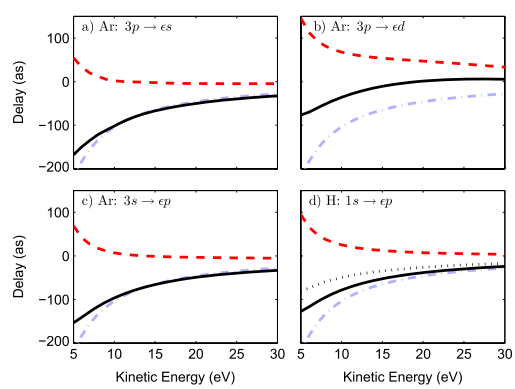

FIG. 3 (color online). Computed delays associated with the following ionization channels: (a) $3p \to \epsilon s$, (b) $3p \to \epsilon d$, (c) $3s \to \epsilon p$ in Ar, and (d) $1s \to \epsilon p$ in H. The dashed lines (red) are the one-photon Wigner time delays. The dash-dotted lines (blue) represent the estimated delays induced by the measurement τ_{cc}. The sum of the two delays is shown as a solid line (black). The dotted line (black) in (d) is the result of an exact calculation in H.

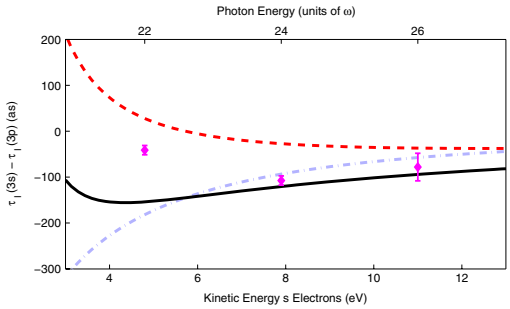

FIG. 4 (color online). Comparison between the measured delay differences for ionization of Ar from the $3s$ and $3p$ shells (diamonds) with calculations performed according to the approximate theory developed in this work (solid black line). Also shown is the delay expected for one-photon ionization (dashed red line) and the laser-driven continuum-continuum transition (dash-dotted blue line).

and leads to an apparent quicker escape for the low-energy electrons. Finally, we also indicate in Fig. 3(d) results from exact calculations in H (dotted line). The comparison between the solid and dotted lines gives an estimation of the error made in considering only the asymptotic behaviors of the perturbed and final wave functions. For the energy range considered in the present work the asymmetry parameter remains close to 2 [26], which indicates that the ionization channel $3p \rightarrow \epsilon d$ dominates over $3p \rightarrow \epsilon s$. Neglecting the $3p \rightarrow \epsilon s$ channel, we calculate $\tau_I(3s) - \tau_I(3p)$ at the same excitation energy [Eq. (8)]. Figure 4 presents the approximated delays (solid line), together with the experimental results (◆). The experimental results at the two highest energies agree well with the results of our calculation, indicating that the scattering phases [25] and our approximated continuum-continuum transition are reliable in this region. The lowest energy point, however, lies several standard deviations away from the calculated value. In this region the core may play a more important role for the continuum-continuum transition, and the Wigner time delays may differ from those calculated in [25]. In addition, the finite difference approximation to the Wigner time delay in Eq. (8) might break down in the presence of sharp resonances [27]. Using our experimental measurements combined with our estimated continuum-continuum delays, we can tentatively deduce the difference in single photoemission delays to be equal to 140 as at 34 eV and −20 as at 37 and 40 eV.

In conclusion, we have performed experimental measurements of photoemission from the $3s^2$ and $3p^6$ shells in Ar, using interferometry with a weak ir field to probe the created EWPs. We identify two contributions to the measured delays: the Wigner time delay and a delay inherent to the measurement process. Both contributions are most important near threshold and vanish as the energy increases. We believe that the work presented here will stimulate further experiments, aiming at measuring photoemission delays in a variety of systems, and providing data that could be compared to advanced theoretical calculations.

We thank Stefan Haessler, Franck Lépine, and Kenneth J. Schafer for stimulating discussions. This research was supported by the Marie Curie programs ATTOCO (IEF) and ATTOFEL (ITN), the European Research Council (ALMA), the Joint Research Programme ALADIN of Laserlab-Europe II, the Swedish Foundation for Strategic Research, the Swedish Research Council, the Knut and Alice Wallenberg Foundation, and the French ANR ATTO-WAVE.

*anne.lhuillier@fysik.lth.se
http://www.atto.fysik.lth.se

[1] V. Schmidt, Rep. Prog. Phys. **55**, 1483 (1992).
[2] A. L. Cavalieri *et al.*, Nature (London) **449**, 1029 (2007).
[3] J. Itatani *et al.*, Phys. Rev. Lett. **88**, 173903 (2002).
[4] M. Schultze *et al.*, Science **328**, 1658 (2010).
[5] V. S. Yakovlev, J. Gagnon, N. Karpowicz, and F. Krausz, Phys. Rev. Lett. **105**, 073001 (2010).
[6] J. C. Baggesen and L. B. Madsen, Phys. Rev. Lett. **104**, 043602 (2010).
[7] C.-H. Zhang and U. Thumm, Phys. Rev. A **82**, 043405 (2010).
[8] A. S. Kheifets and I. A. Ivanov, Phys. Rev. Lett. **105**, 233002 (2010).
[9] R. Yamazaki and D. S. Elliott, Phys. Rev. Lett. **98**, 053001 (2007).
[10] S. Haessler *et al.*, Phys. Rev. A **80**, 011404 (2009).
[11] M. Swoboda *et al.*, Phys. Rev. Lett. **104**, 103003 (2010).
[12] E. P. Wigner, Phys. Rev. **98**, 145 (1955).
[13] F. T. Smith, Phys. Rev. **118**, 349 (1960).
[14] J. M. Schins *et al.*, J. Opt. Soc. Am. B **13**, 197 (1996).
[15] V. Véniard, R. Taïeb, and A. Maquet, Phys. Rev. A **54**, 721 (1996).
[16] P. M. Paul *et al.*, Science **292**, 1689 (2001).
[17] E. S. Toma and H. G. Muller, J. Phys. B **35**, 3435 (2002).
[18] T. Fordell, M. Miranda, A. Persson, and A. L'Huillier, Opt. Express **17**, 21 091 (2009).
[19] R. López-Martens *et al.*, Phys. Rev. Lett. **94**, 033001 (2005).
[20] M. Swoboda *et al.*, Laser Phys. **19**, 1591 (2009).
[21] http://www.cxro.lbl.gov.
[22] A. Dalgarno and J. T. Lewis, Proc. R. Soc. A **233**, 70 (1955).
[23] M. Aymar and M. Crance, J. Phys. B **13**, L287 (1980).
[24] M. Edwards, X. Tang, and R. Shakeshaft, Phys. Rev. A **35**, 3758 (1987).
[25] D. J. Kennedy and S. T. Manson, Phys. Rev. A **5**, 227 (1972).
[26] R. G. Houlgate, J. B. West, K. Codling, and G. V. Marr, J. Electron Spectrosc. Relat. Phenom. **9**, 205 (1976).
[27] R. P. Madden, D. L. Ederer, and K. Codling, Phys. Rev. **177**, 136 (1969).

Paper III

Photoemission Time-Delay Measurements and Calculations close to the 3s Ionization Minimum in Argon

D. Guénot, K. Klünder, C. L. Arnold, D. Kroon, J. M. Dahlström, M. Miranda, T. Fordell, M. Gisselbrecht, P. Johnsson, J. Mauritsson, E. Lindroth, A. Maquet, R. Taïeb, A. L'Huillier and A.S. Kheifets.

(2012) *Accepted for publication in Phys. Rev. A* .

Photoemission Time-Delay Measurements and Calculations close to the 3s Ionization Minimum in Argon

D. Guénot[1], K. Klünder[1], C. L. Arnold[1], D. Kroon[1], J. M. Dahlström[2], M. Miranda[1], T. Fordell[1], M. Gisselbrecht[1], P. Johnsson[1], J. Mauritsson[1], E. Lindroth[2], A. Maquet[3], R. Taïeb[3], A. L'Huillier[1] and A. S. Kheifets[4]

[1]*Department of Physics, Lund University, P.O. Box 118, 22100 Lund, Sweden*

[2]*Department of Physics, Stockholm University, Sweden*

[3]*Laboratoire de Chimie Physique-Matière et Rayonnement, Université Pierre et Marie Curie, 11, Rue Pierre et Marie Curie, 75231 Paris Cedex, 05, France and*

[4]*Research School of Physical Sciences, The Australian National University, Canberra ACT 0200, Australia*

(Dated: May 9, 2012)

We present experimental measurements and theoretical calculations of photoionization time delays from the $3s$ and $3p$ shells in Ar in the photon energy range of 32-42 eV. The experimental measurements are performed by interferometry using attosecond pulse trains and the infrared laser used for their generation. The theoretical approach includes intershell correlation effects between the $3s$ and $3p$ shells within the framework of the random phase approximation with exchange (RPAE). The connection between single-photon ionization and the two-color two-photon ionization process used in the measurement is established using the recently developed asymptotic approximation for the complex transition amplitudes of laser-assisted photoionization. We compare and discuss the theoretical and experimental results especially in the region where strong intershell correlations in the $3s \rightarrow kp$ channel lead to an induced "Cooper" minimum in the 3s ionization cross-section.

I. INTRODUCTION

Attosecond pulses created by harmonic generation in gases [1, 2] allow us to study fundamental light-matter interaction processes in the time domain. When an ultrashort light pulse impinges on an atom, a coherent ultrabroadband electron wave packet is created. If the frequency of the pulse is high enough, the electronic wave packet escapes by photoionization [3]. As in ultrafast optics, the *group delay* of an outgoing electron wave packet can be defined by the energy derivative of the phase of the complex photoionization matrix element. When photoionization can be reduced to one non-interacting angular channel (L), this phase is the same as the scattering phase η_L, which represents the difference between a free continuum wave and that propagating out of the effective atomic potential for the L-angular channel. In fact, the concept of time delay was already introduced by Wigner in 1955 to describe s-wave quantum scattering [4]. In collision physics, with both ingoing and outgoing waves the (Wigner) time delay is twice the derivative of the scattering phase.

In general, photoionization may involve several strongly interacting channels. Only in some special cases, the Wigner time delay can be conveniently used to characterize delay in photoemission. One such case might be valence shell photoionization of Ne in the 100 eV range [5, 6]. In this case, there is no considerable coupling between the $2s \rightarrow \epsilon p$ and $2p \rightarrow \epsilon s$ or ϵd channels and ϵd is strongly dominant over ϵs, following Fano's propensity rule [7]. The case of valence shell photoionization of Ar in the 40 eV range [8] is more interesting. In this case, the $3s$ photoionization is radically modified by strong intershell correlation with $3p$ [9]. As a result, the $3s$ photoionization cross-section goes through a deep "Cooper" minimum at approximately 42 eV photon energy [10]. Such a feature is a signature of inter-shell correlation and cannot be theoretically described using any independent electron, e.g. Hartree-Fock (HF) model.

Recent experiments [5, 8] reported the first measurements of delays between photoemission from different subshells from rare gas atoms, thus raising considerable interest from the scientific community. Different methods for the measurements of time delays were proposed, depending on whether single attosecond pulses or attosecond pulse trains were used. The streaking technique consists in recording electron spectra following ionization of an atom by a single attosecond pulse in the presence of a relatively intense infrared (IR) pulse, as a function of the delay between the two pulses [11, 12]. Temporal information is obtained by comparing streaking traces from different subshells in an atom [5] or from the conduction and valence bands in a solid [14]. On the other hand, the so-called RABBIT (Reconstruction of attosecond bursts by interference of two-photon transitions) method consists in recording photoelectron above-threshold-ionization (ATI) spectra following ionization of an atom by a train of attosecond pulses and a weak IR pulse, at different delays between the two fields [15]. Temporal information on photoionization is obtained by comparing RABBIT traces from different subshells in an atom [8]. The name of the technique, which we will use throughout, refers to its original use for the measurement of the group delay of attosecond pulses in a train [16].

Both methods involve absorption or stimulated emission of one or several IR photons, and it is important to understand the role of these additional transitions for a correct interpretation of the measured photoemission delays. A temporal delay difference of 21 as was measured for the photoionization from the $2s$ and $2p$ shells in neon using single attosecond pulses of 100 eV central energy [5]. Interestingly, the electron issued from $2p$ shell was found to be delayed compared to the more bound $2s$ electron. Similarly, delay differences on the order of ~ 100 as were measured for the photoionization from the $3s$ and $3p$ shells in argon using attosecond pulse trains with central energy around 35 eV. Again, the $3p$ electron appears to be delayed relative to the $3s$-electron, with a difference which depends on the excitation energy [8].

These experimental results stimulated several theoretical investigations, ranging from advanced photoionization calculations, including correlations effects [6], time-dependent numerical approaches [5, 17–19] to semi- analytical developments aiming at understanding the effect

of the IR field on the measured time delays [20–22]. The picture which is emerging from this productive theoretical activity is that when the influence of the IR laser field is correctly accounted for, such time delay measurements may provide very interesting information on temporal aspects of many-electron dynamics.

The present work reports theoretical and experimental investigation of photoionization in the 3*s* and 3*p* shells in argon in the 32-42 eV photon energy range. Besides providing a more extensive description of the experimental and theoretical methods in [8], we improve the results in three different ways:

- We performed more precise measurements using a *stabilized* Mach- Zehnder interferometer [23] for the RABBIT method. The stabilization allows us to take scans during a longer time and thus to extract the phase more precisely. Some differences with the previous measurements are found and discussed.
- For the comparison with theory, we determined the phases of the single-photon ionization amplitudes using the Random Phase Approximation with Exchange (RPAE) method, which includes intershell correlation effects [9, 24, 25]. This represents a clear improvement to the calculations presented in [8], using Hartree-Fock data [26], especially in the region above 40 eV where photoionization of Ar passes through an interference minimum, owing to 3s-3p intershell correlation effects.
- Finally, we improved our calculation of the phase of a two-photon ionization process, thus making a better connection between the experimental measurements and the single photoionization calculated phases [21].

The paper is organized as follows. Section II presents the experimental setup and results. Section III describes the phase of one- and two-photon ionization processes using perturbation theory in an independent-electron approximation. Section IV includes inter-shell correlation using the RPAE method. A comparison between theory and experiment is presented in Section V.

II. EXPERIMENTAL METHOD AND RESULTS

The experiments were performed with a Titanium:Sapphire femtosecond laser system delivering pulses of 30 fs (FWHM) duration, centered at 800 nm, with 1 kHz repetition rate, and a pulse energy of ~ 3 mJ. A beam splitter divides the laser output into the probe and the pump arm of a Mach-Zehnder interferometer (see Fig. 1). The energy of the probe pulses can be adjusted by a $\lambda/2$-plate followed by an ultra-thin polarizer. The pump arm is focused by a f = 50 cm focusing mirror into a pulsed argon gas cell, synchronized with the laser repetition rate, in order to generate an attosecond pulse train via high-order harmonic generation. An aluminum filter of 200 nm thickness blocks the fundamental radiation and subsequently a chromium filter of the same thickness selects photon energies of about 10 eV bandwidth in the range of harmonics 21 to 27.

The probe and the pump arm of the interferometer are recombined on a curved holey mirror, transmitting

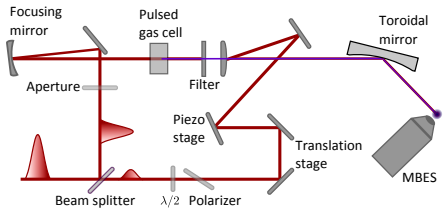

FIG. 1: (color online) Schematic illustration of our experimental setup.

the pump attosecond pulse train, but reflecting the outer portion of the IR probe beam. The exact position of the recombination mirror with respect to the focal position of the pump arm is essential in order to precisely match the wavefronts of the probe and XUV (extreme ultraviolet) beams. A toroidal mirror (f = 30 cm) focuses both beams into the sensitive region of a magnetic bottle electron spectrometer (MBES), where a diffusive gas jet provides argon as detection gas. The relative timing between the ultrashort IR probe pulses and the attosecond pulse train can be reproducibly adjusted on a sub-cycle time scale due to an active stabilization of the pump-probe interferometer length [23].

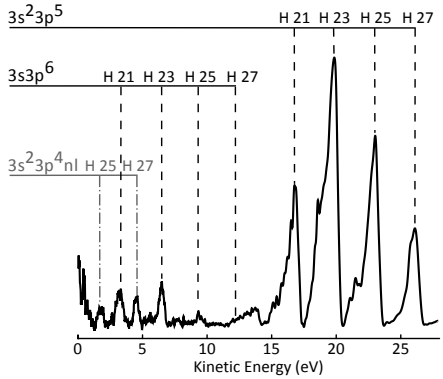

FIG. 2: Electron spectrum obtained by ionizing Ar with four harmonics of orders 21, 23, 25 and 27. The ionization channels are shown on the top.

Figure 2 presents an electron spectrum obtained by ionizing Ar atoms with harmonics selected by both Al and Cr filters, with orders ranging from 21 to 27. We can clearly identify three ionization channels towards the $3s^2p^5$, $3s^1p^6$, and $3s^23p^4n\ell$ ($n\ell = 4p$ or $3d$) continua [27]. The corresponding ionization energies are 15.76, 29.2 and ~ 37.2 eV. Note that the settings of the MBES were here chosen to optimize the spectral resolution at low energy. The large asymmetric profile obtained at high electron energy can be reduced by optimizing the MBES settings differently. The spectrum due to 3*p*-ionization is strongly affected by the behavior of the ionization cross-section in this region. The relative intensities of the 21$^{\text{st}}$ to the 27$^{\text{th}}$ harmonics are approximately 0.2:0.7:1:1.

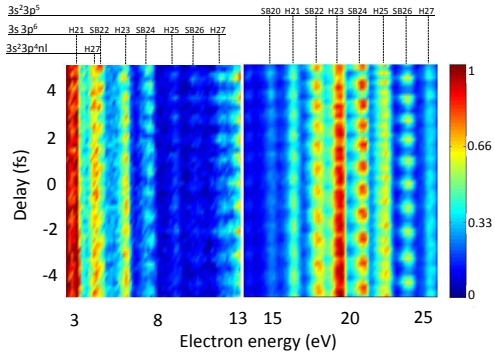

FIG. 3: (color online) Electron spectrum as a function of time delay between the attosecond pulses and the IR laser. The signal strength is indicated by colors. The spectrum on the right ($3p$) follows that on the left ($3s$) with a factor of 6 reduction in the color code, and a slight overlap in energy.

Figure 3 shows a typical RABBIT spectrogram, i.e. electron spectra as a function of delay between pump and probe pulses. The electron yield is indicated as colors. Compared to the spectra obtained with the harmonics only, Fig. 3 includes electron peaks at sideband frequencies, including additional absorption or emission of one IR photon (see Fig. 4). The intensity of these sidebands oscillates with a delay at a frequency equal to 2ω, ω being the IR laser photon energy, according to

$$S_{2q}(\tau) = \alpha + \beta\cos(2\omega\tau - \Delta\phi_{2q} - \Delta\theta_{2q}), \qquad (1)$$

where α and β are constant quantities, independent of the delay and $2q$ represents the total number of IR photons involved, i.e. an odd number to create harmonic $2q-1$ or $2q-1$ plus or minus one IR photon. $\Delta\phi_{2q}$ denotes the phase difference between two harmonics with order $2q+1$ and $2q-1$, while $\Delta\theta_{2q}$ arises from the difference in phase between the amplitudes of the two interfering quantum paths leading the same final state [Fig. 4 (a)]. At high IR intensity, other quantum paths involving more than one IR photon become possible and may change the retrieved RABBIT phase [13]. We kept the IR laser intensity low enough to avoid such higher-order effects, which can be identified through oscillations at higher frequencies. $\tau_A = \Delta\phi_{2q}/2\omega$ can be interpreted as the group delay of the attosecond pulses [16]. We define in a similar way $\tau^{(2)} = \Delta\theta_{2q}/2\omega$ arising from the two-photon ionization process. Since the same harmonic comb is used for ionization in the $3s$ and $3p$ shells, the influence of the attosecond group delay can be subtracted and the delay difference $\tau^{(2)}(3s) - \tau^{(2)}(3p)$ can be deduced. The results of these measurements are indicated in Table 1 for sidebands 22, 24 and 26. We also indicate in the same table, previous results from [8]. It is quite difficult in such an experiment to estimate the uncertainty of our measurement. The stability of the interferometer is measured to be ~ 50 as. The relative uncertainty in comparing the phase offsets of different sideband oscillations is estimated to be of the same magnitude or even slightly better.

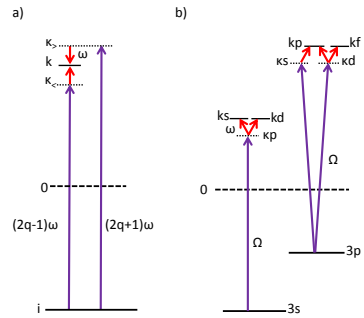

FIG. 4: (color online) Energy level scheme of the processes discussed in the present work; (a) RABBIT principle; (b) Different channels in 2-photon ionization from the $3s$ and $3p$ subshells.

TABLE I: Time delay measurements

Sideband	22	24	26
Photon energy (eV)	34.1	37.2	40.3
$\tau^{(2)}(3s) - \tau^{(2)}(3p)$ this work (as)	-80	-100	10
$\tau^{(2)}(3s) - \tau^{(2)}(3p)$, [8] (as)	-40 (-90)	-110	-80
$\tau_{cc}(3s) - \tau_{cc}(3p)$ (as)	-150	-70	-40
$\tau^{(1)}(3s) - \tau^{(1)}(3p)$(as)	70	-30	50

Our measurements agree well with those of [8] for sideband 24. For sideband 22, the measurements performed in [8] could not resolve the sideband peak from electrons ionized by harmonic 27 towards the continuum $3s^23p^4n\ell$ (see Fig. 3). A new analysis done by considering only the high energy part of the sideband peak leads to the number indicated in parenthesis in the table, which is in good agreement with the present measurement. There is, however, a difference for the delay measured at sideband 26. We will comment on this difference in Section V.

III. THEORY OF ONE AND TWO-PHOTON IONIZATION

To interpret the results presented above, we relate the one-photon ionization delays to the delays measured in the experiment. Using lowest-order perturbation theory, the transition matrix elements in one and two-photon ionization are

$$M^{(1)}(\vec{k}) = -iE_\Omega\langle\vec{k}|z|i\rangle, \qquad (2)$$

$$M^{(2)}(\vec{k}) = -iE_\omega E_\Omega \lim_{\varepsilon\to 0^+}\sum_\nu \frac{\langle\vec{k}|z|\nu\rangle\langle\nu|z|i\rangle}{\epsilon_i + \Omega - \epsilon_\nu + i\varepsilon}. \qquad (3)$$

Atomic units are used throughout. We choose the quantization axis (z) to be the (common) polarization vector of the two fields. The complex amplitudes of the laser and harmonic fields are denoted by E_ω and E_Ω, with photon energies ω and Ω, respectively. The initial state is denoted $|i\rangle$ and the final state $|\vec{k}\rangle$. The energies of the initial and intermediate states are denoted ϵ_i and ϵ_ν,

respectively. The sum in $M^{(2)}$ is performed over all possible intermediate states $|\nu\rangle$ in the discrete and continuum spectrum. The infinitesimal quantity ε is added to ensure the correct boundary condition for the ionization process, so that the matrix element involves an outgoing photoelectron. The magnitude of the final momentum is restricted by energy conservation to $\epsilon = k^2/2 = \Omega + \epsilon_i$ for one photon and $\epsilon = k^2/2 = \Omega + \omega + \epsilon_i$ for two-photon absorption. The two-photon transition matrix element involving emission of a laser photon can be written in the same way, with ω replaced by $-\omega$ in the energy conservation relation and E_ω replaced by its conjugate.

The next step consists in separating the angular and radial parts of the wavefunctions. The different angular channels involved are indicated in Fig. 4(b). We split the radial and angular dependence in the initial state as $\langle \boldsymbol{r}|i\rangle = Y_{l_i m_i}(\hat{r}) R_{n_i l_i}(r)$ and use the partial wave expansion in the final state

$$\langle \boldsymbol{r}|\vec{k}\rangle = (8\pi)^{\frac{3}{2}} \sum_{L,M} i^L e^{-i\eta_L(k)} Y^*_{LM}(\hat{k}) Y_{LM}(\hat{r}) R_{kL}(r). \quad (4)$$

We perform the spherical integration in Eq. (1) and obtain

$$M^{(1)}(\vec{k}) \propto \sum_{\substack{L=l_i\pm 1 \\ M=m_i}} e^{i\eta_L(k)} i^{-L} Y_{LM}(\hat{k}) \begin{pmatrix} L & 1 & l_i \\ -M & 0 & m_i \end{pmatrix} T^{(1)}_L(k), \quad (5)$$

where the reduced dipole matrix element is defined as

$$T^{(1)}_L(k) = \hat{L}\hat{l}_i \begin{pmatrix} L & 1 & l_i \\ 0 & 0 & 0 \end{pmatrix} \langle R_{kL}|r|R_{n_i l_i}\rangle \quad (6)$$

using $3j$-symbols and with the notation $\hat{l} = \sqrt{2l+1}$. The reduced matrix element (6) is real. When the dipole transition with the increased momentum $L = l_i + 1$ is dominant, which is often the case [7], the phase of the complex dipole matrix element $M^{(1)}$ is simply equal to

$$\arg[M^{(1)}(k)] = \eta_L(k) - L\pi/2. \quad (7)$$

(There is also a contribution from the fundamental field which we do not write here, as well as trivial phases, e.g from the spherical harmonic when $M \neq 0$ [21]). Similarly, for two-photon ionization,

$$M^{(2)}(\vec{k}) \propto \sum_{\substack{L=\lambda\pm 1, \lambda=l_i\pm 1 \\ M=\mu=m_i}} e^{i\eta_L(k)} i^{-L} Y_{LM}(\hat{k}) \quad (8)$$
$$\begin{pmatrix} L & 1 & \lambda \\ -M & 0 & \mu \end{pmatrix} \begin{pmatrix} \lambda & 1 & l_i \\ -\mu & 0 & m_i \end{pmatrix} T^{(2)}_{L\lambda}(k).$$

where

$$T^{(2)}_{L\lambda}(k) = \hat{L}\hat{\lambda}^2\hat{l}_i \begin{pmatrix} L & 1 & \lambda \\ 0 & 0 & 0 \end{pmatrix} \begin{pmatrix} \lambda & 1 & l_i \\ 0 & 0 & 0 \end{pmatrix} \langle R_{kL}|r|\rho_{\kappa\lambda}\rangle. \quad (9)$$

Here, we have introduced the radial component of the perturbed wave function,

$$|\rho_{\kappa\lambda}\rangle = \lim_{\varepsilon\to 0^+} \sum_\nu \frac{|R_{\nu\lambda}\rangle\langle R_{\nu\lambda}|r|R_{n_i l_i}\rangle}{\epsilon_i + \Omega - \epsilon_\nu + i\varepsilon}, \quad (10)$$

where the sum is performed over the discrete and continuum spectrum. κ denotes the momentum corresponding to absorption of one harmonic photon such that the energy denominator goes to zero ($\kappa^2/2 = \epsilon_i + \Omega$). The summation can be decomposed into three terms, the discrete sum over states with negative energy, a Cauchy principal part integral where the pole has been removed (both these terms are real) and a resonant term which is purely imaginary. The important conclusion is that in contrast to the radial one-photon matrix element, the radial two-photon matrix element is a complex quantity.

To evaluate the phase of this quantity, as explained in more details in [21], we approximate $R_{kL}(r)$ and $\rho_{\kappa\lambda}(r)$ by their asymptotic values. We have, for example,

$$\rho_{\kappa\lambda}(r) \approx -\sqrt{\frac{2}{\pi\kappa}} \langle R_{\kappa\lambda}|r|R_{n_i l_i}\rangle \frac{1}{r} \exp\left\{ i\left[\kappa r + \frac{\ln(2\kappa r)}{\kappa} + \eta_\lambda(\kappa) - \frac{\pi\lambda}{2} \right] \right\} \quad (11)$$

This allows us to evaluate analytically the integral $\langle R_{kL}|r|\rho_{\kappa\lambda}\rangle$ in Eq. (9). We obtain

$$\arg\left[T^{(2)}_{L\lambda}(k)\right] \approx (L-\lambda)\frac{\pi}{2} + \eta_\lambda(\kappa) - \eta_L(k) + \phi_{cc}(k,\kappa), \quad (12)$$

where $\phi_{cc}(k,\kappa)$ is the phase associated to a continuum-continuum radiative transition resulting from the absorption of IR photons in the presence of the Coulomb potential. It is independent from the characteristics of the initial atomic state, in particular its angular momentum. An important consequence is that, when inserting the asymptotic form Eq. (11) in Eq. (8), the scattering phase η_L is canceled out, so that *the total phase will not depend on the angular momentum of the final state*. In the case of a dominant intermediate channel λ, the phase of the complex two-photon matrix element $M^{(2)}(k)$ is equal to

$$\arg[M^{(2)}(k)] = \eta_\lambda(\kappa) - \lambda\pi/2 + \phi_{cc}(k,\kappa). \quad (13)$$

It is equal to the one-photon ionization phase towards the intermediate state with momentum κ and angular momentum λ plus the additional "continuum-continuum" phase. The difference of phase which is measured in the experiment is therefore given by

$$\Delta\theta_{2q} = \eta_\lambda(\kappa_>) - \eta_\lambda(\kappa_<) + \phi_{cc}(k,\kappa_>) - \phi_{cc}(k,\kappa_< \quad (14)$$

where $\kappa_>$, $\kappa_<$ are the momenta corresponding to the highest (lowest) continuum state in Fig. 4(a). Dividing this formula by 2ω, we have

$$\tau^{(2)}(k) = \tau^{(1)}(k) + \tau_{cc}(k), \quad (15)$$

where

$$\tau^{(1)}(k) = \frac{\eta_\lambda(\kappa_>) - \eta_\lambda(\kappa_<)}{2\omega}, \quad (16)$$

is a finite difference approximation to the Wigner time delay $d\eta_\lambda/d\epsilon$ and thus reflects the properties of the electronic wave packet ionized by one-photon absorption into the angular channel λ. $\tau^{(2)}$ also includes a contribution from the IR field which is independent of the angular momentum,

$$\tau_{cc}(k) = \frac{\phi_{cc}(k,\kappa_>) - \phi_{cc}(k,\kappa_<)}{2\omega}. \quad (17)$$

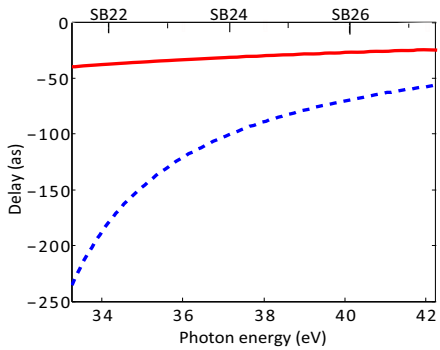

FIG. 5: (color online) Continuum-continuum delay τ_{cc} as a function of excitation photon energy for the two subshells $3s$ (red solid line) and $3p$ (blue dashed line) for an IR photon energy of 1.55 eV (800 nm wavelength).

We refer the reader to [21] for details about how to calculate τ_{cc}. Fig. 5 shows τ_{cc} as a function of photon energy, for the two subshells $3s$ and $3p$ and for the IR photon energy $\omega = 1.55$ eV used in the experiment. The corresponding difference in delays for the $3s$ and $3p$ subshells is only due to the difference in ionization in energy between the two shells (13.5 eV). We also indicate in Table I the measurement-induced delays for the three considered sidebands.

The processes discussed in this section can be represented graphically by Feynman-Goldstone diagrams displayed Fig. 6(a,b). The straight lines with arrows represent electron (arrow pointing up) or hole (arrow pointing down) states, respectively. The violet and red wavy lines represent interaction with the XUV and IR fields. We are neglecting here two-photon processes where the IR photon is absorbed first [21].

IV. INTERSHELL CORRELATION EFFECTS

To include inter-shell correlation effects, we use the random phase approximation with exchange (RPAE) [9]. In this approximation, the dipole matrix element of single photoionization is replaced by a "screened" matrix element $\langle k|Z|i\rangle$, which accounts for correlation effects between the $3s$ and $3p$ subshells. These screened matrix elements, represented graphically in Fig. 6(c), are defined by the self-consistent equation:

$$\langle \vec{k}|Z|i\rangle = \langle \vec{k}|z|i\rangle + \lim_{\varepsilon\to 0^+} \sum_{j\nu} \left[\frac{\langle \nu|Z|j\rangle\langle j\vec{k}|V|\nu i\rangle}{\Omega - \epsilon_\nu + \epsilon_j + i\varepsilon} - \frac{\langle j|Z|\nu\rangle\langle \nu\vec{k}|V|ji\rangle}{\Omega + \epsilon_\nu - \epsilon_j} \right], \quad (18)$$

where i and j are $3s$ or $3p$ or vice versa and $V = 1/r_{12}$ is the Coulomb interaction. The sum is performed over the discrete as well as continuum spectrum. The Coulomb interaction matrices $\langle j\vec{k}|V|\nu i\rangle$ and $\langle \nu\vec{k}|V|ij\rangle$, represented

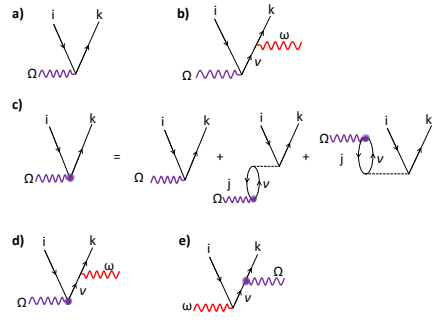

FIG. 6: (color online) Feynman-Goldstone diagrams representing one-photon (a) and two-photon (b) ionization processes. (c) Diagrammatic representation of the RPAE equations. The second and third diagrams on the right hand side refer to time-forward and time-reversed respectively. (d) Two-photon ionization including intershell correlation effects. (e) Two-photon ionization with the XUV photon absorbed after the IR photon.

by dashed lines in Fig. 6(c), describe the so-called time-forward and time-reversed correlation processes (Note that the time goes upwards in the diagrams). If we replace Z by z in the right term in Eq. (18), we obtain a perturbative expansion to the first order in the Coulomb interaction. More generally, the use of the self-consistent screened matrix elements [Eq.(18)] implies infinite partial sums over two important classes of so-called "bubble" diagrams. Each bubble consists of an electron-hole pair νj, which interacts via $1/r_{12}$ with final electron-hole pair $\vec{k}i$. The energy integration in the time-forward term of Eq. (18) (first line) contains a pole and the screened matrix element acquires an imaginary part and therefore an extra phase. For a single dominant channel L, the phase of the one-photon matrix element [see Eq.(7)] becomes:

$$\arg[M^{(1)}(k)] = \eta_L(k) + \delta_L(k) - L\pi/2, \quad (19)$$

where $\delta_L(k) = \delta_{i\to kL}$ denotes the additional phase due to the correlations accounted within the RPAE. The photoemission time delay is then determined by the sum of two terms:

$$\tau^{(1)} = \frac{d\eta_L}{d\epsilon} + \frac{d\delta_L}{d\epsilon}. \quad (20)$$

The first term represents the time delay in the independent electron approximation, equal to the derivative of the photoelectron scattering phase in the combined field of the nucleus and the remaining atomic electrons. The second term is the RPAE correction due to inter-shell correlation effects.

We solve the system of integral equations (18) numerically using the computer code developed by Amusia and collaborators [28]. The basis of occupied atomic states (holes) $3s$ and $3p$ is defined by the self-consistent HF method [29]. The excited electron states are calculated within the frozen-core HF approximation [30]. We present some results for one-photon ionization in Fig. 7.

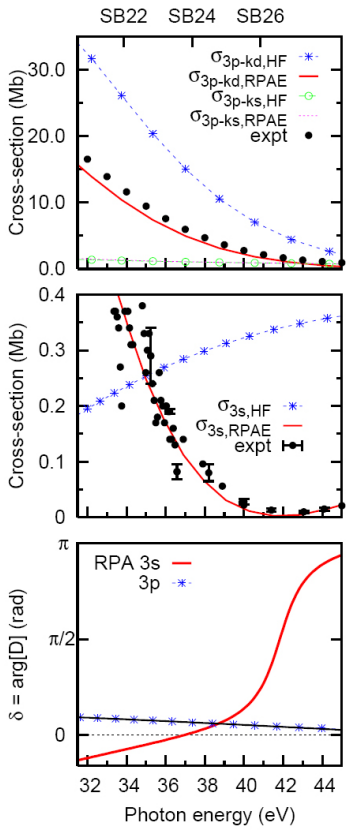

FIG. 7: (color online) Top panel: The photoionization cross-sections $\sigma_{3p\to kd}$ calculated in the HF (blue dotted line) and RPAE (red solid line) approximations, are compared with the $\sigma_{3p\to ks}$ cross-sections (HF, green open circles, RPAE, purple dashed line). The experimental data for the σ_{3p} cross-section are from Ref. [31]. Middle panel: Photoionization cross-sections σ_{3s} calculated in the HF (blue dotted line) and RPAE(red solid line) approximations, are compared with experimental data [10]. Bottom panel: Correlation-induced phase shifts for the $3s$ and $3p$ dipole matrix elements.

On the top panel, we show the partial photoionization cross-sections from the $3p$-state calculated using the HF and RPAE approximations (see figure caption). From this plot, we see that the $3p \to kd$ transition is clearly dominant at low photon energies. Intershell correlation effects are more important for the $3p \to ks$ than for the $3p \to kd$ transition. The sum of the two partial cross sections calculated with the RPAE correction (red and green lines) is very close to the the experimental data (solid circles) [31]. The middle panel presents the calculated cross-section for $3s$-ionization and compares it to the experimental data from [10]. The RPAE correction is here essential to reproduce the behavior of the cross-section which, in this spectral region, is a rapid decreasing function of photon energy.

The bottom panel shows the correlation-induced phase shifts $\delta_{3s\to kp}$ and $\delta_{3p\to kd}$ from the same RPAE calculation. We observe that the RPAE phase correction $\delta_{3p\to kd}$ is relatively weak. In contrast, $\delta_{3s\to kp}$ varies significantly with energy, especially near the "Cooper" minimum. This qualitative difference can be explained by a different nature of the correlations in the $3p$ and $3s$ shells. In the $3p$ case, the correlation takes place mainly between the electrons that belong to the same shell with not much influence of the inter-shell correlation with $3s$. We confirmed this conclusion by performing a separate set of RPAE calculations with only the $3p$ shell included. These calculations lead to essentially the same results for $3p$ ionization as the complete calculations. In the case of intrashell correlation, the time-forward process [see Fig. 6(c)] is effectively accounted for by calculating the photoelectron wave function in the field of a singly charged ion. It is therefore excluded from Eq. (18) to avoid double count. The remaining time-reversed term [second line in Eq. (18)] does not contain any poles and therefore does not contribute to an additional phase to the corresponding dipole matrix element. The small phase $\delta_{3p\to kd}$ is due to intershell correlation which is indeed weak. In contrast, $3s$-ionization is strongly affected by correlation with the $3p$ shell. Consequently, the RPAE phase correction $\delta_{3s\to kp}$, which comes from the correlation with the $3p$ shell in the time-forward process, is large and exhibits a rapid variation with energy (a π phase change) in the region where the cross section decreases significantly.

Finally, we generalize our theoretical derivation of two-photon ionization to including the effect of inter-shell correlation on the XUV photon absorption. As shown graphically in the diagram in Fig. 6 (d), we replace the (real) transition matrix element corresponding to one-XUV photon absorption by a (complex) screened matrix element, with an additional phase term. As a consequence the phase of the two-photon matrix element becomes:

$$\arg[M^{(2)}(k)] = \eta_\lambda(\kappa) + \delta_\lambda(\kappa) - \lambda\pi/2 + \phi_{cc}(k,\kappa). \quad (21)$$

The time delay measured in the experiment is expressed as before as $\tau^{(2)}(k) = \tau^{(1)}(k) + \tau_{cc}(k)$, with $\tau^{(1)}(k)$ modified by intershell correlation:

$$\tau^{(1)}(k) = \frac{\eta_\lambda(\kappa_+) - \eta_\lambda(\kappa_-)}{2\omega} + \frac{\delta_\lambda(\kappa_+) - \delta_\lambda(\kappa_-)}{2\omega}. \quad (22)$$

Figure 8 presents calculated time delays $\tau^{(1)}$ for $3s \to kp$, $3p \to ks$ and $3p \to kd$ channels. The ionization delays from the $3p$ channel do not vary much with photon energy and remain small. The $3p \to ks$ delay is negligible while it takes about 70 as more time for the wave packet to escape towards the d channel, due to the angular momentum barrier. The wave packet emitted from the $3s$ channel takes considerably more time to escape, especially in the region above 40 eV, owing to strong intershell correlation leading to screening by the $3p$ electrons.

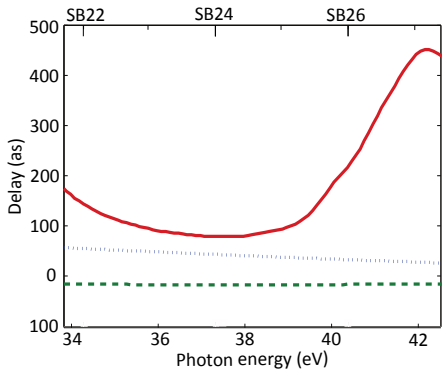

FIG. 8: (color online) Ionization delay for the three angular channels $3p \rightarrow kd$ (blue dashed), $3p \rightarrow ks$ (green dashed) and $3s \rightarrow kp$ (red solid line).

V. COMPARISON BETWEEN THEORY AND EXPERIMENT

We present in Fig. 9 a comparison between our experimental results (see Table 1) and our calculations. The dashed blue and solid red lines refer to the independent-electron HF and RPAE calculations, respectively. The circles refer to the results of [8], while the other symbols (with error bars both in central energy and delay) are the results obtained in the present work. Regarding the two sets of experimental results, they agree very well, except for that obtained at the highest energy corresponding to the sideband 26. Our interpretation is that we may be approaching the rapidly varying feature due to 3s 3p intershell correlation. Therefore a small change in the photon energy between the two measurements may lead to an important change in the delay. The experimental and RPAE results agree well for the first sideband but less for the two higher energy sidebands. Surprisingly and perhaps accidentally the HF calculation gives there a closer agreement with the experiment.

We now discuss possible reasons for the discrepancy. Our calculation of the influence of the dressing by the IR laser field is approximate. It only uses the asymptotic form of the continuum wave functions (both in the final and intermediate states), thereby neglecting the effect of the core. This approximation should be tested against theoretical calculations, and especially in a region where correlation effects are important. We also neglect the influence of the two-photon processes where the IR photon is absorbed (or emitted) first [32] [see Fig. 6 (e)]. The corresponding matrix elements are usually small, except possibly close to a minimum of the cross section, where the other process, usually dominant, is strongly reduced. Interestingly, in such a scenario, the IR radiation would not simply be a probe used for the measurement of the phase of a one-photon process, but would modify (control) the dynamics of the photoemission on an attosecond time scale. Finally, in our theoretical calculation, correlation effects are only accounted for in the single ionization process (XUV absorption). Additional correlation

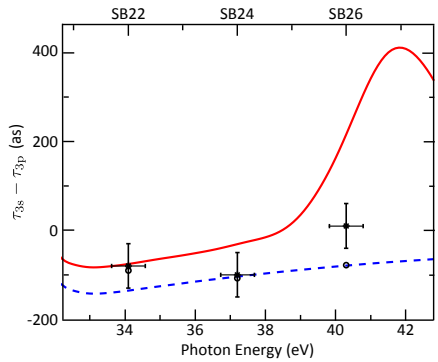

FIG. 9: (color online) Comparison between our theoretical calculations (dashed blue line, HF, red line, RPAE) and experiments (circles [8], crosses, present work)

effects surrounding the probing, *e.g.* after the IR photon is absorbed might play a role.

In conclusion, the results shown above point out to the need for explicit time-dependent calculations, which would account for many-electron correlation and include not only one-photon but also two-photon ionization. We also plan to repeat these experimental measurements using attosecond pulses with a large and tunable bandwidth. Our results demonstrate the potential of the experimental tools using single attosecond pulses [5] or attosecond pulse trains [8]. These tools now enable one to measure atomic and molecular transitions, more specifically, quantum phases and phase variation, i.e. group delays, which could not be measured previously.

Acknowledgements

We thank G. Wendin for useful comments. This research was supported by the Marie Curie program ATTOFEL (ITN), the European Research Council (ALMA), the Joint Research Programme ALADIN of Laserlab-Europe II, the Swedish Foundation for Strategic Research, the Swedish Research Council, the Knut and Alice Wallenberg Foundation, the French ANR-09-BLAN-0031-01 ATTO-WAVE program, COST Action CM0702 (CUSPFEL).

[1] P. B. Corkum and F. Krausz, Nat. Phys.**3**, 381 (2007).
[2] F. Krausz and M. Ivanov, Rev. Mod. Phys. **81**, 163 (2009).
[3] V. Schmidt, Rep. Prog. Phys. **55**, 1483 (1992).
[4] E. P. Wigner, Phys. Rev. **98**, 145 (1955).
[5] M. Schultze *et al.*, Science **328**, 1658 (2010).

[6] A.S. Kheifets and I.A. Ivanov, Phys. Rev. Lett. **105**, 233002 (2010).
[7] U. Fano, Phys. Rev. A **32**, 617 (1985).
[8] K.Klünder *et al.*, Phys. Rev. Lett. **106**, 143002 (2011).
[9] M. Y. Amusia *et al.*, Phys. Lett. A **40**, 361 (1972).
[10] B. Möbus *et al.*, Phys. Rev. A **47**, 3888 (1993).
[11] E. Goulielmakis *et al.*, Science **305**, 1267 (2004).
[12] G. Sansone *et al.*, Science **314**, 443 (2006).
[13] Swoboda *et al.*, Laser Physics **19**, 1591 (2009))
[14] Cavalieri, A. *et al.*, Nature **449**, 1029 (2007).
[15] P. M. Paul *et al.*, Science **292**, 1689 (2001).
[16] Y. Mairesse *et al.*, Science **302**, 1540 (2003).
[17] V.S. Yakovlev, J. Gagnon, N. Karpowicz and F. Krausz, Phys. Rev. Lett. **105**, 073001 (2010).
[18] S. Nagele, R. Pazourek, J. Feist and J. Burgdorfer, J. Phys. B: Atom. Molec. Opt. Phys. **44**, 081001 (2011); Phys. Rev. A **85**, 033401 (2012).
[19] L. R. Moore, M. A. Lysaght,J. S. Parker, H. W. vander-Hart and K. T. Taylor, Phys. Rev. A **84**, 061404 (2011).
[20] C.-H. Zhang and U. Thumm, Phys. Rev. A **84**, 033401 (2011).
[21] J. M. Dahlstrom *et al.*, Chem. Phys., in press (2012). http://dx.doi.org/10.1016/j.chemphys.2012.01.017
[22] M. Ivanov and O. Smirnova, Phys. Rev. Lett. **107**, 213605 (2011).
[23] D. Kroon *et al.*, in preparation.
[24] G. Wendin, J. Phys. B: Atom. Molec. Opt. Phys. **5**, 110 (1972).
[25] A. L'Huillier, L. Jönsson and G. Wendin, Phys. Rev. A **33**, 3938 (1986).
[26] D.J. Kennedy and S.T. Manson, Phys. Rev. A **5**, 227 (1972).
[27] A.Kikas *et al.*, J. Electron Spectrosc. Rel. Phenom. **77** 241, (1996).
[28] M. Ia. Amusia and L. V. Chernysheva, *Computation of atomic processes : A handbook for the ATOM programs.* Institute of Physics Pub., Bristol, UK, 1997.
[29] L. V. Chernysheva, N. A. Cherepkov, and V. Radojevic, Comp. Phys. Comm. **11**, 57 (1976).
[30] L. V. Chernysheva, N. A. Cherepkov, and V. Radojevic, Comp. Phys. Comm. **18**, 87 (1979).
[31] J.A.R. Samson and W.C. Stolte, J. Electron Spectrosc. Rel. Phenom. **123**, 265 (2002).
[32] V. Véniard, R. Taïeb, and A. Maquet, Phys. Rev. A **54**, 721 (1996).

Paper IV

Theory of Attosecond Delays in Laser-Assisted Photoionization

J. M. Dahlström, D. Guénot, K. Klünder, M. Gisselbrecht, J. Mauritsson, A. L'Huillier, A. Maquet and R. Taïeb.

(2012) *Accepted for publication in Chem. Phys.*.

Theory of attosecond delays in laser-assisted photoionization

J. M. Dahlström[a,b], D. Guénot[a], K. Klünder[a], M. Gisselbrecht[a], J. Mauritsson[a], A. L'Huillier[a], A. Maquet[c,d], R. Taïeb[c,d]

[a] *Department of Physics, Lund University, P.O. Box 118, 22100 Lund, Sweden*
[b] *Atomic Physics, Fysikum, Stockholm University, AlbaNova University Center, SE-106 91 Stockholm, Sweden*
[c] *UPMC Université Paris 6, UMR 7614, Laboratoire de Chimie Physique-Matière et Rayonnement, 11 rue Pierre et Marie Curie, 75231 Paris Cedex 05, France*
[d] *CNRS, UMR 7614, LCPMR, Paris, France*

Abstract

We study the temporal aspects of laser-assisted extreme ultraviolet (XUV) photoionization using attosecond pulses of harmonic radiation. The aim of this paper is to establish the general form of the *phase* of the relevant transition amplitudes and to make the connection with the time-delays that have been recently measured in experiments. We find that the overall phase contains two distinct types of contributions: one is expressed in terms of the phase-shifts of the photoelectron continuum wavefunction while the other is linked to continuum–continuum transitions induced by the infrared (IR) laser probe. Our formalism applies to both kinds of measurements reported so far, namely the ones using attosecond pulse trains of XUV harmonics and the others based on the use of isolated attosecond pulses (streaking). The connection between the phases and the time-delays is established with the help of finite difference approximations to the energy derivatives of the phases. The observed time-delay is a sum of two components: a one-photon Wigner-like delay and an *universal* delay that originates from the probing process itself.

1. Introduction

The dynamics of photoionization can now be explored with unprecedented time resolution thanks to high-order harmonic-based sources that deliver pulses of XUV radiation with duration in the attosecond range. Recent measurements performed with single attosecond pulses have shown the existence of an unexpected time-delay between the single-photon ionization from the 2s and the 2p subshells of Ne atoms in gas phase [1]. The "streak camera" technique used in these experiments [2] implied nontrivial ejection times of the photoelectrons, depending on the sub-shell from which they originate. Similar delays between the ejection times from the 3s and 3p sub-shells in Ar have been measured also using trains of attosecond pulses [3], with the help of another technique based on interferometry called RABBIT (Reconstruction of Attosecond Beating By Interference of Two-photon transitions) [4–6]. In both cases, delays of several tens of attoseconds have been measured. As photoionization is one of the most fundamental processes in light-matter interactions, these results have motivated a large number of theoretical investigations [7–13].

The two kinds of measurements share many similarities since they involve a laser-assisted single-photon ionization process and they rely on a phase-locked IR laser field to probe the temporal aspects of the XUV photoionization. However, they differ in the analysis used to determine the time-delays and in the range of IR laser intensity.

The motivation of the present paper is to present an unified theoretical analysis of these processes. To achieve this goal, we shall expose first the theoretical background which has conducted us to conclude in [3], that in interferometric measurements, the measured delays arise from the combination of two distinct contributions: One is related to the electronic structure of the atomic target while the other is induced by the measurement process itself. The first one can be identified as a "Wigner time-delay" [14, 15] that is directly related to the energy dependence of the different phase-shifts experienced by the photoelectrons ionized from distinct sub-shells in atoms. The other contribution is induced by the IR laser field that is used to probe the photoionization process. This latter contribution results from the continuum–continuum transitions induced by the probe IR laser field in the presence of the Coulomb potential of the ionic core. When simplifying the analysis to the cases when the process is dominated by the asymptotic form of the relevant second-order matrix elements, a characteristic measurement-induced delay can be identified, that is independent from the details of the electronic structure of the ionic core. This shows how the experimental signal can be related to the temporal dynamics of one-photon ionization.

Regarding the streaking measurements realized with a single attosecond pulse of XUV radiation [1], the experi-

Email addresses: marcus.dahlstrom@fysik.su.se (J. M. Dahlström), anne.lhuillier@fysik.lth.se (A. L'Huillier), richard.taieb@upmc.fr (R. Taïeb)

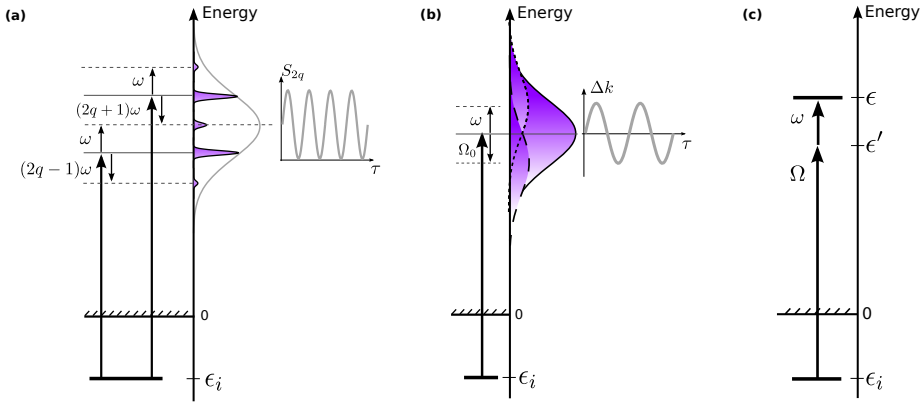

Figure 1: (a) Laser-assisted photoionization by an attosecond pulse train, corresponding to odd XUV harmonics, H_{2q-1}, where q is a positive integer. The sideband S_{2q} can be reached by either absorbing H_{2q-1} and then absorbing a IR laser photon ω or by absorbing H_{2q+1} and then emitting ω. The sideband signal, S_{2q}, oscillates as a function of the subcycle-delay, τ, between the attosecond pulses and the IR laser probe field. (b) Laser-assisted photoionization by a single attosecond pulse, corresponding to a broad XUV continuum. To first order, the electron is ionized by absorbing one XUV photon, Ω, resulting in a wave packet centered at $\epsilon = \epsilon_i + \Omega_0$. To second order, the electron may absorb an additional laser photon ω resulting in an upshifted wave packet centered at $\epsilon = \epsilon_i + \Omega_0 + \omega$; or it may emit a laser photon resulting in a downshifted wave packet centered at $\epsilon = \epsilon_i + \Omega_0 - \omega$. The interference of these three wave packets leads to a modulation, Δk, of central momentum of the photoelectron as function of the subcycle-delay, τ, between the laser field and the attosecond pulse. (c) Two-photon XUV-IR Above-Threshold Ionization from an initial bound state with energy ϵ_i, to a final state with energy ϵ.

mental data were obtained for IR field intensities significantly higher than those obtained with attosecond pulse trains [3]. Understandably, the questions related to the role of the probe IR field on the photoelectron dynamics in streaking measurements have motivated several theoretical studies [7–13]; see also the earlier papers: [16–19]. Then, a natural issue arises which is to determine to what extent the "streaking delays" so obtained differ from those derived from the interferometric data. Although both the experimental techniques and the theory treatments differ, it is of interest to compare the two approaches. Indeed, as we shall show below, a link can be found when reducing the laser intensity of the streaking field so that one reaches the domain of applicability of the recently developed Phase-Retrieval by Omega Oscillation Filtering (PROOF) scheme, [20]. An interesting outcome of our analysis is to show the importance of the long-range Coulomb potential for understanding the absolute time-delays in the streaking experiments as well.

The interpretation of the attosecond delays in photoionization relies on our ability to determine the *phases* of the relevant transition amplitudes. Thus, before going into the details of the derivation of such phases, we shall outline the main features of the two techniques in Section 2. Then, Section 3 is devoted to the presentation of the general expressions for two-color, two-photon, complex transition amplitudes that are relevant for Above-Threshold Ionization (ATI) in single-active electron systems. The theoretical background is based on a perturbative approach and the emphasis will be on the derivation of a closed-form approximate expression that is of interest for evaluating the phase of the amplitudes. The basis of exact computations in hydrogen will be outlined, and a simplified classical treatment will be presented. Applications to the determination of the relation between the phases and the time-delays is presented in Section 4. Here we consider first ionization by an attosecond pulse train and then by a single attosecond pulse, in the presence of a relatively weak IR field. This discussion provides an interesting connection between the two types of measurements. Section 5 contains a comparison of the results extracted from the approximate evaluation of the delays to the ones deduced from exact calculations performed in hydrogen from different initial states. Also, we present our conclusions and perspectives.

2. Laser-Assisted XUV Photoionization: Attosecond Pulse Train vs. Single Attosecond Pulse

The principle of the measurements of the delays using an attosecond pulse train is illustrated in Fig. 1 (a), which represents schematically the ionization of an atom in the simultaneous presence of a set of several XUV (odd) harmonics and of the IR field, used to generate the harmonics (atomic units will be used throughout the paper, unless otherwise stated). In the time domain, both pulses are "long", *i.e.* the IR laser pulse is multi-cycle, with typical duration of a few tens of femtoseconds, and the XUV harmonic field is constituted of a train of attosecond pulses

(or equivalently of a comb of coherent odd harmonic frequencies $(2q+1)\omega$: H_{2q+1}). Under these conditions, the photoelectron spectrum consists of equidistant lines separated by 2ω that are associated to one-photon ionization of the target by each harmonic. In-between these lines are sidebands associated to two-photon transitions involving the absorption of one harmonic and the exchange of one IR photon. The signal intensities, S_{2q}, of the sidebands labelled $2q$ vary periodically with the delay τ between the IR and the harmonic pulses, according to a generic expression that involves the phases of the fields together with atom-dependent contributions:

$$S_{2q} = \alpha + \beta \cos[2\omega\tau - \Delta\phi_{2q} - \Delta\theta_{2q}], \qquad (1)$$

where $\Delta\phi_{2q} = (\phi_{2q+1} - \phi_{2q-1})$ is the phase difference between the consecutive harmonics H_{2q+1} and H_{2q-1} and $\Delta\theta_{2q}$ is an intrinsic atomic quantity, associated to the difference of the phases of the transition amplitudes associated to the distinct quantum paths leading to the sideband [5].

To make clearer the connection between the above phase differences and the time-delays we shall discuss here, it is convenient to rewrite the formula in Eq. (1) under the form:

$$S_{2q} = \alpha + \beta \cos[2\omega(\tau - \tau_{2q} - \tau_\theta)], \qquad (2)$$

where $\tau_{2q} = \Delta\phi_{2q}/2\omega$ is a finite difference approximation to the group delay $GD = \partial\phi/\partial\Omega$ of the harmonic radiation at the considered frequency, $\Omega \approx 2q\omega$, as presented in refs. [21, 22]. On the other hand, $\tau_\theta = \Delta\theta_{2q}/2\omega$ is an intrinsic time-delay associated to the atomic phase difference, $\Delta\theta_{2q}$. As reported in [3] and as we shall describe in more details here, the determination of τ_θ gives access to the temporal dynamics of atomic photoionization. Before closing this brief presentation of the RABBIT scheme, we stress that the intensities of both fields must be kept moderate, so that the phases of the transition amplitudes associated to the sidebands can be derived from a standard time-dependent perturbation theory calculation, limited to second-order.

As represented schematically in Fig. 1 (b), streaking relies on the ionization of the atom by a single attosecond pulse, in the presence of a few-cycle IR pulse. One requirement to realize streaking is that the effective duration of the attosecond pulse has to be significantly shorter than the IR pulse cycle [2] (more rigorously it is actually the spectral bandwidth of the attosecond pulse that must be larger than the probe photon frequency). The measurement consists then in recording the momentum, $\vec{k}_f(t)$, of the ejected photoelectron, as deflected by the instantaneous IR probe vector potential, $\vec{A}_\omega(t)$, so that its wave vector is given approximately by:

$$\vec{k}_f \approx \vec{k} - \vec{A}_\omega(t), \qquad (3)$$

where $\vec{k}$ is the field-free momentum. We note that this simple relation is being derived by assuming that the photoelectron does not experience the effects of the residual Coulomb potential of the ionic core [2]. In this article, we will recover this streaking phenomenon using an interferometric interpretation, which includes the full effect of the ionic core, thereby, obtaining the correct absolute delay of the momentum modulation relative to the probe field.

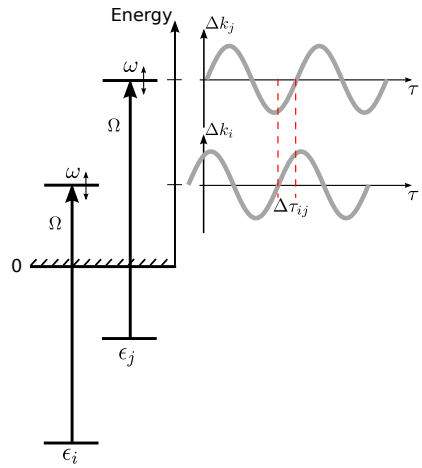

Figure 2: Sketch of an attosecond photoionization time-delay experiment between two different initial states with energies, ϵ_i and ϵ_j. The attosecond XUV field, Ω, ionizes the electron in the presence of a phase-locked IR laser field, ω. Since the same single attosecond pulse (or attosecond pulse train) is used to promote the electrons from either state, the observed delays of the modulation of the central momenta (or sidebands), $\Delta\tau_{ij}(\Omega)$, are directly related to the atomic delay difference $\tau_\theta^{(i)}(\Omega) - \tau_\theta^{(j)}(\Omega)$ defined in Eq. (2), which, in turn, is related to the difference of the corresponding two-photon matrix element phases.

If the XUV field frequency is high enough to ionize electrons from either one of two valence sub-shells of an atom (typically the 2s and 2p states in Ne atoms) one can record two distinct streaking traces corresponding to the two photoelectron lines associated to each sub-shell. This situation is schematically displayed in Fig. 2. A delay between the ejection times of the photoelectrons from the different atomic sub-shells can be determined by comparing the corresponding streaking traces, corrected from possible biases introduced by the experimental procedure [1]. The same idea can be applied to attosecond pulse trains, by using the interferometric set-up [3]. We turn now to the presentation of the theoretical background that is common to the two kinds of techniques, in the limit of weak IR probe fields.

3. Phases of Laser-Assisted Photoionization Transition Amplitudes

3.1. Two-photon Above-Threshold Ionization

A representative laser-assisted photoionization transition is depicted in Fig. 1 (c): It displays the sequential absorption of one XUV harmonic photon with frequency Ω, followed by the absorption of one IR laser photon with frequency ω. It corresponds to the lowest-order perturbative amplitude for an Above-Threshold Ionization (ATI) process observed when the XUV frequency is larger than the ionization energy of the system: $\Omega > I_p$. Obviously, other quantum paths are contributing to this type of two-color ionization process, *e.g.* the IR photon can be absorbed before the XUV photon, but ATI amplitudes of the former type are dominant in the class of experiments considered here.

For two fields with the same linear polarization $\vec{\epsilon}$, it is natural to choose this direction as the quantization axis $\hat{z}$, and the matrix element associated to the path shown in Fig. 1 (c), is of the form:

$$M(\vec{k};\epsilon_i+\Omega) = \frac{1}{i}E_\omega E_\Omega \lim_{\varepsilon\to 0^+}\sum_\nu \frac{\langle\, \vec{k}\,|\, z\,|\,\nu\,\rangle\langle\,\nu\,|\, z\,|\, i\,\rangle}{\epsilon_i+\Omega-\epsilon_\nu+i\varepsilon}, \tag{4}$$

where E_Ω and E_ω are the complex amplitudes of the harmonic and IR laser fields, respectively; $\varphi_{n_i,\ell_i,m_i}(\vec{r}) = \langle\vec{r}|i\rangle$ is the initial state wavefunction, with negative energy ϵ_i and $\varphi_{\vec{k}}(\vec{r}) = \langle\vec{r}|\vec{k}\rangle$ is the final state wavefunction with positive energy $\epsilon_k = k^2/2 = \epsilon_i + \Omega + \omega$. The sum over the index ν runs over the whole spectrum (discrete plus continuous) of the atom. The partial wave expansion of the final state wavefunction is:

$$\varphi_{\vec{k}}(\vec{r}) = (8\pi)^{3/2}\sum_{L,M} i^L e^{-i\eta_L(k)} Y^*_{L,M}(\hat{k}) Y_{L,M}(\hat{r}) R_{k,L}(r),$$

where the $Y_{L,M}$ are spherical harmonics, the $R_{k,L}(r)$ are (real) radial wavefunctions normalized on the energy scale and $\eta_L(k)$ are the phase-shifts. We note that this wavefunction behaves asymptotically as the superposition of a plane wave plus an *ingoing* spherical wave, as required to treat photoionization [24]. Thus, the phase-shifts $\eta_L(k)$ account for the phase difference between the free motion of a plane wave and that of a photoelectron wave ejected from an atomic bound state.

The angular dependence of the matrix element can be factorized out for an initial state

$$\varphi_{n_i,\ell_i,m_i}(\vec{r}) = Y_{\ell_i,m_i}(\hat{r}) R_{n_i,\ell_i}(r)$$

and with $z = \sqrt{4\pi/3}\, r\, Y_{1,0}(\hat{r})$, it becomes:

$$\begin{aligned} M(\vec{k},\epsilon_i+\Omega) = {} & \frac{4\pi}{3i}\,(8\pi)^{3/2}\, E_\omega E_\Omega \\ & \times \sum_{L,M}(-i)^L e^{i\eta_L(k)} Y_{L,M}(\hat{k}) \\ & \times \sum_{\lambda,\mu}\langle Y_{L,M}|Y_{1,0}|Y_{\lambda,\mu}\rangle\langle Y_{\lambda,\mu}|Y_{1,0}|Y_{\ell_i,m_i}\rangle \\ & \times T_{L,\lambda,\ell_i}(k,\epsilon_i+\Omega), \end{aligned} \tag{5}$$

where the angular momentum components of the intermediate states are labelled (λ,μ) and the quantity, $T_{L,\lambda,\ell_i}(k;\epsilon_i+\Omega)$, is the radial part of the amplitude. The span of accessible angular momentum states in the intermediate and final states is governed by the dipole selection rules: One has $\lambda = \ell_i \pm 1; L = \ell_i, \ell_i \pm 2$ and $M = \mu = m_i$ respectively. The explicit form of the radial amplitude $T_{L,\lambda,\ell_i}(k;\epsilon_i+\Omega)$ is:

$$\begin{aligned} T_{L,\lambda,\ell_i}(k;\epsilon_i+\Omega) = {} & \sum_{\nu:\epsilon_\nu<0}\frac{\langle R_{k,L}|r|R_{\nu,\lambda}\rangle\langle R_{\nu,\lambda}|r|R_{n_i,\ell_i}\rangle}{\epsilon_i+\Omega-\epsilon_\nu} \\ & + \lim_{\varepsilon\to 0^+}\int_0^{+\infty} d\epsilon_{\kappa'}\frac{\langle R_{k,L}|r|R_{\kappa',\lambda}\rangle\langle R_{\kappa',\lambda}|r|R_{n_i,\ell_i}\rangle}{\epsilon_i+\Omega-\epsilon_{\kappa'}+i\varepsilon}, \end{aligned} \tag{6}$$

where we have separated the contributions of the discrete and continuous spectra.

Since the frequency of the XUV harmonic is larger than the ionization potential of the atom, $\Omega > I_p = |\epsilon_i|$, it is also larger than the excitation energies of the atom, $\Omega > \epsilon_\nu - \epsilon_i$. Accordingly, the denominators of the terms in the sum over the discrete states are positive and relatively large, which makes the overall contribution of these terms significantly smaller than that of the continuous spectrum. In the integral running on the continuous spectrum of energies $\epsilon_{\kappa'} = \kappa'^2/2$, the denominator becomes zero at the energy $\epsilon_\kappa = \kappa^2/2 = \epsilon_i + \Omega$. Taking the limit $\varepsilon \to 0^+$, the integral becomes:

$$\begin{aligned} & \lim_{\varepsilon\to 0^+}\int_0^{+\infty} d\epsilon_{\kappa'}\frac{\langle R_{k,L}|r|R_{\kappa',\lambda}\rangle\langle R_{\kappa',\lambda}|r|R_{n_i,\ell_i}\rangle}{\epsilon_i+\Omega-\epsilon_{\kappa'}+i\varepsilon} \\ & = \mathcal{P}\int_0^{+\infty} d\epsilon_{\kappa'}\frac{\langle R_{k,L}|r|R_{\kappa',\lambda}\rangle\langle R_{\kappa',\lambda}|r|R_{n_i,\ell_i}\rangle}{\epsilon_i+\Omega-\epsilon_{\kappa'}} \\ & \qquad -i\pi\langle R_{k,L}|r|R_{\kappa,\lambda}\rangle\langle R_{\kappa,\lambda}|r|R_{n_i,\ell_i}\rangle. \end{aligned} \tag{7}$$

where the first term is the Cauchy principal value of the integral, which turns out to be real, and the second term is purely imaginary. The latter is associated with a two-step transition as it contains the product of the one-photon ionization amplitude towards the state of energy $\epsilon_\kappa = \epsilon_i + \Omega$, times the continuum–continuum transition amplitude from ϵ_κ towards the final state of energy $k^2/2 = \epsilon_\kappa + \omega$ that is reached upon the absorption of the IR photon ω.

The overall phase of the radial matrix element, Eq. (6), is thus governed by the ratio of the imaginary term in Eq. (7) to the sum of the integral principal part in the same

equation plus the contribution of the discrete spectrum contained in Eq. (6). Accurate computations of such amplitudes and phases represent a formidable task for most atomic systems. This entails to rely on approximate representations of the atomic potential for each angular momentum dependent state [25, 26] or to use many-electron techniques [27, 28]. There is however the notable exception of hydrogenic systems, where "exact" calculations of these amplitudes are feasible [29–32], see below. It is thus of importance to derive an approximate treatment which should allow to get correct estimates of the phases of interest to address the questions of the time-delays.

3.2. Asymptotic approximation for 2-photon ATI matrix elements

Let us re-express the radial amplitude in terms of the first-order *perturbed wavefunction* denoted $\rho_{\kappa,\lambda}(r)$:

$$T_{L,\lambda,\ell_i}(k;\epsilon_i+\Omega) = \langle R_{k,L}|r|\rho_{\kappa,\lambda}\rangle. \tag{8}$$

The function $\rho_{\kappa,\lambda}(r)$ solves the inhomogeneous differential equation:

$$[H_\lambda - \epsilon_\kappa]\rho_{\kappa,\lambda}(r) = -rR_{n_i,\ell_i}(r), \tag{9}$$

where H_λ is the radial atomic Hamiltonian for angular momentum λ. The fully developed eigenfunction expansion of $\rho_{\kappa,\lambda}(r)$ can be identified using Eqs. (6) and (7):

$$\begin{aligned}\rho_{\kappa,\lambda}(r) = &\sum_{\nu:\epsilon_\nu<0} \frac{R_{\nu,\lambda}(r)\langle R_{\nu,\lambda}|r|R_{n_i,\ell_i}\rangle}{\epsilon_\kappa-\epsilon_\nu} \\ &+ \mathcal{P}\int_0^{+\infty} d\epsilon_{\kappa'} \frac{R_{\kappa',\lambda}(r)\langle R_{\kappa',\lambda}|r|R_{n_i,\ell_i}\rangle}{\epsilon_\kappa-\epsilon_{\kappa'}} \\ &- i\pi R_{\kappa,\lambda}(r)\langle R_{\kappa,\lambda}|r|R_{n_i,\ell_i}\rangle. \end{aligned}\tag{10}$$

We note that it describes the radial part of the *intermediate* photoelectron wave packet created upon absorption of the XUV photon Ω, before absorbing the IR laser photon ω.

The essence of the approximate treatment that we have implemented to get an estimate of $T_{L,\lambda,\ell_i}(k;\epsilon_i+\Omega)$, is based on using the asymptotic forms of both the final state function $R_{k,L}(r)$ and of the perturbed wavefunction $\rho_{\kappa,\lambda}(r)$ for large values of their radial coordinate. This is *a priori* justified by the fact that we are interested in the *phases* of the amplitudes which are governed by the asymptotic behavior of these functions. As an additional verification, we will compare the predictions of the model to those derived from an exact treatment in Hydrogen.

The asymptotic limit of the radial continuum wavefunction of the final state with angular momentum L is of the generic form [24]:

$$\lim_{r\to\infty} R_{k,L}(r) \;=\; \frac{N_k}{r}\sin[kr+\Phi_{k,L}(r)], \tag{11}$$

where $N_k = \sqrt{2/(\pi k)}$ is the normalization constant in the energy scale and the phase has the general form:

$$\Phi_{k,L}(r) = Z\ln(2kr)/k + \eta_L(k) - \pi L/2. \tag{12}$$

We note that this phase includes the logarithmic divergence characteristic of the Coulomb potential of the ionic core with charge Z, in the asymptotic region. The Coulomb potential influences also the scattering phase-shift $\eta_L(k)$, which can be rewritten under the form: $\eta_L(k) = \sigma_L(k) + \delta_L(k)$ where $\sigma_L = \arg[\Gamma(L+1-iZ/k)]$ is the Coulomb phase-shift and where the correction $\delta_L(k)$ originates from the short range deviation of the ionic potential from a pure Coulomb potential, see for instance [26, 28]. Obviously, in the case of an hydrogenic system, one has $\delta_L(k) = 0$.

To derive the asymptotic form of the perturbed wavefunction $\rho_{\kappa,\lambda}(r)$, it is in principle enough to establish the limiting structure of the differential equation it verifies. From Eq. (9), one observes that, in the asymptotic limit $r\to\infty$, the second member vanishes, as a result of the exponential decay of the bound state wavefunction $R_{n_i,\ell_i}(r)$. One is left with a standard Schrödinger equation for positive energy ϵ_κ which is solved by imposing outgoing wave boundary conditions to the solutions [32]:

$$\lim_{r\to\infty}\rho_{\kappa,\lambda}(r) \propto \frac{N_\kappa}{r}\;\exp\left[i(\kappa r+\Phi_{\kappa,\lambda}(r))\right]. \tag{13}$$

It is also of interest to derive explicitly the limiting forms of the terms entering the expression of $\rho_{\kappa,\lambda}(r)$ in Eq. (10). Regarding its real part, the sum over the discrete states ν can be neglected, as each term goes asymptotically to zero. Thus, for large r, it reduces to a principal part integral:

$$\Re[\rho_{\kappa,\lambda}(r)] \approx \mathcal{P}\int_0^{+\infty} d\epsilon_{\kappa'}\frac{R_{\kappa',\lambda}(r)\langle R_{\kappa',\lambda}|r|R_{n_i,\ell_i}\rangle}{\epsilon_\kappa-\epsilon_{\kappa'}}. \tag{14}$$

This integral can be estimated by extending the integration range $\epsilon_{\kappa'}\to-\infty$ and replacing the radial continuum function $R_{\kappa',\lambda}(r)$ by its asymptotic limit according to the prescription in Eq. (11). Then, writing the sine function under its exponential form and performing contour integrations, with semi-circles around the pole at ϵ_κ, one gets:

$$\lim_{r\to\infty}\Re[\rho_{\kappa,\lambda}(r)] \approx -\frac{\pi N_\kappa}{r}\cos[\kappa r+\Phi_{\kappa,\lambda}(r)]\langle R_{\kappa,\lambda}|r|R_{n_i,\ell_i}\rangle. \tag{15}$$

Regarding the imaginary part given by the last term in Eq. (10), it is enough to substitute again the asymptotic form of $R_{\kappa,\lambda}(r)$, so that:

$$\lim_{r\to\infty}\Im[\rho_{\kappa,\lambda}(r)] \approx -\frac{\pi N_\kappa}{r}\sin[\kappa r+\Phi_{\kappa,\lambda}(r)]\langle R_{\kappa,\lambda}|r|R_{n_i,\ell_i}\rangle. \tag{16}$$

Then by regrouping the real and imaginary parts, one gets the final expression:

$$\lim_{r\to\infty}[\rho_{\kappa,\lambda}(r)] \approx -\frac{\pi N_\kappa}{r}\exp\left[i\kappa r+i\Phi_{\kappa,\lambda}(r)\right]\langle R_{\kappa,\lambda}|r|R_{n_i,\ell_i}\rangle, \tag{17}$$

which corresponds to a complex outgoing wave [32], as expected from Eq. (13), weighted by the dipole matrix

element associated to the one-photon transition from the initial state. We note that adopting the so-called "pole-approximation", which consists in neglecting the off-shell part (*i.e.* the real part given in Eq. (15)), would lead to a loss of the phase information of the process since the perturbed wavefunction then would be a standing wave rather than an outgoing wave.

The corresponding asymptotic approximation for the second-order radial matrix element, Eq. (6), is obtained by substituting in Eq. (8) the asymptotic expressions, Eqs. (11) and (17), for the radial wavefunctions of the final state and of the intermediate state, respectively. One has explicitly:

$$T_{L,\lambda,\ell}(k;\epsilon_\kappa) \approx -\pi \, \langle R_{\kappa,\lambda}|r|R_{n_i,\ell_i}\rangle N_k N_\kappa \times \int_0^\infty dr \sin[kr + \Phi_{k,L}(r)] \; r \; e^{[i(\kappa r + \Phi_{\kappa,\lambda}(r))]}. \tag{18}$$

To introduce the next step in our approximate treatment, one rewrites the sine in its exponential form and develop the expressions of the phases $\Phi_{\kappa,\lambda}(r)$ as given in Eq. (12). One is left with two distinct contributions containing integrals either of the type J_+ or J_- that are defined as follows:

$$\begin{aligned} J_\pm &= \pm \frac{1}{2i} \int_0^\infty dr \; r^{1+iZ(1/\kappa \pm 1/k)} \exp\left[i(\kappa \pm k)r\right] \\ &= \pm \frac{1}{2i} \left(\frac{i}{\kappa \pm k}\right)^{2+iZ(1/\kappa \pm 1/k)} \Gamma[2 + iZ(1/\kappa \pm 1/k)], \end{aligned} \tag{19}$$

where we have used an integral representation of a Gamma function $\Gamma(z)$ with complex argument. In our case, the contribution of the J_+ integral is vanishingly small as compared to that of J_-. This is due to the IR photon energy being small compared to the final kinetic energy of the electron, $\omega = k^2/2 - \kappa^2/2 \ll k^2/2$, so that the difference $|\kappa - k| \approx \omega/k$ is much smaller than the sum $\kappa + k \approx 2k \pm \omega/k$. As a result, the fast oscillations of $\exp[i(\kappa+k)r]$ lead to a relative cancellation of the corresponding integral, as compared to the one containing the factor $\exp[i(\kappa - k)r]$. Neglecting the J_+ contribution, the asymptotic expression reduces to:

$$\begin{aligned} T_{L,\lambda,\ell_i}(k;\epsilon_\kappa) \approx \frac{\pi}{2} \, N_k N_\kappa \, \langle R_{\kappa,\lambda}|r|R_{n_i,\ell_i}\rangle \\ \times \frac{1}{|\kappa - k|^2} \, \exp\left[-\frac{\pi Z}{2}\left(\frac{1}{\kappa} - \frac{1}{k}\right)\right] \\ \times i^{L-\lambda-1} \exp[i(\eta_\lambda(\kappa) - \eta_L(k))] \\ \times \frac{(2\kappa)^{iZ/\kappa}}{(2k)^{iZ/k}} \frac{\Gamma[2 + iZ(1/\kappa - 1/k)]}{(\kappa - k)^{iZ(1/\kappa - 1/k)}}, \end{aligned} \tag{20}$$

which was used by us [3] to obtain estimates of the phases occurring in two-photon transitions entering RABBIT transition amplitudes. The first two lines in Eq. (20) are real, they contain a one-photon matrix element from the bound state into the continuum, but also an exponential factor describing the strength of the continuum–continuum transition from κ to k. The exponential factor decreases with the probe photon energy, $\omega = k^2/2 - \kappa^2/2$, which indicates that large energy leaps in the continuum are strongly suppressed. At a given laser probe energy, however, the exponential factor increases with the final momentum, k, which indicates that it becomes easier for the photoelectron to interact with the probe field. The third line is a simple phase factor containing the scattering phases of the continuum states. Finally, the fourth line is a complex factor that depends on three quantities: final momentum, k; the laser probe frequency, ω; and the charge of the ion, Z.

A more formal derivation of this result, based on a closed-form representation of the Coulomb Green's function is given in the Appendix A. [We have found a typo in Eq. (7) in ref. [3]: The ratio, $(2k)^{i/k}/(2k_a)^{i/k_a}$, should be inverted, as is evident from Eq. (20) in the present work].

Thus, in the asymptotic limit, the *phase* of the radial component takes the form:

$$\begin{aligned} \arg\left[T_{L,\lambda,\ell_i}(k;\epsilon_\kappa)\right] \approx \frac{\pi}{2}(L - \lambda - 1) \\ + \eta_\lambda(\kappa) - \eta_L(k) + \phi_{cc}(k,\kappa), \end{aligned} \tag{21}$$

where

$$\phi_{cc}(k,\kappa) \; = \; \arg\left[\frac{(2\kappa)^{iZ/\kappa}}{(2k)^{iZ/k}} \, \frac{\Gamma[2 + iZ(1/\kappa - 1/k)]}{(\kappa - k)^{iZ(1/\kappa - 1/k)}}\right], \tag{22}$$

is the phase associated to a continuum–continuum radiative transition resulting from the absorption of ω, in the presence of the Coulomb potential, Z. It is important to note that it is *independent* from the characteristics of the initial atomic state, as well as from the amplitude of the field. It is illustrative to study the continuum–continuum phase in the limit of a small photon energy, $\omega \approx k(k - \kappa)$, which yields a simplified expression:

$$\phi_{cc}^{(soft)}(k;\omega) \; = \; \arg\left[\left(\frac{2k^2}{\omega}\right)^{iZ\omega/k^3} \; \Gamma[2 + iZ\omega/k^3]\right], \tag{23}$$

where it becomes clear that it is the product: $Z\omega/k^3$, which determines the size of the continuum–continuum phase. This expression is expected to be valid in the so-called "soft-photon" limit, $k^2/2 \gg \omega$, where the exchange of energy ω and the corresponding momentum transfer $\Delta k = \omega/c$ do not significantly modify the electron state [23]. The substitution, $\omega \to -\omega$, yields the (Fourier) component corresponding to stimulated emission of light. We note that the phases corresponding to absorption and emission have opposite signs, but that they are otherwise identical in the soft-photon limit.

Replacing the formula obtained in Eq. (20) for the radial component in the expression of the full transition amplitude $M(\vec{k}, \epsilon_i + \Omega)$ given in Eq. (5), one gets its general

form in the asymptotic limit:

$$M(\vec{k};\epsilon_\kappa) \approx -\frac{2\pi^2}{3}(8\pi)^{3/2}E_\omega E_\Omega N_k N_\kappa \times \frac{1}{|k-\kappa|^2}\exp\left[-\frac{\pi Z}{2}\left(\frac{1}{\kappa}-\frac{1}{k}\right)\right] \times \frac{(2\kappa)^{iZ/\kappa}}{(2k)^{iZ/k}}\frac{\Gamma[2+iZ(1/\kappa-1/k)]}{(\kappa-k)^{iZ(1/\kappa-1/k)}} \times \sum_{L=\ell_i,\ell_i\pm2} Y_{L,m_i}(\hat{k}) \sum_{\lambda=\ell_i\pm1} \langle Y_{L,m_i}|Y_{1,0}|Y_{\lambda,m_i}\rangle \times \langle Y_{\lambda,m_i}|Y_{1,0}|Y_{\ell_i,m_i}\rangle\langle R_{\kappa,\lambda}|r|R_{n_i,\ell_i}\rangle i^{-\lambda}e^{i\eta_\lambda(\kappa)} \quad (24)$$

To address the question of its phase, one notices that besides a trivial contribution from the spherical harmonic in the final state, $Y_{L,m_i}(\hat{k})$, it contains only phase-shifts that are governed by the angular momentum λ of the intermediate state, *i.e.* a state that can be reached via *single*-photon ionization. More precisely, for a given transition channel characterized by the angular momenta of the intermediate and final state $\ell_i \to \lambda \to L$, the phase of the matrix element reduces to:

$$\arg\left[M_{L,\lambda,\ell_i}(\vec{k},\epsilon_\kappa)\right] = \pi + \arg[Y_{L,m_i}(\hat{k})] + \phi_\Omega + \phi_\omega - \frac{\pi\lambda}{2} + \eta_\lambda(\kappa) + \phi_{cc}(k,\kappa), \quad (25)$$

where ϕ_Ω and ϕ_ω are the phases of the XUV field Ω and of the IR laser ω, respectively. We stress that the final state scattering phase, $\eta_L(k)$, cancels out and that it enters neither in Eq. (24) nor in Eq. (25).

Eq. (25) represents one of the major results of our theoretical analysis. It shows that, within the asymptotic approximation and besides trivial spherical harmonic contributions and the phases of the fields [line 1 in Eq. (25)], the phase of a two-color ATI transition amplitude has two components: i) One is directly linked to the quantum-mechanical phase-shift of the one-photon XUV ionization amplitude, here $-\pi\lambda/2 + \eta_\lambda(\kappa)$; ii) The other, denoted $\phi_{cc}(k,\kappa)$, is in some sense "universal", it describes the phase brought by the absorption of the probe photon ω, in the presence of the Coulomb potential with charge Z. Then, as shown below, when comparing laser-assisted ionization originating from distinct atomic states, the energy derivative of the phase-shifts in the first term contribute to a Wigner-like time-delay. On the other hand, the difference between the "universal" terms ϕ_{cc} gives rise to a measurement-induced delay, associated to continuum–continuum stimulated radiative transitions in the presence of the Coulomb potential of the ionic core.

In Fig. 3, we present the continuum–continuum phases, associated with absorption (red) and emission (blue) of a probe photon leading to the same final energy, calculated using the asymptotic approximation, Eq. (22). The continuum–continuum phases for probe photon absorption are positive while those for stimulated emission are negative, but approximately equal in absolute value. In the next subsection, we show that, still in a single-active electron picture, it is feasible to improve the accuracy of our approximate treatment with the help of semi-classical arguments.

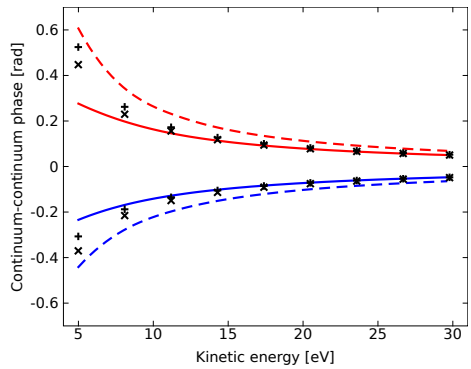

Figure 3: Continuum–continuum phases for absorption (red, upper curves) and emission (blue, lower curves) calculated using the asymptotic approximation (dashed curves) [Eq. 22] and the long-range amplitude-corrected asymptotic approximation (full curves) [Eq. 30]. These approximate phases are compared with the exact calculations (black symbols) from the 1*s* state in hydrogen. The exact results for final angular momentum $L = 0$ (+ symbol) and $L = 2$ (× symbol) are computed by subtracting the one-photon scattering phase from that of the exact two-photon matrix elements. The data correspond to $Z = 1$ and to a laser probe with $\omega = 1.55$ eV. It is interpolated between the discrete harmonic orders.

3.3. Long-range amplitude effects

In order to go to the next level of our asymptotic approximation, we must include not only long-range phase variations of the continuum states, but also long-range variations of the amplitudes. Indeed, the normalization constants contained in the asymptotic forms of the radial functions $R_{k,L}(r)$ and $\rho_{\kappa,\lambda}(r)$ can be modified to account for the long-range influence of the Coulomb potential. For instance, the modified final state normalization constant is:

$$N_k(r) = \sqrt{\frac{2}{\pi p(r)}}, \quad (26)$$

where

$$p(r) = \sqrt{2(\epsilon - V(r))} \approx k - V(r)/k, \quad (27)$$

is the local momentum from Wentzel–Kramers–Brillouin (WKB) theory [36]. The same remark applies to $N_\kappa(r)$ for the perturbed radial function. Long-range amplitude effects can be approximated by expanding the quantities $N_k(r)$ and $N_\kappa(r)$,

$$N_k(r)N_\kappa(r) \approx \sqrt{\frac{4}{\pi^2 k\kappa}}\left[1 - \frac{1}{2}\left(\frac{1}{\kappa^2}+\frac{1}{k^2}\right)\frac{Z}{r}\right], \quad (28)$$

to first-order in the Coulomb potential. The second term within the brackets in Eq. (28) contains the first-order amplitude correction to the matrix element. Evaluation of the long-range amplitude contribution leads to a correction to the continuum–continuum phase:

$$\alpha_{cc}(k,\kappa) = \arg\left[1 + \frac{iZ}{2}\left(\frac{1}{\kappa^2}+\frac{1}{k^2}\right)\frac{\kappa-k}{1+iZ(1/\kappa-1/k)}\right]. \quad (29)$$

The final continuum–continuum transition phase is:

$$\tilde{\phi}_{cc}(k,\kappa) = \alpha_{cc}(k,\kappa) + \phi_{cc}(k,\kappa) \quad (30)$$

where $\phi_{cc}(k,\kappa)$ is given in Eq. (22). In Fig. 3, we show that including such long-range effects improves the accuracy of the approximation greatly, leading to accurate quantitative result already at relatively low energies in the continuum. The accuracy in the lower energy range can be further improved by using a regularization method designed to remove the effect of the singularity in Eq. (28) as r, k and κ go to zero.

Going beyond the approximations given here, namely performing *exact ab initio* computations of the matrix elements $M(\vec{k},\epsilon_i+\Omega)$ in polyelectronic systems, is out of reach of present computational capabilities. It is only in the special case of hydrogenic systems, that such 2-photon amplitudes can be computed with arbitrary precision. Thus, with objective to delineate the range of validity of our approximation, we turn now to a brief presentation of the "exact" calculations in hydrogen.

3.4. Exact calculations of 2-photon ATI matrix elements in hydrogenic systems

The principle of the calculation is outlined here for s-states. Numerical data for other states will be given below. We first express the transition amplitude given in Eq. (5) for the case $\ell_i = 0, m_i = 0$ which implies $\lambda = 1$ so that the angular momentum of the photoelectron is either $L = 0, 2$. Accordingly, two distinct amplitudes contribute to ATI transitions like the one depicted in Fig. 1 (c):

$$\begin{aligned} M(\vec{k},\epsilon_\kappa)\Big|_{\ell_i=0} &= \frac{1}{3i}(8\pi)^{3/2}E_\omega E_\Omega \\ &\times \left[e^{i\sigma_0(k)}Y_{0,0}(\hat{k})T_{0,1,0}(k;\epsilon_\kappa)\right. \\ &- \left.\frac{2}{\sqrt{5}}e^{i\sigma_2(k)}Y_{2,0}(\hat{k})T_{2,1,0}(k;\epsilon_\kappa)\right], \end{aligned} \quad (31)$$

where the radial components for $s-$states are of the form:

$$T_{L,1,0}(k;\epsilon_\kappa)|_{\ell_i=0} = \langle R_{k,L}|r|G_1(\epsilon_\kappa)|r|R_{n_i,0}\rangle, \quad (32)$$

with $L = 0, 2$; n_i labels the initial atomic $s-$state and $G_{\lambda=1}(\epsilon_\kappa)$ is the radial component of the Coulomb Green's function for angular momentum $\lambda = 1$. The general form of the Green's function with energy argument ϵ_κ is:

$$G_\lambda(r',r;\epsilon_\kappa) = \lim_{\varepsilon\to 0^+}\sum_\nu \frac{R_{\nu,\lambda}(r')R_{\nu,\lambda}(r)}{\epsilon_\kappa - \epsilon_\nu + i\varepsilon}. \quad (33)$$

As already mentioned, the infinite sum over the index ν runs over the whole (discrete + continuous) spectrum of the hydrogenic system. Closed form expressions for G_λ are known, see for instance [33]. Here, we have used the expression given as an expansion over a discrete Sturmian basis:

$$G_\lambda(r',r;\epsilon_\kappa) = \sum_{\nu=\lambda+1}\frac{S_{\nu,\lambda,x}(r')S_{\nu,\lambda,x}(r)}{1-\nu x}, \quad (34)$$

where $x = \sqrt{-2\epsilon_\kappa}$ and the so-called Sturmian functions $S_{\nu,\lambda,x}(r)$ have a structure similar to the bound-state hydrogenic radial functions [34, 35]:

$$\begin{aligned} S_{\nu,\lambda,x}(r) &= 2x\sqrt{\frac{(\nu-\lambda-1)!}{(\nu+\lambda)!}} \\ &\times e^{-xr}(2xr)^\lambda L^{2\lambda+1}_{\nu-\lambda-1}(2xr), \end{aligned} \quad (35)$$

where $L^{2\lambda+1}_{\nu-\lambda-1}(z)$ are associated Laguerre polynomials. In the amplitudes for ATI transitions, $\epsilon_\kappa = \epsilon_i + \Omega > 0$, and the quantity, $x = i\sqrt{2|\epsilon_\kappa|}$, is pure imaginary. It is then convenient to use Padé-like resummation techniques to compute the infinite sum over the index ν, see, for instance ref. [31].

In Fig. 3, we present the exact continuum–continuum phases from the $1s$ state in hydrogen. These phases are defined as the total phase of the exact matrix element, $M_{L,1,0}(\vec{k};\epsilon_\kappa)$, *minus* the one-photon phase [see line 2 of Eq. (25)]. Our approximate calculation including long-range amplitude effects, Eq. (30), is in excellent agreement with the exact calculations except at low energy.

3.5. Phase of the classical dipole

Finally, we present a simplified derivation of the continuu continuum phase, $\phi_{cc}(k,\kappa)$, using a classical approach. The dipole associated with the absorption of radiation at frequency ω by a free electron in the presence of a Coulomb potential, can be calculated using Larmor's formula,

$$d_C(k;\omega) = \int_0^\infty dt\; r_k(t)\exp[-i\omega t], \quad (36)$$

where it is assumed that the electron follows a *field-free* trajectory, $r_k(t)$, that starts close to the ion, $r_k(0)\approx 0$, and then moves out away from the ion with an asymptotic velocity, k. The integral can be cast from time to space using the $r-$dependence of the velocity:

$$v_k(r) = \sqrt{k^2 - 2V(r)}, \quad (37)$$

where $k^2/2$ is the final kinetic energy of the electron at large distance from the ion. Using the differential $dt = dr/v(r)$, the time can be written as $t(k;r) = \int^r dr'/v_k(r') + C$, where C is an integration constant. In the case of the Coulomb potential, $V(r) = -Z/r$, the integral becomes

$$\begin{aligned} t(k;r) &= \int^r dr'\;\frac{1}{\sqrt{k^2+2Z/r'}} + C \\ &\approx \frac{r}{k} - \frac{Z}{k^3}\ln(r) + C, \end{aligned} \quad (38)$$

in the asymptotic limit, *i.e.* when $k^2/2 \gg Z/r$. This provides an approximate time–position relation valid at large distances from the origin. In the special case where the electron starts from the origin $[t, r] = [0, 0]$, the exact integration in Eq. (38) leads to $C = -Z\ln[2k^2/Z]/k^3$. Keeping for the moment this value of the constant and replacing the asymptotic form of the time in the expression of the dipole Eq. (36), one gets:

$$\begin{aligned} d_C(k;\omega) \approx & \frac{1}{k}\int_0^\infty dr\; r \exp\left[-i\frac{\omega}{k}\left(r - \frac{Z}{k^2}\log[2k^2 r/Z]\right)\right] \\ = & \frac{1}{k}\left(\frac{2k^2}{Z}\right)^{iZ\omega/k^3}\int_0^\infty dr\; r^{1+iZ\omega/k^3}\exp\left[-i\frac{\omega}{k}r\right] \\ = & -\frac{k}{\omega^2}\exp\left[-\frac{3\pi Z\omega}{2k^3}\right] \\ & \times \left(\frac{2k^3}{Z\omega}\right)^{iZ\omega/k^3}\Gamma(2+iZ\omega/k^3), \end{aligned} \tag{39}$$

where the next-to-last line is real, with an exponential factor that decreases with ω, but increases with k, in excellent agreement with the quantum mechanical result, Eq. (24). Furthermore, the last line contains the complex gamma function times an algebraic factor, also in close connection to the quantum counterpart. Clearly, the dipole corresponding to absorption is a complex quantity with phase:

$$\begin{aligned} \phi_C(k;\omega) = & \arg\left[d_C(k;\omega)\right] \\ \approx & \arg\left[-\left(\frac{2k^3}{Z\omega}\right)^{iZ\omega/k^3}\Gamma(2+iZ\omega/k^3)\right], \end{aligned} \tag{40}$$

which is closely related, but *not* identical to its soft-photon quantum counter part $\phi_{cc}^{(soft)}$, given in Eq. (23).

In the quantum mechanical case, the electron starts in a bound state with some spatial extent and not exactly from $r = 0$. In order to account for this uncertainty on the initial position, we may choose a different value of the integration constant C, introduced in Eq. (38), in order to come closer to the quantum mechanical dipole. This matching-procedure is reminiscent of the method used in ref. [12], to determine the "best" initial radial position for the electron within the eikonal Volkov approximation. Within the lowest-order approximation of Eq. (38), we find a simple relation between the initial position and the integration constant:

$$r_0 \approx \exp\left[\frac{Ck^3}{Z}\right], \tag{41}$$

which is valid at high-energy. It is convenient to set $C = -Z\ln[2k]/k^3$, a choice corresponding to an initial radial position $r_0 \approx 1/(2k)$, as was identified in ref. [12]. Clearly, when the first-order amplitude correction is included, Eq. (30), the initial position is adjusted accordingly. The continuum–continuum phase being only one part of the total quantum mechanical phase, we have also to include the scattering phase if we want to deduce the "true" initial position. Interestingly, in our approach this exact inital position is not critical. In fact, our results are stable with respect to rather substantial modifications of the wavefunctions close to the core. It is the behavior of the wavefunctions far away from the core that must be described accurately, using the asymptotic approximation. We now turn our attention to the applications of the complex ATI matrix elements, to the determination of attosecond delays in photoionization.

4. Attosecond Time-delays

The complex amplitude $M(\vec{k}, \epsilon_i + \Omega)$ (denoted $M^{(a)}$ for conciseness in the following) for the joint absorption of an XUV photon Ω and of an IR laser photon ω, is of course *not* a direct observable in any experiment. Only the square modulus of a complex transition amplitude can be measured. Thus, if $M^{(a)}$ is the only amplitude leading to a given final state, there is no way to determine its absolute phase. However, in the cases of interest here, with attosecond XUV pulses in the presence of a probe IR laser field, several other channels are open which can lead to the same final state, thus making it feasible to observe phase-dependent interference patterns. This property is exploited in the following schemes.

4.1. Attosecond delay measurements using pulse trains

In the RABBIT scheme there are two dominant complex amplitudes (quantum paths), $M^{(a)}$ and $M^{(e)}$, associated with the absorption of harmonic H_{2q-1} or H_{2q+1} plus absorption or emission of a laser photon with phase, $\pm\omega\tau \equiv \pm\phi_\omega$, leading to the same final sideband, S_{2q}. The photoelectron will transit via different intermediate states: $\kappa_<$ and $\kappa_>$, corresponding to different intermediate energies: $\epsilon_< = \epsilon_i + 2q\omega - \omega = \kappa_<^2/2$ and $\epsilon_> = \epsilon_i + 2q\omega + \omega = \kappa_>^2/2$. Clearly, the energy of the corresponding intermediate states are one photon below and above the sideband, as is illustrated in Fig. 1 (a). This implies that the measured intensity of the sideband, S_{2q}, will depend on the *phase difference* between the two quantum paths:

$$\begin{aligned} P_{2q} \propto & |M^{(a)} + M^{(e)}|^2 = |M^{(a)}|^2 + |M^{(e)}|^2 \\ & + 2|M^{(a)}||M^{(e)}|\;\cos\left[\arg\left(M^{(a)*}M^{(e)}\right)\right] \end{aligned} \tag{42}$$

which corresponds to a standard interference phenomenon, as summarized in Eqs. (1) or, equivalently in (2) displayed in the introduction (Sec. 1). If we now apply Eq. (25), and assume that the total contribution to the complex amplitudes can be approximated by a single intermediate angular momentum component, λ, the phase difference is

$$\begin{aligned} \arg\left(M^{(a)*}_{L,\lambda,\ell_i}M^{(e)}_{L,\lambda,\ell_i}\right) \approx & -2\omega\tau + \overbrace{\phi_{2q+1} - \phi_{2q-1}}^{\Delta\phi_{2q}} \\ & + \underbrace{\eta_\lambda(\kappa_>) - \eta_\lambda(\kappa_<) + \phi_{cc}(k,\kappa_>) - \phi_{cc}(k,\kappa_<)}_{\Delta\theta_{2q}}. \end{aligned} \tag{43}$$

Here the first line contains the phases of the fields, while the second line is $\Delta\theta_{2q}$, in terms of scattering and continuum–continuum phases. The corresponding measurement delay, τ_θ as defined in Eq. (2), is the sum of finite-difference approximations to a Wigner-like time-delay:

$$\tau_\lambda(k) \approx \frac{\eta_\lambda(\kappa_>) - \eta_\lambda(\kappa_<)}{2\omega} \tag{44}$$

and to a continuum-continuum delay:

$$\tau_{cc}(k;\omega) \approx \frac{\phi_{cc}(k,\kappa_>) - \phi_{cc}(k,\kappa_<)}{2\omega}, \tag{45}$$

so that $\tau_\theta \approx \tau_\lambda + \tau_{cc}$.

In a more general case, the interference will result from complex amplitudes with two terms for absorption and for emission, $M^{(a/e)} = M^{(a/e,+)} + M^{(a/e,-)}$, corresponding to different intermediate angular momenta, $\lambda = \ell_i \pm 1$. The interesting point is that the τ_{cc} will not be affected, since the phases ϕ_{cc} are independent of λ as well as of the final angular momenta $L = \ell_i, \ell_i \pm 2$, see Eq. (22). The remaining part can be interpreted as an *effective* Wigner-like delay, $\tilde{\tau}_{\lambda=\ell_i\pm1}$, which has to be computed taking into account the relative weights of the *four* components entering the expression of the transition probability amplitude.

4.2. Attosecond delay measurements using single pulses

In this section we apply the perturbative treatement to laser-assisted photoionization by a single-attosecond pulse (SAP) and a probing laser field. The ionizing attosecond field is

$$\tilde{E}_{SAP}(t) = \int d\Omega\ E_\Omega \exp[-i\Omega t]/2\pi, \tag{46}$$

with $E_\Omega = |E_\Omega|\ \exp[i\phi_\Omega]$ being complex Fourier coefficients. While our approach is very general, it can be illustrated by considering a Gaussian frequency distribution centered on the frequency Ω_0, as depicted in the left panel of Fig. 4. The probing laser field is assumed to be monochromatic and real, $\tilde{E}(t) = 2|E_\omega| \cos[\omega(t-\tau)]$, so that it can account for both absorption and emission processes. Our perturbative approach cannot be used to fully account for the large momentum shifts that are typical of streaking spectrograms, but it does allow us to study the *onset* of streaking. As we shall see below, streaking-like behavior is clear already in the perturbative regime. In the right panel of Fig. 4, we sketch the interfering processes to a certain energy ϵ: (d), (a) and (e) from lowest-order perturbation theory. The dominant contribution (d) corresponds to absorption of a single XUV photon, while the upshifted (a) and downshifted (e) photoelectron spectra corresponds to absorption and emission of an additional laser photon ω, respectively.

The matrix element for *one-photon* ionization with a

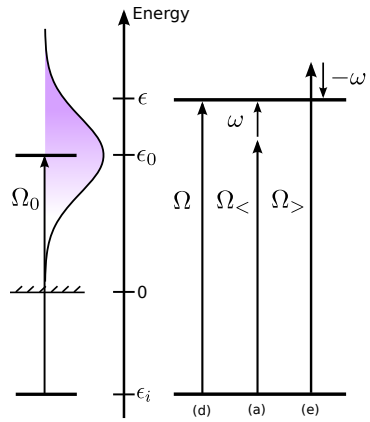

Figure 4: Sketch of the quantum paths describing the onset of "streaking" for a photoelectron ionized by a single attosecond pulse and probed by a monochromatic laser field. The first-order photoelectron wave packet is centered at $\epsilon_0 = \epsilon_i + \Omega_0$. Within the bandwidth of the attosecond pulse, any energy, ϵ, can be reached by path (d), where a single XUV photon with frequency Ω is absorbed. Alternatively, the same energy can reached by path (a) by absorbing a less energetic photon, $\Omega_<$, and a laser photon, ω; or by path (e) by absorbing a more energetic photon, $\Omega_>$, and then emitting a laser photon, $-\omega$. At the high-energy end of the photoelectron distribution (indicated by ϵ), the dominant contributions to the photoelectron wave packet are (d) and (a), due to $\Omega_>$ being far in the upper energy range of the XUV bandwidth.

photoelectron emitted along the polarization axis is

$$M^{(d)}(k\hat{z};\epsilon_i+\Omega) = \frac{(8\pi)^{3/2}}{i} E_\Omega \sum_\lambda (-i)^\lambda \sqrt{\frac{2\lambda+1}{3}} e^{i\eta_\lambda(k)} \times \langle Y_{\lambda,0}|Y_{1,0}|Y_{\ell_i,0}\rangle \langle R_{k,\lambda}|r|R_{n_i,\ell_i}\rangle\ \delta_{m_i,0}, \tag{47}$$

where the XUV frequency satisfies $\epsilon_i + \Omega = \epsilon = k^2/2$ for process (d). Note that only initial states with zero magnetic quantum number, $m_i = 0$, will contribute to photoelectron emission along $\hat{z}$, as indicated by the Kronecker delta at the end of Eq. (47) that originates from the explicit properties of the spherical harmonics along $\hat{z}$: $Y_{\lambda,m_i}(\hat{z}) = \sqrt{(2\lambda+1)/3}\ \delta_{m_i,0}$.

The *two-photon* matrix element for photoelectrons along the polarization direction is

$$M(k\hat{z};\epsilon_i+\Omega_<) = \frac{(8\pi)^{3/2}}{i} E_{\Omega_<} E_\omega \sum_L (-i)^L \sqrt{\frac{2L+1}{3}} e^{i\eta_L(k} \times \sum_\lambda \langle Y_{L,0}|Y_{1,0}|Y_{\lambda,0}\rangle \langle Y_{\lambda,0}|Y_{1,0}|Y_{\ell_i,0}\rangle \times T_{L,\lambda,\ell_i}(k;\epsilon_i+\Omega_<)\ \delta_{m_i,0}, \tag{48}$$

where $\epsilon_i + \Omega_< + \omega = \epsilon$ for process (a). A similar expression, $M(k\hat{z},\epsilon_i+\Omega_>)$, can be written for process (e) where $\epsilon_i +$

$\Omega_> - \omega = \epsilon$, and where the complex conjugate of the laser field, E^*_ω, is used for emission of a laser photon. Again, only initial states with zero magnetic quantum number contribute.

The PROOF method [20] relies on the interference between these three quantum paths, denoted $M^{(d)}$, $M^{(a)}$ and $M^{(e)}$, as a function of the XUV-laser delay, τ. The probability for emission of an electron with final momentum k along the polarization axis $\hat{z}$ is

$$P(k\hat{z}) \propto |M^{(d)} + M^{(a)} + M^{(e)}|^2, \tag{49}$$

where only cross-terms lead to delay dependent modulations. Provided that the laser field is *relatively* weak, we expect the interference cross-terms (d)-(a) and (d)-(e), will dominate over the cross-term (a)-(e), because the former involve the exchange of only one laser photon while the latter contributes to higher order terms in a perturbative treatment, involving the exchange of two laser photons ω.

In order to illustrate the origin of the attosecond delay within this framework, we consider a final energy that is higher than the central energy of the photoelectron wave packet, $\epsilon = \epsilon_i + \Omega > \epsilon_i + \Omega_0$. In this region, the ω modulation is dominated by the (d)-(a) interference, because path (a) goes through a central part of the XUV distribution, while path (e) passes through a higher frequency range, in the upper part of the XUV bandwidth [Fig. 4]. Increasing the bandwidth of the attosecond pulse or decreasing the probe photon frequency makes this distinction less pronounced. We restrict our analysis to the case of an initial s-state, $\ell_i = 0$, and study the interference of the cross term (d)-(a). The relevant phase reads

$$\begin{aligned}\arg[M^{(a)*}M^{(d)}] \approx & -\omega\tau + \phi_\Omega - \phi_{\Omega_<} \\ & + \eta_\lambda(k) - \eta_\lambda(\kappa_<) - \phi_{cc}(k,\kappa_<) - \frac{\pi}{2},\end{aligned} \tag{50}$$

where we have used the asymptotic approximation for the phase of the two-photon matrix element as in Eq. (25), thereby, introducing the continuum–continuum phase into the framework of laser-assisted photoioization by single attosecond pulses. Also, we note that the phase-shifts present in the two-photon matrix element are those of $p-$waves ($\lambda = 1$). In terms of the temporal delays, the ω modulation is displaced by

$$\begin{aligned}\tau &\approx \frac{\phi_\Omega - \phi_{\Omega_<}}{\omega} + \frac{\eta_\lambda(k) - \eta_\lambda(\kappa_<)}{\omega} - \frac{\phi_{cc}(k,\kappa_<)}{\omega} - \frac{\pi}{2\omega} \\ &\equiv \tau_\Omega \ + \ \tau_\lambda(k) \ + \ \tau_{cc}(k;\omega) \ - \ \frac{\pi}{2\omega},\end{aligned} \tag{51}$$

where we have used the definition of the continuum–continuum delays τ_{cc}, Eq. (45), and the following relation for the continuum–continuum phases ϕ_{cc}:

$$\phi_{cc}(k,\kappa_<) \approx -\phi_{cc}(k,\kappa_>), \tag{52}$$

which is exact in the soft-photon limit. Similarly to Eq. (51), we can compute the modulation at the low energy end of the electron distribution using the cross term (d)-(e), and we find the same result but shifted by a half laser period, *i.e.* out of phase by π. This $\pi-$shift of the modulation is important to explain the onset of streaking, because it ensures that the high-energy probability of the electron spectra is maximized when the low-energy part is minimized. In the central region, $\epsilon \approx \epsilon_i + \Omega_0$, the (d)-(a) and (d)-(e) contributions will be comparable, leading to a relative cancellation of the ω modulation, leaving only the 2ω modulation. In total, the electron momentum distribution is slightly shifted up or down depending on the sub-cycle delay between the laser field and the attosecond pulse: It is *streaked* as expected from the classical (or strong-field) picture. Using Eq. (51), we find that this streaking modulation is displaced by a Wigner-like delay, $\tau_\lambda(k)$, and by the continuum–continuum delay, $\tau_{cc}(k;\omega)$. We can interpret this delay as the time it takes for the electron to be photoionized *plus* the time it takes for the measurement process to occur, *i.e.* for a lower energy electron to absorb one probe photon so that it may interfere with the direct path. We stress that this analysis was made assuming a monochromatic probe field, while it is common in streaking experiments to use few-cycle IR laser pulse, which leads to a convolution (a blurring effect) of the momentum modulation and of the attosecond time-delays.

4.3. Comparison between the two measurements

We now briefly discuss the small differences of τ_{cc} occuring between the RABBIT method and the streaking method. Eq. (52) implies that

$$\begin{aligned}\tau_{cc}(k;\omega) &\equiv \frac{\phi_{cc}(k,\kappa_>) \ - \ \phi_{cc}(k,\kappa_<)}{2\omega} \\ &\approx \ \frac{\phi_{cc}(k,\kappa_>)}{\omega},\end{aligned} \tag{53}$$

where the first line corresponds to the RABBIT method and the second line corresponds to the streaking method. These different "flavours" of τ_{cc} merge completely in the soft-photon limit, $\epsilon \gg \omega$, but differ slightly at low kinetic energies, where the phases are not exact opposites. In both methods, τ_{cc} varies with k inside the bandwidth of the photoelectron wavepacket.

Furthermore, it is interesting to note that the group delays of the attosecond pulses and Wigner delays of the photoelectrons appear as discrete derivatives over one and two ω photons in the streaking and RABITT methods respectively. Here, we have assumed that all delays are slowly varying so that the discrete derivatives are equivalent. We also note that the streaking method relies on the cross-terms: (d)-(a) and (d)-(e); while the RABBIT method relies on the (a)-(e) contribution. The weaker signal in the RABBIT method is not a problem, since it is recorded between the harmonics, on "zero background". Consequenty, the modulation frequency of the streaking/PROOF signal is ω due to the single laser photon involved in each appropriate cross term, while the corresponding RABBIT

frequency is 2ω due to the two laser photons involved in the latter cross term. Another important difference between the methods is related to symmetry (parity): The ω signal is somewhat restricted to the $\hat{z}$ direction and it is not observed if photoelectrons are collected in all directions; while the 2ω signal is more general and it prevails also when electrons in all directions are collected. Interestingly, we have shown that all three attosecond characterization methods (RABITT, PROOF and streaking) provide equivalent temporal information about the XUV ionization process, even though they are built from different sets of cross-terms associated to different interfering quantum paths.

5. Results

5.1. Calculations of attosecond time-delays

In Fig. 5, we plot atomic delays relevant for laser-assisted photoionization. The Wigner-like delays, τ_λ, are

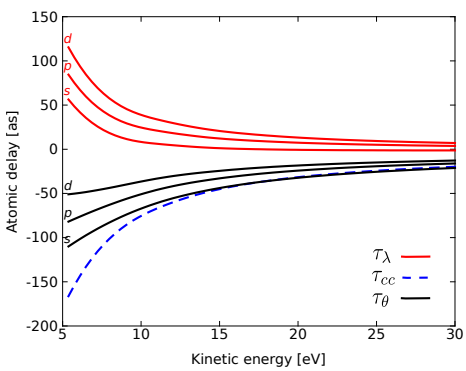

Figure 5: Atomic delays of laser-assisted photoionization in hydrogen for three different angular momenta of the wave-packet wavefunction in the intermediate state (s, p and d : $\lambda = 0$, 1 and 2). The delays are calculated using the regularized approximation. The data correspond to $Z = 1$ and a laser probe with $\omega = 1.55$ eV.

calculated from the finite-difference derivative of the scattering phase of hydrogen for angular momentum, $\lambda = [0, 1, 2]$, corresponding to s, p and d continuum wave packets. The universal continuum–continuum delay, τ_{cc}, plus these Wigner-like delays yields the total atomic delay, τ_θ. Notice that the sign of τ_λ and τ_{cc} are opposite, so that τ_θ is smaller than either of the contributions individually. The increase of τ_λ with the angular momentum can be understood as due to the repulsive, short-range, centrifugal potential. The total delay is negative in this example, which implies that the electron appears as being *advanced* compared to the probe field.

In Fig. 6, we evaluate the accuracy of τ_{cc} as derived by various degrees of the asymptotic approximation by comparison with exact calculations in hydrogen from the $1s$ state along two different angular momentum sequences: $s \to p \to s$ (+) and $s \to p \to d$ (×). Indeed, we find

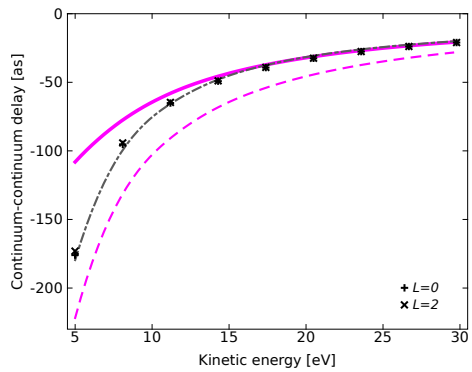

Figure 6: Continuum–continuum delays calculated using the asymptotic approximation (dashed curve), Eq. (22), the long-range amplitude-corrected asymptotic approximation (thick curve), Eq. (30), and the regularized asymptotic approximation (dash-dot curve). The approximate delays are compared with exact delays computed from the $1s$ state in hydrogen by subtracting the intermediate Wigner delay. The data correspond to $Z = 1$ and to a laser probe with $\omega = 1.55$ eV.

that the exact τ_{cc} are almost completely independent of the final state angular momentum. The asymptotic approximation (dashed curve) predicts the correct qualitative behavior of the delay, but it slightly overestimates its magnitude. By taking into account the long-range amplitude effects, the agreement is excellent at high kinetic energies. The disagreement at low energy can be removed by avoiding the radial singularity in Eq. (28), namely by an *ad hoc* substitution of $r \to r + i(1 - |k - \kappa|/2)$. In this way, we obtain a "regularized" continuum–continuum delay (dot–dashed curve), which is excellent at *all* energies in the range.

In Fig. 7, we address the question of the universality of τ_{cc} by computing the exact two-photon phases from three different intial states in hydrogen: $1s$, $2s$ and $2p$. We find that all seven different angular-momentum sequences, $\ell_i \to \lambda \to L$, line up on the same universal curve, in excellent agreement with the regularized continuum–continuum delay. In this way, we have verified that not only $s-$type initial states have similar τ_{cc}, but also initial $p-$states with non-zero angular momentum.

In Fig. 8, we present a contour plot that provides a rough overview of the magnitude of τ_{cc} as a function of the kinetic energy of the photoelectron and of the wavelength of the probe field. In general, τ_{cc} decreases with the kinetic energy and it increases with the wavelength of the probe field. We note that a softer probe photon leads to an increased delay. A few selected τ_{cc} curves are displayed in Fig. 9 for a more quantitative comparison at some experimentally relevant wavelengths. We conclude that τ_{cc} is

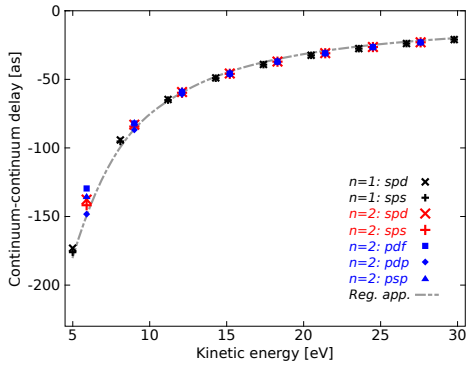

Figure 7: Continuum–continuum delays from exact calculations in hydrogen from different intial states: $1s$ (black symbols), $2s$ (red symbols) and $2p$ (blue symbols). This data demonstrates the *universality* of the continuum–continuum delay and that it is valid not only for initial states of $s-$character. The exact data is in excellent agreement with the regularized approximation. The data correspond to $Z = 1$ and a laser probe with $\omega = 1.55$ eV.

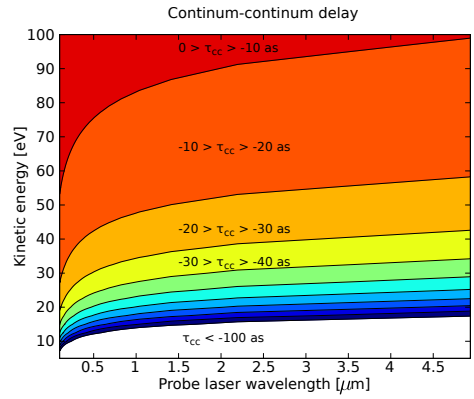

Figure 8: Contour plot of continuum–continuum delays at different kinetic energy and laser probe wavelength. The delays are calculated using the regularized asymptotic approximation.

not extremely sensitive to the probe wavelength, except at low kinetic energies, where it takes larger negative values when the probe wavelength increases. As already mentioned, the delays converge to zero as the kinetic energy is increased, however, the convergence is rather slow and there is still ~ -10 as of delay remaining at a relatively high kinetic energy of ~ 100 eV.

Finally, in Fig. 10, we examine the validity of the soft-photon approximation by comparing τ_{cc} and $\tau_{cc}^{(soft)}$, calculated using Eq. (22) and Eq. (23), respectively. The soft-photon limit over-estimates the magnitude of the delay at low energies, but it converges rapidly towards the quantum mechanical result as the kinetic energy is increased.

5.2. Conclusions

The main result of this work is the determination of the *phase* associated with two-photon transition matrix elements for laser-assisted XUV photoionization, namely Eq. (25). These phases have broad applications in attosecond science as they enter naturally in most characterization methods, as well as in quantum control schemes and delay experiments of more general character. We have demonstrated that the phase is composed of two distinct atomic contributions: i) The one-photon scattering phase of the intermediate state and ii) a quantity, given in Eq. (22), that we call the continuum–continuum phase. The latter is *universal* and it describes the added phase induced by the transition from the intermediate continuum state to the final continuum state. It is independent of the short-range behavior of the atomic potential and it depends only on three quantities: the final momentum, the laser-probe frequency and the charge of the remaining ionic core. As expected from the strong-field approach, the transition phase is reduced to that of the one-photon (intermediate) scattering phase when the charge of the remaining ion is neglected, *i.e.* for a short-range potential. Other interesting findings are related to the classical–quantum correspondence: First, the phase of the classical dipole, for exchange of radiation in the continuum, Eq. (40), is closely related, but not identical, to the soft-photon limit of the quantum mechanical continuum–continuum phase, Eq. (23). Further, as epitomized in Eq. (41), there exists a relationship between the initial radial position of the ejected electron (a classical concept) and the asymptotic quantum phase. We have also demonstrated how the theory of complex transition matrix elements, originally developed for RABBIT, can help to better understand attosecond streaking measurements. In our interferometric interpretation of streaking, we stressed the benefits of a weak and monochromatic laser probe field. Given such experimental conditions, quantitative analysis of more complex systems can be carried out using two-photon transition matrix elements, corrected by many-body perturbation theory.

Acknowledgements

This research was supported by the Marie Curie program ATTOFEL (ITN), the European Research Council (ALMA), the Joint Research Programme ALADIN of Laserlab-Europe II, the Swedish Foundation for Strategic Research, the Swedish Research Council, the Knut and Alice Wallenberg Foundation, the French ANR-09-BLAN-0031-01 ATTO-WAVE program, COST Action CM0702 (CUSPFEL).

Parts of the computations have been performed at IDRIS and part of the work was carried out at the NORDITA workshop: "Studying Quantum Mechanics in the Time

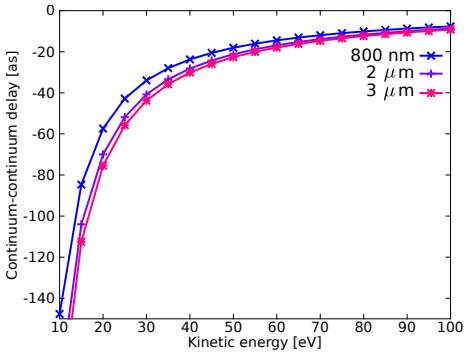

Figure 9: Continuum–continuum delays for different IR laser photon energies: 1.55 eV (× symbol), 0.62 eV (+ symbol) and 0.41 eV (∗ symbol). The delays are calculated using the regularized asymptotic approximation.

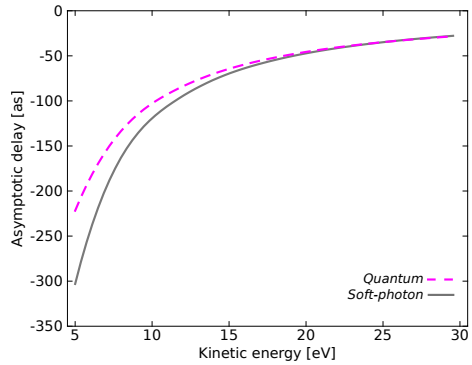

Figure 10: Continuum–continuum delays calculated using the asymptotic approximation (dashed curve) using Eq. (22). They are compared to the corresponding soft-photon limit (curve) using Eq. (23). The data correspond to $Z = 1$ and to a laser probe with $\omega = 1.55$ eV.

Domain", in Stockholm. One of us (J.M.D.) would like to thank Professor Eva Lindroth for helpful discussions.

Appendix A: Formal derivation of the approximate expression for the radial component of the 2-photon ATI transition amplitudes

The radial component of the two-photon ATI matrix elements given in Eq. (6) can be rewritten:

$$T_{L,\lambda,\ell_i}(k;\epsilon_i+\Omega) = \lim_{\varepsilon\to 0^+}\langle R_{k,L}|r\,G_\lambda(\epsilon_i+\Omega+i\varepsilon)\,r|R_{n_i,\ell_i}\rangle. \tag{54}$$

Here the initial atomic state is represented by the radial wavefunction $R_{n_i,\ell_i}(r)$, while $R_{k,L}(r)$ is the wavefunction of the photoelectron with energy $k^2/2 = \epsilon_i + \Omega \pm \omega$. $G_\lambda(r_2, r_1; \epsilon_i + \Omega)$ is the radial component, of the Green's function given in Eq. (33) for angular momentum λ and positive energy argument $\kappa^2/2 = \epsilon_i + \Omega > 0$. We note the presence of the positive imaginary infinitesimal $i\varepsilon$ in the argument of G: It corresponds to the change $\kappa \to \kappa + i\varepsilon/\kappa$, which ensures the presence of a converging factor $e^{-\epsilon r}$ in the integrals below, which otherwise would be divergent. For the sake of conciseness, we will omit this factor in the following.

In the limit of large values of the coordinates r_1 and r_2, the Green's function takes the following limiting form, written for the case of a Coulomb potential, [37, 38]:

$$G_\lambda(r_2,r_1;\epsilon_i+\Omega) \approx -\frac{2}{r_1 r_2\kappa}e^{i[\kappa r_> + \Phi_{\kappa,\lambda}(r_>)]} \times \sin[\kappa r_< + \Phi_{\kappa,\lambda}(r_<)] \tag{55}$$

where $r_>$ (resp. $r_<$) denotes the larger (resp. smaller) of (r_1, r_2) and the phases $\Phi_{\kappa,\lambda}(r)$ are defined in Eq. (12).

We consider now the case of two-photon ATI from the $1s$ state of a hydrogenic system with $R_{1,0}(r) = C_{1,0}e^{-Zr}$ and normalization constant $C_{1,0} = 2Z^{3/2}$, while the photoelectron is described by a continuum wavefunction with asymptotic form given in Eq. (11). In the case considered here, $\lambda = 1$ while $L = 0, 2$. Replacing in the general expression of the amplitude Eq. (54), one has:

$$T_{L,1,0}(k;\epsilon_{1s}+\Omega) = -\frac{2}{k}C_{1,0}N_k\int_0^\infty dr_2 r_2 \sin[kr_2+\Phi_{k,L}(r_2)] \int_0^\infty dr_1 r_1^2 e^{-Zr_1}e^{i[\kappa r_> + \Phi_{\kappa,\lambda}(r_>)]}\sin[\kappa r_< + \Phi_{\kappa,\lambda}(r_<)] \tag{56}$$

and splitting the integration ranges over $r_>$ and $r_<$, one gets:

$$T_{L,1,0}(k;\epsilon_{1s}+\Omega) = -\frac{2}{k}C_{1,0}N_k\int_0^\infty dr_2 r_2 \sin[kr_2+\Phi_{k,L}(r_2)] \times\{e^{i[\kappa r_2+\Phi_{\kappa,1}(r_2)]}\int_0^{r_2} dr_1 r_1^2 e^{-Zr_1}\sin[\kappa r_1+\Phi_{\kappa,1}(r_1)] + \sin[\kappa r_2+\Phi_{\kappa,1}(r_2)]\int_{r_2}^\infty dr_1 r_1^2 e^{-Zr_1}e^{i[\kappa r_1+\Phi_{\kappa,1}(r_1)]}\} \tag{57}$$

From the two r_1-integrals present within the braces, the first one is by far dominant. This comes from the presence of the exponentially decaying wavefunction of the ground state, which ensures that the integration range containing the origin is dominant. Thus, one can neglect the second term and one has:

$$T_{L,1,0}(k;\epsilon_{1s}+\Omega) \approx -\frac{2}{k}C_{1,0}N_k \int_0^\infty dr_2 r_2 \sin[kr_2+\Phi_{k,L}(r_2)]e^{i[\kappa r_2+\Phi_{\kappa,1}(r_2)]} \times\int_0^{r_2} dr_1 r_1^2 e^{-Zr_1}\sin[\kappa r_1+\Phi_{\kappa,1}(r_1)] \tag{58}$$

We remark that the r_1-integral contained in this expression is real: $\int dr_1 ... \in \mathbf{R}$ and its precise value does not affect the overall phase of the amplitude which becomes:

$$\arg[T_{L,1,0}(k;\epsilon_{1s}+\Omega)] \approx$$
$$\arg\{-\int_0^\infty dr r \sin[kr+\Phi_{k,L}(r)] e^{i[\kappa r+\Phi_{\kappa,1}(r)]}\} \qquad (59)$$

or, making explicit the expressions of the Coulomb phases Φ, writing the sine function under its exponential form and keeping only the $r-$dependent terms in the integrand, the amplitude can be expressed in terms of the integrals $J_\pm$ defined in Eq. (19). Following the same line of reasoning as the one followed in Sec 3.2, one can neglect the contribution of the J_+ integral, so that:

$$\arg[T_{L,1,0}(k;\epsilon_{1s}+\Omega)] \approx \arg\{(-)^{\frac{L+2}{2}}(2\kappa)^{iZ/\kappa} e^{i\sigma_1(\kappa)}$$
$$(2k)^{-iZ/k} e^{-i\sigma_L(k)} \int_0^\infty dr r^{1+iZ(1/\kappa-1/k)} e^{i(\kappa-k)r}]\}. \quad (60)$$

where the last integral represents a Gamma function of complex argument times algebraic factors, so that one recovers the expression of the phase of the radial amplitude given in Eq. (21).

This expression, which has been established for an initial $1s$ hydrogenic state with nuclear charge Z, remains valid for any s bound state with an exponentially decaying wavefunction. As already mentioned, for non-hydrogenic systems, the Coulomb phase-shifts have to be replaced by the relevant scattering phase-shifts .

For the sake of reference, we give the complete expression of the asymptotic form of the amplitude, including real factors:

$$T_{L,1,0}(k;\epsilon_{1s}+\Omega) \approx (-)^{\frac{L+2}{2}} \frac{1}{k} C_{1,0} N_k e^{-\frac{\pi Z}{2}(\frac{1}{\kappa}-\frac{1}{k})}$$
$$\frac{(2\kappa)^{iZ/\kappa}}{(2k)^{iZ/k}} e^{i[\sigma_1(\kappa)-\sigma_L(k)]} \frac{\Gamma[2+iZ(1/\kappa-1/k)]}{(\kappa-k)^{2+iZ(1/\kappa-1/k)}}$$
$$\times \int_0^\infty dr r^2 e^{-Zr} \sin[\kappa r+\Phi_{\kappa,1}(r)] \qquad (61)$$

[1] M. Schultze *et al.*, Science **328**, 1658 (2010).
[2] E. Goulielmakis *et al.*, Science **305**, 1267 (2004).
[3] K. Klünder *et al.*, Phys. Rev. Lett. **106**, 143002 (2011).
[4] V. Véniard, R. Taïeb and A. Maquet, Phys. Rev. Lett. **74**, 4161 (1995).
[5] V. Véniard, R. Taïeb and A. Maquet, Phys. Rev. A **54**, 721 (1996).
[6] H. G. Muller, Appl. Phys. B **74**, S17 (2002).
[7] V.S. Yakovlev *et al.*, Phys. Rev. Lett. **105**, 073001 (2010).
[8] A.S. Kheifets and I.A. Ivanov, Phys. Rev. Lett. **105**, 233002 (2010).
[9] I.A. Ivanov, Phys. Rev. A **83**, 023421 (2011).
[10] S. Nagele *et al.*, J. Phys. B: Atom. Molec. Opt. Phys. **44**, 081001 (2011).
[11] C.-H. Zhang and U. Thumm, Phys. Rev. A **84**, 033401 (2011).
[12] Misha Ivanov and Olga Smirnova, Phys. Rev. Lett. **107**, 213605 (2011).
[13] R. Pazourek, S. Nagele, K. Doblhoff-Dier, J. Feist, C. Lemell, K. Tőkési and J. Burgdörfer, arXiv:1111.4172 v1 [physics.atom-ph] 17 Nov 2011.
[14] E.P. Wigner, Phys. Rev. **98**, 145 (1955).
[15] C. A. A. de Carvalho and H. M. Nussenzveig, Physics Reports **364**, 83 (2002).
[16] O. Smirnova, M. Spanner and M.Y. Ivanov, J. Phys. B: Atom. Molec. Opt. Phys. **39**, S323 (2006).
[17] O. Smirnova *et al.*, J. Phys. B **40**, F197 (2007).
[18] C.-H. Zhang and U. Thumm, Phys. Rev. A **82**, 043405 (2010).
[19] J.C. Baggesen and L.B. Madsen, Phys. Rev. Lett. **104**, 209903 (2010).
[20] M. Chini, S. Gilbertson, S.D. Khan and Z. Chang, Opt. Express, **18**, 13006 (2010).
[21] P.M. Paul, E.S. Toma, P. Breger, G. Mullot, F. Augé, Ph. Balcou, H.G. Muller, and P. Agostini, Science **292**, 1689 (2001).
[22] Y. Mairesse, A. de Bohan, L.J. Frasinski, H. Merdji, L.C. Dinu, P. Monchicourt, P. Breger, M. Kovačev, R. Taïeb, B. Carré, H.G. Muller, P. Agostini, P. Salières, Science **302**, 1540 (2003).
[23] A. Maquet and R. Taïeb, J. Mod. Opt. **54**, 1847 (2007).
[24] L.D. Landau and E.M. Lifshitz, *Quantum Mechanics: Nonrelativistic Theory* 3rd edition, Pergamon Press, Oxford (1977); §136.
[25] E.S. Toma and H.G. Muller, J. Phys. B: Atom. Molec. Opt. Phys. **35**, 3435 (2002).
[26] D.J. Kennedy and S.T. Manson, Phys. Rev. A **5**, 227 (1972).
[27] A. L'Huillier, L. Jönsson and G. Wendin, Phys. Rev. A 33, 3938 (1986)
[28] Ref. [26] uses an Hartree-Fock calculation. In case of strong intershell correlations, a better description is needed, A. Kheifets, private communication (to be published).
[29] W. Zernik and R.W. Klopfenstein, J. Math. Phys. **6**, 262 (1965).
[30] S. Klarsfeld and A. Maquet, Phys. Lett. **73A**, 100 (1979).
[31] S. Klarsfeld and A. Maquet, J. Phys. B: Atom. Molec. Phys. **12**, L553 (1979).
[32] M. Aymar and M. Crance, J. Phys. B: Atom. Molec. Phys. **13**, L287 (1980).
[33] A. Maquet, V. Véniard and T. Marian, J. Phys. B: Atom. Molec. Opt. Phys. **31**, 3743 (1998).
[34] M. Rotenberg, in *Advances in Atomic and Molecular Physics* edited by D.R. Bates and I. Estermann (Academic Press, New-York, 1970) Vol. 6, pp. 233.
[35] A. Maquet, Phys. Rev. A **15**, 1088 (1977).
[36] H. Friedrich, 'Theoretical Atomic Physics', Springer-Verlag Berlin Heidelberg (2006).
[37] B.A. Zon, N.L. Manakov, and L.P. Rapoport, Sov. Phys. Doklady **14** 904 (1970).
[38] M. Edwards, X. Tang and R. Shakeshaft, Phys. Rev. A **35**, 3758 (1987).

Paper V

Phase Measurement of Resonant Two-Photon Ionization in Helium

M. Swoboda, T. Fordell, K. Klünder, J. M. Dahlström, M. Miranda, C. Buth, K. J. Schafer, J. Mauritsson, A. L'Huillier and M. Gisselbrecht.

Phys. Rev. Lett. **104**, 103003 (2010).

PRL 104, 103003 (2010) PHYSICAL REVIEW LETTERS week ending 12 MARCH 2010

Phase Measurement of Resonant Two-Photon Ionization in Helium

M. Swoboda,[1] T. Fordell,[1] K. Klünder,[1] J. M. Dahlström,[1] M. Miranda,[1,2] C. Buth,[3,4] K. J. Schafer,[3,4] J. Mauritsson,[1] A. L'Huillier,[1,*] and M. Gisselbrecht[1]

[1]*Department of Physics, Lund University, P.O. Box 118, 22100 Lund, Sweden*
[2]*Departamento de Física, Universidade do Porto, Rua do Campo Alegre 687, 4169-007 Porto, Portugal*
[3]*Department of Physics and Astronomy, Louisiana State University, Baton Rouge, Louisiana 70803, USA*
[4]*PULSE Institute, SLAC National Accelerator Laboratory, Menlo Park, California 94025, USA*

(Received 18 December 2009; published 12 March 2010)

We study resonant two-color two-photon ionization of helium via the $1s3p\ ^1P_1$ state. The first color is the 15th harmonic of a tunable Ti:sapphire laser, while the second color is the fundamental laser radiation. Our method uses phase-locked high-order harmonics to determine the *phase* of the two-photon process by interferometry. The measurement of the two-photon ionization phase variation as a function of detuning from the resonance and intensity of the dressing field allows us to determine the intensity dependence of the transition energy.

DOI: 10.1103/PhysRevLett.104.103003 PACS numbers: 32.80.Rm, 32.70.Jz, 32.80.Qk, 42.65.Ky

Multicolor resonant ionization is at the heart of numerous and diverse applications in fundamental and applied sciences. Examples are studies of very high Rydberg states [1], investigations of biomolecules [2] and specific selection of radioactive species [3]. In the simplest scheme, resonantly enhanced two-photon ionization (R2PI) occurs via the absorption of two photons, generally of different colors, one tunable (ω_1) used to scan across a resonant state (r), and the second (ω) ionizing from the excited state. In traditional R2PI, the *yield* of the produced ion species is recorded as a function of laser wavelength, and the position and shape of the observed resonance provides information on the underlying electronic and rovibrational structures. These studies rely on spectroscopic information using narrow-bandwidth lasers, which do not allow any temporal resolution. Here, we present an ultrafast time-resolved-technique to retrieve also the *phase* of R2PI when sweeping through the resonance. We demonstrate it by studying R2PI of He via the $1s3p\ ^1P_1$ state which lies 23.087 eV above the ground state.

The basic principle of our experiment is illustrated in Fig. 1. We study the interference between two pathways to the same ionized final state (f_1), one through the resonance with absorption of two photons with frequency ω_1 and ω, and the second through a continuum path, using a third color (ω_2), involving absorption of a photon with frequency ω_2 and emission of a photon with frequency ω. The phase of the R2PI is encoded in the modulation of the photoelectron signal S_{f_1} as a function of the delay τ between the (ω_1, ω_2) fields and the ω field [Fig. 1(b)]. When the energy of the exciting radiation ω_1, and thus the detuning from the resonance is changed, the phase variation of the resonant transition leads to a measurable shift of the S_{f_1} oscillation. This phase shift needs to be referenced against another modulation S_{f_2} that is independent of the resonance and thus providing a *clock* to our measurement. A process providing an independent modulation requires a fourth color (ω_3) and involves another final state (f_2) (see Fig. 1).

An essential requirement for our measurement is the use of phase-locked radiation fields with commensurate frequencies, and a temporal precision better than the periodicity of the interference signal, in our case 1.3 fs. Another requirement, is a high spectral resolution for the excitation of a narrow resonance. These requirements can be simultaneously fulfilled by using the high-order harmonic frequency combs produced when an intense laser field interacts with a gas of atoms or molecules [4]. As is now well understood [5,6], harmonics arise due to interferences

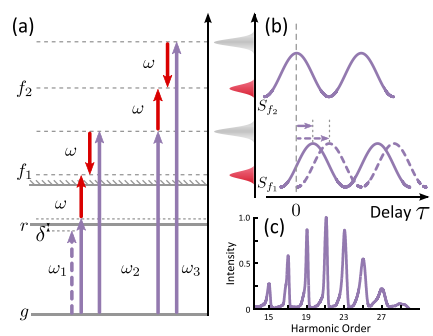

FIG. 1 (color online). (a) Schematic diagram illustrating the phase measurement of R2PI. The dashed and solid ω_1 lines represent two excitation energies on either side of the resonance. The photoelectron peaks used in the measurement are S_{f_1} and S_{f_2}. (b) Illustration of modulated sideband signals S_{f_1} and S_{f_2}. Two S_{f_1} modulations are indicated, corresponding to the two excitation energies in (a). (c) Experimental harmonic spectrum used in the measurements.

between attosecond pulses produced by tunnel ionization, acceleration of the created wave packet in the field and recombination back to the ground state at each half cycle of the laser field. The spectral width of the individual harmonics is thus related to the number of attosecond pulses, and decreases as the laser pulse duration increases [7]. In this process, a comb of phase-locked harmonics of odd order is generated.

In the present work, we use high-order harmonics to study two-color photoionization of He via the $1s3p\ ^1P_1$ state [8,9]. In contrast to the "reconstruction of attosecond bursts by interference of two-photon transition" (RABITT) technique, used to determine the pulse duration of attosecond pulses [10,11] and similarly to previous work performed in Ne [12] and N_2 [13], we eliminate the influence of the temporal characteristics of the attosecond pulses to concentrate on the influence of the atomic properties. We study the R2PI phase as a function of detuning from the resonance, by varying the fundamental wavelength (around 805 nm) or alternatively by increasing the fundamental intensity. We apply these measurements to determine the intensity-dependence of the energy of the $1s^2 \rightarrow 1s3p$ transition, and interpret the results using theoretical calculations consisting of solving the time-dependent Schrödinger equation (TDSE) in conditions close to the experimental ones [14].

Our experiments were performed with a 1-kHz 35-fs 4-mJ Ti:sapphire laser system. An acousto-optic programmable dispersive filter (DAZZLER) was used to change the central wavelength between 802.5 and 809.3 nm, while maintaining the spectral width of the amplified pulses approximately equal to 25 nm. High-order harmonics were generated in a pulsed Ar gas cell, filtered using a spatial aperture and a 200-nm thick Al thin film [15], and focused by a toroidal mirror into a vacuum chamber containing an effusive He gas jet. A magnetic bottle electron spectrometer (MBES) allowed us to record and analyze in energy the ejected electrons. Part of the laser field was extracted before the generation of harmonics, and recombined downstream collinearly with the harmonics, after a variable time delay that could be adjusted with sub-100-as precision [12].

A comb of about seven phase-locked harmonic fields [Fig. 1(c)], corresponding in the time domain to a train of attosecond pulses of 260 as duration, was thus sent into the interaction chamber together with the dressing field at frequency ω with an adjustable phase φ (or time $\tau = \varphi/\omega$) delay. In addition, a half-wave plate and polarizer in the dressing IR field arm allowed precise control of the pulse energy and therefore the intensity in the interaction region of the MBES. The detuning was determined from $\delta = 15hc/\lambda_0 - E_{3p}$, where E_{3p} is 23.087 eV and λ_0 is the barycenter of the fundamental frequency spectrum, shifted to the blue by $\delta\lambda \simeq 3.5$ nm to account for the blueshift from free electrons in the generation gas [16,17]. The dressing laser intensity was determined by measuring the energy shifts of the photoelectron peaks of harmonics 17 to 23 in the presence of the laser field, which is simply equal to the ponderomotive energy $U_p \approx 6.0I$ eV where the intensity I is in units of 10^{14} W cm^{-2} for a laser wavelength of 800 nm [18,19].

Figures 2(a) and 2(b) present electron spectra as a function of delay between the harmonics and the dressing field, obtained for two different detunings. Electrons are observed at energies corresponding to one-photon absorption of the harmonics (from the 17th) and at "sideband" energies due to two-photon ionization processes, which we label by the corresponding net number of infrared photons (16, 18, etc.). These sideband peaks strongly oscillate with the delay at a frequency equal to 2ω. The oscillations of sidebands 18, 20, 22, and 24 do not depend on the detuning, while sideband 16 is strongly affected by it. A Fourier transform of the sideband signal over about 10 fs (four cycles) allows us to determine the relative phases of the sideband oscillations with a precision of 0.1 rad. The phases are plotted in Fig. 2(c) for the two cases shown in (a),(b).

The relationship between the R2PI phase and the experimental results in Fig. 2 can be understood within second-order perturbation theory [10,12]. Using the notation from Fig. 1, the photoelectron signal S_{f_1} can be expressed as

$$S_{f_1} = |a_1^a + a_2^e|^2, \tag{1}$$

where a_1^a and a_2^e are the two-photon probability amplitudes with the superscript a or e referring to an absorption or emission of an ω photon and with the subscript 1 or 2 referring to absorption of an ω_1 or ω_2 photon. Introducing φ_1 and φ_2 as the phases of the radiation fields, as well as

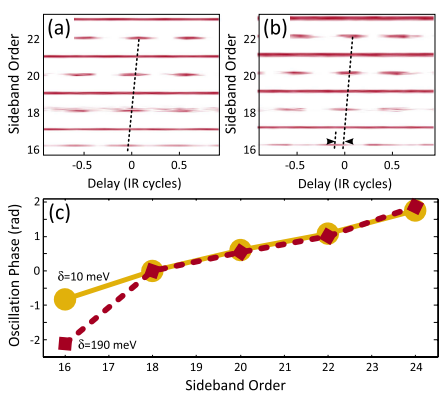

FIG. 2 (color online). Electron spectra as a function of delay for detunings $\delta = 10$ meV (a) and $\delta = 190$ meV (b). The oscillation of the 16th sideband depends on the detuning while the others do not (see dashed line) (c) Phase of the oscillations of the sideband peaks in light orange for (a) and dark red for (b). The two results have been superposed at sideband 18.

φ_1^a and φ_2^e as the phase terms involved in the two-photon transitions, Eq. (1) becomes

$$S_{f_1} = ||a_1^a|e^{i\varphi_1^a + i\varphi_1 + i\varphi} + |a_2^e|e^{i\varphi_2^e + i\varphi_2 - i\varphi}|^2$$
$$= |a_1^a|^2 + |a_2^e|^2 + 2|a_1^a a_2^e|\cos(\varphi_1^a - \varphi_2^e + 2\varphi + \varphi_1 - \varphi_2). \quad (2)$$

The cosine term leads to the modulation of the signal observed in the experiment. In general, the phase terms involved do not depend much on the photon energies. In two-photon ionization via a resonant state, however, the phase (φ_1^a) changes by π across the resonance. The study of the variation of φ_1^a as a function of detuning δ provides interesting information on the two-photon ionization process, e.g., on the relative importance of resonant and nonresonant contributions, ac Stark shift of the resonant state, depending on the spectral characteristics of the XUV and laser fields.

The variation of φ_1^a with the detuning can be experimentally obtained from $S_{f_1}(\varphi)$ provided the other phase terms φ_2^e, φ_1, φ_2 do not depend on δ and provided the phase delay φ is known in absolute value, which is generally not the case. $S_{f_1}(\varphi, \delta)$ is therefore referenced against $S_{f_2}(\varphi)$, assuming that the phase terms involved, φ_2^a and φ_3^e, are independent of the detuning and thus removing the need of knowledge of the absolute φ. When changing δ, the laser intensity used to generate the harmonics varies slightly, leading to a (small) variation of the group delay of the attosecond pulses and thus of $\varphi_1 - \varphi_2$. We take this effect into account by assuming a linear group delay [20], which we experimentally determine using higher-order sidebands. Its contribution is then subtracted from the measured phases and the phase of sideband 18 is set to zero for all detunings. The results are presented in Fig. 3(a). As expected, the phases corresponding to all sidebands except the 16th are almost superposed to each other and show no influence of detuning.

Figure 3(b) shows the variation of the R2PI phase as a function of detuning. We can tune only over half the resonance since for lower (negative detunings) sideband 16 moves progressively below the ionization threshold, thus making our phase measurement inaccurate. We also compare our measurements with the results of two different calculations (solid lines): The dark red line is obtained by a simple perturbative model [21], only considering the resonant state. Gaussian envelopes were used for the ir and XUV pulses with FWHMs of 30 and 10 fs, respectively. The light orange curve shows the result of calculations performed by numerically integrating the TDSE in the single active electron approximation [14] in conditions close to the experiment. We use a He pseudopotential with the energy of the $1s3p$ state equal to 23.039 eV. The result is therefore shifted by 40 meV for comparison with the experiment. The result shown in Fig. 3(b) agrees very well with the experiment, thus confirming our detuning calibration.

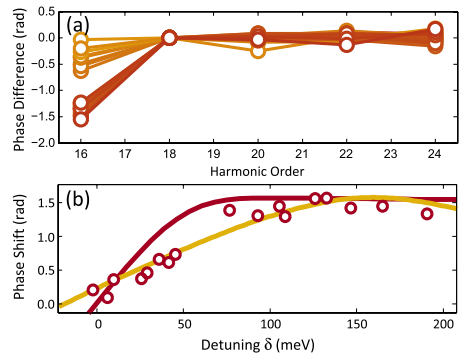

FIG. 3 (color online). (a) Measured sideband phases corrected for the attosecond group delay and normalized at zero for sideband 18. Different detunings are indicated by the color code [going from 11 meV below the resonance (dark red, lower points in order 16) to 190 meV above the resonance (light orange, upper in order 16)]. (b) Measurements (circles) of the R2PI phase as a function of detuning. The dark red line indicates results of a simple perturbative model while the light orange line shows results of simulations based on solving the TDSE.

In order to investigate how the $1s3p$ resonance behaves in a laser field, we measured the dependence of the R2PI phase on the dressing laser intensity. Figure 4(a) shows the R2PI phase determined similarly to Fig. 3(a) but keeping the wavelength constant at 805.5 nm and gradually increasing the dressing intensity. We verified that even at the highest intensity, higher-order multiphoton transitions were still negligible [22], thus not affecting our phase determination. Increasing the intensity from 0.1 to 1.8×10^{12} W/cm^2, the R2PI phase varies from -0.7 to 0.9 radians. Figure 4(b) presents the intensity dependence of all of the measured phases (circles). We find an almost linear increase of the phase with intensity, as indicated by the dark red curve obtained by averaging, with a saturation at around 1.3×10^{12} W/cm^2, due to the suppression of R2PI when part of the two-photon excitation bandwidth moves partly below the ionization threshold. The light orange line obtained by TDSE calculations agrees well with our measurements.

Combining our previous phase measurements as a function of detuning for a fixed (low) intensity and as a function of intensity (for a fixed detuning) allows us to determine the intensity dependence of the $1s^2 \rightarrow 1s3p$ transition energy. Both experimental (dark red solid) and TDSE (light orange solid) results are shown in Fig. 5(a). The dashed line is equal to $\Delta E_{1s^2} + U_p$, representing the variation of the transition energy if the $1s3p$ state was moving as a high-lying Rydberg state, following U_p [19]. The ac Stark shift of the fundamental state ΔE_{1s^2} is very small, equal to $-0.3I$ eV where the intensity I is in units of 10^{14} W cm^{-2} [23,24] so that $\Delta E_{1s^2} + U_p \approx U_p$. We find that the measured transition energy increases about 40%

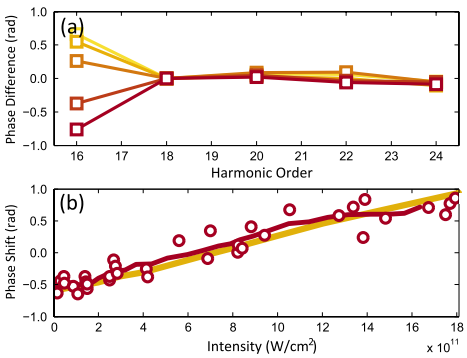

FIG. 4 (color online). Intensity dependence of the R2PI phase. (a) Harmonic phase differences at dressing intensities from 0.1 (dark red) to 2.2×10^{12} W cm^{-2} (light orange), with attosecond chirp correction and normalization at sideband 18. (b) R2PI phase (circles) as a function of intensity, with a six-point moving average (dark red line) and TDSE (light orange).

more rapidly with the laser intensity than U_p, up to the saturation at 1.3×10^{12} W cm^{-2}.

To better understand this faster than ponderomotive shift, we have calculated the XUV absorption cross section for helium in the presence of an 800 nm field by numerically solving the TDSE as a function of both XUV wavelength and laser intensity [Fig. 5(b)]. Using an XUV bandwidth of 50 meV or smaller we find that beyond 1×10^{11} W cm^{-2}, the $3p$ resonance has at least two components the higher of which shifts significantly faster than the ponderomotive energy. With the experimental XUV bandwidth (150 meV), however, the different components cannot be resolved. As a result, we observe shifts exceeding $E_{1s^2} + U_p$. Experimentally, the predicted structure in the $3p$ resonance could be observed using longer fundamental laser pulses, leading to spectrally narrower harmonic peaks.

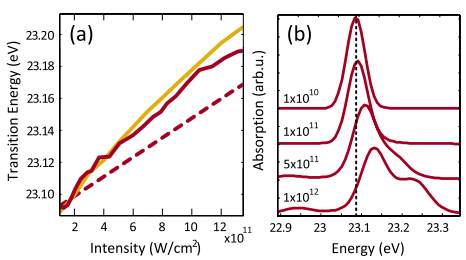

FIG. 5 (color online). (a) Measured transition energy of the $1s3p$ state. Experimental results (solid dark red), compared with $\Delta E_{1s^2} + U_p$ (dashed) and TDSE calculation (solid light orange). (b) TDSE calculation of XUV absorption for three different intensities with 50 meV resolution. The position of the $1s3p$ state is indicated by the dashed line.

In conclusion, we have shown how well-characterized phase-locked high-order harmonics can be used to measure the phase of R2PI and we have applied it to the determination of the ac Stark shift of the $1s3p\ ^1P_1$ state. Although our resolution was unsufficient to detect the splitting of the excited state, we observed a nontrivial, faster than ponderomotive, ac Stark shift. Our method, here demonstrated in He, could be applied to the study of numerous resonant or quasiresonant processes in atoms and molecules.

We thank A. Maquet and R. Taïeb for fruitful suggestions at the beginning of this work. This research was supported by the Marie Curie Intra-European Fellowship ATTOCO, the Marie Curie Early Stage Training Site (MAXLAS), the European Research Council (ALMA), the Knut and Alice Wallenberg Foundation and the Swedish Research Council. Funding at LSU is provided by the National Science Foundation through grant numbers PHY-0449235 and PHY-0701372.

*anne.lhuillier@fysik.lth.se
URL: http://www.atto.fysik.lth.se

[1] A. Osterwalder and F. Merkt, Phys. Rev. Lett. **82**, 1831 (1999).
[2] E. G. Robertson and J. P. Simons, Phys. Chem. Chem. Phys. **3**, 1 (2001).
[3] U. Koster, V. Fedoseyev, and V. Mishin, Spectrochim. Acta, Part B: At. Spectrosc. **58**, 1047 (2003).
[4] M. Ferray *et al.*, J. Phys. B **21**, L31 (1988).
[5] J. L. Krause, K. J. Schafer, and K. C. Kulander, Phys. Rev. Lett. **68**, 3535 (1992).
[6] P. B. Corkum, Phys. Rev. Lett. **71**, 1994 (1993).
[7] F. Brandi, D. Neshev, and W. Ubachs, Phys. Rev. Lett. **91**, 163901 (2003).
[8] P. Ranitovic *et al.*, New J. Phys. **12**, 013008 (2010).
[9] L. H. Haber, B. Doughty, and S. R. Leone, Phys. Rev. A **79**, 031401(R) (2009).
[10] V. Véniard, R. Taïeb, and A. Maquet, Phys. Rev. A **54**, 721 (1996).
[11] P. M. Paul *et al.*, Science **292**, 1689 (2001).
[12] K. Varjú *et al.*, Laser Phys. **15**, 888 (2005).
[13] S. Haessler *et al.*, Phys. Rev. A **80**, 011404(R) (2009).
[14] K. J. Schafer and K. C. Kulander, Phys. Rev. Lett. **78**, 638 (1997).
[15] R. López-Martens *et al.*, Phys. Rev. Lett. **94**, 033001 (2005).
[16] C. G. Wahlström *et al.*, Phys. Rev. A **48**, 4709 (1993).
[17] M. B. Gaarde, M. Murakami, and R. Kienberger, Phys. Rev. A **74**, 053401 (2006).
[18] R. K. Freeman *et al.*, Phys. Rev. Lett. **59**, 1092 (1987).
[19] K. Burnett, V. Reed, and P. Knight, J. Phys. B **26**, 561 (1993).
[20] Y. Mairesse *et al.*, Science **302**, 1540 (2003).
[21] N. Dudovich, D. Oron, and Y. Silberberg, Phys. Rev. Lett. **88**, 123004 (2002).
[22] M. Swoboda *et al.*, Laser Phys. **19**, 1591 (2009).
[23] M. D. Perry, A. Szoke, and K. C. Kulander, Phys. Rev. Lett. **63**, 1058 (1989).
[24] H. Rudolph *et al.*, Phys. Rev. Lett. **66**, 3241 (1991).

Paper VI

Attosecond Pump-Probe Electron Interferometry

J. Mauritsson, T. Remetter, M. Swoboda, K. Klünder, A. L'Huillier, K. J. Schafer, O. Ghafur, F. Kelkensberg, W. Siu, P. Johnsson, M. J. J. Vrakking, I. Znakovskaya, T. Uphues, S. Zherebtsov, M. F. Kling, F. Lépine, E. Benedetti, F. Ferrari, G. Sansone and M. Nisoli.

Phys. Rev. Lett. **105**, 053001(2010).

PRL 105, 053001 (2010) PHYSICAL REVIEW LETTERS week ending 30 JULY 2010

Attosecond Electron Spectroscopy Using a Novel Interferometric Pump-Probe Technique

J. Mauritsson,[1] T. Remetter,[1] M. Swoboda,[1] K. Klünder,[1] A. L'Huillier,[1] K. J. Schafer,[2] O. Ghafur,[3] F. Kelkensberg,[3] W. Siu,[3] P. Johnsson,[3] M. J. J. Vrakking,[3,4] I. Znakovskaya,[5] T. Uphues,[5] S. Zherebtsov,[5] M. F. Kling,[5] F. Lépine,[6] E. Benedetti,[7] F. Ferrari,[7] G. Sansone,[7] and M. Nisoli[7]

[1]*Department of Physics, Lund Institute of Technology, P. O. Box 118, SE-221 00 Lund, Sweden*
[2]*Department of Physics and Astronomy, Louisiana State University, Baton Rouge, Louisiana 70803-4001, USA*
[3]*FOM-Institute AMOLF, Science park 113, 1098 XG Amsterdam, The Netherlands*
[4]*Max-Born-Institut für Nichtlineare Optik und Kurzzeitspektroskopie (MBI), Max-Born-Straße 2 A, 12489 Berlin, Germany*
[5]*4 Max-Planck-Institut für Quantenoptik, Hans-Kopfermann-Strasse 1, D-85748 Garching, Germany*
[6]*Université Lyon 1; CNRS; LASIM, UMR 5579, 43 bvd. du 11 novembre 1918, F-69622 Villeurbanne, France*
[7]*Politecnico di Milano, Department of Physics Istituto di Fotonica e Nanotecnologie, CNR-IFN Piazza L. da Vinci 32, 20133 Milano, Italy*

(Received 24 March 2010; published 27 July 2010)

We present an interferometric pump-probe technique for the characterization of attosecond electron wave packets (WPs) that uses a free WP as a reference to measure a bound WP. We demonstrate our method by exciting helium atoms using an attosecond pulse (AP) with a bandwidth centered near the ionization threshold, thus creating both a bound and a free WP simultaneously. After a variable delay, the bound WP is ionized by a few-cycle infrared laser precisely synchronized to the original AP. By measuring the delay-dependent photoelectron spectrum we obtain an interferogram that contains both quantum beats as well as multipath interference. Analysis of the interferogram allows us to determine the bound WP components with a spectral resolution much better than the inverse of the AP duration.

DOI: 10.1103/PhysRevLett.105.053001 PACS numbers: 32.80.Rm, 32.80.Qk, 42.65.Ky

Attosecond science [1,2] promises to achieve temporal resolution comparable to the duration (τ) of the light pulses, e.g., of the order of 100 as [3,4] or even below [5]. An important issue, however, is whether this is possible only to the detriment of spectral resolution, thus considerably limiting the scientific interest of such light sources. When attosecond pulses (APs) interact with atoms or molecules, they create broad electron wave packets (WPs), partly in the continuum, but often including also a number of bound states excited by direct absorption [6] and/or by shake-up processes [7]. A spectral resolution given by the Fourier limit, i.e., of the order of $1/\tau$, prevents any detailed analysis of such complex WPs.

Because of the low intensity of currently available APs, most of the techniques used to characterize attosecond electron WPs have used as a probe an infrared (IR) pulse which is synchronized to the extreme ultraviolet (XUV) AP. The required XUV-IR synchronization is inherent to the AP generation process and several methodologies, such as chronoscopy [7], streaking [8,9], stroboscopy [10], and interferometry [11] have been demonstrated. All of these techniques require that the attosecond and IR pulses overlap temporally. The IR field is therefore not only probing the electron WP after it has been created but it also perturbs the formation. In addition, the spectral resolution of these techniques is Fourier limited.

Several techniques could be considered to achieve a spectral resolution higher than the inverse of the pulse duration. Although trains of pulses, i.e., frequency combs, have the potential to achieve extremely high spectral resolution [12], pairs of pulses, as in traditional Ramsey spectroscopy, might be easier to implement for time-resolved measurements [13]. In this Letter we present a novel interferometric technique, using a single AP and a delayed IR pulse, that resolves both issues previously discussed: The spectral resolution is much better than the Fourier limit of the exciting pulse and the delayed probe pulse does not perturb the excitation process (see Fig. 1).

In our method, an AP is used to excite a bound WP in an atom or a molecule and a delayed IR pulse, locked in phase with the XUV pulse, is used to probe it. Coincident with the creation of the bound WP, we also create a continuum WP, which serves as a reference. After a variable delay, the bound WP is ionized by the IR pulse, and both continuum WPs, created directly by the XUV pulse, or by the two-step (XUV + IR) process, interfere. The analysis of the interferogram obtained when measuring the photoelectron spectrum as a function of delay allows us to determine the spectral components of the bound WP. This technique enables us to obtain a spectral resolution given by the inverse of the IR-XUV delay, which is typically a few tens of femtoseconds, i.e., more than a factor 100 better than the Fourier limit of the excitation pulse. We demonstrate the technique experimentally using an AP with 350 as duration and central energy of 24 eV which excites a broad WP in helium, including bound (unknown) and continuum (reference) components. A few-cycle IR pulse probes the bound WP, and analyzing the electron spectra allows us to recover the composition of the WP.

PRL **105,** 053001 (2010) PHYSICAL REVIEW LETTERS week ending 30 JULY 2010

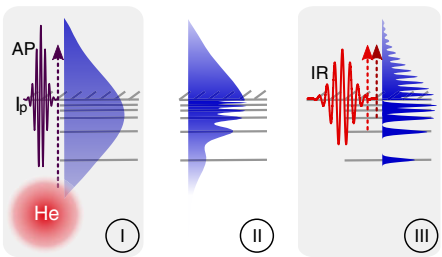

FIG. 1 (color online). Principle of attosecond electron interferometry. A broadband, AP with a spectrum centered on the ionization threshold of helium is used to coherently excite an electron WP consisting of a superposition of bound and continuum p states (region I). The created WP evolves freely during a certain delay (II). The bound part of the WP is finally ionized by a few-cycle IR pulse (III), which is locked in phase to the AP and interferences with the previously created free WP are observed in the photoelectron spectra. In addition, several excited states can be excited leading to quantum beats in the ionization signal.

In the experiments, a linearly polarized phase stabilized 5-fs IR laser pulse is divided into a central and annular part using a mirror with a hole in the center. The polarization gating technique is used on the central part to obtain a laser pulse with a temporal window of linear polarization with duration of less than half an optical cycle [14]. This laser beam is focused into a xenon gas cell to generate XUV radiation via high order harmonic generation. The low order harmonics and the collinear IR radiation are removed using a 100 nm thick aluminum filter. This metallic filter also provides partial dispersion compensation of the intrinsic positive chirp of the emitted pulse [15], compressing it to a duration of 350 attoseconds. The APs are focused using a grazing incidence toroidal mirror into the active region of a velocity map imaging spectrometer (VMIS) [16], used to record the photoelectron momentum distributions.

The APs have a central frequency of 24 eV with a bandwidth exceeding 10 eV and excite helium from its ground state to a coherent superposition of bound and continuum p states. At a controllable time delay the bound WP is ionized by the probe IR laser (bandwidth 0.53 eV), which is collinearly recombined with the AP using a second mirror with a hole in the center and which is focused by a spherical mirror. The IR intensity was close to 1×10^{13} W/cm^2, well below that necessary to tunnel ionize He in its ground state, but high enough to induce "streaking" when both IR and XUV pulses overlap [3,17], allowing us to determine the delay between the two pulses. The XUV and IR beams are crossed with an effusive He gas jet emerging from a capillary incorporated into the repeller electrode of the VMIS [18]. Using a set of electrostatic lenses, the electrons emitted in the two-color photoionization process are accelerated onto multichannel plates coupled to a phosphor screen detector. The effusive gas jet allows us to obtain a gas density of $\sim 3 \times 10^{15}$ cm^{-3} in the interaction region, while keeping a low enough pressure close to the multichannel plates. Two-dimensional images are acquired with a CCD camera and used for the retrieval of the 3D initial velocity distribution [19].

A scan of the photoelectrons emitted in a small angle around the polarization axis in the upward direction is shown in Fig. 2. Both fields are vertically polarized. The color indicates the photoelectron intensity $S_{\mathrm{exp}}(E, t)$ as a function of observation energy E and delay t. When the two pulses overlap temporally (at 0 fs delay), the photoelectron spectra are streaked, indicating photoionization by an isolated AP in the presence of a laser field [3,17]. In the more interesting region where the AP precedes the IR probe, interference fringes are observed in the low-energy region of the spectrum, up to about 2 eV. As explained below, interferences fringes are expected also at higher energy, but the spectrometer resolution in this region prevents their observation [20]. This interference pattern is due to the multiple pathways leading to the same final continuum energy. During the delay, t, a continuum state with energy E and a bound, stationary state with energy E_i accumulate a phase difference $(E - E_i)t/\hbar$. The interference fringes, defined as the curves of constant phase difference, are therefore hyperboles, which become more closely spaced as the delay increases.

In Fig. 3, we present quantum calculations based on the single active electron approximation [6] under conditions that are close to those of the experiment. The probe has a 6 fs duration with a $\cos^2$ shape and an intensity of 1×10^{13} W/cm^2, while the AP duration is 180 as which is shorter that the 350 as in the experiment but chosen to match the experimental bandwidth [20]. The theoretical spectra as a function of delay, $S_{\mathrm{theo}}(E, t)$, shows electrons emitted in the direction of the IR and XUV polarization axis. Interference fringes appear as soon as the excitation of the bound states is separated in time from their ionization by the probe field, meaning that we have two clearly delineated routes into the continuum. The hyperbolic shape

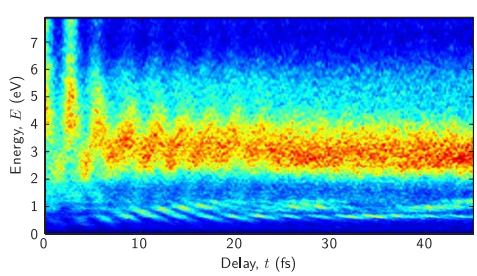

FIG. 2 (color online). Experimental photoelectron spectra in He as a function of delay. The electron distribution is recorded using a VMIS and the spectra are obtained by selecting a small collection angle along the polarization direction. The interference fringes are clearly visible at low energies.

PRL 105, 053001 (2010) PHYSICAL REVIEW LETTERS week ending 30 JULY 2010

of the fringes is visible in the calculation and the fringe spacing in energy decreases as the delay increases.

A quantum beat signal [21,22] is also visible in Fig. 3(a), due to simultaneous excitation of several bound states (i,j). Interferences between quantum paths leading to the same final energy, for example $E_i + n\hbar\omega = E_j + n'\hbar\omega'$, ω, ω' being within the IR laser bandwidth and the number of photons n and n' not necessarily the same (typically one or two), give rise to periodic structures in the ionization probability. The accumulated phase difference between the quantum paths, equal to $(E_j - E_i)t/\hbar$, is independent on the observation energy and the quantum beat signal appears as periodic vertical structures. The beat signal observed in Fig. 3 has a main periodicity of about 2 fs, corresponding to the beating between the outgoing electrons from the $2p$ and the $3p$ states. The periodicity of the beat signal carries information on the relative energy separation of the states involved, while the absolute timing of the beating depends on the relative phase of the pairs of states contributing to the signal. As we now discuss, analysis of the "direct-indirect" interferences, involving bound states and a reference continuum state allow us to go well beyond quantum beat spectroscopy.

To begin with, the different components of the excited WP can be extracted by Fourier analysis of the delay-dependent photoelectron signal $S_{\text{theo}}(E, t)$. We first analyze the simulation shown in Fig. 3. The Fourier transform at all the possible observation energies yields a two dimensional function of the observation energy E and the Fourier frequency (represented as an energy E'). This function, $\mathcal{S}_{\text{theo}}(E, E')$, is presented as a color plot in Fig. 3(b) as a function of E and E'. Figure 3(c) shows a line out at $E =$ 4 eV. It exhibits six prominent peaks. The three lowest peaks are from the quantum beat between $3p$-$4p$, $2p$-$3p$, and $2p$-$4p$ pairs of states, respectively, while the other peaks at 4.9, 5.6, and 7.4 eV in Fig. 3(c) are due to the direct-indirect interferences involving the $4p$, $3p$ and $2p$ states, respectively. When the observation energy E is varied, the Fourier frequency of the quantum beats does not change and they appear as vertical lines in Fig. 3(b). In contrast, the Fourier frequency E' of the direct-indirect interferences increases with E, since the accumulated phase difference between the direct and indirect ionization pathways is proportional to it. This linear relationship results in lines tilted at 45° in Fig. 3(b). The energies of the bound intermediate states $(4p, 3p, 2p)$ in the WP can be read directly from the intersections of the 45° lines with the horizontal zero energy line. In addition, the relative strengths of the 45° lines are directly related to the contributions from each bound state to the ionization signal.

Turning to the experimental data, we find that quantum beats and direct-indirect interferences are also present. Figure 4 presents an extended analysis of our experimental results. Figure 4(a) is a zoom of the low-energy region in Fig. 2, while Fig. 4(b) presents the Fourier transform of the experimental data. The observed 45° lines which are characteristic for the direct-indirect interferences allow us to identify the composition of the bound WP and identify the contributions from the $3p$, $4p$ and $5p$ states. A weak indication of the $4p$-$5p$ quantum beat can also be seen as a beating with a 13 fs periodicity in Fig. 4(a) and as a vertical line near 0.5 eV in Fig. 4(b). Additional information is encoded in the angular distributions since the two interference processes are fundamentally different and involve different angular momentum states. Figures 4(c)–4(f) present a more complete analysis making use of the full angular-resolved photoelectron distribution $F(E, \theta, t)$, which can be expanded as a sum of Legendre polynomials

$$F(E, \theta, t) = \sum_{j=0}^{2L_{\max}} \beta_j(E, t) P_J[\cos(\theta)], \qquad (1)$$

where P_J is the Legendre polynomial of Jth order, β_J an expansion coefficient, and $L_{\max}$ the maximum angular momentum component of the ionized wave function, which corresponds to the maximum absorbed angular momentum. After extraction of the individual expansion coefficients, $\beta_J(E, t)$, we apply the same Fourier analysis that was already applied to the photoelectron spectrum measured along the laser polarization axis. Figures 4(c) and 4(e) show the extracted expansion coefficients $\beta_1(E, t)$

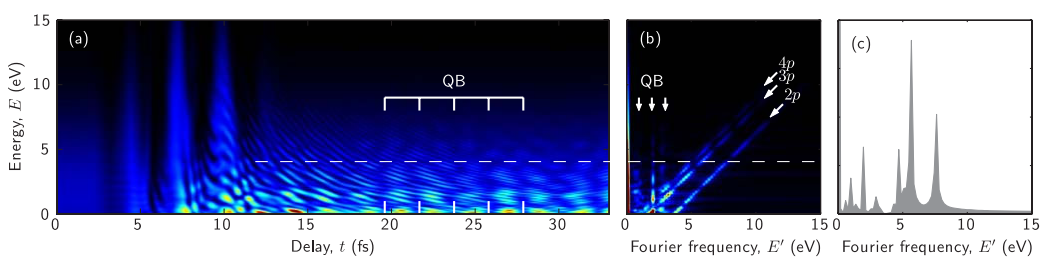

FIG. 3 (color online). (a) Calculated photoelectron spectra in He as a function of delay between the AP and the IR pulse. Interference fringes are clearly seen where the AP precedes the IR probe. (b) Fourier transform of the photoelectron spectrum allowing the identification of the states that form the bound WP. The beat signals from the $2p$, $3p$ and $4p$ states can be seen as vertical lines while the direct-indirect interference gives rise to contributions at an angle of 45°. A line out of the transform at 4 eV is presented in (c).

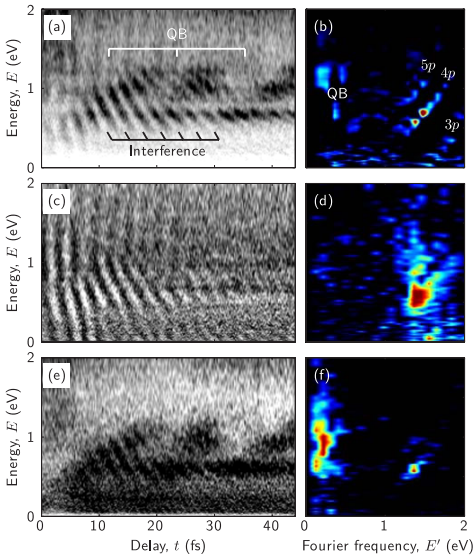

FIG. 4 (color online). Analysis of experimental results. (a) Zoom of the low-energy region in Fig. 2. (b) Fourier analysis showing the WP components $3p$, $4p$, $5p$ as well as a quantum beat $4p$-$5p$. (c) $\beta_1(E, t)$ and (d) its Fourier analysis. (e) $\beta_2(E, t)$ and (f) its Fourier analysis.

and $\beta_2(E, t)$ respectively, together with their Fourier transforms in Figs. 4(d) and 4(f). Simple parity arguments dictate that interference between ionization processes that end in states of definite parity will appear in the even J expansion coefficients, while interference between ionization processes that end in mixed parity states will appear in the odd J expansion coefficients. The direct-indirect interference process involves electrons that have absorbed different numbers of photons resulting in a mixed parity state. Indeed, we see that the characteristic hyperbolic interference fringes appear clearly in $\beta_1(E, t)$ [Figs. 4(c) and 4(d)]. In contrast, the process that produces quantum beats results in states of definite parity. Accordingly, the quantum beat signal dominates $\beta_2(E, t)$ [Figs. 4(e) and 4(f)], thus confirming the interpretation presented above.

Using the above analysis, we can determine which states are excited by the AP ($3p$, $4p$, $5p$) and obtain a measure of their relative strengths. Our ultimate goal is of course a complete characterization in both amplitude and phase. Determining the amplitudes and phases of a wavelike object by interference with a reference wave is a well-known approach. The experiment and the analysis we have presented demonstrates that we can probe an attosecond electron WP using a coherent reference WP that is in the continuum. The method can be extended to include the retrieval of a phase associated with each WP component from the interferogram. This phase retrieval yields the phase difference between the two paths into the continuum and includes a phase contribution from both XUV and IR ionization steps. If it can be arranged that both ionization leading to the creation of the reference WP and ionization by the probe field do not add extra amplitude or phase variation or that these possible variations are well-known then a complete phase characterization can be made.

In conclusion we have demonstrated experimentally a new interferometric technique using a reference continuum WP and a delayed probe excitation. The method demonstrated can be used to probe the temporal evolution of bound or quasibound electron WPs, e.g., composed of autoionizing states [23] or created by shake-up [7] with high spectral and temporal resolution simultaneously, thus providing an increased precision when doing attosecond experiments.

This research was supported by the Marie Curie IEF (ATTOCO), RTN (XTRA), EST (MAXLAS) programs, the I3 Laserlab-Europe, the Swedish and European Research Councils, the National Science Foundation through grant No. PHY-0701372, the DFG through the Emmy-Noether program and the Cluster of Excellence: Munich Center for Advanced Photonics and the "Stichting voor Fundamenteel Onderzoek der Materie" (FOM), which is financially supported by the "Nederlandse Organisatie voor Wetenschappelijk Onderzoek" (NWO).

[1] P. M. Paul *et al.*, Science **292**, 1689 (2001).
[2] M. Hentschel *et al.*, Nature (London) **414**, 509 (2001).
[3] G. Sansone *et al.*, Science **314**, 443 (2006).
[4] E. Gustafsson *et al.*, Opt. Lett. **32**, 1353 (2007).
[5] E. Goulielmakis *et al.*, Science **320**, 1614 (2008).
[6] P. Johnsson *et al.*, Phys. Rev. Lett. **99**, 233001 (2007).
[7] M. Uiberacker *et al.*, Nature (London) **446**, 627 (2007).
[8] R. Kienberger *et al.*, Science **297**, 1144 (2002).
[9] J. Itatani *et al.*, Phys. Rev. Lett. **88**, 173903 (2002).
[10] J. Mauritsson *et al.*, Phys. Rev. Lett. **100**, 073003 (2008).
[11] T. Remetter *et al.*, Nature Phys. **2**, 323 (2006).
[12] M. Swoboda *et al.*, Phys. Rev. Lett. **104**, 103003 (2010).
[13] A. Pirri *et al.*, Phys. Rev. A **78**, 043410 (2008).
[14] I. J. Sola *et al.*, Nature Phys. **2**, 319 (2006).
[15] R. López-Martens *et al.*, Phys. Rev. Lett. **94**, 033001 (2005).
[16] A. T. J. B. Eppink and D. H. Parker, Rev. Sci. Instrum. **68**, 3477 (1997).
[17] E. Goulielmakis *et al.*, Science **305**, 1267 (2004).
[18] O. Ghafur *et al.*, Rev. Sci. Instrum. **80**, 033110 (2009).
[19] M. J. J. Vrakking, Rev. Sci. Instrum. **72**, 4084 (2001).
[20] The experimental spectrum was also a little modulated, leading to a minimum at 1.5 eV and a maximum at 3 eV.
[21] J. A. Yeazell and C. R. Stroud, Jr., Phys. Rev. Lett. **60**, 1494 (1988).
[22] A. ten Wolde *et al.*, Phys. Rev. Lett. **61**, 2099 (1988).
[23] L. Argenti and E. Lindroth, Phys. Rev. Lett. **105**, 053002 (2010).

Paper VII

Reconstruction of Attosecond Electron Wave Packets with Quantum State Holography

K. Klünder, P. Johnsson, M. Swoboda, A. L'Huillier, M. J. J. Vrakking, K. J. Schafer and J. Mauritsson.

(2012) *Manuscript in preparation.*

Reconstruction of Attosecond Electron Wave Packets with Quantum State Holography

K. Klünder,[1] P. Johnsson,[1] M. Swoboda,[1] J. M. Dahlström,[1]
A. L'Huillier,[1] M. J. J. Vrakking,[2] K. J. Schafer,[3] and J. Mauritsson[1]

[1]*Department of Physics, Lund University, P. O. Box 118, SE-221 00 Lund, Sweden*
[2]*Max Born Institute, Max-Born-Straße 2a, D-12489 Berlin, Germany*
[3]*Department of Physics and Astronomy, Louisiana State University, Baton Rouge, Louisiana 70803-4001, USA*

We present a new method of doing quantum state holography to completely characterize excited attosecond electron wave packets. Quantum state holography is a method to measure the wavefunction of a quantum system in both amplitude and phase. The presented approach is an extension of a recent publication (J. Mauritsson *et al.* Phys. Rev. Lett. **105**, 053001 (2010)) in which we demonstrated experimentally that we can characterize the energies and amplitudes of an attosecond electron wave packet using electron interferometry. Here we show theoretically that attosecond electron interferometry can be extended to retrieve also the phases of all the states that make up the wave packet. We demonstrate the feasibility of our method using a simple model of shake-up wave packets where we can add arbitrary phases and/or life times to the different eigenstates.

PACS numbers: 32.80.Rm, 32.80.Qk, 42.65.Ky

I. INTRODUCTION

The interaction of short light pulses with atoms or molecules leads to the creation of localized electron wave packets, either through direct excitation or through indirect processes such as shake-up excitation. These electron wave packets, which can be viewed as a coherent superposition of excited eigenstates, are localized in both time and space and the localization determines the number of states and the bandwidth that they cover. Therefore, if we want to capture and ultimately control fast localized electron motion we have to characterize broadband wave packets consisting of many excited states spread over many electron volts. A complete reconstruction of such wave packets requires that we characterize both the time-dependent amplitudes and the phases of all these states.

Determining the amplitudes and phases of a wave-like object by interference with a reference wave is a well-known approach. It is the essence of holography, and has been used to great advantage in the characterization of optical fields [1]. The method has also been applied to vibrational and highly excited Rydberg wave packets (where the motion takes place on a picosecond to femtosecond time scale) [2–4], but in those cases two bound wave packets were used, one the object to be measured and the other a known reference that spectrally overlapped the unknown one. The challenge in attosecond science is to develop a similar technique without requiring that the reference wave packet interferes with the unknown wave packet while it is still bound. This would alter the properties of the unknown wave packet. We propose a method to solve this problem by having the reference be a free wave packet, which does not interfere with the unknown wave packet during the evolution of the electron dynamics of interest, but only in the course of the detection step, when the bound wave packet is ionized by a coherent probe pulse and the resulting angle- and energy-resolved photoelectron spectrum is measured.

In a recent publication [5] we demonstrated experimentally an interferometric pump-probe technique that utilizes attosecond electron interferometry. We showed that we could obtain the high experimental stability necessary to spectrally resolve the states of a bound wave packet (the np series in Helium starting from the $3p$-state). Similar to quantum state holography [2] we demonstrated the ability to measure independently the amplitude of each state in the wave packet. The interferometric nature of the method used implies that also phase information should be embedded in the recorded interferogram. In this article we demonstrate that this is indeed the case and that the techniques for amplitude and phase retrieval work irrespectively of the way the wave packet is created. We do this using a simplified model of shake-up/shake-off process and show that the time-dependence of the electron wave packet can be completely reconstructed since we retrieve both the time-dependent amplitudes and phases of any given state in the coherent superposition. This is a prerequisite if we want a complete reconstruction of the wave packet since even minor phase changes alters the electron motion.

The basic idea of the attosecond electron interferometry is illustrated in Fig. 1. When an attosecond pulse is applied to an atom or a molecule at time $t_0 = 0$ it excites a broad coherent superposition of bound states spread over several electron volts. This can either happen by direct excitation or as a subsequent process, *e.g.* by a shake-up process [6]. The coherent superposition, and hence the electron dynamics that take place, is completely characterized by the states that are part of the superposition,

$$\Psi_b(t > 0) = \sum_i A_i \Psi_i e^{-i(E_i t/\hbar - \varphi_i)}, \qquad (1)$$

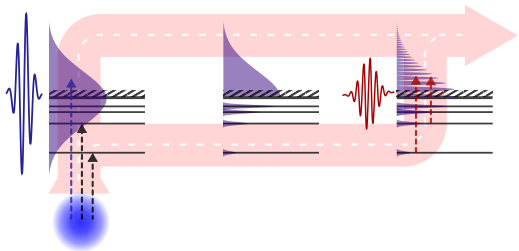

FIG. 1: (Color online). Principle of the attosecond electron interferometer. A bound wave packet is created either directly by excitation with an attosecond pulse or through a subsequent process after ionization. Simultaneously a continuum reference wave packet is created. Both wave packet evolve freely in time and after a variable delay the bound wave packet is ionized using a synchronized probe pulse which leads to interference.

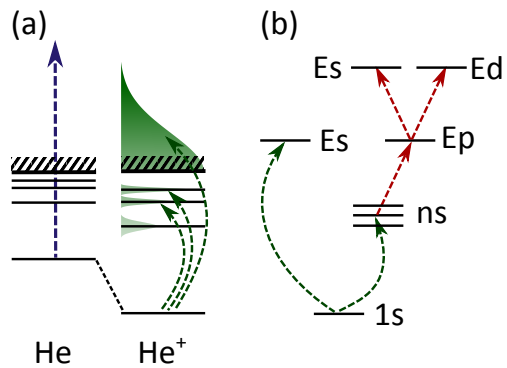

FIG. 2: (Color online). Possible pathways in the interferometer. (a) The rapid removal of an electron excites the remaining electron(s) to excited bound or even continuum states. (b) Ionization of the bound states with one or two probe photons after the shake-up excitation.

where E_i, Ψ_i are the bound state energies and wave functions and φ_i, A_i the phases and amplitudes.

Simultaneously with the bound wave packet a continuum wave packet is created that will serve as a reference in the following. After the initial excitation both wave packets evolve freely in time. The bound wave packet is probed through a further excitation step after a variable delay t using a probe pulse that is locked in phase with the event that initiated the wave packet. The subsequent ionization leads to interference between the direct path of the continuum wave packet and the indirect pathway via the bound states. In this article we demonstrate that it is possible to determine the initial phases φ_i and any possible lifetime effects of the bound states Ψ_i as well as the energies, E_i and the amplitudes, A_i.

This article is organized as follows. In Sec. II the simplified shake-up model is described together with the pulse parameters used in the calculations followed by a brief explanation about how to analyze the resulting interferograms. In Sec. III the separation of the angular resolved data into Legendre polynomials is presented and how this information can be used to separate different ionization pathways. This is followed in Sec. IV by an explanation how the encoded lifetime and phase information can be retrieved form the spectrograms ending with conclusions in Sec. V.

II. ANALYSIS OF A SHAKE-UP WAVE PACKET

Shake-up processes occur after the sudden removal of one electron, *e.g.*, by photoionization with high-energy photons [6]. The abrupt changes in the atomic potential create a perturbation that may 'shake' the remaining electron(s) into an excited bound or even continuum state [see Fig. 2]. We simulated such a shake-up and shake-off process in helium using a sudden approximation, consisting in removing one electron and projecting the wave function onto the eigenstates of the ionic system [7]. This process produces a wave packet that is a coherent superposition of ns-bound states and a continuum s-wave packet [see Fig. 2 (b)]. We further ionize the excited bound states after a variable delay by a two-cycle pulse at 200 nm central wavelength with a $\cos^2$ shape envelope, which corresponds to a bandwidth of 6 eV FWHM. Recent advances in source development indicate that ultra-short pulses in this wavelength regime are now experimental feasible [8]. We calculated the angular-resolved electron spectra $\mathcal{F}(E,\theta,t)$ as a function of delay (t) between the shake-up/shake-off excitation (pump) and the probe laser pulse by solving the time-dependent Schrödinger equation [9, 10]. E denotes the final energy, while θ is the angle between the direction of emission of the electron and the direction of polarization of the probe field, which coincides with the quantization axis. Note that due to the revolution symmetry of the problem, $\mathcal{F}(E,\theta,t)$ does not depend on the azimuthal angle ϕ.

In Fig. 3(a) the results of the calculations are presented for the electrons emitted in the direction of the polarization vector. The electron signal in one direction is plotted as a function of E and t. The spectrogram $\mathcal{F}(E,\theta,t)$ (here with $\theta = 0$) exhibits a series of tilted interference fringes with a tilt varying from almost vertical at small time delays to almost horizontal at large delays [see Fig. 3(a)]. We analyze the interferences by Fourier transform along the delay axis for all final energies [5]. The result shown in Fig. 3(b) is a two dimensional func-

tion $S(E, E')$ of the continuum energy E and the energy E', the conjugate variable of t from the Fourier transform. This function presents a series of tilted lines at 45° corresponding to "direct-indirect" interferences, *i.e.*, between the wave packet ionized by the probe pulse and the reference continuum wave packet created by the shake-off process.

The structure of the interference pattern both in the $E-t$ interferogram or in the $E-E'$ representation can be understood by expressing the accumulated phase difference $\Delta\Phi$ along the two branches of the interferometer (see Fig. 1). Considering a final energy E and an excited bound state E_i the accumulated phase difference at time t (assuming that the initial shake-up excitation takes place at time $t = 0$) is

$$\Delta\Phi(E,t) = (E - E_i)t/\hbar + \varphi_i + \delta\phi(E)\,, \qquad (2)$$

where $\delta\phi(E) = \phi_{dir}(E) - \phi_{ind}(E)$ is the difference in phase that is picked up during the ionization process for the two pathways [11, 12]. In the simplest case, *i.e.*, no phase due to the initial excitation and no correlation effect, $\delta\phi(E)$ is given by the difference of the scattering phases for the outgoing wave packet between the direct pathway with $\ell = 0$ and the indirect pathway with $\ell = 1$, $\eta_0(E) - \eta_1(E)$. The phases, φ_i, which characterize the bound wave packet, are those that we want to determine using our interferometric technique. Note that we are only interested in the relative phases of the wave packet components. Let us therefore, in a first step and for the sake of simplicity, neglect any state and energy-dependence of $\delta\phi(E)$ over the range considered (for example assuming that the probe pulses are transform limited) and therefore treat $\delta\phi$ as a small constant phase offset, which does not alter the relative phase difference of the wave packet components. The position of the interference fringes is determined by the families of hyperbolic curves $E = E_i + (n\pi - \varphi_i)\hbar/t$, with n integer. For a given energy E, the frequency of the oscillation as a function of t is $(E - E_i)/h$, leading to straight lines with a tilt of 45° in the Fourier plane, which intersects $E = 0$ at the bound state energies, E_i. In this way we can identify the $3s$, $4s$, $5s$, $6s$ and $7s$ states with the binding energies 6.04 eV, 3.40 eV, 2.18 eV, 1.50 eV and 1.10 eV with an accuracy given by the numerical resolution. Note that no information is obtained for the population of $2s$ state since the photon energy of the probe pulse is not sufficient to ionize it. The relative strength of each Fourier component is directly related to its relative contribution to the wave packet.

III. LEGENDRE ANALYSIS

A deeper understanding of the interference pattern can be achieved by performing a Legendre analysis of the

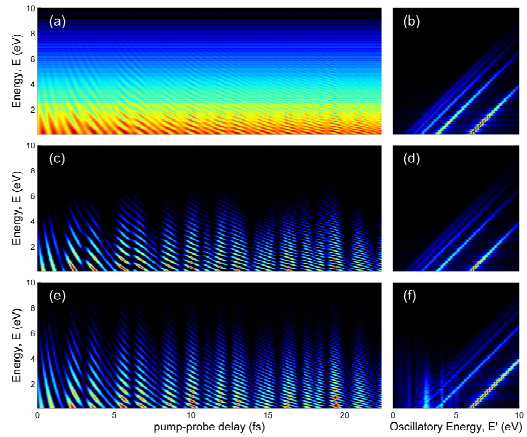

FIG. 3: (Color online). Analysis of a shake-up wave packet in a helium ion. (a) Complete on-axis spectrogram. (b) Fourier analysis showing the components of the wave packet. (c) $\beta_1(E,t)$ and the corresponding Fourier analysis (d). (e) $\beta_2(E,t)$ and (f) its Fourier analysis.

calculated angular distribution. $\mathcal{F}(E,\theta,t)$ is numerically decomposed as

$$\mathcal{F}(E,\theta,t) = \sum_{\ell=0}^{2} \beta_\ell(E,t)\, P_\ell^0(\cos\theta), \qquad (3)$$

where P_ℓ^0 are Legendre polynomials, related to the spherical harmonics by

$$P_\ell^0(\cos\theta) = \sqrt{\frac{4\pi}{2\ell+1}}\, Y_\ell^0(\theta,\phi). \qquad (4)$$

Fig. 3(c) and (e) show the extracted coefficients $\beta_1(E,t)$ and $\beta_2(E,t)$ together with the Fourier analysis $S_1(E,E')$, $S_2(E,E')$ in Fig. 3(d) and (f). The hyperbolic fringes appear clearly in $\beta_1(E,t)$ and $\beta_2(E,t)$. They are modulated in intensity due to the presence of several bound states and therefore several families of fringes leading to a Moire pattern and also quantum beats in $\beta_2(E,t)$. The Fourier transforms show lines at 45° which are characteristic of direct-indirect interferences as well as a few vertical lines (in (f)) which can be identified as quantum beats [5].

To understand the information contained in this analysis, we express the shake-off amplitude for the ejection of an electron in the direction given by (θ,ϕ) as:

$$M_{dir}(\theta,\phi) = e^{i\phi_{dir}}\alpha_E\; Y_0^0(\theta,\phi)\,. \qquad (5)$$

Similar, the amplitude for shake-up into states i or j (we only consider two states) followed by ionization by the probe field can be written as:

$$\begin{aligned} M_{ind}(\theta,\phi) \;=\; & [e^{\frac{i(E-E_i)t}{\hbar}+i\varphi_i}\alpha_i + e^{\frac{i(E-E_j)t}{\hbar}+i\varphi_j}\alpha_j] \\ & \times e^{i\phi_{ind}} Y_1^0(\theta,\phi)\,. \end{aligned} \qquad (6)$$

In Eqs. (5) and (6) α_E, α_i, α_j are the probability amplitudes for the different processes. The interference signal for a given direction is proportional to $|M_{dir} + M_{ind}|^2$. We easily identify the coefficients of the Legendre polynomial expansion for this simple case as:

$$\begin{aligned}
\beta_0 &\propto |\alpha_E|^2 + |\alpha_i|^2 + |\alpha_j|^2 + \\
&\quad +2Re\{\alpha_i\alpha_j^* e^{i\frac{(E_j-E_i)t}{\hbar}+i(\varphi_i-\varphi_j)}\}, \\
\beta_1 &\propto Re\{\alpha_E^*\alpha_i e^{i\frac{(E-E_i)t}{\hbar}+i\varphi_i+i\delta\phi} \\
&\quad +\alpha_E^*\alpha_j e^{i\frac{(E-E_j)t}{\hbar}+i\varphi_j+i\delta\phi}\}, \qquad (7) \\
\beta_2 &\propto |\alpha_i|^2 + |\alpha_j|^2 + 2Re\{\alpha_i\alpha_j^* e^{i\frac{(E_j-E_i)t}{\hbar}+i(\varphi_i-\varphi_j)}\}.
\end{aligned}$$

Processes with different parity, such as the interference between shake-off and ionization of the shake-up wave packet by one-photon absorption appear in the odd coefficient β_1. Quantum beats between states i and j show up in the even coefficients β_0 and β_2. Additionally β_0 (not plotted) has a strong background contribution $|\alpha_E|^2$ from the shake-off, which is missing in β_2. Besides the quantum beats that are clearly visible in the Fourier analysis in Fig. 3(f), the direct-indirect interferences with the reference wave packet are still observable. These are due to ionization of the shake-up wave packet by absorbing two probe photons. Fig. 2(b) indicate the different processes considered in this discussion.

The probability amplitude corresponding to two-photon absorption with final angular momentum ℓ ($\ell = 0, 2$) can be expressed as:

$$\begin{aligned}
M_{ind}^{(2)}(\theta,\phi) &= [e^{i\frac{(E-E_i)t}{\hbar}+i\varphi_i}\alpha_{i,\ell}^{(2)} + e^{i\frac{(E-E_j)t}{\hbar}+i\varphi_j}\alpha_{j,\ell}^{(2)}] \\
&\quad \times e^{i\phi_{ind}^{(2)}} Y_\ell^0(\theta,\phi)\,, \qquad (8)
\end{aligned}$$

where $\alpha_{i,\ell}^{(2)}$ indicate the probability amplitude for shake up to the i state, followed by two-photon absorption and $\phi_{ind}^{(2)}$ is the associated two-photon ionization phase [12, 13], which, for simplicity, we assume to be state and energy-independent. β_1 is unchanged while β_2 becomes:

$$\begin{aligned}
\beta_2 &\propto |\alpha_i|^2 + |\alpha_j|^2 + 2Re\{\alpha_i\alpha_j^* e^{i\frac{(E_j-E_i)t}{\hbar}+i(\varphi_i-\varphi_j)}\} \\
&\quad +2Re\{\alpha_E\alpha_{i,2}^{(2)*} e^{i\frac{(E-E_i)t}{\hbar}+i\varphi_i+i\delta\phi^{(2)}} \\
&\quad +\alpha_E\alpha_{j,2}^{(2)*} e^{i\frac{(E-E_j)t}{\hbar}+i\varphi_j+i\delta\phi^{(2)}}\}, \qquad (9)
\end{aligned}$$

with $\delta\phi^{(2)} = \varphi_{dir} - \phi_{ind}^{(2)}$. β_2 includes both quantum beats and direct-indirect interferences with two-photon absorption.

Comparing the signal strength in Fig. 3(d) and (f) the center of intensity within the tilted lines is shifted towards higher energies for β_2. The two-photon case takes the electron to a higher observation energy clearly observable for the $3s$ state. Both quantum beating and interferences involving absorption of two probe photons, scale with the square of the amplitude of the probe field $|E_{probe}|^2$.

IV. LIFETIME AND PHASE RETRIEVAL

In order to illustrate that our technique can be used to resolve bound state dynamics we artificially impose a short lifetime of 5 fs on the $3s$ state. To access the dynamics, the $3s$ contribution to the expansion coefficient $\beta_1(E,t)$ is filtered out using a window function in $S_1(E,E')$ and an inverse Fourier transform back to the time domain. Fig. 4 illustrates the different steps. In Fig. 4(a) $\beta_1(E,t)$ is shown with the corresponding Fourier analysis $S_1(E,E')$ in Fig. 4(b). The edges of the filter function are indicated as dashed lines in Fig. 4(b). $S_1(E,E')$, after filtering, is inverse Fourier transformed back to the time domain. The result is shown in Fig. 4(c). The separated $3s$ signal shows a clear decay. The $3s$ amplitude $|A_{3s}(t)|^2$ is also plotted. We determine a lifetime of 5 fs, in agreement with the imposed one.

Finally, we explain here how to retrieve the phases of the wave packet components from this type of measurements. We make again use of the fact that we can separate all states via the Fourier analysis $S_1(E,E')$. Window functions are used to filter out the contributions from each single state as explained in Fig. 4(a)-(c). In an experimental situation, t denotes the delay between the excitation pulse and the probe field and is not known in absolute value and we now replace t by $t - t_0$, where t_0 is the instant of excitation. The phase of the detected oscillation (see Fig. 4(c)) is given by:

$$\Delta\Phi(E,t) = \frac{(E-E_i)(t-t_0)}{\hbar} + \varphi_i. \qquad (10)$$

There is an additional phase term due to the scattering phase of the reference wave packet, but since we compare the interference signal for all the states at the same final energy this additional phase leads to a constant offset that is that same for all the states (see also the previous discussion). An illustration of the phase evolution is sketched in Fig. 4(d). For two states i and j the measured phase $\Delta\Phi(E,t)$ is plotted for three different observation energies E. Tracing the linear phase evolution back to its origin it will intersect at the same starting point t_0 for all observation energies - the time of creation of the wave packet. The phase offset at t_0 is the initial phase. The slope of each line is given by the difference between continuum and binding energy $E - E_i$, $E - E_j$.

To correctly retrieve the phase, φ_i, we need to know precisely the energy of the state, E_i, and the exact time of creation of the reference wave packet, t_0. This information can be obtained by utilizing the fact that we measure $\Delta\Phi(E,t)$ as a function of both delay and energy. E_i is already extracted from the Fourier transform, while t_0 is obtained by differentiating $\Delta\Phi(E,t)$ with respect to E, yielding $t - t_0$, from which t_0 can be determined [see Eq. 10]. We differentiate $\Delta\Phi(E,t)$ for observation energies from threshold up to 1 eV. The ionization time for the wave packet, t_0, is determined to -0.66 fs, or

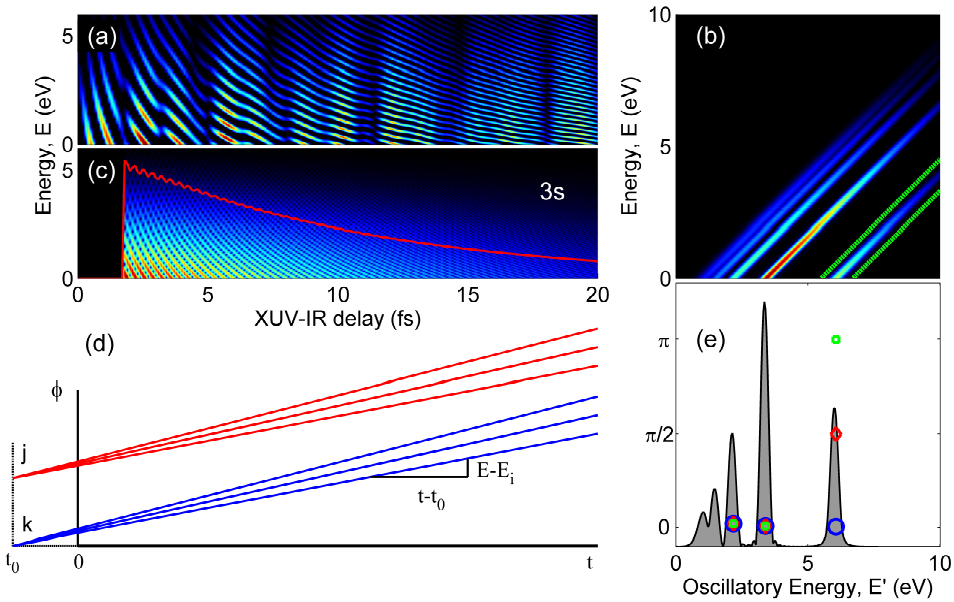

FIG. 4: (Color online). Lifetime analysis and phase retrieval. (a) $\beta_1(E,t)$ for shake-up excitation in a helium ion. (b) Fourier analysis of $\beta_1(E,t)$ and an example of a window function (green, dashed lines) to separate single states. (c) Back transformation into the time domain for the $3s$ state with a lifetime of 5 fs. (d) Idea of the phase retrieval: $\Delta\Phi$ for different continuum energies for two different states j and k. The evolution of $\Delta\Phi$ depends on the initial phase at time t_0. (e) Spectrum at threshold and retrieved phases for three calculation under different initial conditions.

one period of the probe field, which corresponds to the time when the sudden shake-up process takes place in the calculation. The initial time t_0 is independent of the state we choose for the analysis. We impose an initial phase of 0, $\pi/2$ and π to the $3s$ state for different runs of our calculation while leaving all other conditions identical. The result of our phase retrieval is shown in Fig. 4(e). As expected the initial phases for the $4s$ and $5s$ state are unaffected while the initial phases for the $3s$ state can be retrieved within the numerical precision to 0.01, 0.497π and 0.996π.

The phase retrieval method presented here relies on the fact that we measure the phase difference between the reference wave packet and the bound wave packet via a delayed ionization. As a consequence it is also possible to compare the phase difference with respect to other pathways, namely the two-photon ionization shown in Fig. 2(b). As we have shown previously we can easily distinguish between one- or two-photon ionization by means of the Legendre analysis. While the $\beta_1(E,t)$ coefficient contains information about the one-photon case the $\beta_2(E,t)$ gives us access to the two-photon contribution [compare Eqs. (7) and (9)]. Assuming an identical phase imprint for the shake-up transitions and the one photon-ionization the phase difference between the one- and two-photon ionization ($\phi_{ind} - \phi^{(2)}_{ind}$) would yield solely the phase contribution due to the second photon. This could be of great interest in time delays measurements [12].

V. CONCLUSION

In this article we have demonstrated that attosecond electron interferometry can be used as quantum state holography and retrieve the wavefunction of a quantum system in both amplitude and phase. The presented method can be further developed by also measuring these phases as a function of detection energy in which case the difference in scattering phases between the two ionization pathways could be directly measured.

This research was supported by the Swedish Foundation for Strategic Research, the Marie Curie program ATTOFEL (ITN), the European Research Council (ALMA), the Swedish Research Council, the National Science Foundation through grant number PHY-0701372 and the Knut and Alice Wallenberg Foundation. KJS ac-

knowledges support from the Ball Family Professorship.

[1] M. Sandtke and L. Kuipers, Nature Photonics **1**, 573 (2007).
[2] C. Leichtle *et al.*, Phys. Rev. Lett. **80**, 1418 (1998).
[3] T. C. Weinacht, J. Ahn, and P. H. Bucksbaum, Phys. Rev. Lett. **80**, 5508 (1998).
[4] T. C. Weinacht, J. Ahn, and P. H. Bucksbaum, Nature **397**, 233 (1999).
[5] J. Mauritsson *et al.*, Phys. Rev. Lett. **105**, 053001 (2010).
[6] V. Schmidt, Rep. Prog. Phys. **55**, 1483 (1992).
[7] T. Schneider, P. L. Chocian, and J.-M. Rost, Phys. Rev. Lett. **89**, 073002 (2002).
[8] A. Wirth *et al.*, Science **334**, 195 (2011).
[9] K. J. Schafer and K. C. Kulander, Phys. Rev. Lett. **78**, 638 (1997).
[10] K. Kulander and T. Rescigno, Computer Physics Cornmumcations **63**, 523 (1991).
[11] D. J. Kennedy and S. T. Manson, Phys. Rev. A **5**, 227 (1972).
[12] K. Klünder *et al.*, Phys. Rev. Lett. **106**, 143002 (2011).
[13] J. Dahlström *et al.*, Chemical Physics in press (2012).

Paper VIII

Attosecond Stark Effect in Molecules

Ch. Neidel, J. Klei, C. Yang, A. Rouzée, M. J. J. Vrakking; K. Klünder, M. Miranda, C. Arnold, T. Fordell, A. L'Huillier, M. Gisselbrecht, P. Johnsson and F. Lépine.

(2012) *Manuscript in preparation.*

Attosecond Stark Effect in Molecules

Ch. Neidel, J. Klei, C. Yang, A. Rouzée, M. J. J. Vrakking
FOM-Institute AMOLF, Kruislaan 407, 1098 SJ Amsterdam, The Netherlands & Max-Born Institut, Max-Born Strasse 2A, 12489 Berlin, Germany.

K. Klünder, M. Miranda, C. Arnold, T. Fordell, A. L'Huillier, M. Gisselbrecht, P. Johnsson
Department of Physics, Lund University, P. O. Box 118, SE-221 00 Lund, Sweden.

F. Lépine
Université Lyon 1; CNRS; LASIM, UMR 5579, 43 bvd. du 11 novembre 1918, F-69622 Villeurbanne, France.

ABSTRACT

We report two-color attosecond pump-probe experiments, where the time-dependent polarization of a neutral molecule under the influence of a moderately strong near-infrared laser field is monitored with attosecond time resolution. A series of small to medium-size molecules (N_2, O_2, CO_2 and C_2H_4) are exposed to a femtosecond IR laser pulse and a co-propagating attosecond pulse train, and pronounced oscillations are observed in the parent molecular ion yield as a function of the pump-probe delay. Our measurements are the first demonstration of the probing of attosecond time-scale electron dynamics in neutral molecules and may be regarded as a first example of attosecond Stark spectroscopy in molecules.

Introduction

The emergence of attosecond laser techniques permits addressing fundamental questions regarding the interactions between light and matter, by providing access to electronic properties in real time (*1*). One of the most fascinating possible applications of attosecond pump-probe spectroscopy concerns the observation of electronic motion on the atomic scale in atoms, molecules and condensed matter. Using intense attosecond laser pulses generated by high-harmonic generation (*2*), in future, it may be possible to configure pump-probe experiments where a first, attosecond pump pulse creates a non-stationary electronic state whose time-dependent evolution is subsequently probed by a second, attosecond probe pulse that interacts with the system after a variable delay. Already, the combination of phase-locked femtosecond and attosecond laser pulses has been used to unravel a wide range of attosecond timescale phenomena in atoms (*3-6*), molecules (*7*) and on surfaces (*8*). In these experiments, several spectroscopies have already been applied towards the elucidation of attosecond timescale dynamics, including photoelectron spectroscopy (streaking (*9, 10*) and RABBITT (*11*) measurements), ion momentum imaging (*7*) and transient absorption (*5*). Efforts to experimentally probe the inner workings of molecules and to reveal the electronic motion in neutral molecules on the attosecond timescale have so far not been successful, since the observed attosecond timescale effects were thus far attributed to dynamics in the ionized system (*7, 12, 13*). These first experimental efforts have been complemented by theoretical work that have described several scenarios for inducing and observing attosecond time-scale electron dynamics in neutral molecules (*14*). In general, an experimental approach that would allow us to observe these attosecond electron dynamics remained to be developed. Addressing, in particular, the probing of this electron dynamics, Yudin and co-workers studied ionization of a coherent superposition of electronic states of H_2^+, and concluded that the motion of the time-dependent electron wave packet could be inferred from photoelectron energy and angular distributions measured upon attosecond XUV ionization (*15*).

It is known that the absorption of a photon requires that both the photon energy and momentum are absorbed. Consequently, shorter wavelength radiation is absorbed in the vicinity atomic nuclei (*16*), explaining, for example, why in X-ray photo-absorption inner-shell excitation is favored over valence excitation. Therefore, we may anticipate that

attosecond XUV/X-ray pulses should be very suitable for probing time-dependent electron localization in molecules, since the short wavelength/high photon energy of the attosecond pulses provides a highly local, time-dependent probe of the electron density near the atomic centers in the molecule. For example, molecules where the electron density is periodically modulated as a result of the interaction with a moderately strong laser field (*17*), might display a sub-cycle time-dependence in the photoionization yield under the influence of a time-delayed attosecond laser pulse. The observation of polarization-induced time-dependent changes to the photo-absorption yield is consistent with the occurrence and observation of Stark shifts in molecular photo-absorption. Indeed, attosecond probing of IR-induced molecular electron dynamics may be regarded as an ultrafast variant of molecular Stark spectroscopy, which is a well-established tool for extracting information on structure and chemical bonds in molecules (*18*). In molecular Stark spectroscopy, a sample experiences a static (or oscillatory) electric field that induces a Stark shift of the electronic states and the variation of the absorption of incident light tuned to a specific resonance is measured. In other words, Stark spectroscopy measures the sensitivity of a given transition to an external electric field, thereby providing direct information on the polarizabilities of the molecular sample. We note that the possible advantages of the use of an intense laser field in Stark spectroscopy (enabling extensive control over the field strength, oscillation period, etc.) was already pointed out in (*18*).

In this article we present first results illustrating - with attosecond time resolution - the effect of a moderately strong near-infrared laser field on the photoionization efficiency of a series of small to medium-size molecules. In the experiments, a moderately strong near-IR, femtosecond laser pulse interacts with a molecule and induces a time-dependent polarization that is probed by attosecond photoionization. Experiments have been performed for relatively simple diatomic molecules like N_2 and O_2, but also for CO_2 and mid-size molecules like Ethylene (C_2H_4). Our results demonstrate the viability of attosecond Stark spectroscopy as a tool for observing time-dependent electron dynamics that is applicable to a large variety of molecules.

The principle of our measurements is illustrated in Figure 1, which shows the results of TDDFT calculations performed on a C_2H_4 molecule that is polarized by a static electric field. First the ground state geometry of the molecule was optimized using DFT. Then, the oscillator strength was computed in the linear response approximation, using the B3LYP

functional and an extended 6-31G*(d) basis set. The calculations were performed with and without an 10^9 V/cm external electric field that was applied along the molecular axis. Such a field is too weak to field ionize the molecule, but, as shown in Figure 1, can induce significant changes in the absorption spectrum of the molecule. The modifications of the photo-absorption spectrum are due to the Stark induced modification of the electronic states, as well as the accompanying changes in the transition probabilities for the individual transitions between molecular orbitals. In other words, the induced modification of the electronic properties of the molecule under the influence of the electric field induces a modification of its absorption properties. The electronic response of the molecule to the electric field depends on the polarizability α, the energy is given by $E(F) = E_0 + \alpha.F^2$. For a transition between two states, this leads to: $\Delta E(F) = \Delta E_0 + \Delta\alpha.F^2$. The field-dependent variations of the molecular photo-absorption result from changes in these transitions and thus from the molecule´s polarizability.

The results presented in Figure 1 illustrate the response of C_2H_4 to a static electric field in order to introduce the concept of attosecond Stark spectroscopy. A more realistic theoretical description of our experiment requires using the TDDFT real time/real space framework. In Figure 2 calculations are shown illustrating the dynamical response of an N_2 molecule interacting with a femtosecond IR pulse synchronized to a co-propagating attosecond pulse train (APT). In our approach, the ground state orbitals of the molecule were first determined in a static DFT calculation. Next the molecule was exposed to a 30 fs long, 800 nm near-IR laser pulse polarized along the N_2 inter-nuclear axis with a peak intensity of $5*10^{12}$ W/cm^2, in order to minimize the ionization of the molecule. As illustrated in Figure 2, the light-induced dipole adiabatically follows the near-IR light electric field. This is due to the fact that the laser frequency is not resonant and therefore doesn't generate electronic excited states (*14*). Moreover, the light intensity is chosen to minimize the ionization.

The time-dependent dipole oscillation classically corresponds to the motion of the electron along the molecular axis. This motion is illustrated in the Figure 2, where the time-dependent electron localization function (TD-ELF) defined by Silvi and Savin (*19*) is plotted, allowing one to observe the laser-induced modifications of the molecular bonds. When no field is present, the TD-ELF shows the 2 lone-pair orbitals localized on the N-atoms and the triple bond expected in N_2 in between. The time-dependent polarization of the molecule corresponds to a dynamical modification of these bonds, in which the electron

alternatively localizes on one or the other side of the molecule. This laser induced dynamical modification of the molecular bonds has been previously considered in TDDFT calculations (*17*), but until now no experiment could resolve these processes in real time. The time-dependent electron localization in the molecule can induce a variation of the light absorption. As a consequence, the absorption of XUV light and therefore the ionization efficiency can vary when the molecule is under the influence of a fs pulse. This is illustrated in Figure 2, where the ionization yield of a molecule resulting from the interaction with an APT (300 as individual pulse duration, 10^9 W/cm^2 XUV, one pulse per half IR cycle) and a fs IR pulse. The ionization yield is defined as the total charge transferred into the continuum at the end of the 500 fs long integration time. The calculation uses a finite box (R=5Å) followed by an absorbing region where the wave function vanishes. The size of the box remains modest, since due to the low IR intensity and XUV induced ionization, no returning electrons are expected. Moreover no reflection from the absorbing boundaries is observed. The pump-probe ionization signal was determined by calculating the total charge for different delays between the APT and the IR light. Oscillation of the ionization yield is observed and these oscillations are following the variation dipole and therefore of the light electric field. This demonstrates that the time-dependent polarization of the molecule can be observed through the measurements of the ionization efficiency.

The experimental realization uses a Mach-Zehnder-type interferometer. One arm of the interferometer contains the near-infrared (800 nm) pump beam, whose intensity was varied by using the combination of a half wave-plate and a thin polarizer at Brewster angle. The XUV APT that was used as probe beam was generated in the other arm of the interferometer, by focusing approximately 1 mJ, near-infrared (800 nm) laser pulses into a gas cell containing various rare gasses (Kr, Xe, Ar). An Al thin film (200 nm thickness) spectrally filtered the radiation and eliminated the IR fundamental beam as well as low-order harmonics with orders below 11. The probe beam was recombined with the IR pump beam using a holey mirror which simultaneously serves as a hard aperture to spatially filter out the long trajectories in the HHG process (*20*). The recombination mirror was slightly convex to match the wave fronts of the XUV and IR pulses. The XUV probe and IR pump beams were focused onto the molecular target by a toroidal mirror. The molecular target was introduced into the experiment by a pulsed valve (PMB) or a capillary integrated in the

repeller electrode (*21*) of the velocity map imaging spectrometer (*22*) . Using a static electric field, ions formed in the experiment were accelerated towards a set of micro-channel plates followed by a phosphor screen and a CCD camera. Both ion velocity map images and time-of-flight measurements were performed. To corroborate the results, some of the experiments were repeated in different laboratories, located at Lund University, AMOLF (Amsterdam) and MBI (Berlin). Illustrating the wide applicability of APTs to Stark spectroscopy, as discussed in the theory section, measurements were made both for simple diatomic molecules (N_2 and O_2) and for polyatomic molecules CO_2, C_2H_4. The IR intensity was chosen avoiding any significant ionization of the molecule, and the XUV photons were generated in Xe, in order to restrict the ionization to valence states.

In figure 3, the variation of the N_2^+ yield versus pump-probe delay is shown. We observe an oscillation with a modulation depth of 0.5%. Notice that the appearance of these oscillations is very sensitive to the properties of the light pulses. The modulation vanishes when higher XUV photon energies are used (harmonic generation in Ar or Kr) or when IR intensity is decreased. In addition, when the IR intensity is increased to the point where it induces noticeable ionization of the molecules, the oscillations also vanishes. Similar experiments were performed on other molecules and oscillations with various amplitudes are shown for O_2^+ (0.5%), CO_2^+ (0.3 %) and $C_2H_4^+$ (1%). Notice that the amplitude of the oscillations is smaller than the one calculated with TDDFT. This is expected due to several averaging effects: first of all, in the experiment the molecules are not aligned along the laser polarization; moreover the signal measured corresponds to focal volume averaged effect where the IR intensity is not constant. Nevertheless, the amplitude of the oscillations is a function of the chosen molecule. This is explained by the fact that the response of the molecule to the driving IR field is determined by the polarizabilities of the states involved in the absorption of the XUV light. For the chosen molecules the total polarizability are: O_2 (1.562 A^3), N_2 (1,71 A^3), CO_2 (2.507 A^3), C_2H_4 (4.18 A^3) and therefore increases with the size of the molecule. This is consistent with the amplitude of the oscillations measured. In fact the XUV induced ionization is sensitive to the local electron localization, as a consequence, the time-dependent modification of the chemical bond that is visualized by the TD-ELF can be directly probed. Further theoretical and experimental developments will allow us to characterize how this is shown in our attosecond stark approach.

Conclusion:

In this article we have demonstrated that IR driven attosecond electron dynamics in neutral molecules can be observed through variation of ionization efficiency. In our experiment, the electrons are driven in a neutral molecule by a non-resonant mid-IR fs pulse. This motion is probed by using a train of attosecond pulses that ionizes the molecule. The ionization efficiency varies with the pump-probe delay, which traduces the time-dependent localization of the electrons in the molecule. Moreover, the amplitude of the time-dependent oscillations is a direct signature of the electronic properties of the molecule and depends on the polarizabilities of the electronic states involved in the XUV absorption. It is therefore the first implementation of Stark spectroscopy on the attosecond timescale. Our approach could be used to observe electron dynamics in a complex molecule, to follow bond formation and deformation and to reconstruct the 3D polarizability of the molecular electronic states. We have shown that it can be applied to any molecule.

Acknowledgements

This work is part of the research program of the Stichting voor Fundamenteel Onderzoek der Materie (FOM), which is financially supported by the Nederlandse Organisatie voor Wetenschappelijk Onderzoek (NWO). This research was supported by the Marie Curie program ATTOFEL (ITN), the European Research Council (ALMA), the Access programme and Joint Research Activity ALADIN of Laserlab-Europe II, the Swedish Foundation for Strategic Research, the Swedish Research Council, the Knut and Alice Wallenberg Foundation, the European initiative of infrastructures, and the Sträng foundation.

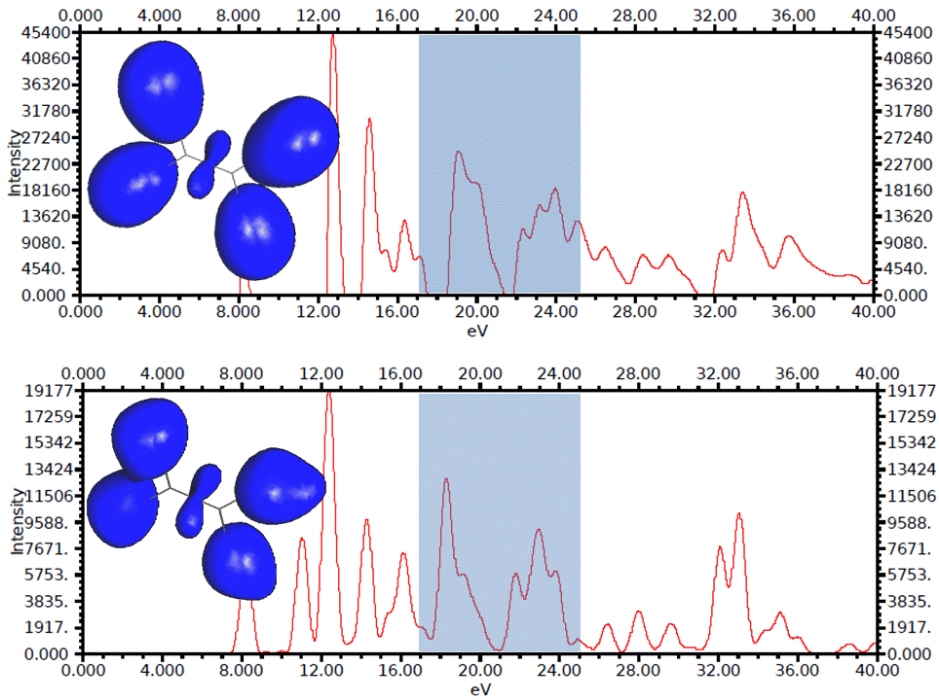

Figure 1:

TDDFT calculation of the photoabsorption spectrum of C_2H_4 in the presence of a static electric field. A comparison between the calculated spectrum without (A) and with a 10^9 V/cm dc electric field (B) shows strong modifications due to field-induced changes in the electronic transitions. Calculated ELF shows the modification of the chemical bond due to the polarization of the molecule by the electric field.

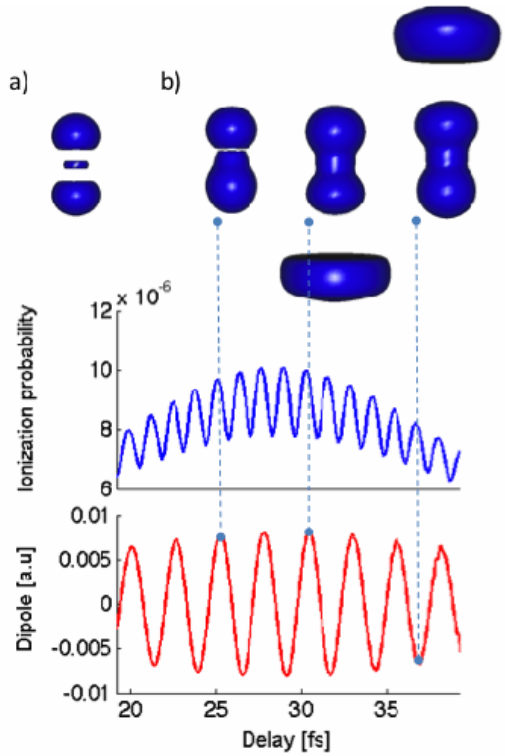

Figure 2:

Calculated "movie" of the laser driven electron motion. We show the time-dependant electron localization function in the case of N_2 interacting with a 30 fs, 800 nm, 10^{12} W/cm^2 laser pulse. On the first image a), the triple covalent bond is observed while later in the pulse the bond is modified by the laser field b). The TD-DFT calculation of the ionization probability, as a function of the delay between the fs pulse and attosecond pulse train shows strong oscillations. The oscillations observed are correlated with the variation of the dipole of the molecule in the laser field. The maximum ionization is obtained when the attosecond pulse is synchronized with the maximum of the electric field.

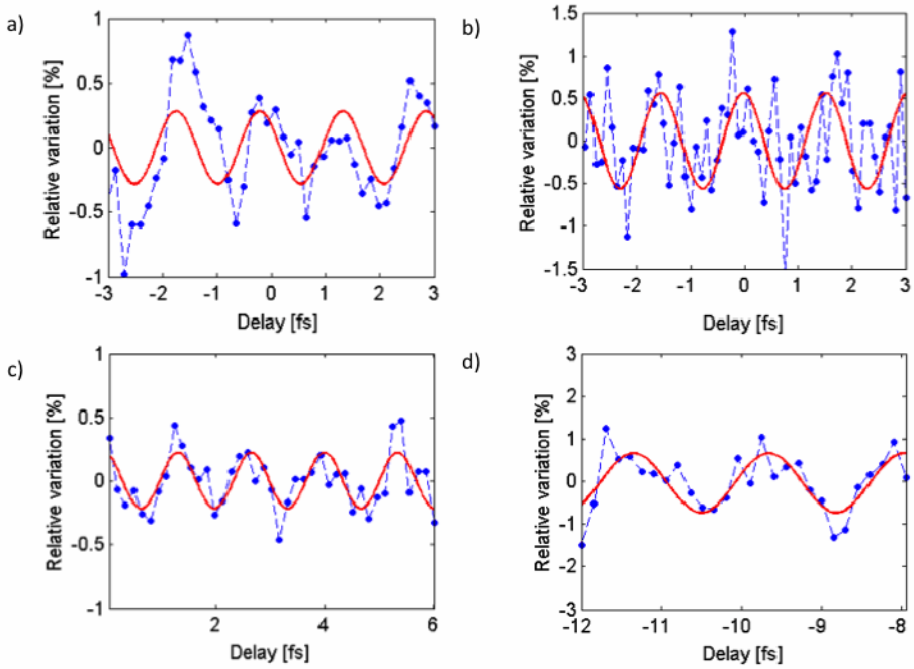

Figure 3:

Experimentally measured ion yields for the diatomic molecules a) N_2 , b) O_2 , c) CO_2, d) C_2H_4 as a function of the delay between the IR pump and the XUV probe pulses. The yield oscillates with a periodicity corresponding to half the period of the IR field. These oscillations traduce the attosecond electronic motion while the amplitude of these oscillations varies for different molecules.

References

1. F. Krausz, M. Ivanov, *Reviews of Modern Physics* **81**, 163 (Jan-Mar, 2009).
2. P. Agostini, L. F. DiMauro, *Reports on Progress in Physics* **67**, 813 (2004).
3. M. Drescher *et al.*, *Nature* **419**, 803 (2002).
4. M. Uiberacker *et al.*, *Nature* **446**, 627 (2007).
5. E. Goulielmakis *et al.*, *Nature* **466**, 739 (Aug 5, 2010).
6. M. Schultze *et al.*, *Science* **328**, 1658 (Jun 25, 2010).
7. G. Sansone *et al.*, *Nature* **465**, 763 (Jun 10, 2010).
8. A. L. Cavalieri *et al.*, *Nature* **449**, 1029 (2007).
9. J. Itatani *et al.*, *Physical Review Letters* **88**, 173903 (2002).
10. R. Kienberger *et al.*, *Science* **297**, 1144 (2002).
11. P. M. Paul *et al.*, *Science* **292**, 1689 (2001).
12. F. Kelkensberg *et al.*, *Physical Review Letters* **107**, 043002 (Jul 19, 2011).
13. W. Siu *et al.*, *Physical Review A* **84**, 063412 (2011).
14. F. Remacle, M. Nest, R. D. Levine, *Physical Review Letters* **99**, 183902 (2007).
15. G. L. Yudin, S. Chelkowski, J. Itatani, A. D. Bandrauk, P. B. Corkum, *Physical Review A* **72**, (2005).
16. J. W. J. Verschuur, H. B. van Linden van den Heuvell, *Chemical Physics* **129**, 1 (1989).
17. T. Burnus, M. A. L. Marques, E. K. U. Gross, *Physical Review A* **71**, (Jan, 2005).
18. G. U. Bublitz, S. G. Boxer, *Annual Review of Physical Chemistry* **48**, 213 (1997).
19. B. Silvi, A. Savin, *Nature* **371**, 683 (Oct 20, 1994).
20. R. Lopez-Martens *et al.*, *Physical Review Letters* **94**, 033001 (2005).
21. O. Ghafur *et al.*, *Review of Scientific Instruments* **80**, 033110 (2009).
22. A. T. J. B. Eppink, D. H. Parker, *Review of Scientific Instruments* **68**, 3477 (1997).